Synthesis and characterization of new functional metal oxides

Thesis submitted in accordance with the requirements of the University of Liverpool for the degree of Doctor in Philosophy

by Christopher Ian Thomas

September 2010

Synthesis and characterization of new functional metal oxides

Christopher Ian Thomas

The synthesis and characterization of a number of functional ceramics are presented in this thesis with a view to use in either solid oxide fuel cells or multiferroic devices.

Chapter 1 gives an introduction to solid oxide fuel cells and multiferroic materials, the chapter also introduces the main structures that are investigated in the thesis. Both solid oxide fuel cells and multiferroic materials are active areas of research for solid-state scientists. Multiferroic materials are seen as useful materials for the next generation of electronic memory applications while fuel cells can be used for energy applications. Chapter 2 describes the experimental methods used to synthesize and characterise the materials.

The later chapters deal with the results of the synthesis efforts and the subsequent characterization. Chapters 3-5 deal with materials synthesised under ambient pressure with a focus on use in fuel cells. Chapter 3 investigates oxide ion conduction in the melilite structure for use as electrolytes. The conduction mechanism in melilites is interstitial conduction rather than the more common vacancy conduction mechanism. Chapter 4 investigates the pyrochlore and fluorite structures for use as anodes. During the investigations a zirconolite-3T phase was also synthesized. Chapter 5 as well as investigating Y and Yb doped Sr_2CeO_4 for use as a proton-conducting electrolyte (rather than an oxide ion conducting electrolyte such as melilite) also presents attempts to synthesize RP2 structures as potential anodes.

Chapter 6 deals with materials synthesized under high pressure for use as multiferroic materials. High-pressure methods allow structures that cannot be synthesized under atmospheric pressure to form and be investigated. Many materials discovered at high pressures have since been synthesized as thin films.

Chapter 7 summarises all of the work carried out and points to future directions of the work presented.

Acknowledgements

Firstly I would like to thank my supervisors Professor Matthew Rosseinsky and Dr John Claridge for giving me the opportunity to work in Liverpool, I have learnt a great deal from our discussions.

I would also like to thank all of the people who I have worked with over the years both from the MJR group as well as the Fogg and Khimyak groups, in particular I wish to thank Matthew, Jamie, Sam and Sean. Outside of the lab I would like to thank the members of John Mitchells GAA for both providing a break from chemistry and for keeping me fit.

Finally I would like to thank my family who have supported me during my time at Liverpool.

The work presented in this thesis was carried out by myself, except where stated, at the Chemistry Department, University of Liverpool between October 2006 and March 2010 under the supervision of Prof. Matthew J. Rosseinsky and Dr John B. Claridge. This work has not been submitted for any other degree at this or any other university.

Chris Thomas Date

Contents **Page**

Chapter 1 : Introduction

Mankind has used ceramic materials for thousands of years starting with the use of pottery in prehistoric times to make pots and decorative items. The word ceramic is derived from the Greek keramikos derived from keramos meaning "of pottery" [1]. However there is an earlier Indo-European base for keramos meaning 'to burn' so originally keramos and therefore ceramic meant 'the burnt stuff'. The burnt reference alludes to the early ceramic production method of heating local clay-rich earth in the fire or in primitive kilns. As some local earth produced more desirable ceramics, trade in ceramic objects and consequently development started allowing present-day archaeologists to date ceramic finds. By the 20th century ceramics began to be used for applications apart from traditional uses as containers and building materials such as use in electrical components. Development of these functional ceramics has continued and today research into these materials forms a large part of solid-state chemistry and physics. Looking forward to the next century significant challenges face mankind such as climate change and depletion of natural resources and new materials will be required to help meet these challenges.

The aim of the work reported in this thesis is to synthesize and characterize new functional ceramic materials. The first section deals with materials synthesized at atmospheric pressure for potential use in fuel cells while the second section deals with materials that have been synthesized at high pressure. To introduce the work the remainder of this chapter is divided into three sections, described on the following page, to explain the purpose of the research and structure of the ceramic materials presented in the thesis.

1) **Fuel cells.** Fuel cells have been proposed as one method of reducing green house gas emissions and so research into the area has greatly increased in recent years. This section briefly explains fuel cells, focusing on solid oxide fuel cells, as materials for this type of fuel cell were the target materials for this thesis.

2) **Multiferroics.** Multiferroics have been suggested as materials for novel memory applications as they posses more than one order parameter. This section briefly explains the types of magnetic and electric ordering that can be used in multiferroics.

3) **Structures.** Ceramic materials are capable of forming a vast variety of structures, in this section only the structures that are used in this thesis are presented.

1.1 Fuel cells

Fuel cells are devices that convert chemical energy directly into electrical energy without first converting heat into mechanical energy. German scientist Christian Friedrich Schönbein[2] while conducting electrolysis experiments discovered the principle of the fuel cell, Sir William Grove then built the first fuel cell which he termed a "gas voltaic battery"[3] in 1839. The reasoning behind these early experiments into fuel cells was that if running an electric current through a substance (usually water) produced gases (hydrogen and oxygen), when these gases react a current should be produced. The term 'fuel cell' is credited to Ludwig Mond and Carl Langer who in 1889 were using air and coal gas in their cells[4] showing the early potential of fuel cells to use fossil fuels.

There are many different types of fuel cell normally characterized by the type of electrolyte used such as the polymer electrode membrane (PEM), molten carbonate fuel cell (MCFC) and the solid oxide fuel cell (SOFC) . Figure 1-1 gives a schematic of an oxide ion conductor SOFC .

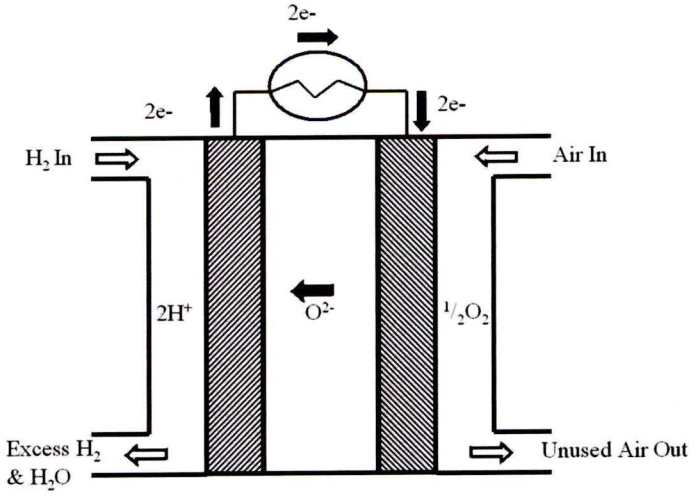

Figure 1-1 Fuel cell diagram with empty arrows showing gas flow and solid arrows showing the completed circuit.

In Figure 1-1 from left to right the reaction at the anode produces $2H^+$ and $2e^-$ (Equations 1-1). These electrons move through the external circuit providing useable current. At the cathode the electrons combine with O_2 to form O^{2-} ions (Equation 1-2) which can move through the electrolyte where they react with the H^+ ions at the anode (Equation 1-3) and so complete the circuit. A proton conducting SOFC would look much the same except that the H^+ ions rather than the O^{2-} ions would move through the electrolyte.

$$1)\ 2H_2 \leftrightarrow 4H^+ + 4e^-$$

$$2)\ O_2 + 4e^- \leftrightarrow 2O^{2-}$$

$$3)\ 4H^+ + 2O^{2-} \leftrightarrow 2H_2O$$

Equations 1-1, 1-2 and 1-3 describe the processes at the anode (1+3) and cathode (2).

Solid oxide fuel cells have particular advantages over other types of fuel cells such as modularity and fuel flexibility[5] with the ability to use a range of fuels from high purity H_2 to readily available hydrocarbons[6]. If hydrocarbons are used the emissions of NO_x from a SOFC are negligible compared to a traditional heat engine[7]. Having this fuel flexibility allows SOFCs to be used a bridging technology from the hydrocarbon economy to the possible future hydrogen economy. When in operation SOFCs produce large amounts of waste heat that can either be used in a secondary generation system (such as a gas turbine) or as part of a combined heat and power unit (CHP). However current SOFCs require high temperatures to allow the ions to become mobile and the cell to operate efficiently. For example Yttria Stabilized Zirconia (YSZ) based systems require temperatures above 700 °C[8] and above 500 °C for gadolinium doped cerium oxide (CGO) based systems.[9] At these elevated

temperatures thermal expansion and reactivity of the fuel cell components becomes problematic making fuel cell assemblies that operate at lower temperatures desirable[10].

SOFCs can be split into several component parts each with its own set of material requirements:

1) Anode: The anode due to being in contact with both the fuel and the electrolyte must both be stable in a reducing atmosphere and must not react with the electrolyte. Exhaust gasses such as steam (Figure 1-1) must also be considered, as must impurities such as sulfur in the fuel that can react with the anodes. Anodes should also be mixed ionic\electronic conductors.

2) Cathode: Cathodes at the opposite site of the fuel cell must be stable in the oxidizing atmosphere present at the cathode and again must not react with the electrolyte. Cathodes also should be mixed conductors.

3) Electrolyte: ionic conductors with a transport number close to unity are desirable as electronic conduction across the electrolyte reduces current in the external circuit. As the electrolyte is in contact with both the anode and the cathode the electrolyte cannot react with either.

4) Interconnect: The interconnect is a material that serves as an electrical conductor between two fuel cells in a stack and keeps the cathode and anode gases separate. Interconnects must be both good electronic conductors and ionic insulators, also interconnects must be stable in both the cathode and anode gasses. They must also be stable with respect to both the anode and cathode materials that they are in contact with to prevent degradation of the cell.

1.2 Introduction to multiferroics

Schmid[11] used the term multiferroic in 1994 to describe materials with two or more ferroic orders (e.g. magnetic, electric, elastic) at the same time and that can couple. General usage of the term has now included antiferromagnetic ferroelectrics, in this thesis, the term multiferroics implies simultaneous ferroelectric and magnetic ordering rather than ferroelastic ordering. For use in memory applications the multiferroic should ideally possess a strong magnetic moment that can couple to a strong ferroelectric moment at room temperature.

1.2.1 Magnetic order

Every material exhibits some kind of magnetic behaviour and there are many different origins of magnetic behaviour proposed for different materials. Measurement of the magnetic behaviour both as a function of temperature and field can often help in the determination of the cause of the observed behaviour. Interpretation of magnetic measurements however is often complicated leading to the Encyclopaedia Britannica stating 'few subjects in science are more difficult to understand'[12]. Magnetic behaviour is often due to ordering and as there are several types of magnetic ordering the main ones are described in this section.

1.2.1.1 Paramagnetic

In the classical interpretation of a paramagnet, each atom, molecule or ion is assigned a magnetic dipole moment. When an external field is applied these dipoles will attempt to align along the direction of the field. However they are unable to do so as thermal motion randomises the orientation of the dipoles. The simplest form of paramagnetism is Curie paramagnetism (paramagnetism that obeys the Curie law in Equation 1-4)

Paramagnets that obey the Curie are relatively uncommon, more often paramagnets follow the Curie -Weiss law variation where in addition to the Curie constant (C) and the temperature (T) a further parameter θ is introduced. θ is the Weiss temperature and is typically positive for ferromagnets and negative for antiferromagnets.

$$\chi = C/T$$

Equation 1-4 Curie law where χ is the magnetic susceptibility, C is known as the Curie constant and T is the temperature in K.

$$\chi = C/(T-\theta)$$

Equation 1-5 Curie -Weiss law

When the inverse magnetic susceptibility ($1/\chi$) is plotted against temperature (T) the result for a material obeying the Curie-Weiss law should be a straight line with the intercept of the x axis being the Weiss constant (θ) and the gradient being the inverse of the Curie constant (C). For materials with more complex behaviour the Curie-Weiss law is usually applied to the highest temperature region with linear behaviour in the ($1/\chi$) versus (T) plot. Ideally the Curie-Weiss law should be fitted over a large temperature range (50-100) and at higher temperatures (>150 K) otherwise erroneous values can be obtained. A particular problem with the Curie-Weiss law occurs when the fitted region is actually a very slight curve (appearing linear to the eye) rather than a straight line as the Curie-Weiss law is only applicable to linear regions. To see if a region is curved or not the only real solution is to collect more data over a wider range but this is not always possible as maximum and minimum temperatures are determined by experimental setup. If the data shows a slight curve at high (>150 K) temperatures then often the true paramagnetic (linear) region is at >400 K .

If the dipole moments are represented by arrows showing the direction of the moment then the schematic diagram in Figure 1-2 can be used to represent a paramagnetic substance.

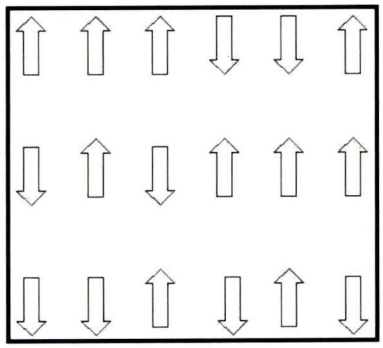

Figure 1-2 Schematic diagram of a paramagnetic substance with the randomly aligned arrows representing the magnetic dipole moments of the ions.

1.2.1.2 Ferromagnetic

If the dipoles align parallel to each other the cooperative magnetism that results is termed ferromagnetism. Above a certain temperature known as the Curie temperature (T_c) a ferromagnet will become a paramagnet again with a large drop in susceptibility. Ferromagnetic ordering is reinforced by applied external magnetic fields or by reducing the temperature. As T tends to 0 or a strong external magnetic field is applied the magnetisation reaches a limiting value known as the saturation magnetism (M_{sat}). Measuring the magnetization (M) versus field (H) not only reveals the magnitude of the external field required to saturate the magnetism but also the hysteresis of the sample. In a M versus H plot such as that in Figure 1-3 the intercept with the x (field) axis is the coercive field and the intercept with the y (magnetisation) axis is the remnant magnetization. Materials that have large remnant magnetizations are termed hard ferromagnets and those with small remnant magnetizations are soft ferromagnets.

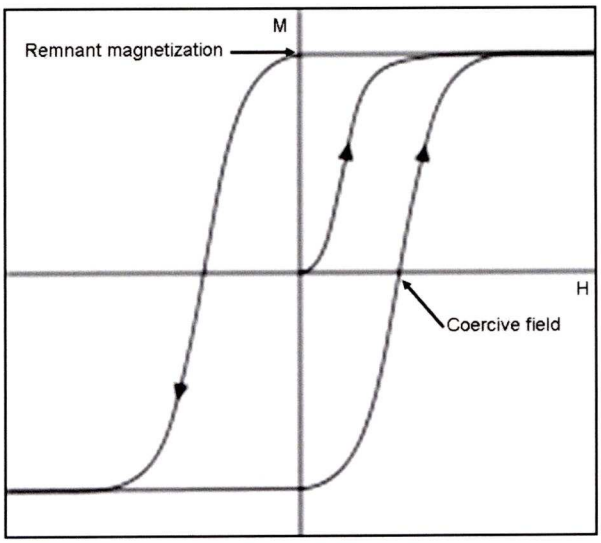

Figure 1-3 Schematic diagram of a M versus H plot showing the remnant magnetization and coercive field of a ferromagnetic material.

Ferromagnets are generally metallic conductors as the coupling of dipoles is partly transmitted by the conduction electrons. There are however some notably exceptions to this such as $LiNiO_2$ (Tc = 6 K) and EuO (Tc = 77 K). Figure 1-4 shows a schematic diagram of the dipole moments in a ferromagnetic substance.

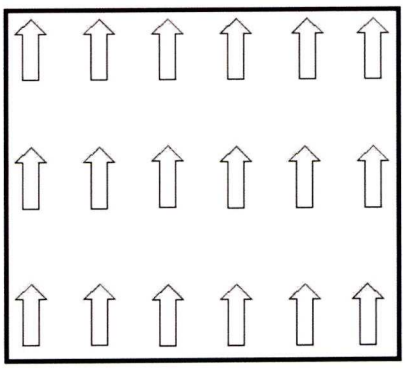

Figure 1-4 Schematic diagram of a ferromagnetic substance with the arrows representing the magnetic dipole moments of the ions.

1.2.1.3 Antiferromagnetic

If the dipoles instead of aligning parallel align antiparallel then an antiferromagnet will result. When a moderate external magnetic field is applied the moments will attempt to align parallel to the field. For some moments the coupling between dipoles is stronger than the interaction with the field some dipoles remain antiparallel to each other regardless of field direction. The susceptibility of an antiferromagnet increases until a transition point known as the Néel temperature (T_N) after which it declines sharply. Figure 1-5 shows a schematic diagram of the dipole moments in an antiferromagnetic substance.

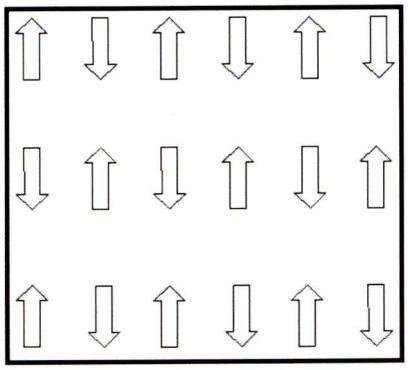

Figure 1-5 Schematic diagram of an antiferromagnetic substance with the arrows representing the magnetic dipole moments of the ions.

1.2.1.4 Ferrimagnetic

So far only one type of dipole has been considered, if a material has two sets of ordered dipoles with differing magnitude then ferrimagnetism may result. When an external field is applied to a ferrimagnet the stronger dipoles align parallel to the field, the weaker dipoles then align antiparallel to the field. The result is that the material has a net moment parallel to the field and so behavior is similar to a ferromagnet. Ferrimagnets however tend to be electrically insulating.

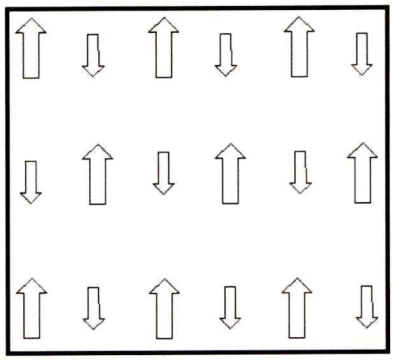

Figure 1-6 Schematic diagram of a ferrimagnetic substance with the arrows representing the magnetic dipole moments of the ions with the size of the arrows is a representation of the magnitude of the magnetic dipole.

1.2.1.5 Superexchange

The interaction of the magnetic ions in a solid can either be through direct exchange where there is direct coupling of magnetic ions or via superexchange where the coupling uses an intermediary ion. Superexchange was first proposed by Kramers[63] in 1934 when he noted that in MnO the manganese ions interact with each other despite the nonmagnetic oxygen ions being between them.

In the 1950's Goodenough and Kanamori[64-66] developed a set of empirical rules which for simple cases readily allows the prediction of the net magnetic exchange. The rules are based on the overlap and electron occupancy of the orbitals of the magnetic ions and the intermediary ion. Using the Pauli Exclusion Principle the electrons in the intermediary ion must be able to overlap with both the magnetic ions, if they can't one of the magnetic ions flip all of their spins so they can overlap with the intermediary. This is illustrated for perovskites in Figure 1-7 and Figure 1-8 where the magnetic ions are in octahedral coordination and the overlapping orbitals are d orbitals with an oxygen 2p intermediary. For the d^4 to d^5 case (Figure 1-7) both the oxygen 2p electrons can couple with d orbitals without breaking the Pauli Exclusion Principle meaning both magnetic moments are aligned parallel so the

interaction is ferromagnetic. For the d^5 to d^6 case (Figure 1-8) for the Pauli Exclusion Principle to hold one of the ions needs to flip (d^5 flipping is shown) making the magnetic moments of the ions antiparrallel so the interaction is antiferromagnetic.

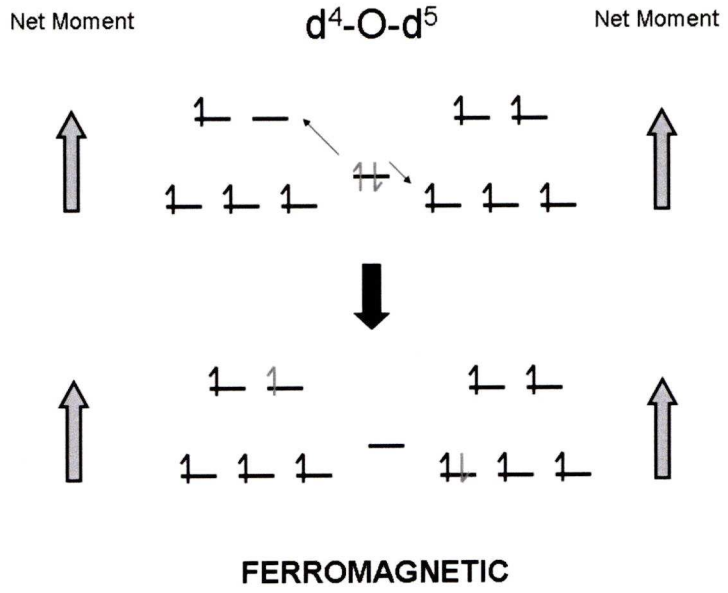

Figure 1-7 Diagram to show the superexchange interaction for a ferromagnetic interaction.

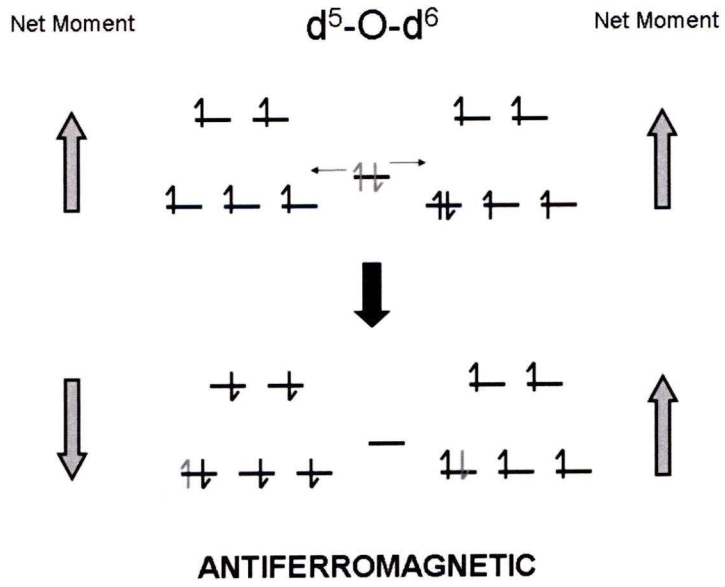

Figure 1-8 Diagram to show the superexchange interaction for an antiferromagnetic interaction.

The Goodenough-Kanamori rules break down when direct and superexchange mechanisms compete, when the bond angle deviates from 180°, when the electron

occupancy is non-static and when spin-orbit coupling becomes important. However despite these limitations the Goodenough-Kanamori rules are widely use to predict the magnetic behavior of compounds in solid state chemistry.

1.2.2 Electric order

In solids many types of electrical properties are possible including the dielectric and ferroelectric behaviour described here.

1.2.2.1 Dielectric

Dielectric materials are good electrical insulators and are used in capacitors and electrical insulators. For the material to be useful in practical applications the material should posses the following properties. They should have a *high dielectric strength* meaning they can withstand high voltages and remain insulating. Application of a voltage across a dielectric does lead to a polarization of charge within the material but long range motion of electrons or ions is prevented. Dielectric materials should also have low *dielectric loss* meaning the heat loss resulting from an alternating electric field should be minimized. Dielectric properties are defined by the materials behaviour between two plates of area A and separated by a distance d compared to a vacuum between the two plates. For the case of the vacuum if a voltage (V) is applied across the two plates charge (Q) will store on the plates according to **Equation 1-6** where C is capacitance. ε_o is the relative permittivity of free space (8.854×10^{-12} F m^{-1}). As ε_o is a constant the capacitance depends only on the dimensions of the capacitor.

$$Q_0 = C_0 V \qquad \textbf{Equation 1-6}$$

$$C_0 = \varepsilon_o A/d. \qquad \textbf{Equation 1-7}$$

When a dielectric material is placed between the plates then the value of the charge stored will alter allowing the dielectric constant (relative permittivity) to be calculated as

$$\varepsilon' = Q_1/Q_0 = C_1/C_o \quad \textbf{Equation 1-8}$$

Using C_o from $\mathbf{C_0 = \varepsilon_o A/d}$. Equation 1-7 the equation then becomes

$$\boldsymbol{\varepsilon' = C/\varepsilon_o \times d/A} \quad \textbf{Equation 1-9}$$

The magnitude of ε' depends on the degree of charge displacement or polarization that can occur in the material. For example $\varepsilon' \approx 1$ for air ε'= 5-10 for ionic solids and $\varepsilon' = 10^3$-10^4 for ferroelectric materials (section 1.2.2.2).

The polarizability (α) of a dielectic is defined by $\mathbf{p = \alpha E}$ Equation 1-10

$$p = \alpha E \quad \textbf{Equation 1-10}$$

Where p is the dipole moment that is induced by the local electric field, E. The polarizability, α , can be made up of a number of components (**Tan δ = ε''/ ε'** Equation 1-13)

$$\boldsymbol{\alpha = \alpha_e + \alpha_i + \alpha_d + \alpha_s} \quad \textbf{Equation 1-11}$$

The components of the polarizability are described as follows:

a) *Electronic polarizability*, α_e, is the displacement of the negatively charged electron clouds relative to the positive nucleus. Interestingly this occurs in all solids but in diamond it is the only source of polarization.

b) *Ionic polarizability*, α_i, is the relative displacement of the anions and cations in the solid and is the main source of polarization in ionic crystals.

c) *Dipolar polarizability*, α_d, is caused when the material has a permanent dipole that can change orientation and align with the electric field. Often the movement of the dipole can be 'frozen' at low temperatures meaning α_d is highly temperature dependant.

d) *Space charge polarizability*, α_s, occurs when the material is not a perfect dielectric and long range charge carrier migration can occur. For example in NaCl the cations migrate towards the negative electrode causing an electric double layer builds up. When the effect becomes appreciable high dielectric constants (10^6 to 10^7) can be measured but these are meaningless in the dielectric sense and the material should be regarded as a conductor.

The magnitude of these polarization components follows $\alpha_e < \alpha_i < \alpha_d < \alpha_s$ but note that not all materials show all components.

To investigate dielectric materials experimentally measurements over a wide range of a.c. frequencies are required as differing polarization components are active at differing frequencies. At low frequencies ($\approx 10^3$ Hz) all polarization components can contribute to the polarization, at $\approx 10^6$ Hz there is not enough time for charge build up (α_s component relaxed out). Higher frequencies cause more components to be relaxed out, at $\approx 10^9$ Hz dipoles can't reorient so α_d relaxes out and at $\approx 10^{12}$ Hz ionic polarizations don't occur so α_i relaxes. If a low frequency sinusoidal e.m.f. is applied across the dielectric the polarizations act to transmit energy through the dielectric material and are equivalent to an alternating current that leads the voltage by 90° in an ideal dielectric. As the cross product of the vectors I and V is zero there is no loss of energy but if at higher frequencies the ionic polarizations can't keep up the voltage begins to lead the current by less than 90° i.e. 90-δ. Now the current has a component (Isinδ) in phase with the voltage giving rise to loss of energy as heat (dielectric loss). If the permittivity, ε, is represented as a complex number (**$\varepsilon = \varepsilon' - j\varepsilon''$** Equation 1-12) the measured dieclectric constant, ε', forms the real part while the dielectric loss, ε'', forms the imaginary part.

$$\varepsilon = \varepsilon' - j\varepsilon'' \quad \textbf{Equation 1-12}$$

Dielectric loss is normally reported as the tangent of the angle of lag referred to as tan δ, it is often used as a measure of conductance and its relation to ε'' is shown in Equation 1-13.

$$\text{Tan}\,\delta = \varepsilon''/\varepsilon' \quad \textbf{Equation 1-13}$$

1.2.2.2 Ferroelectric

A ferroelectric material differs from ordinary dielectric materials as ferroelectrics have extremely large permittivities and they differ in response to an applied voltage. For a dielectric, as voltage increases so does the charge stored but a ferroelectric material saturates and displays hysteresis (similar to Figure 1-3 except now polarisation (P) verses volatage (V) instead of M versus H) as the material has a spontaneous polarisation. This spontaneous polarisation can be switched using an applied electric field and is similar to the ferromagnetic moment being switched by an applied magnetic field. Ferroelectricity is most often observed at low temperatures as thermal motion breaks down the dipole interactions leading to a paraelectric state (section 1.2.2.4). The temperature at which a ferroelectric becomes paraelectric is known as the Curie temperature (T_c). High dieclectric constants still occur above the T_c but when the electric field is removed there is no spontaneous polarisation.

Spontaneous polarisations are also present in pyroelectrics and piezoelectrics where the degree of polarisation is dependent on temperature and mechanical stress respectively. For a material to display a spontaneous polarisation the space group of the material must be non centrosymmetric[13] as a centrosymmetic space group causes polarisations to cancel out. The Landolt-Bornstein[14] series give hundreds of examples of ferroelectric materials all with non-centrosymmetric space groups. However although all polar materials are non centrosymmetric not all non centrosymmetric materials are polar. It remains possible for the polarizations (if

present) to cancel each other out in non centrosymmetric groups but it is required in centrosymmetric ones.

1.2.2.3 Antiferroelectric

Antiferroelectrics show similar behaviour to antiferromagnets except that instead of magnetic moments electric polarisations are involved. As in the antiferromagnetic case these align anti parallel to each other resulting in zero net polarisation.

Again above a certain temperature also known as the Curie temperature, T_c, antiferroelectrics become paraelectrics. Unlike ferroelectrics antiferroelectrics have low permittivity but these rise dramatically close to the T_c often by a factor of 10 or more. Antiferroelctrics can also convert to ferroelectrics on the application of a large enough electric field i.e. if the dipole interaction with the field becomes greater than the inter dipole anti parallel interaction. The magnitude of the field is temperature dependent.

Ferrielectrics are possible if the interactions of the electric polarisations produce an antiferroelectric interaction in certain directions only.

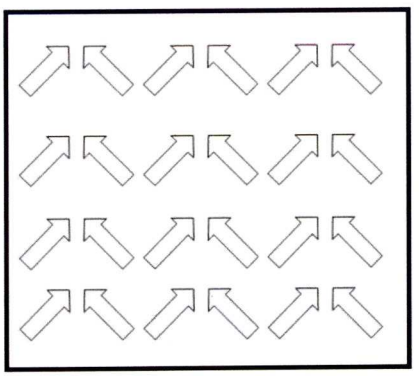

Figure 1-9 Schematic diagram of a ferrielectric with the arrows showing the electric dipole moments.

1.2.2.4 Paraelectric

Paraelectrics are materials that require an external electric field to become polarised with the polarization returning to zero when the field is removed. Paraelectricity

results when electric dipoles are unaligned but have the ability to reorient in an electric field to strengthen it. The response of ε' with temperature is given by the Curie-Weiss law (Equation 1-5) with ε' replacing χ.

1.3 Introduction to structures

There are many and varied structures that solid materials can adopt only a small selection of which are discussed in this thesis. Those structures that are considered include:

1) Perovskite (1.3.1)
2) Ruddlesden Popper (1.3.2)
3) Melilite (1.3.3)
4) Fluorite (1.3.4)
5) Pyrochlore (1.3.5)
6) Zirconolite (1.3.6)
7) Rhombohedral distorted fluorite (1.3.7)
8) Sr_2PbO_4 (1.3.8)

1.3.1 Perovskite

$CaTiO_3$ was discovered by German mineralogist Gustav Rose in 1839 and named after a Russian mineralogist L. A. Perovski [15] . Perovskite has since become the general description of a structural family where the ideal structure ABX_3 (A is a larger electropositive ion and B a small transition metal or main group element, X is normally O^{2-} or a halide ion). Despite being discovered in the 19th century it was not until the 1940's that the structure type began to be systematically studied[16]. Perovskites have since become the mainstay of the electroceramics industry worth

over twenty billion dollars per year[15]. The usefulness of this structure to industry is due to perovskites showing a range of properties from ferroelectric behaviour to superconductivity and colossal magnetoresistance. Perovskite is also of great interest to geologists as high pressure experiments have shown that the mineral that contains the majority of the silicate in the earths mantle is the perovskite structured $MgSiO_3$ [17]. In its ideal state the perovskite structure consists of corner sharing octahedrally coordinated B site ions with 12 coordinate A site ions sitting in the centre (see Figure 1-10) . However there are a number of possible distortions from this ideal structure such as tilting of the BX_6 octahedra, Jahn Teller distortions and lone pair effects. Lufaso[18] estimates that ideal cubic perovskites only make up approximately 10% of all perovskites, the other 90% showing some form of tilting distortion . The vast majority of perovskites are oxides or fluorides but other halides,[19] sulfides, [20],hydrides[21] as well as oxyfluorides[22] and oxynitides [23] have also been reported. When metals or rare earths occupy the X sites such as in $InOEu_3$[24] the resulting structure is termed an inverse perovskite (sometimes referred to as an antiperovskite) to emphasize the fact that the X sites are occupied by a rare earth not O.

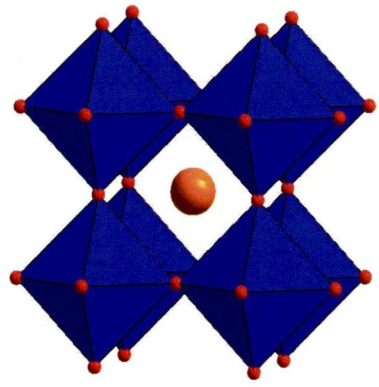

Figure 1-10 General perovskite structure, example shown high temperature Pm $\bar{3}$m form of $CaTiO_3$[25]. Ti is at the center of the blue octahedra with red spheres representing the O ions and the large orange sphere representing Ca.

1.3.1.1Tolerance factor

A method of investigating the distortion away from ideal is to use the Goldschmidt tolerance factor[26]. Equation 1-14 , shows how the tolerance factor, t, is related to the mean inter-atomic distances of the A and B coordination polyhedra (<A-O> and <B-O> respectively).

$$t = \langle A\text{-}O\rangle / \sqrt{2}\langle B\text{-}O\rangle$$

Equation 1-14 Goldschmidt tolerance factor

As the octahedral tilting is a result of the size mismatch between the size of the A site cation and the cavity formed by the octahedra the above equation quantifies this mismatch. Ideal cubic perovskites have $t \approx 1$ while $t \approx 0.85$ has been suggested as the stability limit for perovskites[27].

1.3.1.2 Glazer tilt symbols

Tilting of the octahedral has been studied in detail by Glazer[28] who developed a notation to explain tilt systems. The notation uses tilts along the x, y and z axes of the ideal cubic structure with the magnitude of rotation being denoted a, b and c meaning abb would have y and z rotations of the same magnitude. By looking at the sense of rotation with respect to the successive layers of octahedra a + superscript is applied if rotations are the same sense, a 0 superscript is used if there is no rotation and a – superscript is used for rotations are of alternating sense.

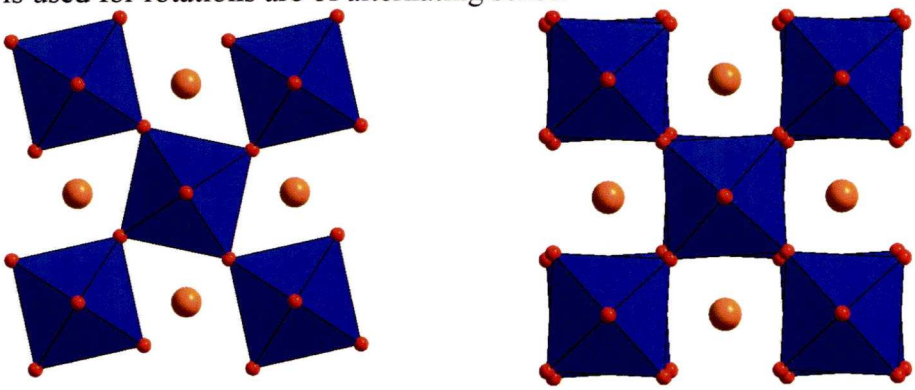

Figure 1-11 Glazer tilt systems $a^0a^0c^+$ (left) and $a^0a^0c^-$ (right) viewed down the c axis to demonstrate the in-phase and anti-phase rotations of the octahedra

1.3.1.3 Double perovskites and ordering

In double perovskites with the general formula $AA'BB'O_6$, rather than occupy a statistical arrangement of sites, some display an ordered arrangement. Of the two sites (A and B) B site ordering is more commonly found, with ordering of both sites simultaneously being very unusual.

The two main types of order observed are rock salt and layered with a schematic shown in Figure 1-12.

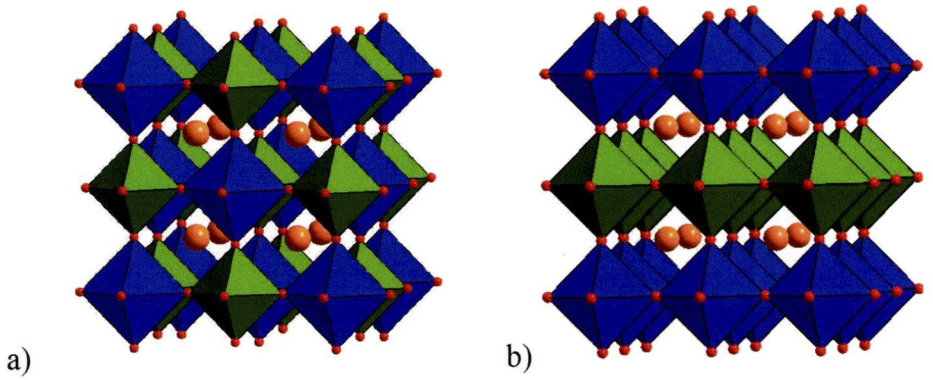

Figure 1-12 Schematic diagrams of a) rock salt order and b) layered order.

Rock salt ordering is the most common form of ordering found on the B site of perovskites while layered ordering is the most common form of ordering on the A site. This is despite electrostatics predicting that both the A and B site should order in a rock salt fashion in a classic $AA'BB'O_6$. The cause of the discrepancy is thought to be due to the fact that rock salt order forces the anion coordinated to the A and A' ions onto a special site (Wyckoff 24d $(0,{}^1/_4,{}^1/_4)$) in the undistorted aristotype $Fm\bar{3}m$ structure preventing distortion. Layered ordering however puts 2/3 on a general site (Wyckoff 4i) which allows for a shift away from the ideal position and so helps stabilise A-site ions of differing size in layered ordering.

Empirical rules for predicting B site ordered materials were developed by Setter and Cross[29] and summarised by Zhang[30];

- Structure: In order to reduce energy requirements for ordering the structure should be simple. So B site ordering between two different types of B site ion will be more favourable than B site ordering between three different types of B site ion.
- Cation ratio: The B:B' ratio should be ideally 1:1
- B site charge: A large charge difference in B and B' produces a strong tendency to order caused by electrostatics.
- A site size: Reducing the size of the A site ion helps order the B site.
- B site size: When B and B' are ions with a large size difference the ions are strongly driven towards ordering.

Evidence for ordering can be seen in the XRD as strong 111 and 311 peaks are associated with rock salt B site order and 001 and 201 are associated with a layered A site. For rocksalt ordering the all odd hkl indices in $Fm\bar{3}m$ are the superlattice reflections while the all even hkl are independent of ordering . The ratio I_{111}/I_{220} is often used to give the degree of B site order. Layered A site ordering along [001] gives the superlattice peaks 001 and 201 seen in the powder XRD of A site ordered perovskites.

1.3.2 Ruddlesden Popper n = 2 Phase

Ruddlesden Popper (RP) phases became known as such after the description of $Sr_3Ti_2O_7$ and $Sr_4Ti_3O_{10}$ by Ruddlesden & Popper in 1957.[31] RP phases consist of blocks of rock salt structured material interspersed with varying integer numbers of perovskite structured blocks giving the general formula $A_{n+1}B_nX_{3n+1}$ where X is most commonly O. An alternative way of representing the general formula is to emphasize the differing blocks is $AX\text{-}(ABX_3)_n$. Using this representation perovskite can be thought of as a $n = \infty$ RP phase but the perovskite phase is far more common than RP1, RP2 or RP3. Higher values of n are extremely rare and require layer by layer growth methods such as pulsed laser deposition[32] to form the desired structure.

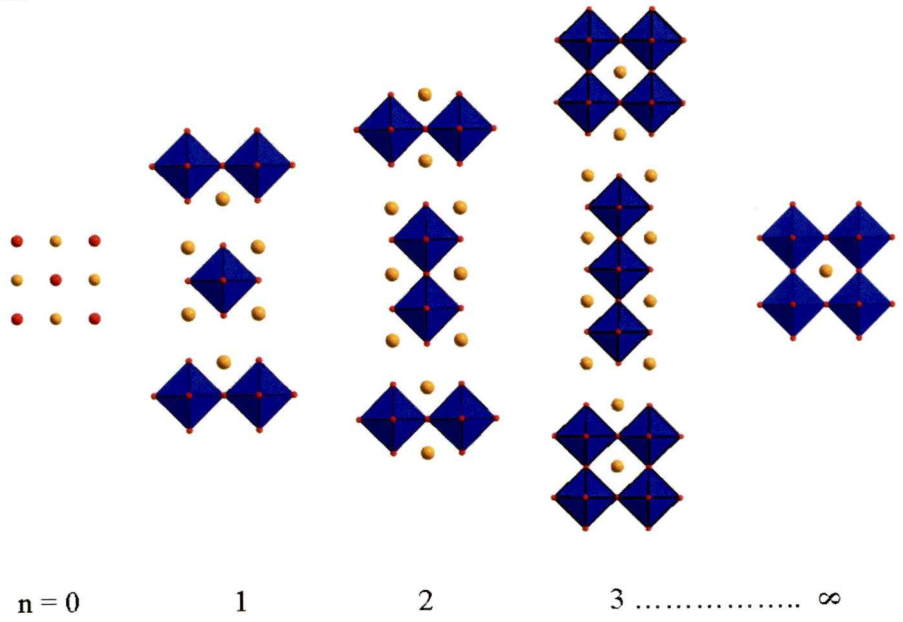

Figure 1-13 Diagram showing the relationship between differing RP phases with general formula $A_{n+1}B_nX_{3n+1}$. Light grey spheres A site, dark grey octahedra B site and black spheres X.

The RP phases targeted in this project are RP2 although RP1 phases were also formed. RP phases are related to Aurivillius[33-35] and Dion Jacobson phases[36-39] which instead of rock salt (AX) blocks have $(Bi_2O_2)^{2+}$ structured blocks or blocks of A cations respectively.

1.3.3 Melilite

The name Melilite is from the Greek meli lithos meaning honey stone (source webmineral.com) due to the natural melilite $(CaNa)_2(AlMgFe)[(AlSi)SiO_7]$ discovered in 1793 near Rome being honey coloured. Melilites have the general formula $A_2T^1T^2{}_2X_7$. The melilite structure can accommodate a number of different ions into its structure with Sr, Ca, Ba, Eu, Ce, La, Pr, Nd, Sm, Gd, Pb being found on the A site, Cu, Cd, Fe, Mn, Zn, Co, Mg, Ga, Al, Be, Si, B and Ge on T^1 and Si, Ge, Ga, B and Al on T^2 (see Kaminskii[40] and refs therein). X is almost always O but S and N are also possible, for example $MLaGa_3S_6O$ (M = Ca or Sr)[41] and $Sm_2Si_4O_3N_4$[42] . The archetypal melilite has a tetragonal structure in space group $P\bar{4}2_1m$,all melilites display this structure at elevated temperatures however there can be considerable structural complexity (often incommensurate structures) in the lower temperature forms.[43] Some natural melilite samples also show incommensurate structure such as the 5D natural melilite from San Venanzo in Italy[44]. The stability of the melilite structure is related to the size of the A cation and the distortion of the T layers.[43]

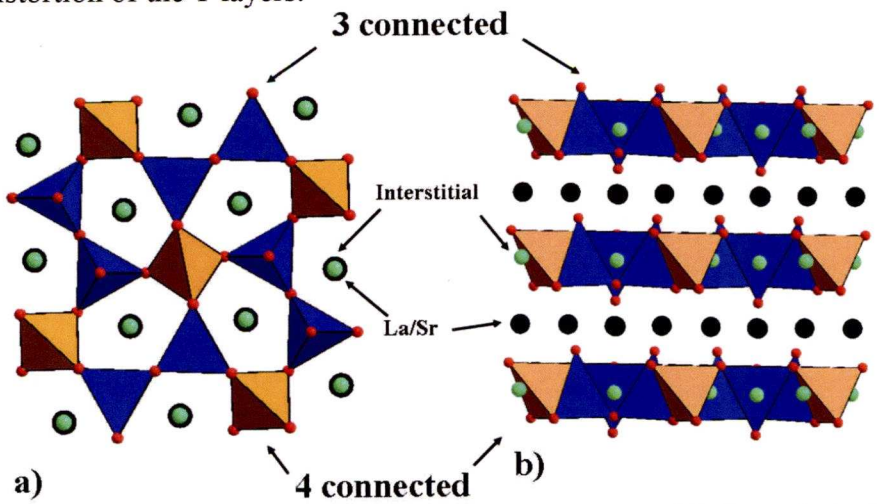

Figure 1-14 The melilite structure of $LaSrGa_3O_7$ showing the two types of GaO_4 tetrahedra (orange 4-connected, blue 3-connected). Black spheres show the La/Sr sites and the red spheres and green spheres show oxygen. The spheres for the interstitial oxygen sites (green spheres) are larger than those for the framework oxygens (red spheres). In a) the view is down the c axis showing the Ga tetrahedra and the pentagonal tunnels. The view in b) along [110] shows that the interstitial oxygen sits in the center of the Ga layers with La/Sr cations above and below.

1.3.4 Fluorite

Fluorite is derived from the Latin *fluo*, meaning "to flow" and the greek lithos (stone) because the mineral fluorite (CaF_2) has a relatively low melting point and was used as a flux in smelting. Fluorite has a cubic crystal structure with the general formula AX_2 (space group $Fm\bar{3}m$) where the A ions are eight coordinate and form alternating cubes and spaces (Figure 1-15).

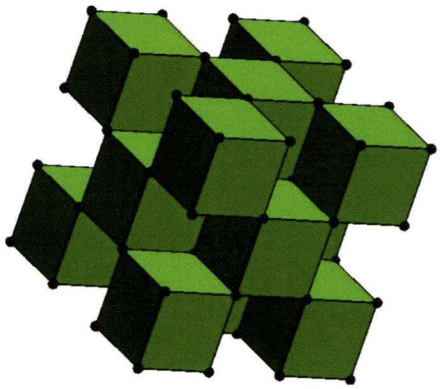

Figure 1-15 Fluorite AX_2 general structure with the A site at the center of the green cubes with X ions represented by black spheres.

1.3.5 Pyrochlore

The mineral pyrochlore $(Na,Ca)_2Nb_2O_6(OH,F)$ was named in 1826 from the Greek for fire and green because when ignited some specimens turned green.[45] Pyrochlore has a cubic structure (space group $Fd\bar{3}m$) determined by Gaertner in 1930 [46] with a general formula $A_2B_2X_7$ that is related to fluorite. If half of the AX_8 cubes in the fluorite structure are replaced with a BX_6 octahedron so that rows of A and B polyhedra form along [110] then the pyrochlore structure shown in Figure 1-16 results. The ordering of the polyhedra results in the pyrochlore structure being a superstructure of fluorite, having a lattice parameter that is double that of fluorite

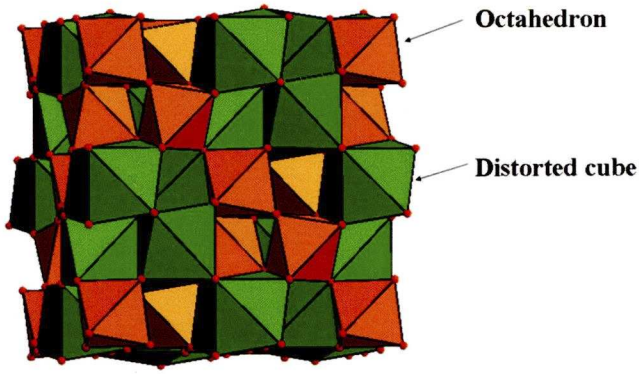

Figure 1-16 Pyrochlore general $A_2B_2O_7$ structure adapted from. [47] Green distorted cubes A site and orange distorted octahedra B site with red spheres showing O positions.

1.3.6 Zirconolite

Another type of ordering in oxygen-deficient fluorite occurs to form the zirconolite phases originally based on compositions close to $CaZrTi_2O_7$. Vance [48] describes the structure as related to pyrochlore by a compression normal to one set of (111) planes giving a layered compound along (001). The nomenclature of these phases is confusing with zirkelite being used to describe a non-crystalline material, a hexagonal material, a monoclinic mineral and a trigonal mineral. As a result the International Mineralogical Association Commission on New Minerals and Mineral Names (IMA-CNMMN) in 1988 approved a nomenclature scheme which labels the material based on layer stacking sequence. White [49, 50] describes these structures as having alternating layers, one layer being made up of octahedra similar to hexagonal tungsten bronzes (HTB) (green in Figure 1-17). The other layer being a plane of the interlayer cations (IC) in distorted cubes (green in Figure 1-17) or monocaped octahedral (green in Figure 1-17) forming a HTB-IC slab. Overall this gives a stacking sequence HTB-IC-HTB-IC..... . As the HTB-IC slabs can rotate relative to the HTB-IC slabs above and below the amount of rotation leads to differing structures. If the slabs are rotated by 180 ° the result is a monoclinic structure which is given the name zirconolite-2M. If the slabs rotate by 120 ° then the structure

becomes trigonal and as 3 rotations are required to give a total 360 ° rotation the structure is labelled zirconolite-3T. If instead of rotating there is a shear then orthorhombic structures like zirconolite–3O can be produced. Zirconolite is still used to describe the non crystalline mineral or mineral with undetermined layer sequence while zirkelite is used for the cubic mineral $(Ti,Ca,Zr)O_{2-x}$. A similar nomenclature scheme has been approved by the IMA-CNMMN[51] for another set of fluorite-related structures named weberites[52]. The structures are very similar consisting of HTB and IC layers that form slabs that can move relative to each other but in weberite one of the oxygens sits in an octahedral interstitial rather than all oxygens being in tetrahedral interstitial. Zanazzi[53] suggests that by using high pressure (>11 GPa) the oxygen interstitial will migrate causing a phase transition from weberite to zirconolite.

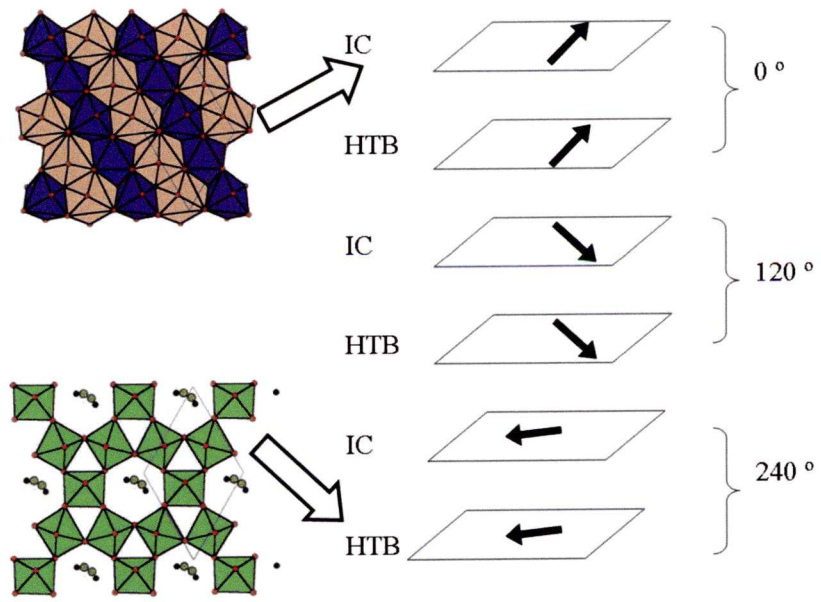

Figure 1-17 Zirconolite- 3T structure broken down into component layers with brackets to indicate slabs. The black arrows are a guide for the eye to illustrate the effect of the rotations of the slabs. In the zirconolite-3T structure there are 3 separate rotations of 120° each in the unit cell.

1.3.7 Rhombohedral distorted fluorite

The rhombohedral distorted fluorite is a superstructure of oxygen deficient fluorite [54] with ideal compostion A_6BX_{12} (i.e. $MO_{1.714}$) and is produced by vacancy ordering. The vacancies are on 1/7 of the anion fluorite positions along the [111] direction. This vacancy ordering causes a lattice distortion and slight shifts of atomic positions away from the ideal fluorite sites. The coordination environment of the B ion is an almost undistorted octahedra while the A site ion sits in a heavily distorted AO_7 polyhedron.

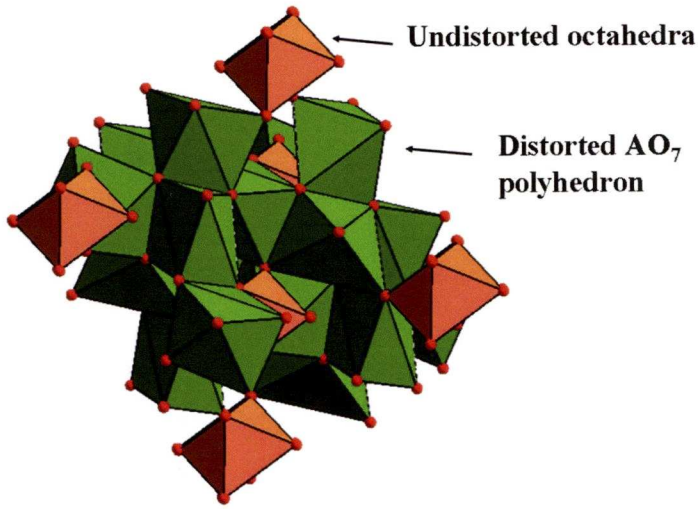

Figure 1-18 Rhombohedral distorted fluorite with general formula A_6BO_{12} with the undistorted BO_6 being shown by orange and heavily distorted AO_7 being shown by green.

Many other fluorite related structure exist such as rare earth C (bixbyite)[55], scheelite and fergusonite[56] but investigation of these structures is beyond the scope of this thesis.

1.3.8 Sr_2PbO_4

Trömel [57] in 1965 discovered this new structure type which consists of linear chains of edge sharing distorted PbO_6 octahedra surrounded by inter-chain Sr^{2+}. Other elements that can be incorporated into the structure are Ce[58] or Sn for the Pb with either Ca or Cd for Sr[59, 60]. Mn_2GeO_4 at high pressure has been found by Morimoto [61] to crystallize in the Sr_2PbO_4 rather than the ambient pressure olivine structure.

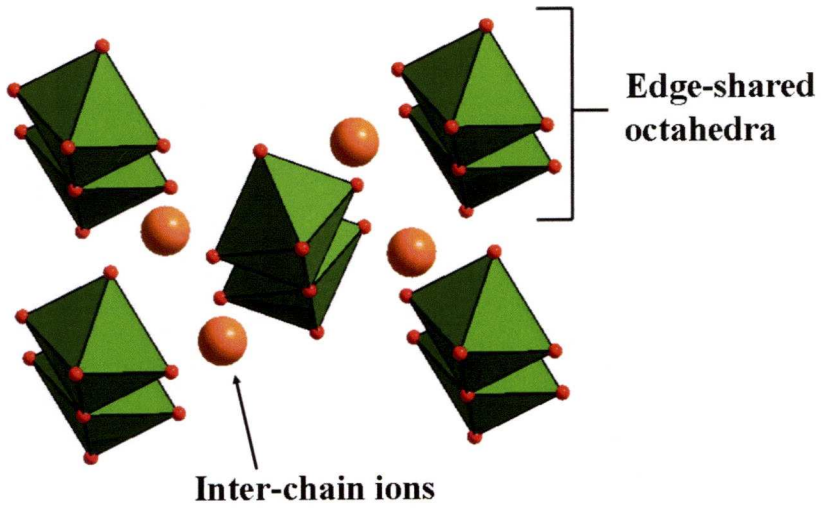

Figure 1-19 Sr_2PbO_4 structure showing the edge shared chains of Pb octahedra in green and the interchain Sr^{2+} ions shown by orange spheres, O^{2-} ions are shown by red spheres.

There is some similarity between RP1 structure and the Sr_2PbO_4 structure with the major difference between them being the connectivity of the octahedra (corner sharing RP1 edge sharing for Sr_2PbO_4) (Figure 1-20). The edge sharing in the Sr_2PbO_4 isolates the chains of octahedra which in the RP1 structure form corner shared sheets and causes two of the chains to rotate relative to the other three.

Muller-Buschbaum[62] found that size plays an important role in determining structure stating for the Sr_2PbO_4 structure ' it is evident that the differences in size of the participating metal ions are too small to build up K_2NiF_4 (RP1) type structure.'

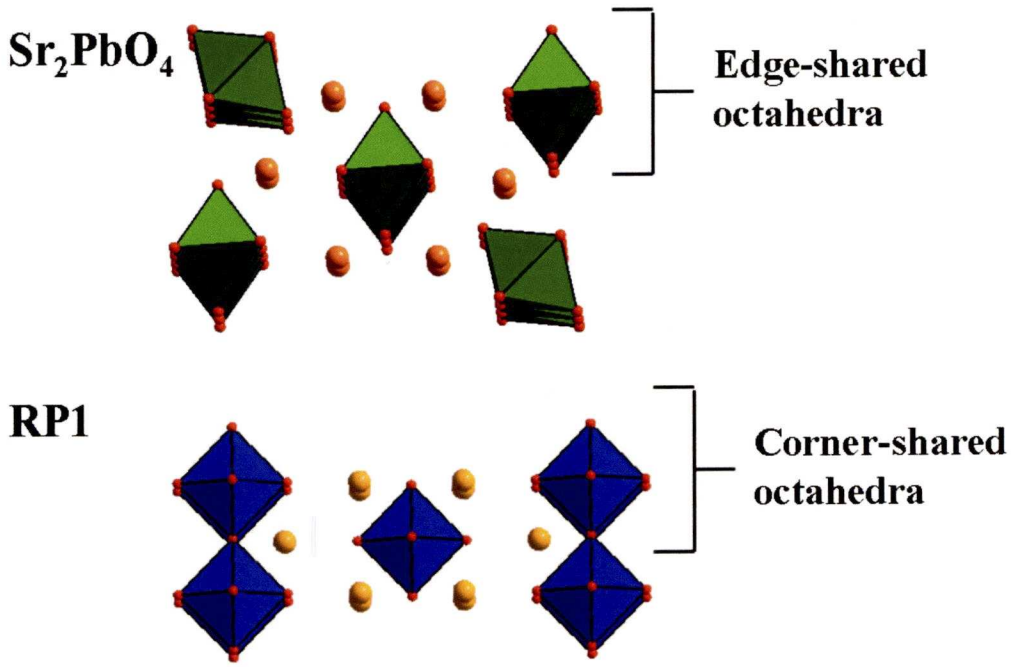

Figure 1-20 Comparison of the Sr_2PbO_4 structure showing the edge shared chains of octahedra and the RP1 structure with corner shared octahedra.

1.4 References

[1] W. A. Oldfather, *Journal of the American Ceramic Society* **1920**, *3*, 537.

[2] C. F. Schœnbein, *Philosophical Magazine* **1839**, *14*, 43.

[3] W. R. Grove, *Philosophical Magazine* **1839**, *14*, 127.

[4] L. Mond, C. Langer, *Proc. R. Soc. Lond* **1889**, *46*, 296.

[5] K. Eguchi, R. Kikuchi, T. Takeguchi, *Proceedings- Electrochemical Society* **2003**, *2002-2026*, 38.

[6] N. Q. Minh, *Journal of the American Ceramic Society* **1993**, *76*, 563.

[7] K. Huang, J. B. Goodenough, *Solid oxide fuel cell technology Principles, performance and operations*, Woodhead Publishing Limited, Cambridge **2009**.

[8] D. J. L. Brett, A. Atkinson, N. P. Brandon, S. J. Skinner, *Chemical Society Reviews* **2008**, *37*, 1568.

[9] B. C. H. Steele, *Solid State Ionics* **2000**, *129*, 95.

[10] A. Lashtabeg, S. J. Skinner, *Journal of Materials Chemistry* **2006**, *16*, 3161.

[11] H. Schmid, *Ferroelectrics* **1994**, *162*, 665.

[12] M. McElfresh, *Quantum Design Inc SQUID MANUAL* **1994**.

[13] P. S. Halasyamani, K. R. Poeppelmeier, *Chemistry of Materials* **1998**, *10*, 2753.

[14] Landolt-Bornstein, *Ferroelectrics and Related Substances*, Vol. III/36/A/Part1, **2001**.

[15] R. M. Hazen, *Scientific American* **1988**, *258*, 74.

[16] B. Raveau, *Progress in Solid State Chemistry* **2007**, *35*, 171

[17] R. J. Hemley, R. E. Cohen, *Annual Review of Earth and Planetary Sciences* **1992**, *20*, 553.

[18] M. W. Lufaso, P. M. Woodward, *Acta Crystallographica Section B* **2001**, *57*, 725.

[19] V. Luaña, A. Costales, A. M. Pendás, *Physical Review B* **1997**, *55*, 4285.

[20] A. Clearfield, *Acta Crystallographica* **1963**, *16*, 135.

[21] F. Gingl, T. Vogt, E. Akiba, K. Yvon, *Journal of Alloys and Compounds* **1999**, *282*, 125.

[22] S. Carlson, A.-K. Larsson, F. E. Rohrer, *Acta Crystallographica Section B* **2000**, *56*, 189.

[23] R. Marchand, Y. Laurent, J. Guyader, P. L'Haridon, P. Verdier, *Journal of the European Ceramic Society* **1991**, *8*, 197.

[24] M. Kirchner, W. Schnelle, R. Niewa, *Zeitschrift für Anorganische und Allgemeine Chemie* **2006**, *632*, 559.

[25] M. Yashima, R. Ali, *Solid State Ionics* **2009**, - *180*. 120

[26] V. M. Goldschmidt, *Naturwissenschaften* **1926**, *14*, 477.

[27] J.-W. G. Bos, J. P. Attfield, *Zeitschrift fuer Anorganische und Allgemeine Chemie* **2004**, *630*, 2248.

[28] A. M. Glazer, *Acta Crystallographica Section B* **1972**, *28*, 3384.

[29] N. Setter, L. E. Cross, *Journal of Materials Science* **1980**, *15*, 2478.

[30] X. Zhang, Q. Wang, *Journal of the American Ceramic Society* **1991**, *74*.

[31] S. N. Ruddlesden, P. Popper, *Acta Crystallographica* **1958**, *11*, 54

[32] L. Yan, H. Niu, C. A. Bridges, P. A. Marshall, J. Hadermann, G. van Tendeloo, P. R. Chalker, M. J. Rosseinsky, *Angewandte Chemie International Edition* **2007**, *46*, 4539.

[33] B. Frit, J. P. Mercuiro, *Journal of Alloys and Compounds* **1992**, *188*, 27.

[34] B. Aurivillius, *Arkiv foer Kemi* **1949**, *1*, 463.

[35] B. Aurivillius, *Arkiv foer Kemi* **1949**, *1*, 499.

[36] S. Uma, J. Gopalakrishnan, *Journal of Solid State Chemistry* **1993**, *102*, 332.

[37] M. Dion, M. Ganne, M. Tournoux, *Materials Research Bulletin* **1981**, *16*, 1429.

[38] A. J. Jacobson, J. W. Johnson, J. T. Lewandowski, *Inorganic Chemistry* **1985**, *24*, 3727.

[39] A. J. Jacobson, J. T. Lewandowski, J. W. Johnson, *Journal of Less-Common Metals* **1986**, *116*, 137.

[40] A. A. Kaminskii, L. Bohatý, P. Becker, J. Liebertz, P. Held, H. J. Eichler, H. Rhee, J. Hanuza, *Laser Physics Letters* **2008**, *5*, 845.

[41] C. L. Teske, *Zeitschrift fuer Anorganische und Allgemeine Chemie* **1985**, *531*, 52.

[42] R. Lauterbach, W. Schnick, *Zeitschrift fuer Anorganische und Allgemeine Chemie* **1999**, *625*, 429.

[43] F. Rothlisberger, F. Seifert, M. Czank, *European Journal of Mineralogy* **1990**, *2*, 585.

[44] L. Bindi, P. Bonazzi, M. Dusek, V. Petricek, G. Charpuis, *Acta Crystallographica Section B* **2001**, *57*, 739.

[45] T. A. Vanderah, I. Levin, M. W. Lufaso, *European journal of Inorganic Chemistry* **2005**, 2895.

[46] R. A. McCauley, *Journal of Applied Physics* **1980**, *51*, 290.

[47] S. Hull, *Reports on Progress in Physics* **2004**, *67*, 1233.

[48] E. R. Vance, G. R. Lumpkin, M. L. Carter, D. J. Cassidy, C. J. Ball, A. R. Day, B. B. D., *Journal of the American Ceramic Society* **2002**, *85*, 1853.

[49] T. J. White, *American Mineralogist* **1984**, *69*, 1156.

[50] T. J. White, R. L. Segall, J. L. Hutchinson, B. J. C., *Proceedings of the Royal Society London A* **1984**, *392*, 343

[51] I. E. Grey, W. G. Mumme, T. J. Ness, R. S. Roth, K. L. Smith, *Journal of Solid State Chemistry* **2003**, *174*, 285.

[52] L. Cai, J. C. Nino, *Acta Crystallographica Section B* **2009**, *65*, 269.

[53] P. F. Zanazzi, L. Chelazzi, P. Bonazzi, L. Bindi, *American Mineralogist* **2009**, *94*, 352.

[54] D. Michel, A. Kahn, *Acta Crystallographica Section B* **1982**, *38*, 1437.

[55] A. Vegas, R. L. Martin, D. J. M. Bevan, *Acta Crystallographica Section B* **2009**, *65*, 11.

[56] A. Grzechnik, W. A. Crichton, M. Hanfland, *Physica Status Solidi (b)* **2005**, *242*, 2795.

[57] M. Troemel, *Naturwissenschaften* **1965**, *52*, 492.

[58] E. Danielson, M. Devenney, D. M. Giaquinta, H. Golden. J, R. C. Haushalter, E. W. McFarland, D. M. Poojary, C. M. Reaves, W. H. Weinberg, X. D. Wu, *Journal of Molecular Structure* **1998**, *470*, 229

[59] M. Troemel, *Zeitschrift fuer Anorganische und Allgemeine Chemie* **1969**, *371*, 237.

[60] M. Troemel, *Naturwissenschaften* **1967**, *54*, 17.

[61] N. Morimoto, *American Mineralogist* **1972**, *57*, 62.

[62] H. Muller-Buschbaum, *Journal of Alloys and Compounds* **2003**, *349*, 49

[63] H. Kramers, *Physica* **1934**, *1*, 182

[64] J.B. Goodenough, *Physical Review* **1955**, *100*, 564

[65] J.B. Goodenough, *Journal of Physics and Chemistry of Solids* **1958**, *6*, 287

[66] J. Kanamori, *Journal of Physics and Chemistry of Solids* **1959**, *10*, 87

Chapter 2 : Experimental details

This chapter describes the synthetic and characterization methods used in this thesis.

2.1 Synthesis

There are two main methods of synthesis used in this project, traditional ceramic methods and high pressure methods, both of which are described in this section.

2.1.1 Traditional ceramic methods

Samples produced using the standard ceramic techniques were weighed to within 0.0005g using a Sartorius balance. The powders were ground together using an agate pestle and mortar until visibly homogeneous (typically 30 minutes).

Samples were typically fired as loose powders for the first firing to enable decomposition of precursor compounds such as carbonates. After the initial firing samples were typically pressed into pellets using a 13 mm stainless steel die in a hand pulled hydraulic piston press at pressures ranging from 2-5 tons. After each subsequent firing the pellets were ground and repelletized.

Compositions that either showed evidence of reaction with the crucible in a previous synthesis attempt or compositions where this was expected were placed on platinum foil for the reactions.

Quenching experiments were carried out by removing the alumina crucible from the furnace at the synthesis temperature and tipping the pellet out onto a block of aluminium at room temperature.

2.1.2 High pressure methods

High pressure experiments have traditionally been the preserve of geologists and petrologists who are interested in recreating the environment in the earths crust. [1] However high pressure experiments can also be used to form materials that are inaccessible at atmospheric pressure such as Bi_2NiMnO_6[2] and $ScCrO_3$[3]. Unusual oxidation states and coordination numbers can be stabilized by the use of pressure[4] and as a general rule dense phases are favored[5]. Commercially the greatest successes have been in the fields of superhard materials and synthetic gems with the synthetic diamond industry the most significant. For example in 2006 $50 million worth of synthetic diamonds were sold with the market predicted to maintain a compound annual growth rate of 44% until 2015 when the sales will be $2 billion[6]. Materials discovered at high pressures can often be stabilized in thin film form where the substrate is chosen to generate compressive strain as the strain in the film is essentially providing the pressure. Using such a method $YMnO_3$[7] can be produced as a perovskite (normally high pressure synthesized) thin film from a hexagonal (normal ambient pressure phase) PLD target.

High pressure experiments described in this project were carried out using a Rockland Research 600 ton press with the Walker octahedral design.[8] Powders of the starting materials are first ground together in a similar fashion to standard ceramic synthesis. Then the intimately mixed powder is loaded into a small platinum container comprising of two platinum disks either end of platinum tubing (Figure 2-1). The platinum container is itself sitting in a machined aluminium oxide crucible with an aluminium oxide lid. This sits in a machined graphite resistance furnace again with a machined graphite lid. The graphite furnace is then loaded into the center of a cast octahedra with cylindrical

blocks of sintered Al_2O_3 with molybdenum rod at the center. The purpose of the molybdenum is to provide an electrical contact from the outside of the octahedra to the graphite resistance furnace. Cast octahedra are used as the mold includes the fins which when wrapped in fiberglass tape provide the gasketing when in the press.

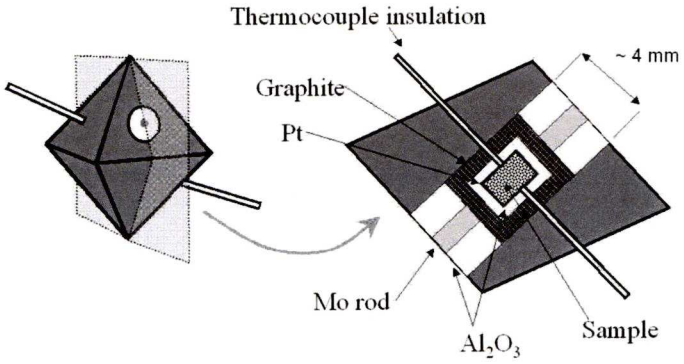

Figure 2-1 Diagram of octahedra with major components labeled

The octahedra are then loaded into the cube made by the truncated WC cubes with the truncations pressing into the faces of the octahedra. Acetate sheets are then super-glued onto the faces of the cube with a hole above the cubes, which contact the molybdenum faces. In these holes copper disks are inserted to ensure electrical connection.

The super glued cube is then placed between the six anvils in the press which in turn are sitting on acetate sheet with a notch cut out with copper foil placed in the gap. The anvil touching the copper disk must be the anvil that is sitting on top of the copper foil to ensure electrical connection.

The press itself consists of a steel containment ring with a hydraulically operated piston (normal max hydraulic pressure 7000 kpsi) pushing up against the steel body of the press. Initially pressure is applied using an Enerpac pump before switching to a motorized hydrallic cyclinder when the hydraulic pressure reaches 300 kpsi.

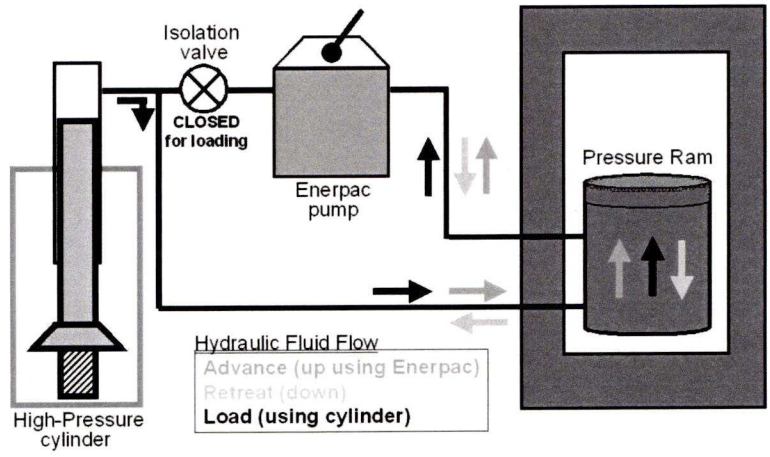

Figure 2-2 Schematic of hydraulic flow in the press.

By applying a voltage across the steel plates above and below the containment ring a current can flow through the graphite resistance furnace and so the sample can be heated.

Temperature is controlled by reference to thermocouple runs using the graphs given in Figure 2-3. As the % power of the eurotherm is known and using a voltmeter and an ammeter the voltage across and the current through the graphite furnace can be measured. Using Equation 2-1 & 2-2 the resistance of the furnace and the power output of the furnace can be calculated.

$$V/I = R \qquad \textbf{Equation 2-1}$$

$$P = IV \qquad \textbf{Equation 2-2}$$

By comparing the resistance trends of the run in progress to the graph the thermocouple run most suited to the run in progress can be selected and so the correct power to temperature relationship on

Figure 2-3 used.

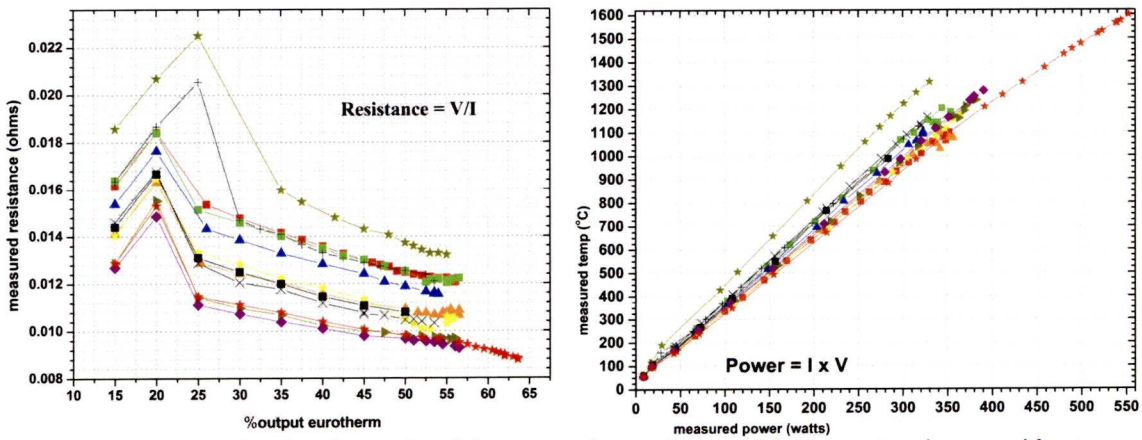

Figure 2-3 Graphs showing the results of thermocouple runs from which temperature in runs without thermocouples or when thermocouple breaks can be determined.

When a new thermocouple run is required the assembly used has some extra additions. First two holes need to be drilled through the octahedra, graphite and machined aluminium oxide to allow for an aluminium oxide shielded Pt/PtRh thermocouple wire to be inserted Figure 2-1. One end of the wire touches the platinum sample container and the other end a truncated WC cube (note this cube can not be the same cube that is touching the copper). Wires then need to be run from the WC cubes touching the Pt/PtRh wires out of the press to the electronics box.

2.2 Diffraction

Diffraction is the main characterization method for the materials used in this thesis with X-ray diffraction, neutron diffraction and electron diffraction all being used.

The periodic arrangement of the atoms in a crystalline material can be thought of as an arrangement of semi-transparent planes (Figure 2-4). When a wave of radiation is scattered back it can interfere with the other radiation waves coming from other planes in either a constructive or destructive manner.

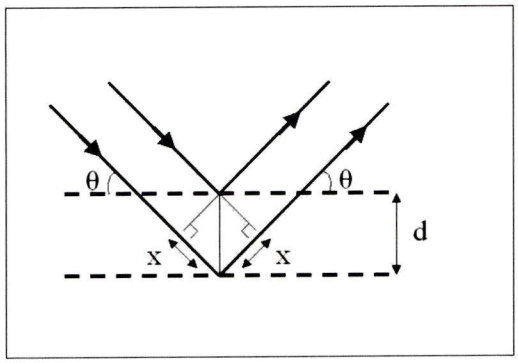

Figure 2-4 Diagram to illustrate path difference.

Using Figure 2-4 as a reference the relevant parameters are;

1) The deviation of beam = 2θ
2) The path difference = $2x = 2d_{hkl}\sin\theta$

So for constructive interference to occur the path difference must be a whole wavelength ($n\lambda$ where n is integer) giving the Bragg equation (Equation 2.3) for diffraction.

$$n\lambda = 2d_{hkl}\sin\theta$$

Equation 2-3 The Bragg equation

It is the collection of angles where the Bragg equation is satisfied that give the diffraction pattern. For a single crystal experiment the diffracted wave from a given allowed diffraction plane will act as a spot on a detector (Figure 2-5 a) at a fixed distance from the crystal. Powder samples however have many crystallites all oriented differently meaning radiation will be diffracted in many directions forming a ring on a flat plate detector (Figure 2-5 b).

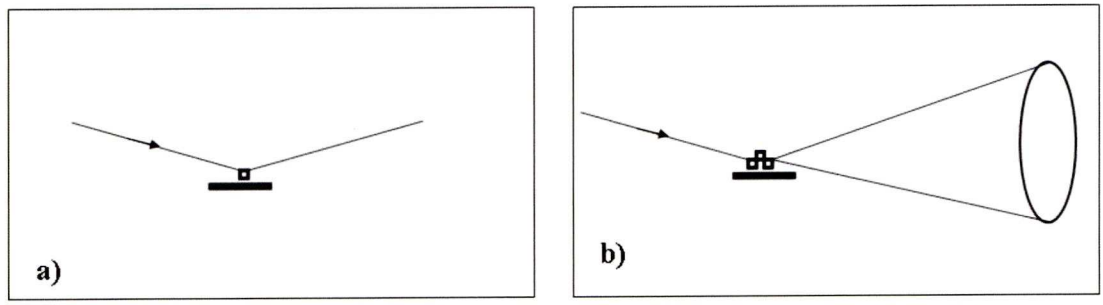

Figure 2-5 Schematic diagrams of how a X-ray beam is diffracted by a single crystal (a) to form a spot on a detector and by a powder (b) to form a ring.

Miller Indices are used to identify planes and are the reciprocals of the intersection distances given in unit cells. For example 200 means the plane intercepts the a axis at 0 (origin) and ½a (where a is a lattice parameter), but doesn't intercept the b axis or c axis. 102 intercepts the a axis at 0 and 1a and c axis at 0 and ½c but again does not intercept the b axis. Note the indices can also be negative such as $\bar{1}10$ which intercepts a axis at 0 and -1a, b axis at 0 and 1b.

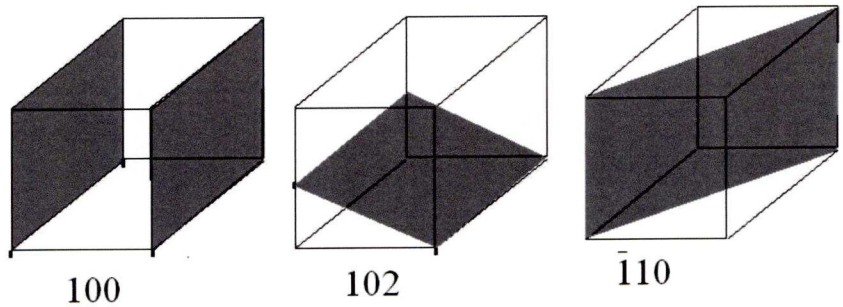

Figure 2-6 Diagram showing Miller indices for planes shaded in dark grey.

The interplanar spacing (d) is thus a function of lattice parameters (a b c α β γ) and miller indices (h k l) with the relation for an orthorhombic cell given in Equation 2.4

$$1/d^2 = h^2/a^2 + k^2/b^2 + l^2/c^2 \qquad \textbf{Equation 2-4}$$

In addition to Bragg's law the symmetry of the material can cause destructive interference for planes allowed by Bragg giving rise to systematic reflection absences in Table 2-1 .

Table 2-1 Selection of some systematic absences and the conditions for their absence

Symmetry element	Affected reflection	Condition for absence
Centered Cells		
Body Centered (I)	hkl	(h+k+l) odd
Face Centered (A)	hkl	(k+l) odd
Face Centered (B)	hkl	(h+l) odd
Face Centered (C)	hkl	(h+k) odd
Face Centered (F)	hkl	(h+k), (h+l), (k+l) odd
Screw axis		
2_1 along a	h00	h = 2n+1
2_1 along b	0k0	k = 2n+1
2_1 along c	00l	l = 2n+1
4_2 along a	h00	h = 2n+1
4_2 along b	0k0	k = 2n+1
4_2 along c	00l	l = 2n+1
6_3 along a	h00	h = 2n+1
6_3 along b	0k0	k = 2n+1
6_3 along c	00l	l = 2n+1
3_1 and 3_2 along c	00l	l = 3n+1 or 3n+2 but not divisible by 3
6_2 and 6_4 along c	00l	l = 3n+1 or 3n+2 but not divisible by 4

4_1 and 4_3 along a	h00	h = 4n+1, 2 or 3
4_2 and 4_3 along b	0k0	k = 4n+1, 2 or 3
4_3 and 4_3 along c	00l	l = 4n+1, 2 or 3
6_1 and 6_5	00l	l = 6n+1,2,3,4,or 5
Glide Planes 90 degrees to a		
b glide	0Kl	k = 2n+1
c glide	0Kl	l = 2n+1
n glide	0Kl	k + l = 2n+1
d glide	0Kl	k+ l = 4n+1,2 or 3
Glide Planes 90 degrees to b		
a glide	h0l	h = 2n+1
c glide	h0l	l = 2n+1
n glide	h0l	h + l = 2n+1
d glide	h0l	h+ l = 4n+1,2 or 3
Glide Planes 90 degrees to c		
a glide	hk0	h = 2n+1
c glide	hk0	k = 2n+1
n glide	hk0	h + k = 2n+1
d glide	hk0	h+ k = 4n+1,2 or 3

As well as the position of the reflections, the intensity of the reflections in a powder pattern contain useful information. The observed intensity of a reflection depends on the experimental technique used, the composition and the physical nature of the crystalline solid. The relative intensity for powder diffraction as a function of angle is given byI α $L(\theta)pA|F_{hkl}|^2$ Equation 2-5 .

$$\mathbf{I \alpha L(\theta)pA|F_{hkl}|^2} \qquad \textbf{Equation 2-5}$$

Where I is the integrated intensity and θ is the Bragg angle and the remaining factors are as follows:

1) Trigonometrical factor, $L(\theta) = (1 + \cos^2 2\theta / \sin^2 \theta \cos \theta)$

The $1 + \cos^2 2\theta$ term accounts for the partial polarization of the reflected beam while the $\sin^2 \theta \cos \theta$ term is the Lorentz factor and is due to the geometry of the measurement.

2) The multiplicity factor, p

This term arises as some reflections are equivalent by symmetry. Consider the 100, (010), (001), ($\bar{1}$00), (0 $\bar{1}$0) and (00 $\bar{1}$) reflections for a cubic system as, a = b = c and $\alpha = \beta = \gamma = 90°$ all six reflections satisfy the Bragg equation (Equation 2-3) for the same value of sin θ. Note also that preferred orientation of crystallites in the sample will affect the relative intensities of reflections, this is a commonly encountered problem with layered materials.

3) The absorption factor A

The absorption factor is a function of the Bragg angle θ and is related to how absorbing (due to composition) the material is and is most often a problem in transmission geometries.

4) The structure factor F_{hkl}

$$|F_{hkl}|.= \Sigma_j f_j N_j (\exp[(2\pi i(hx_j + ky_j + lz_j)])\exp(-Mj)$$ **Equation 2-6**

Where f_j = *atomic scattering factor*

N_j = *occupancy factor of the atom on the site*

x_j, y_j, z_j = *fractional co-ordinates of* j^{th} *atom*

$M_j = 8\pi^2 U_{iso}^2 \sin^2\theta / \lambda^2$

U_{iso} = *square root of the mean thermal parameter*

Note only the $|F_{hkl}|$ (the structure amplitude) can be observed experimentally as F_{hkl} contains multiple phases.

Thermal vibrations of the atoms cause a decrease in intensity of the diffracted beam and increase the amount of background noise. The intensity of each reflection is most usefully thought of as being directly proportional to the structure factor (**Equation 2-7)**

$$I_{hkl} \alpha |F_{hkl}|^2$$ **Equation 2-7**

To analyze a diffraction pattern both the reflection positions and the intensities must be taken into account.

2.2.1 X-ray Diffraction

2.2.1.1 Lab source

Powder X-ray diffraction is a powerful non-destructive technique used to obtain structural data on polycrystalline samples. Two laboratory diffractometers were used in this project a STOE STADI P and Panalytical X-Pert pro. The STOE has a copper target and produces Kα radiation λ = 1.54046Å and was controlled using Stoe WinXPow version 1.10b software package. The Panalytical X-Pert pro has a cobalt target producing Kα radiation λ = 1.7890Å. Both the STOE and Panalytical were used in reflection mode using Bragg-Brentano geometry and operated at 40kV and 40mA

Samples for the Panalytical were mounted on a spinning silicon disk, the disk is cut down a forbidden plane so no reflections from the silicon disk are observed in the diffraction pattern. The samples were rotated to minimize the effect of preferred orientation in the diffraction patterns obtained.

Both machines record data as total counts (Y axis) for the value of 2θ (X axis) but to enable comparisons between samples the data is often scaled and y offsets used. These allow data from different samples, using differing scan lengths with differing total intensities to be compared on the same figure without the data overlapping. However the drawback of such treatment is that the Y axis is now no longer total counts but is now arbitrary and so is labeled as such. Data used for refinements was not scaled or offset so Y axis units are counts rather than arbitrary units.

2.2.1.2 Synchrotron source

Samples were sent to both the Synchrotron Radiation Source (SRS) station 9.1 and to the Diamond Light Source (DLS) station I11 during the course of the project. Synchrotrons use the fact that an accelerating charge will emit radiation, so accelerating an electron round a ring will cause radiation to be given off. It is this radiation that can be used for diffraction experiments amongst many other types of experiments.

Electrons are produced in an electron gun where the cathode is under high voltage and heated in a vacuum. These thermally emitted electrons are then accelerated (to 90keV at Diamond) and then further in a LINAC (to 100MeV at Diamond) using radio frequency cavities before entering the booster synchrotron. The radio frequency voltage source is then used to accelerate the electrons (up to 3GeV at Diamond) in the ring while bending magnets keep the electrons in the ring. The electrons can then be transferred to the storage ring where bending magnets keep the beam going round the ring Figure 2-7.

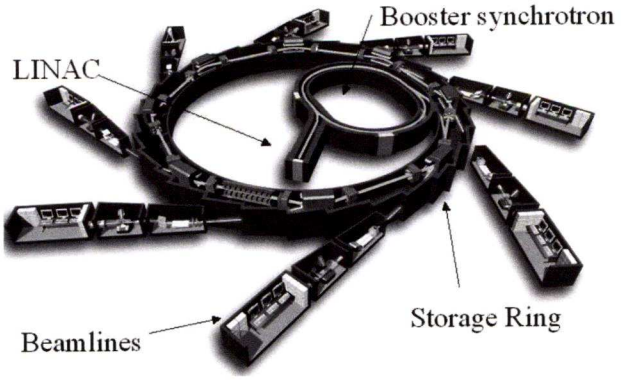

Figure 2-7 Schematic diagram of a synchrotron adapted from a diagram of the Synchrotron Soleil.

2.2.2 Neutron diffraction

Neutron diffraction is often used to compliment X-ray diffraction as X-rays and neutrons are scattering arises from different origins. X-rays are scattered by the electron clouds and so show stronger scattering off elements with high atomic numbers due to larger numbers of electrons. Neutrons however are scattered by the nuclei whose scattering length has no systematic variation allowing neutrons to detect light atoms in the presence of heavier atoms. Neutrons also posses a magnetic moment so long range magnetic order of samples can also be probed using neutron diffraction. Samples were measured at ISIS on the HRPD, GEM and POLARIS instruments during the course of the project. H^- ions are first accelerated in a linear accelerator to 70MeV before being stripped of their electrons by aluminium oxide foil and then being further accelerated in a synchrotron up to 750-800 MeV. The protons are then bunched and extracted from the synchrotron and directed at a tungsten target producing a pulse of neutrons. The pulsed neutrons produced are 'fast' so they are slowed down by a moderator before hitting the sample. As the detectors are at fixed 2θ the diffraction pattern becomes a function of time and neutron wavelength. By combining the de Broglie relationship with Bragg's law;

$$\lambda = h/m_n v_n = 2d_{hkl}\sin\theta$$

Equation 2-8 Bragg equation

the neutron time of flight becomes;

$$t = 2d_{hkl}L(m_n/h)\sin\theta$$

Equation 2-9 Time of flight equation

As the time of flight depends on the d spacing if all other parameters are held constant then the time of flight is proportional to the d_{hkl} value. L is the flight path from the moderator to the detector.

Details of the GEM, HRPD and POLARIS instruments are now given in the following sections.

2.2.2.1 GEM

GEM (GEneral Materials)[9] receives a high intensity of neutrons but collects at a high resolution allowing high quality patterns to be collected in a relatively short period of time.

The sample was held in a cylindrical vanadium can as vanadium has a low scattering cross section.

2.2.2.2 HRPD

HRPD (High Resolution Powder Diffractometer)[10] is the highest resolution neutron powder diffractometer available at ISIS . The high resolution of the HRPD instrument is due to it being situated 100m away from the target as resolution increases with distance from the target. However because the 'slow' neutrons from one pulse can be caught by the 'fast' neutrons from a following pulse, choppers are used to only allow one in five of the target pulses to reach the instrument. As a consequence the neutron flux is lower on HRPD compared to the other instruments available at ISIS so samples can take longer to run. Again samples were held in cylindrical vanadium cans due to the low scattering cross section of vanadium.

2.2.2.3 POLARIS

POLARIS[11] is a high intensity medium resolution diffractometer which allows for data collection on small samples. As well as using the ISIS standard vanadium can POLARIS experiments can also be run with glass capillaries. This allows for data collection on small samples (<5mm^3) albeit with increased data collection time. Polaris has many banks of detectors, in the present work the data is taken from the 145° backscattering bank.

2.2.3 Structure Analysis

Throughout this thesis structure is crucial to understanding not only what has been synthesized but also rationalizing the observed properties. The two main methods of obtaining structural information from the diffraction patterns are LeBail fitting and Rietveld refinement described in this section.

2.2.3.1 LeBail fitting

LeBail fitting (profile matching)[12, 13] of diffraction patterns requires no structural information, just space group, cell parameters, peak shape and background. The General Structural Analysis Suite (GSAS)[14] was used to carry out the LeBail fitting in this thesis.

2.2.3.2 Rietveld Refinement

Least squares refinement as described by Rietveld[15] was predominantly carried out using the General Structural Analysis Suite (GSAS)[14]. Another program used for least squares refinement was TOPAS Academic [22]. As Rietveld refinement is not a structure solution technique a starting model must be obtained by other means, often the structure

of a similar known compound. The program calculates a diffraction pattern using the crystal model, profile and instrument parameters and seeks to minimize the difference between this and the data.

To gauge how good a fit is there are a number of parameters with the most useful being R_{wp} and χ^2 although careful inspection of the pattern and model should always be carried out. The equations for some of these parameters are given on the following page.

$$R_p = \frac{\Sigma_i \mid y_i(obs)-y_i(calc)\mid}{\Sigma_i\, y_i(calc)}$$

Equation 2-10 R-pattern

$$R_{wp} = \left[\frac{\Sigma_i \mid y_i(obs)-y_i(calc)\mid^2}{\Sigma_i\, (y_i(calc))^2} \right]^{1/2}$$

Equation 2-11 R-Weighted Pattern

$$R_e = \left[\frac{(N-P)}{\Sigma_i\, w_i(\, y_i(obs))} \right]^{1/2}$$

Equation 2-12 R- Expected
N= number of observables P= Number of parameters

$$\chi^2 = \left[\frac{R_{wp}}{R_e} \right]^2$$

Equation 2-13 'Goodness of fit'

R_{wp} (R-Weighted Pattern) contains the residual which is being minimized and so the lower R_{wp} goes the lower the mismatch between data and model so the higher quality of the refinement (note R_{wp} is often written as wRp). For a typical refinement this value should be less than 0.1 which corresponds to less than 10%. χ^2 (Goodness of fit) is a

ratio between the R value seen and the R value expected and so should tend to 1. However as it is susceptible to poor quality data artificially low values can be observed with a χ^2 of less than 1 being consistent with this. For a typical refinement χ^2 should be between 1 and 2.

The errors quoted in the values derived from the refinements are quoted as estimated standard deviations (e.s.d's) and as such reflect the precision of the refined parameter not the accuracy[26]. When two values such as lattice parameters from different samples are compared the values obtained should be within 3 esd's to be considered the same.

Thermal parameters in this thesis are quoted as U_{iso} or B_{iso} depending on the refinement program used (GSAS for U_{iso} and TOPAS for B_{iso}) but they related via

$$B_{iso}=8\pi^2U_{iso}$$

Equation 2-14 Showing the thermal parameters B_{iso} and U_{iso} are related.

2.3 Magnetic Measurements

Magnetic characterization was carried out using a Quantum Design MPMS magnetometer[16] which was controlled using MPMS software. The MPMS magnetometer makes use of a thin film radiofrequency (rf) SQUID to give magnetic property measurements over a temperature range of 5 to 400 K and an applied field up to 7 Tesla. The Superconducting Quantum Interface Device (SQUID) which was developed in the 1960's[17] is capable of detecting changes in a magnetic field as small as 10^{-15} T. [18] Inside the rf SQUID there is a superconducting loop which contains a single weak link called a Josephson junction through which Cooper pairs can tunnel. Cooper pairs are electrons coupled together so they cannot change energy continuously below the superconducting transition temperature T_c. This superconducting loop is

inductively coupled via a mutual inductance to a rf current driven tank circuit. When a measured flux is superimposed over a dc bias flux the average value of the phase across the Josephson junction changes. Such a change changes the impedance of the rf drive oscillations and so the rf voltage in the tank circuit which is directly proportional to the magnetic moment of the sample. A SQUID is therefore a flux to voltage transducer with a sensitivity limit approaching that set by the Heisenberg uncertainty principle.

To generate the measured flux the sample is moved through detector coils made out of superconducting wire, if the sample is magnetic it will induce a current in the wire. The current flowing through the superconducting wire will then generate a magnetic flux.

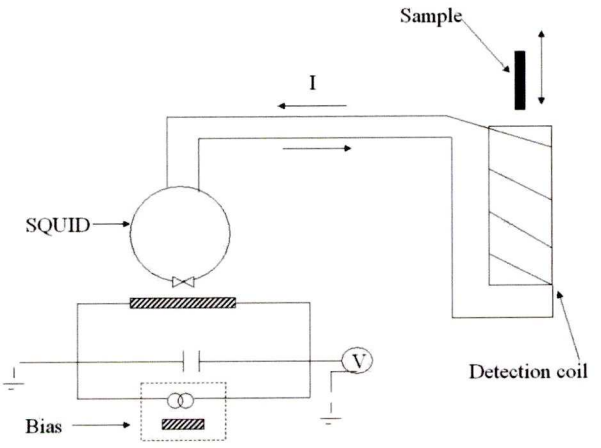

Figure 2-8 Schematic of an rf SQUID based magnetometer

For the experiment setup the sample was loaded into a gelatin capsule, which in turn was placed in a plastic straw. The capsules were held in place by diamagnetic tape, the straw was then pierced before being lowered into the SQUID and was purged with helium to prevent oxygen entering the SQUID. Magnetism as a function of temperature was measured both after cooling in the absence of a magnetic field (zero field cooled, ZFC)

and after cooling in an applied field (field cooled, FC). Magnetism as a function of field at a constant temperature can also be measured to observe any hysteresis behavior.

2.4 Cold Isostatic Pressing

Pellet samples with > 90% of the theoretical density for electrical measurements were made via cold-isostatic pressing (CIP) with 206.85 MPa pressure. Samples are first pelletized as described in section 2.1.1 then sealed in waterproof bags and lowered into the hydraulic fluid. The system is then sealed and brought up to pressure and left to dwell for five minutes before the pressure is slowly released and the sample bag retrieved.

2.5 Conductivity Measurement

Impedance spectroscopy was used as the primary method of testing the conductivity of the materials synthesized in this thesis. Impedance[19] is the ratio of the voltage over current but as an AC voltage is applied there is a phase element providing real (Z') and imaginary (Z'') components. As capacitance values can often assist in assigning responses observed in impedance spectra these values were also measured. Typical values for capacitance of differing components of a ceramic material are given Table 2-2

Table 2-2 Capacitance values for differing components.

Component	**Capacitance (F/ cm)**
Bulk (ferroelectric)	10^{-12} (10^{-10}–10^{-9})
Minor phase	10^{-11}
Grain boundary	$10^{-11} - 10^{-8}$
Electrode	10^{-7} –10^{-5}

AC Impedance Spectroscopy (IS) measurements in air were performed with a Solartron 1255B Frequency Response Analyzer coupled to a Solartron 1287 electrochemical interface over the 10^{-2}-10^{6} Hz frequency range for measurements in the 350-980 °C range.

Pellets were prepared by first polishing both sides with Silicon Carbide paper, (Buehler P800 and P2500) then applying the electrodes. The electrodes used were made by painting the polished pellet with platinum paste (Metalor A4731) and firing at 150 °C for 1 hour, then ramping to 300 °C holding for 1 hour then ramping to 800 °C holding for 1 hour then ramping to 950 °C for the measurement. The ramp rate was set at 5 °C per minute and the wires used to connect the pellet to the Solartron leads were Engelhard CPPT platinum wire.

For each sample the pellet being measured was heated to 950 °C and left to dwell for an hour before the measurement took place. Measurements were then taken every 50 °C down to 350 °C with the measurement for each temperature only occurring after the sample had been left for 1 hour at that temperature to ensure the sample had equilibrated.

For measurements at lower temperatures or higher resistances a Solartron 1296 dielectric interface was used instead of the Solartron 1287 electrochemical interface for measurements over the 10^{-2}-10^{6} Hz frequency range and the temperature range 200 °C – 500 °C on heating and cooling cycles. Instead of platinum electrodes, silver conductive paint which dries in air was used (Agar G3790) to allow for measurement to be carried out without the need to sinter electrodes at high temperatures.

a.c. conductivity as a function of partial pressure of oxygen (pO_2) (monitored by a YSZ potentiometric sensor) was measured at 600 °C over a pO_2 range of $1\text{-}10^{-22}$ atm. The pO_2 value was controlled over $1\text{-}10^{-4}$ atm pO_2 range by dilution of O_2 with Ar, for $10^{-4}\text{-}10^{-22}$ atm by using mixed 1%CO in Ar and 1% CO_2 in Ar. The dwell time ranged from 5 – 24 h (~5-8 h for $pO_2 > 10^{-4}$ and 12-24 h for $pO_2 < 10^{-4}$ to allow equilibration of the samples with the gas environment at each point.

2.6 Dielectric Measurement

Pellets for dielectric measurements were prepared in a similar manner to those used in the conductivity measurement. Again capacitance was measured allowing the calculation of dielectric constant (ε_r) and dielectric loss ($\tan \delta$) (see section 1.2.2).

2.7 Diffuse Reflectance

Reflectance data for band gap determination were collected on a Perkin Elmer LAMDA 650 S UV/Vis spectrometer using $BaSO_4$ reflectance standards and converted to absorbance (using Kubelka-Munk[23,24]). The band gap energy was then obtained by using the Shapiro method of extrapolating the onset of absorption to the wavelength axis.[20]

2.8 Infrared spectroscopy (IR)

Infrared spectroscopy probes the vibrations of a material as differing vibrations will absorb differing IR energies. Only vibrations where the electric dipole moment changes when atoms are displaced due to the vibration are allowed. The most useful aspect of IR

spectroscopy for solid-state crystal structures is the identification of OH groups as these have a characteristic strong broad band at 3500 cm^{-1}.

The IR measurements were carried out on a Perkin Elmer Spectrum 100 with an Attenuated Total Reflectance (ATR) attachment allowing powder samples to be measured directly.

2.9 Thermo gravimetric analysis (TGA)

Thermogravimetric analysis (TGA) allows weight changes in a material to be followed as a function of temperature under varying gas atmospheres. TGA can be used to follow water loss from proton conductors as the loss of H_2O from the structure results in an overall weight loss for the material. TGA can also be used to follow changes in oxygen content as if the oxidation state of a material changes oxygen is either lost or incorporated (causing a weight change) to charge balance.

The TGA measurements was carried out in this thesis were performed using a TA Instruments SDTQ600

2.10 Energy-dispersive X-ray analysis (EDS)

The EDS was carried out using a JEOL 2000FX transmission electron microscope (TEM) operated at 200 kV. The focused electron beam in the electron microscope causes a small proportion of core electrons of the material being measured to be ejected. These ejected electrons leave electron holes in the lower shells that are then filled by electrons from higher shells with emission of radiation characteristic of the element and the shells involved. It is this radiation that is detected and as all the elements in the

material are excited together the recorded spectra gives the emissions from all the elements. By comparing the relative intensities of the emitted radiation the relative ratio of elements present in the material can be calculated. Error of the instrument calculated to be ± 4-5% when the concentration of the element under test is > 5% [25]. To ensure this level of accuracy is achieved for measurements the machine is calibrated for the elements required using standards. These calibrations are then saved in the instruments software to be used for the samples under test. The standards chosen are well characterized materials whose structure and composition can be checked independently of the TEM (XRD and ICP-OES) before use in the calibrations. Maintenance of the JEOL 2000FX and training was provided by Dr S. Romani.

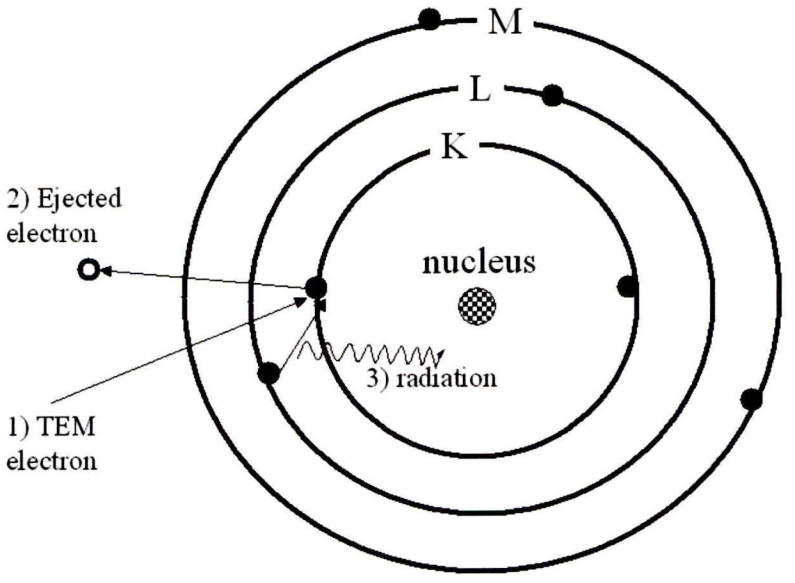

Figure 2-9 Schematic representation of the EDS process. First a TEM electron (1) causes an electron from a core shell (K in diagram) to be ejected (2). To fill the hole left by the ejected electron an electron from a higher shell (L in diagram) drops down with emission of radiation (3).

2.11 X-Ray Absorption Spectroscopy (XAS)

X-Ray Absorption Spectroscopy (XAS) data used in this thesis were collected at the SRS station 9.3 with the aid of Dr S. Fiddy and Dr I. Harvey. A typical example of the data obtained is given in Figure 2-10 with the regions of interest labeled.

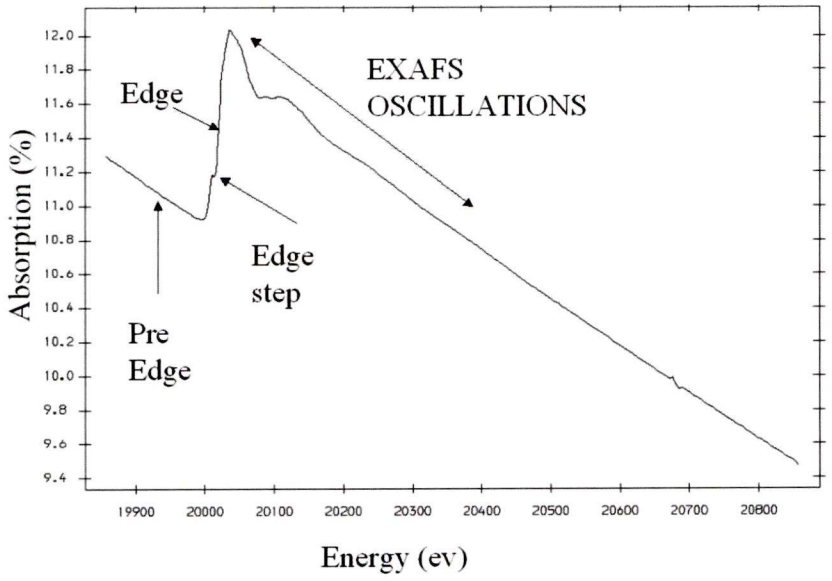

Figure 2-10 Example of an X-Ray Absorption Spectroscopy (XAS) data set showing the pre edge, edge and EXAFS regions.

When the material under investigation is placed in the synchrotron X-Ray beam some of the X-Rays are absorbed by the material. Certain energies of absorbed X-Rays lead to a core electron of one of the elements being ejected (similar to EDS) and this can be seen as a spike in the absorbance corresponding to the energy required for the ejection. As this energy is sensitive to the element, oxidation state and coordination environment information about the differing environments of the elements present in the sample can be obtained. The precise position of the edge is taken as the inflection point and varies

linearly with valence state, increasing of oxidation state results in a shift to higher energies[21].

Above the absorption edge is the Extended X-ray Absorption Fine Structure (EXAFS) region (Figure 2-10). EXAFS appears when the absorbing atom is closely surrounded by other atoms as the origin of the EXAFS oscillation is interference between outgoing and backscattered photoelectrons. As the coordination of the absorbing atom depends on the number of atoms close to the absorbing atom the EXAFS region can be used to indicate coordination number. Distance from the absorbing atom can also be obtained by refining a model against the EXAFS data.

Powdered samples of the material under investigation were mounted on 'sticky backed' plastic. The energy range of the X-ray beam was then selected to cover the absorption edge of the material under test. Standards were always used as comparisons and monitor spectrums of the metal foils were also used to ensure a fair comparison between runs as by matching monitor edges a true comparison of the samples can be made.

2.12 References

[1] F. R. Boyd, *Science* **1964**, *145*, 13.

[2] M. Azuma, K. Takata, T. Saito, S. Ishiwata, Y. Shimakawa, M. Takano, *Journal of the American Chemical Society* **2005**, *127*, 8889.

[3] J. H. Park, J. B. Parise, *Materials Research Bulletin* **1997**, *32*, 1617.

[4] C. T. Prewitt, R. T. Downs, *Ultrahigh-pressure mineralogy* **1998**, *Chapter 9*.

[5] R. M. Hazen, A. Navrotsky, *American Mineralogist* **1996**, *81*, 1021.

[6] D. McAdams, C. Reavis, *MIT Sloan Management case study* **2008**, *07-045*, 1.

[7] P. A. Salvador, T.-D. Doan, B. Mercey, B. Raveau, *Chemistry of Materials* **1998**, *10*, 2592.

[8] D. Walker, M. A. Carpenter, C. M. Hitch, *American Mineralogist* **1990**, *75*, 1020.

[9] W. G. Williams, R. M. Ibberson, P. Day, J. E. Enderby, *Physica B: Condensed Matter* **1997**, *241-243*, 234.

[10] R. M. Ibberson, W. I. F. David, K. S. Knight, *RAL Report* **1992**, *RAL-92-031*.

[11] S. Hull, R. I. Smith, W. I. F. David, A. C. Hannon, J. Mayers, R. Cywinski, *Physica B: Condensed Matter* **1992**, *180-181*, 1000.

[12] A. Le Bail, H. Duroy, J. L. Fourquet, *Materials Research Bulletin* **1988**, *23*, 447.

[13] J. Rodríguez-Carvajal, *Physica B: Condensed Matter* **1993**, *192*, 55.

[14] A. C. Larson, R. B. Von Dreele, *Los Alamos National Laboratory* **2000**, *LAUR 86-748*.

[15] H. M. Rietveld, *J. Appl. Cryst.* **1969**, *2*, 65.

[16] M. McElfresh, *Quantum Design Inc SQUID MANUAL* **1994**.

[17] A. H. Silver, *Superconductor science and technology* **2006**, *19*, 173.

[18] J. Clarke, *Scientific American* **1994**, *August*

[19] J. T. S. Irvine, D. C. Sinclair, A. R. West, *Advanced Materials* **1990**, *2*, 132.

[20] H. W. Eng, P. W. Barnes, B. M. Auer, P. M. Woodward, *Journal of Solid State Chemistry* **2003**, *175*, 94.

[21] I. Arcon, B. Mirtic, A. Kodre, *J. Am. Ceram. Soc* **1998**, *81*, 222.

[22] www.topas-academic.net.

[23] http://www.piketech.com/technical/application-pdfs/Diffuse_Theory&Appl.pdf

[24] P. Kubelka, F Munk , *Zeitschrift fur technische Physik* **1931,** 12, 593.

[25] L. Wang, *http://www.dssc.ece.cmu.edu/news/seminars/lunch05/headsmedia/042605.pdf* **2005**, 1, 6.

[26] L. B. McCusker, R. B. Von Dreele, D. E. Cox, D. Louër, P. Scardi, *Journal of Applied Crystallography* **1999,** 32, 36.

Chapter 3 : Melilites for use as solid oxide fuel cell electrolytes

3.1 Introduction

This chapter reports the synthesis and characterization of the interstitial oxide conductor family $La_{1+x}Sr_{1-x}Ga_3O_{7+x/2}$ (x = 0-0.64). The stability of the systems in varying conditions (both atmosphere and temperature) and for varying durations is discussed. Conduction properties of the materials are also presented, including experiments conducted to ascertain the nature of the charge carrier. Much of the work presented in this chapter has led to publication[1, 2].

Interest in $LaSrGa_3O_7$ melilite was rekindled when it was identified as an insulating impurity in LSGM electrolytes by Goodenough,[3] $LaSrGa_3O_7$ having previously been investigated as a laser material.[4] Subsequent work by Rozumek et al,[5, 6] Raj et al[7]and Kuang et al[8] altered the La:Sr ratio and the conductivity was found to increase. The studies reached differing conclusions on the available ranges of x for $La_{1+x}Sr_{1-x}Ga_3O_{7+x/2}$ Rozumek giving x = -0.15 to x = 0.60, Raj giving x = 0 to x = 0.05 with Kuang presenting data on x = 0 to x = 0.54 . In their report Kuang and coworkers suggest that x = 0.6 is the maximum value of x which will retain the parent tetragonal structure with disordered oxide ion interstitials. Also proposed by Kuang is an interstitial oxide conduction mechanism making melilite an unusual interstitial conductor as the structure contains a 2D network of polyhedra shown in Figure 3-1 . Other oxide ion interstitial conductors such as apatites[9, 10] and $La_2Mo_2O_9$[11-13] based materials typically show isolated polyhedra. The coexistence of the partially occupied interstitial sites and the coordination flexibility of the Ga_2O_6

units are thought to be the features that give rise to the observed interstitial conductivity.

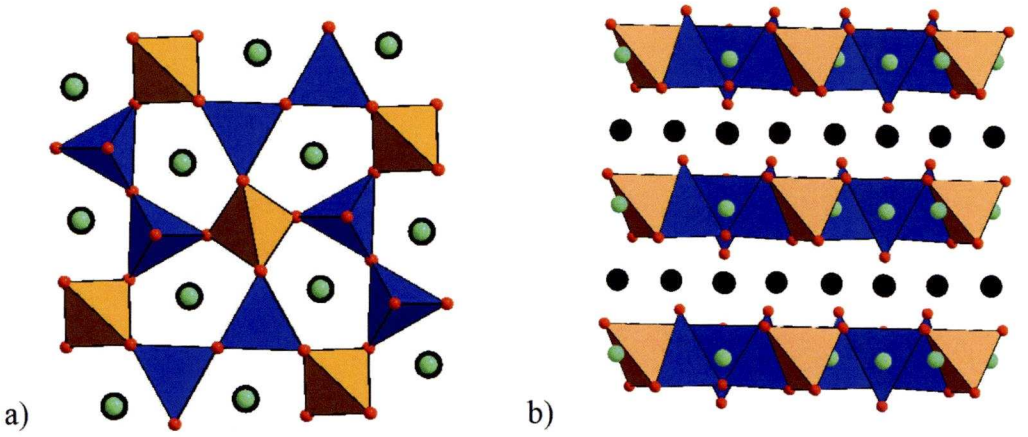

Figure 3-1 The melilite structure of $LaSrGa_3O_7$ showing the 2D network of polyhedra in orange and blue .The spheres for the interstitial oxygen sites (green spheres) are larger than those for the framework oxygens (red spheres). In a) the view is down the c axis while in b) the view is along [110]. A more detailed description of the structure can be found in the introduction.

3.2 Synthesis

Ceramic synthesis with slight excess Ga_2O_3 affords the $La_{1+x}Sr_{1-x}Ga_3O_{7+0.5x}$ ($x \leq 0.64$) samples studied (synthesis of x = 0.65 and x = 0.67 was also attempted with the result being a mixture of melilite and Sr-doped $LaGaO_3$ (LSG)). As 1.7% excess Ga was required by Kuang[8] to form x = 0.54 instead of the 2:3 La/Sr:Ga ratio, this was increased to 2:3.05 (1.7% excess Ga) for x = 0.54 - 0.58 , to 2:3.06 (2% excess Ga) for x = 0.6 and x = 0.62, and to 2:3.07 (2.3% excess Ga) for x = 0.64. All compositions were initially fired as powders at 1200 °C then pressed into pellets and fired at 1400 °C (x = 0-0.54) or 1350 °C (x = 0.56-0.64). Post synthesis XRD and also EDS investigations showed no evidence of Ga_2O_3 or other gallium rich impurities being present.

Composition was checked by EDS showing clustering of the crystallites indicating single phase materials. The average composition of x = 0.6 and x = 0.64 of the crystallites ($La_{1.54(8)}Sr_{0.45(2)}Ga_{3.01(15)}O_{7.275\pm0.35}$ and $La_{1.52(8)}Sr_{0.47(2)}Ga_{3.01(15)}O_{7.2765\pm0.35}$

respectively) . Error of the instrument calculated to be ± 4-5% when the concentration of the element under test is > 5% [14].

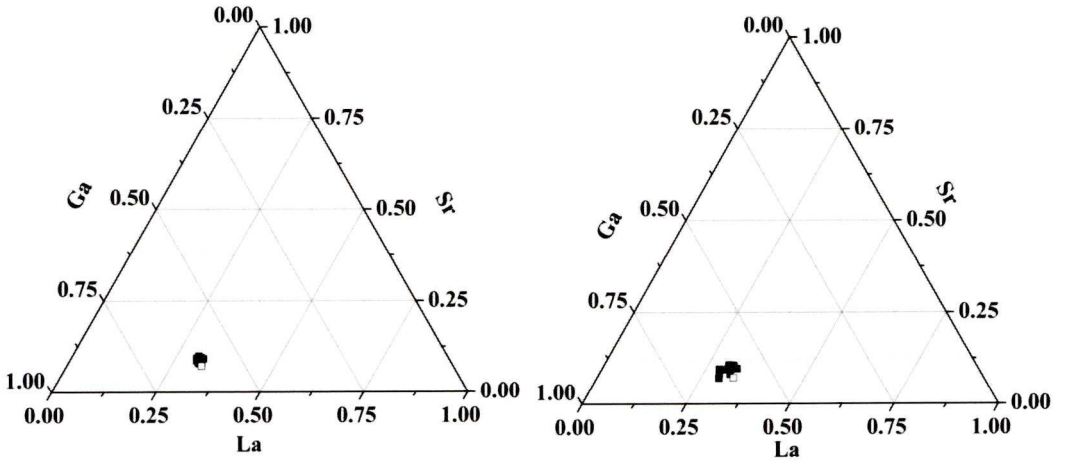

Figure 3-2 EDS of ten grains of $La_{1.6}Sr_{0.4}Ga_3O_{7.3}$ (left) and EDS of ten grains of $La_{1.64}Sr_{0.36}Ga_3O_{7.32}$ (right), hollow squares in both figures are the ideal points average compositions $La_{1.54(8)}Sr_{0.45(2)}Ga_{3.01(15)}O_{7.275}$ and $La_{1.52(8)}Sr_{0.47(2)}Ga_{3.01(15)}O_{7.2765}$ respectively .

3.3 Characterization

To characterize the $La_{1+x}Sr_{1-x}Ga_3O_{7+0.5x}$ ($x \leq 0.64$) materials the phase formation and stability has been investigated along with the conductivity.

3.3.1 Phase formation

The powder X-Ray (XRPD) patterns (Figure 3-3) for $x < 0.6$ can be indexed using the tetragonal cell of the $LaSrGa_3O_7$ parent phase. However, for $x > 0.6$, the broadening, then splitting of the $h,k \neq 0$ tetragonal reflections requires indexing with a pseudo-orthorhombic cell ($a_{orth} \approx b_{orth} \sim \sqrt{2}a_{tetra}$, $c = c_{tetra}$). The true symmetry however may be lower as shown in $La_{1.64}Ca_{0.36}Ga_3O_{7.32}$ which can best be described in the triclinic space group P1.[2] Full structural characterization of the tetragonal

phases was carried out by Kuang[8] while full structural analysis of the pseudo-orthorhombic phases is likely to require the same treatment as $La_{1.64}Ca_{0.36}Ga_3O_{7.32}$ [2]. For both the tetragonal Sr melilites and $La_{1.64}Ca_{0.36}Ga_3O_{7.32}$ full structural characterization was only possible after many experiments at central facilities both synchrotrons (SRS and Diamond) and neutron facilities (ISIS and NIST). The results from the tetragonal melilite study can be used in refinements using laboratory XRD data, see Appendix 2 for examples. However the complexity of the $La_{1.64}Ca_{0.36}Ga_3O_{7.32}$ model cannot easily be applied to the Sr pseudo-orthorhombic cases using laboratory XRD so refinements of these structures require central facilities data.

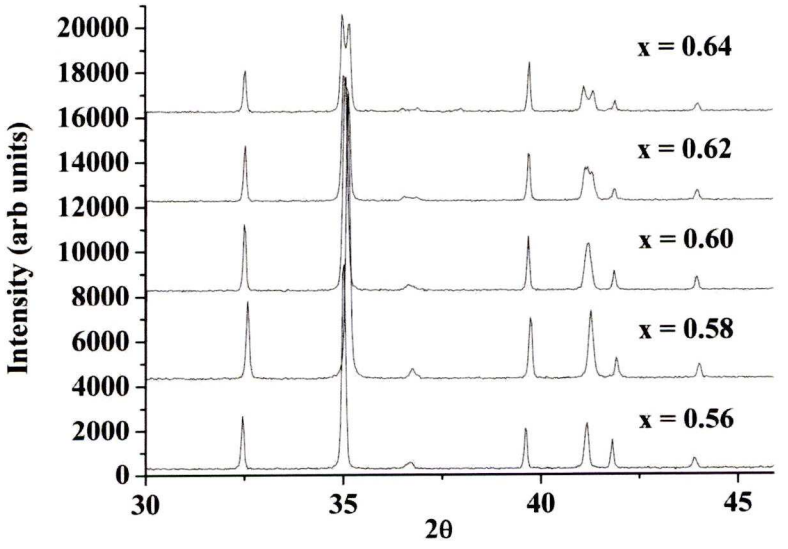

Figure 3-3 XRD patterns of $La_{1+x}Sr_{1-x}Ga_3O_{7+x/2}$ (x = 0.56 -0.64).

As the value of x increases the *a* lattice parameter decreases linearly until the transition to the pseudo-orthorhombic structure, with the *c* lattice parameter and the volume (Figure 3-4) decreasing linearly across the entire composition range, accounted for by the smaller size of La^{3+} (103.2 pm versus 118 pm for Sr^{2+}). x = 0.64 is the highest La content affording an exclusively melilite composition and is a

mixture of pseudo-orthorhombic and tetragonal forms at room temperature (Figure 3-5).

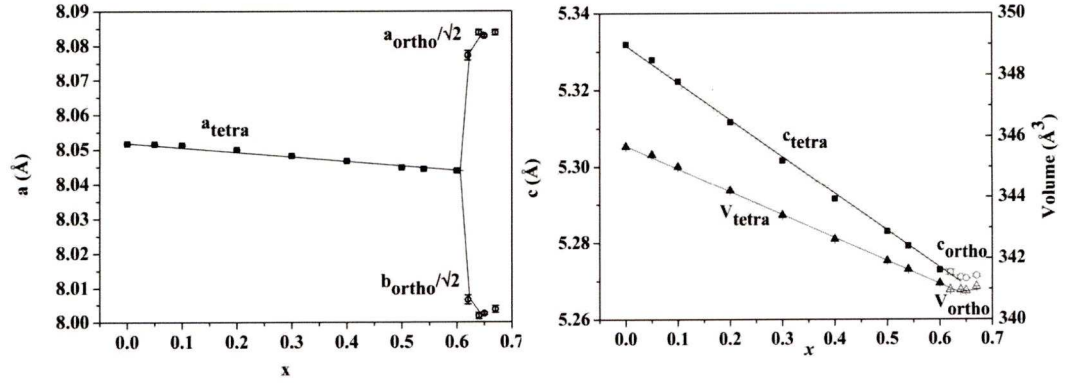

Figure 3-4 a and b lattice parameters (left) and c parameter with the unit cell volume (right) of $La_{1+x}Sr_{1-x}Ga_3O_{7+x/2}$, x=0-0.67.

In the as synthesized materials where x >0.6 the post synthesis XRD collected after standard cooling in a furnace shows a mixture of the tetragonal and the pseudo-orthorhombic phases. If the sample is quenched from 1350 °C by tipping the pellet onto a room temperature block of aluminium the resulting phase is tetragonal shown by sharp single peak at 35° 2θ versus the broad peak when slow cooled (FWHM 0.139 ° versus 0.235 °). Annealing at 400 °C causes the tetragonal phase to transform to the pseudo-orthorhombic (Figure 3-5).

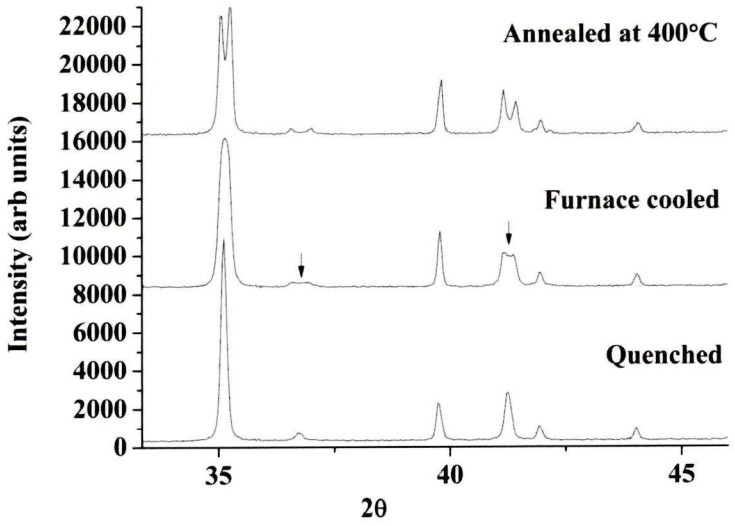

Figure 3-5 $La_{1.64}Sr_{0.36}Ga_3O_{7.32}$ after quenching, furnace cooling, and annealing for 12 h at 400 °C. The arrows indicate the tetragonal peaks in the pseudo-orthorhombic dominated furnace-cooled sample.

This transition from the tetragonal phase (either quenched or part of furnace cooled mix) to the pseudo-orthorhombic phase at 400°C takes place within 30 minutes (Figure 3-6). However if the sample is heated further to 565 °C then the pseudo-orthorhombic phase transforms to the tetragonal phase (Figure 3-6). The transition from pseudo-orthorhombic to tetragonal appears to take 20 minutes while temperature is ramping from 565 °C to 580 °C. After this point the 121 peak doesn't get any sharper meaning the material has completely transformed to the tetragonal form. $La_{1.64}Ca_{0.36}Ga_3O_{7.32}$ also exhibits this type of phase transition from pseudo-orthorhombic to tetragonal at temperatures between 600 °C and 700°C. From these observations all the melilites adopt the tetragonal structure at high temperatures but when x >0.6 at temperatures below 565 °C for Sr the pseudo-orthorhombic structure becomes more stable. The kinetics of this transition while being faster than the Ca melilite phase transitions still allow both phases to be separated.

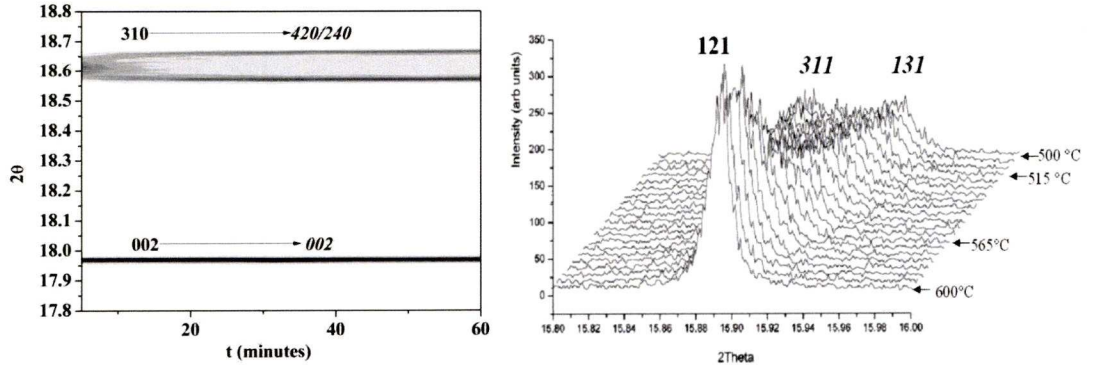

Figure 3-6 Diffraction from $La_{1.64}Sr_{0.36}Ga_3O_{7.32}$ at 400 °C (left) showing the transition from metastable T to stable O phase. T Miller indices in bold and O in italics. High temperature XRD data measured on $La_{1.64}Sr_{0.36}Ga_3O_{7.32}$ between 500 °C and 600 °C. Miller indices for the T phase are in bold and those for the O in italics. The starting and finishing temperatures have been marked as well as the temperatures at which the observed start and end of the structural transition appear.

The synthesized samples are stable to 800 °C in air (Figure 3-7). For $x \geq 0.4$, prolonged annealing above this temperature (for periods longer than the impedance measurements described later – all materials reported were examined by XRD post-measurement to ensure their single phase nature was retained) causes the melilite to partially decompose with formation of the Sr-doped LSG perovskite (Figure 3-7) and Ga_2O_3, rendering conductivity comparisons with $La_{0.8}Sr_{0.2}Ga_{0.83}Mg_{0.17}O_{2.815}$ (LSGM) only meaningful below 800 °C at these higher doping levels.

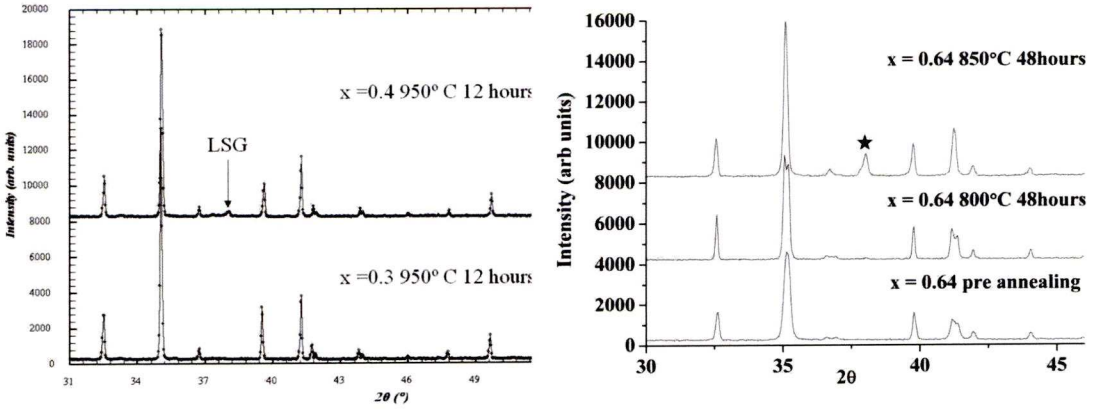

Figure 3-7 x = 0.3 and x = 0.4 post 950 °C annealing for 12 hours (left). XRD patterns of $La_{1.64}Sr_{0.36}Ga_3O_{7.32}$ (right) before annealing, after annealing at 800 °C for 48 h, and after 850 °C for 48 h. The black star shows the formation of strontium doped lanthanum gallate (LSG) perovskite.

Higher doping levels cause the melilite structure to be less stable with respect to the perovskite phase. However even after 120 hours at 950 °C the x = 0.62 sample still shows an appreciable amount of the melilite phase (Figure 3-8).

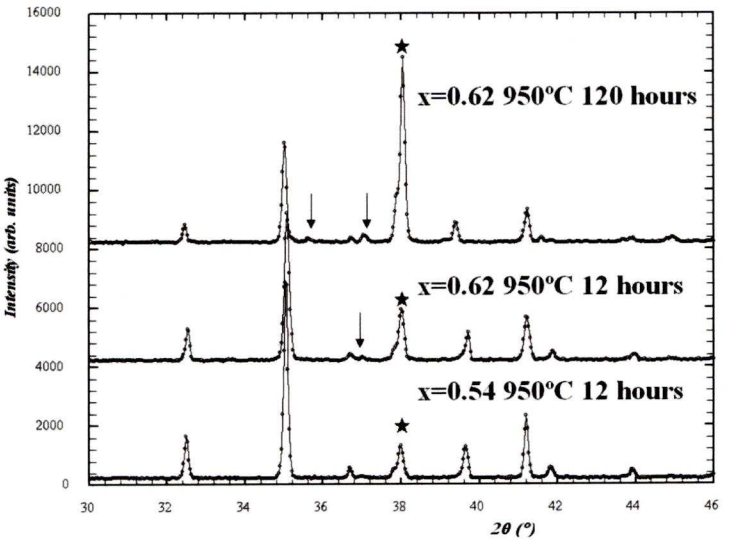

Figure 3-8 XRD patterns of $La_{1.54}Sr_{0.46}Ga_3O_{7.27}$ annealed at 950 °C for 12 hours, $La_{1.62}Sr_{0.48}Ga_3O_{7.31}$ at 950 °C for 12 hours and $La_{1.62}Sr_{0.48}Ga_3O_{7.31}$ at 950 °C for 120 hours. Black stars and arrows show the formation of strontium doped lanthanum gallate (LSG) perovskite and Ga_2O_3 oxides, respectively.

The instability with respect to LSG only occurs over a limited temperature range as reheating the phase separated mixture at 1350 °C recovers the initial melilite, suggesting a complex sequence of phase stability (Figure 3-9).

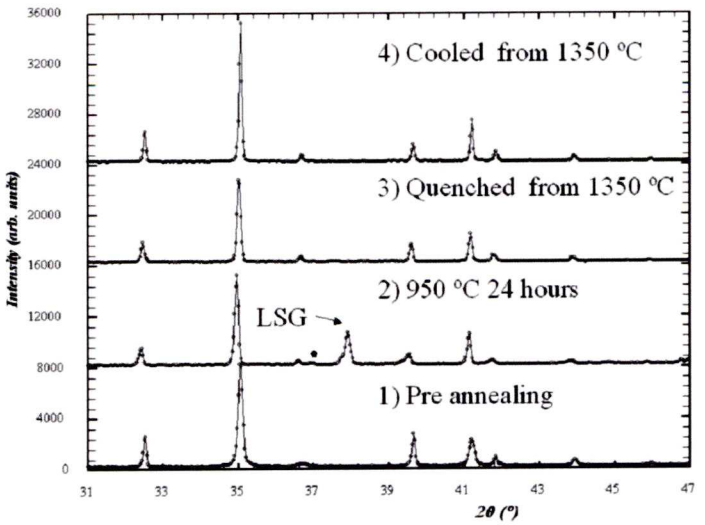

Figure 3-9 shows XRD patterns of a single sample of $La_{1.54}Sr_{0.46}Ga_3O_{7.27}$ 1) as-synthesized 2) annealed at 950 °C for 24 hours, causing a significant amount of LSG-type perovskite and Ga_2O_3 to form. This sample was then split into two separate samples and re-heated to 1350 °C. One of the samples was quenched ((3)) and the other was cooled in the furnace ((4)). In both (3) and (4) the LSG perovskite reacted with Ga_2O_3 to reform the melilite phase, resulting in a single melilite phase.

To further study the stability of the melilite phase with respect to the perovskite phase an XRD pattern of a sample of $La_{1.54}Sr_{0.46}Ga_3O_{7.27}$ annealed at 950 °C for 24 hours was refined quantitatively with the Rietveld method (Figure 3-10). The refinement gives a molar ratio of 6:4:1 (Melilite: Perovskite: Oxide) consistent with the melilite decomposing according to the reaction below.

$$La_{1.54}Sr_{0.46}Ga_3O_{7.27} \longrightarrow 2La_{0.77}Sr_{0.23}GaO_{2.885} + 1/2Ga_2O_3$$

The refined lattice parameters for the remaining melilite phase ($P\bar{4}2_1m$) are as follows;

a = 8.04323(30) Å, c = 5.28230(24) Å which compare to the as synthesized materials parameters of a = 8.0477(7) Å , b = a, c = 5.27814(8) Å. Using the refined volume of the remaining melilite phase and comparing it to Figure 3-4 the remaining melilite composition can be estimated as $La_{1.53}Sr_{0.47}Ga_3O_{7.265}$.

The refined lattice parameters for the $La_{0.77}Sr_{0.23}Ga_3O_{2.885}$ phase (I b m m) are as follows;

a = 5.5219(4) Å, b = 5.4897(4) Å, c = 7.7692(5) Å which compare to the parameters of the reported phase $La_{0.88}Sr_{0.12}GaO_{2.94}$ [15] a = 5.52898 Å, b = 5.48771 Å , c = 7.77031 Å

The refined lattice parameters for the β-Ga_2O_3 phase (C 1 2/M 1) are as follows;

a = 12.241(6) Å, b = 3.0261(15) Å, c = 5.8013(21) Å, β = 103.82(5) ° which compare to the reported[16].

a = 12.214(3) Å, b = 3.0371(9) Å, c = 5.7981(9) Å, β = 103.83(2) °

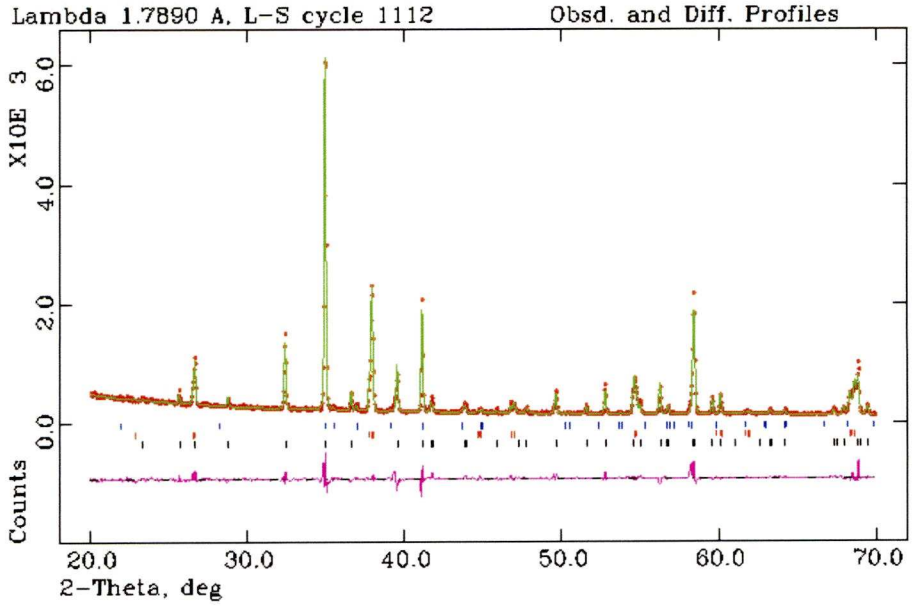

Figure 3-10 Rietveld refinement of $La_{1.54}Sr_{0.46}Ga_3O_{7.27}$ (bottom black tick marks) annealed at 950 °C for 24 hours (λ = 1.7890 Å Rwp = 8.95%). The other phases in the refinement are $La_{0.77}Sr_{0.23}GaO_{2.885}$ (middle red tick marks) and β -Ga_2O_3 (upper blue tick marks). Further data in appendix 2.3. The red crosses are data points the green line is the fit and the purple line the difference plot.

3.3.2 Conductivity

Conductivity measurements were carried out using the equipment described in chapter 2. In the observed impedance spectra the bulk and the grain boundary responses at higher frequencies overlap to exhibit part of an asymmetric semicircular arc. The intercept of the semicircular arc at low frequency was extracted as the total resistivity $R_b + R_{gb}$. Above 400 °C, the electrode response dominated the impedance data and gradually collapsed to a semicircular arc, giving two arcs in the impedance plot. The high frequency intercept of the second arc was taken as total resistivity $R_b + R_{gb}$ while the high frequency intercept of the first arc was taken as the bulk resistivity R_b. This allows the bulk and grain boundary resitivities to be separated over the region where the two arcs are visible (Figure 3-11). As the temperature is increased the arc from the grain boundary response vanishes and only one semicircular arc from the electrode response was seen with the high frequency intercept being taken as the total resistivity $R_b + R_{gb}$.

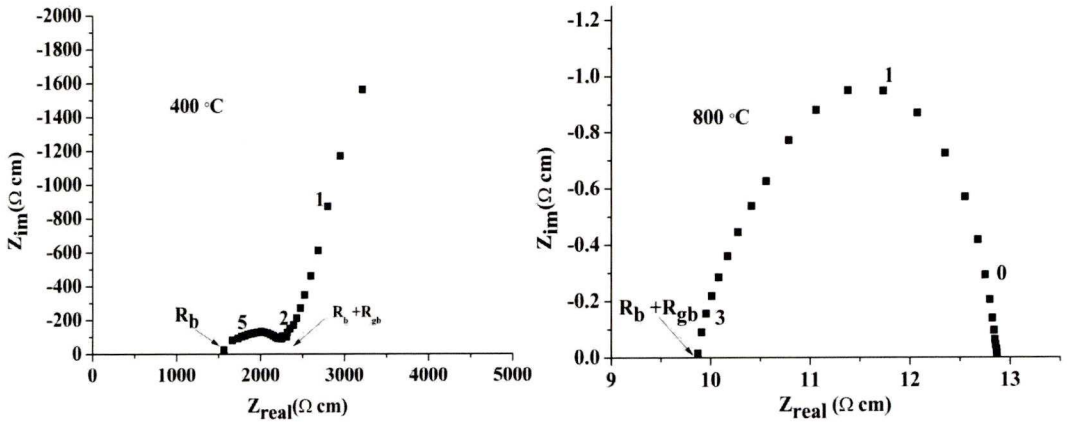

Figure 3-11 Complex impedance plots of $La_{1.6}Sr_{0.4}Ga_3O_{7.3}$ at 400 °C (left) and 800 °C (right). The numbers in bold on the plot indicate the frequency logarithms, the a.c. amplitude used for the measurements was 10 mV.

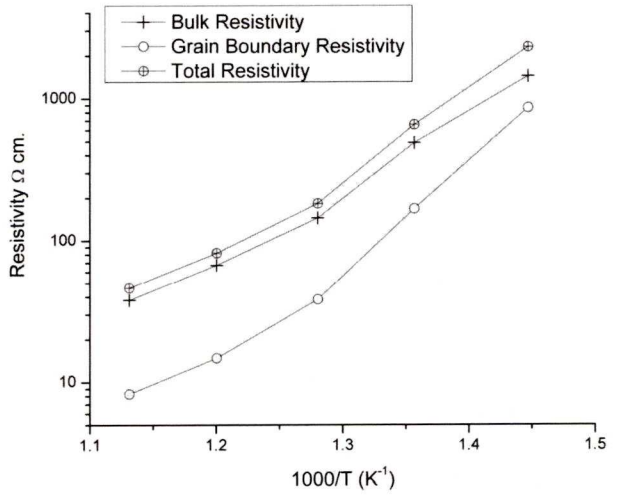

Figure 3-12 gives the temperature dependence of the bulk, grain boundary and total resistivity of $La_{1.6}Sr_{0.4}Ga_3O_{7.3}$

The total conductivity versus temperature in air for $0 \leq x \leq 0.64$ is shown in Figure 3-13 with $La_{0.8}Sr_{0.2}Ga_{0.83}Mg_{0.17}O_{2.815}$ [3] (LSGM) for comparison. The conductivity at $x = 0.54$ is approximately three orders of magnitude greater than the parent material. The total conductivity of $x = 0.6$ $La_{1.6}Sr_{0.4}Ga_3O_{7.3}$ at 500 °C is 6.8×10^{-3} S cm^{-1}, which compares with 4×10^{-3} S cm^{-1} for the bulk conductivity of Mg-doped $La_{10}Si_6O_{27}$, [17] 3.2×10^{-4} S cm^{-1} for the bulk conductivity of Al-doped $La_{10}Ge_6O_{27}$ [18] 5×10^{-3} S cm^{-1} for the total conductivity of LSGM ($La_{0.8}Sr_{0.2}Ga_{0.83}Mg_{0.17}O_{2.815}$) [3] and 0.004-0.01 S cm^{-1} for the total conductivity of $Ce_{0.9}Gd_{0.1}O_{1.95}$.[19-21] Above

600°C and below 400°C, all the interstitial-based melilites are poorer conductors than vacancy-based LSGM, but over the 400-600°C range, the x = 0.58 and x = 0.6 compositions have slightly higher conductivity than LSGM (Figure 3-13).

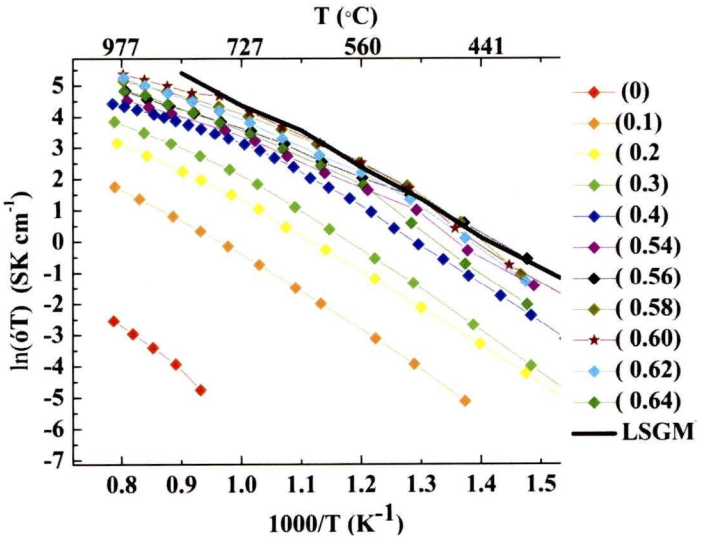

Figure 3-13 Conductivity of $La_{1+x}Sr_{1-x}Ga_3O_{7+x/2}$ where x=0-0.64. LSGM is $La_{0.8}Sr_{0.2}Ga_{0.83}Mg_{0.17}O_{2.815}$.[3]

Considering the conductivity versus x at 800 °C there is a clear rise to a maximum value of conductivity with concurrent fall in E_a to x = 0.6. Past x = 0.6 the slight rise in E_a corresponds to a drop in conductivity. However if conductivity versus x at 450 °C is considered the maximum value of conductivity occurs at x = 0.56.

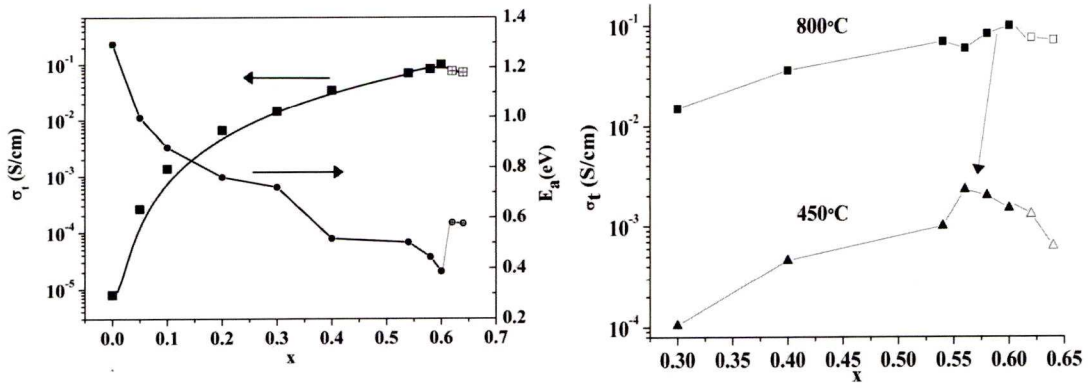

Figure 3-14 Conductivity and activation energy of $La_{1+x}Sr_{1-x}Ga_3O_{7+x/2}$ at 800 °C versus x (left) and a comparison of conductivity at 800 °C and 450 °C versus x. The low temperature stable forms are indicated by filled (T) and empty (O) symbols. The black curved line for the conductivity data is a fit to $\sigma_t = \sigma_0 + AC_{oi}^n$ where C_{oi} = number of interstitials per formula unit, σ_0 =8.01 x10^{-6} S/cm, A=2.2(7), and n=2.7(2). This line is presented as a guide to the eye. At the two different temperatures the conductivity maximum occurs at different compositions (800 °C x = 0.6; 450 °C x = 0.56).

The transition at 565°C to the pseudo-orthorhombic structure on cooling in $La_{1.64}Sr_{0.36}Ga_3O_{7.32}$ produces a sharp reduction in the conductivity (Figure 3-15) associated with an increase in activation energy from 0.57 eV to 1.2 eV, and is thus assigned to the long-range ordering of the oxygen interstitial charge carriers.

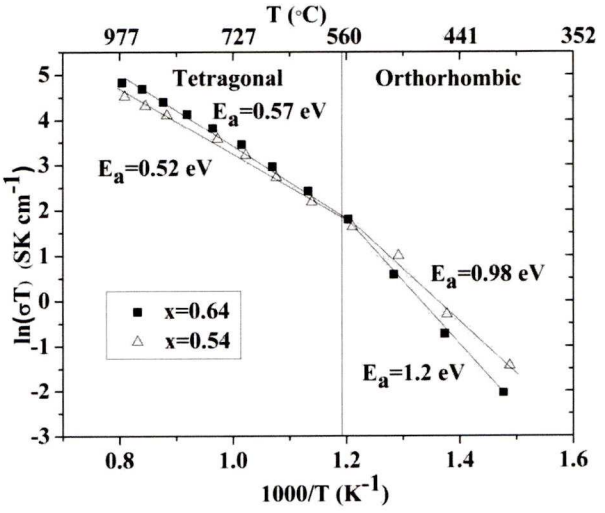

Figure 3-15 Conductivity of $La_{1.64}Sr_{0.36}Ga_3O_{7.32}$ (black squares, T at high temperature, O at low temperature) and $La_{1.54}Sr_{0.46}Ga_3O_{7.27}$ (triangles, T at all temperatures). The lines show the two regions with different activation energies.

Measurement of the conductivity of a quenched T sample of $La_{1.64}Sr_{0.36}Ga_3O_{7.32}$ on heating from 200 °C to 500 °C and subsequent cooling to 200 °C was performed to compare the conduction behaviors of tetragonal (T) and pseudo-orthorhombic phase (O) on materials with same composition. The measurement was taken in 25 °C intervals over the entire temperature range with one hour equilibration time at each temperature.

Note that at each temperature the samples dwell for 1 hour, so the points for both cooling post 500 °C and for the furnace cooled sample will be single phase O. Further measurement on one more heating and cooling cycle from 200 °C to 500 °C after the conversion from the T phase to the O phase described in the text did not

show significant change in the conductivity, suggesting the O phase is stable to thermal cycling.

The total conductivity (Figure 3-16) of a quenched $La_{1.64}Sr_{0.36}Ga_3O_{7.32}$ tetragonal phase pellet on heating over the 200-300°C temperature range is approximately two orders of magnitude higher than that on cooling through this range after heating to 500 °C to form the ordered pseudo-orthorhombic phase (e.g. 1.55 x 10^{-4} Scm^{-1} on heating (tetragonal) against 5.5 x 10^{-6} Scm^{-1} cooling (pseudo-orthorhombic) at 300 °C), consistent with the tetragonal phase corresponding to disordered and the O phase to ordered carriers. The activation energy (0.95eV) for the quenched metastable tetragonal $La_{1.64}Sr_{0.36}Ga_3O_{7.32}$ over 200-300°C measured on heating (Figure 3-16), compares to 0.85eV for tetragonal $La_{1.54}Sr_{0.46}Ga_3O_{7.27}$ at low temperature (250 °C – 400 °C) reported by Kuang[8] and to 0.98 eV for the stable O phase in this temperature range. With increasing temperature the conductivity of the virgin quenched tetragonal phase pellet remains higher than the furnace cooled mixed phase sample until approximately 400 °C, where the conductivity matches that of the furnace cooled sample. This is consistent with formation of the pseudo-orthorhombic phase in quenched samples (Figure 3-6) within 30 minutes at this temperature. The conductivity on cooling post 500°C measurement matched that for the furnace-cooled $La_{1.64}Sr_{0.36}Ga_3O_{7.32}$ pellet.

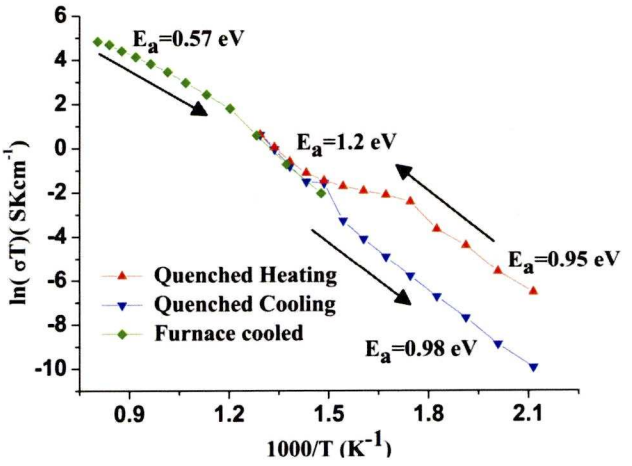

Figure 3-16 Conductivity of quenched $La_{1.64}Sr_{0.36}Ga_3O_{7.32}$ during thermal cycling is given by triangles. Initially the sample is tetragonal converting to orthorhombic on heating above 400 °C; on cooling, this sample retains the orthorhombic structure. The conductivity of a second sample of $La_{1.64}Sr_{0.36}Ga_3O_{7.32}$ which was furnace cooled from1350 °C is also given for comparison and denoted by stars. This material adopts the tetragonal structure above 565 °C below which it reverts to the orthorhombic structure.

The total conductivity of $La_{1.64}Sr_{0.36}Ga_3O_{7.32}$ at 600 °C is independent of oxygen partial pressure over the 1-10^{-22} atm range (Figure 3-17), as found earlier for $La_{1.54}Sr_{0.46}Ga_3O_{7.27}$[8] showing that there is pure ionic conductivity across the entire series $La_{1+x}Sr_{1-x}Ga_3O_{7+x/2}$ to the solid solution limit of x= 0.64. The band gap of $LaSrGa_3O_7$ (measured by diffuse reflectance Figure 3-17) is 5.0 eV, also consistent with the absence of an intrinsic electronic contribution over the entire temperature range measured.

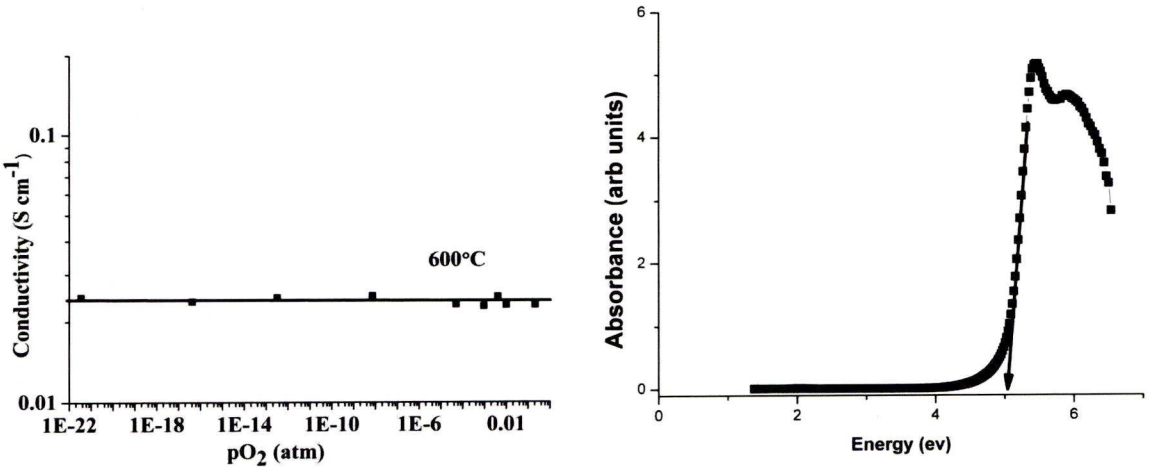

Figure 3-17 pO_2 dependence of the total conductivity of $La_{1.64}Sr_{0.36}Ga_3O_{7.32}$ at 600 °C (left) and diffuse reflectance spectrum of $LaSrGa_3O_7$ the resulting band gap is found to be 5 eV.

Previous investigations by Rozumek[5, 6] reveal a different behavior of the pO_2 indicating electronic conduction in the samples. Conductivity measurements on $La_{1.64}Sr_{0.36}Ga_3O_{7.32}$ synthesized using lower purity starting materials (e.g. Ga_2O_3 99.99% vs 99.999%) was carried out (Figure 3-18). These measurements showed a plateau at low temperatures (below 300 °C) providing evidence of electronic conduction. Incorporation of small amounts of transition metal impurities present in the lower purity starting materials lead to the higher electronic contribution. Despite the electronic conductivity the higher conductivity of the tetragonal quenched pellet (up 1st time) can be seen compared to the furnace cooled sample and the cycling runs (Down 1st and 2nd and up 2nd).

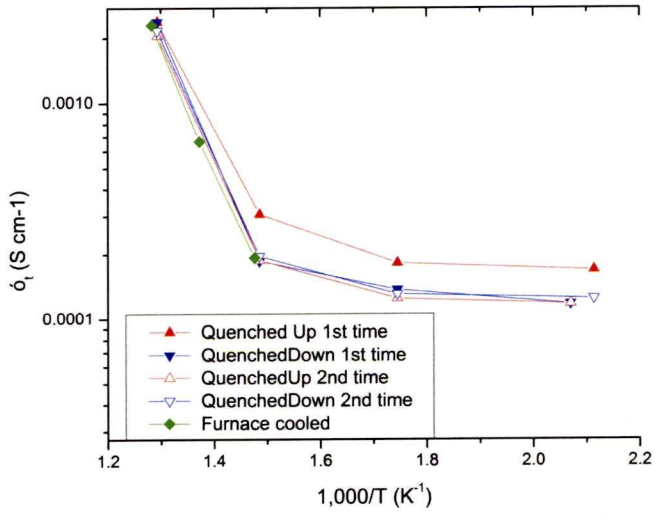

Figure 3-18 $La_{1.64}Sr_{0.36}Ga_3O_{7.32}$ synthesized using Ga_2O_3 (99.99%) . Plateau at low temperatures indicates electronic conduction present.

After the conductivity measurements the pellets were ground and powder patterns measured to ensure the melilite phase survived the measurements (Figure 3-19). For x = 0-0.62 the post conductivity XRD show no evidence of the melilite phase changing during the measurement, however x=0.64 shows a small amount of

lanthanum strontium gallate perovskite (LSG). The small insulating impurity concentration makes it reasonable to deduce that the conductivity of the sample is due to the x = 0.64 melilite not the LSG impurity.

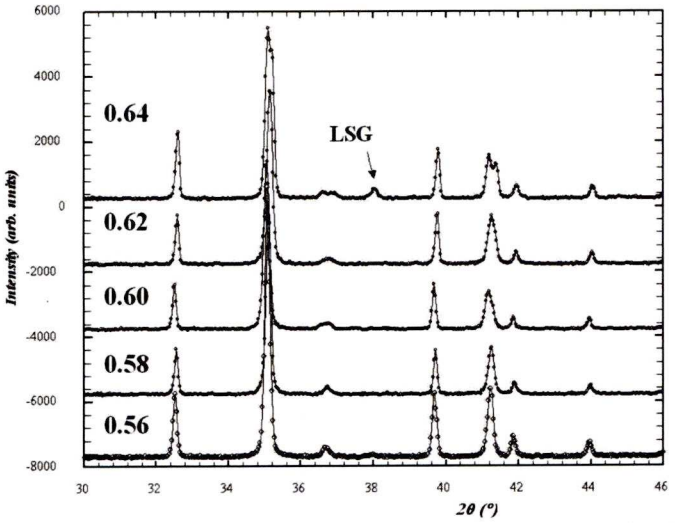

Figure 3-19 XRD patterns of the $La_{1+x}Sr_{1-x}Ga_3O_{7+x/2}$ samples post conductivity measurements where x = 0.56. 0.58, 0.6, 0.62 and 0.64. The x = 0.64 pattern shows that a small amount of the strontium doped lanthanum gallate (LSG) perovskite has formed during the measurement (< 2.6% based on relative intensities of most intense peaks). The other compositions are perovskite-free and the small impurity concentration makes it reasonable to deduce conductivities for x=0.64.

3.3.3 Proton Conduction

Previous investigations into the charge carriers in the melilite system have disagreed, Rozumek proposing proton conduction at higher dopant levels while Kuang reporting pure oxide conduction. For there to be proton conduction some of the interstitial sites must uptake water to give a source of proton defects which in an oxide are present as hydroxide ions.(Equation 3-1)

Equation 3-1 $H_2O + V_{\ddot{O}} + O_o \leftrightarrow 2OH_O$.

Inclusion of water into oxide structures such as the melilite structure can be observed by IR spectroscopy as compounds with water or hydroxide ions show a broad band at $3500cm^{-1}$. When a sample of quenched x = 0.64 was tested the broad band is not observed (Figure 3-20). In addition to the IR spectroscopy, oxides with water

incorporated in them tend to lose the water at elevated temperatures. TGA can be used to follow this release and if water is present in the original compound a weight loss will be observed. The temperature range chosen for the TGA experiment covers the region where the tetragonal form of the melilite (quenched sample) has a higher conductivity than the pseudo orthorhombic form (furnace cooled). The TGA temperature range also covers the temperature regime where the quenched and furnace cooled samples have the same conductivity as the transition from tetragonal to pseudo orthorhombic occurs at 400 °C. The mass loss observed for $La_{1.64}Sr_{0.36}Ga_3O_{7.32}$ is an order of magnitude less than in materials where bulk water incorporation is found (Figure 3-20). For $La_{0.8}Ba_{1.2}GaO_{3.9}$ (a known proton conductor[22-25]) the uptake of water gives $La_{0.8}Ba_{1.2}GaO_4H_{0.2}$, on heating this would show a mass loss of 0.44% giving $La_{0.8}Ba_{1.2}GaO_{3.9}$ and $0.1H_2O$. The small 0.03% loss seen in the TGA of $La_{1.64}Sr_{0.36}Ga_3O_{7.32}$ is presumably due to water being lost from the surface of the powder.

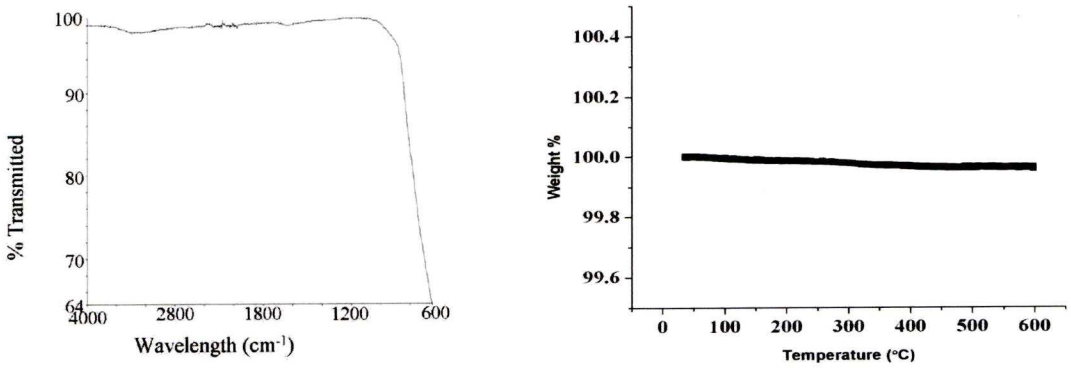

Figure 3-20 Infrared spectrum of quenched $La_{1.64}Sr_{0.46}Ga_3O_{7.32}$ (left) and TGA data of quenched $La_{1.64}Sr_{0.46}Ga_3O_{7.32}$ (right).

The method used by Kuang[8] to test for proton conduction was to carry out conductivity measurements in compressed air then on the same sample pass the compressed air through a water bubbler before gas enters the furnace. This method

will then generate two sets of data points, one set collected in dry air and one set in wet air. If the material conducts protons then the conductivity in the wet air is expected to be higher than the dry air. Kuang observed no difference in the data sets for x = 0.54 and using the same method x = 0.62 was tested with the results given in Figure 3-21 .

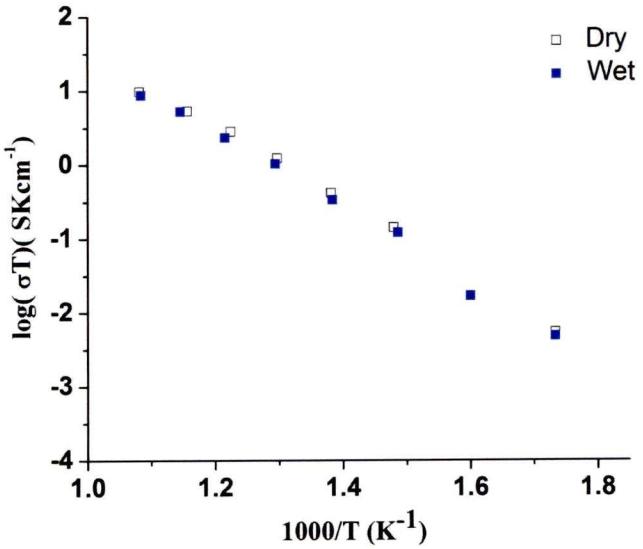

Figure 3-21 Conductivity data of $La_{1.62}Sr_{0.38}Ga_3O_{7.31}$ in a dry and wet flowing compressed air atmosphere.

Both the x = 0.54 and the x = 0.62 data show no difference in dry and wet atmospheres supporting the idea that the melilite is a pure oxide ion conductor. To ensure that the method used would show a difference in a known proton conductor $La_{0.8}Ba_{1.2}GaO_{3.9}$ which has been shown to proton conduct by Slater[22] and Lee[24] was subjected to the same treatment. The data from this experiment (Figure 3-22) show a clear difference between the dry (empty squares) and wet (filled squares) atmospheres both sets of data are comparable with those reported by Slater (shown by stars).

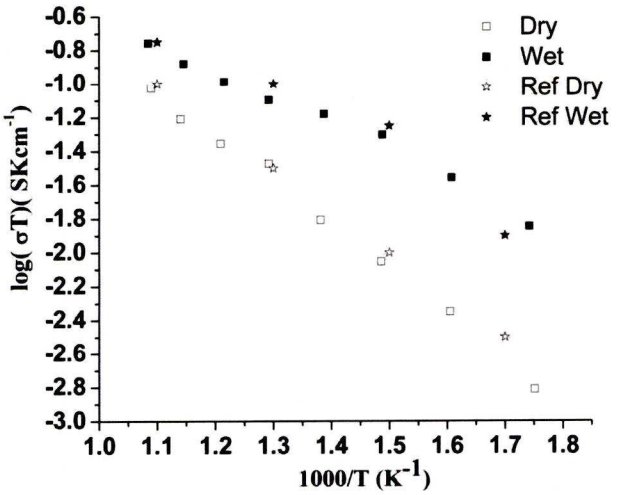

Figure 3-22 Conductivity data of $La_{0.8}Ba_{1.2}GaO_{3.9}$ collected in both a wet and a dry atmosphere with data from Slater[22] shown for comparison.

In conclusion the method used demonstrates proton conductivity in $La_{0.8}Ba_{1.2}GaO_{3.9}$ as expected but not in $La_{1+x}Sr_{1-x}Ga_3O_{7+x/2}$ showing that the charge carriers are oxide ions rather than protons.

Diffusion

Using the conductivity data and the knowledge of the structure and the type of charge carriers the diffusion coefficient per carrier, D, can be computed from Equation 3-2

$$D= \sigma /[(nq^2)/(kT)]$$

Equation 3-2 diffusion equation

where n is the number density and q the charge of the mobile species. Figure 3-23. shows D over the 400-950 °C range. At 950 °C the diffusion coefficients are of the order of 10^{-6} to 10^{-5} cm^2s^{-1} (with a maximum of 1.6 x 10^{-5} cm^2s^{-1} at x = 0.6) which compares with conductivity-derived D of 1 x 10^{-6} cm^2s^{-1} for $La_{0.9}Sr_{0.1}Ga_{0.8}Mg_{0.2}O_3$ [26] (validated with tracer diffusion). The diffusion coefficient at 800 °C (Figure 3-23) increases until x = 0.6, with a 13-fold increase from x = 0.1 to the maximum at 0.6. The decrease of conductivity at higher interstitial content (x = 0.62/0.64) correlates with the reduced diffusion coefficient and E_a increase, associated with short-range structural ordering premonitory to the O phase transition and associated blocking of the interstitial mobility. Such long range interactions of carriers have been observed by Hohnke in $Zr(M)O_{2-x}$ $Ce(M)O_{2-x}$ and $Th(M)O_{2-x}$ (M=Sc Y Ca). [27, 28] Vacancy disordering is also known to produce a threefold increase in conductivity at the fluorite pyrochlore boundary in $Ln_2Zr_2O_7$.[29] In LSGM [3] vacancy carrier trapping premonitory to long-range ordering identified in electron diffraction is proposed to impact the conductivity.

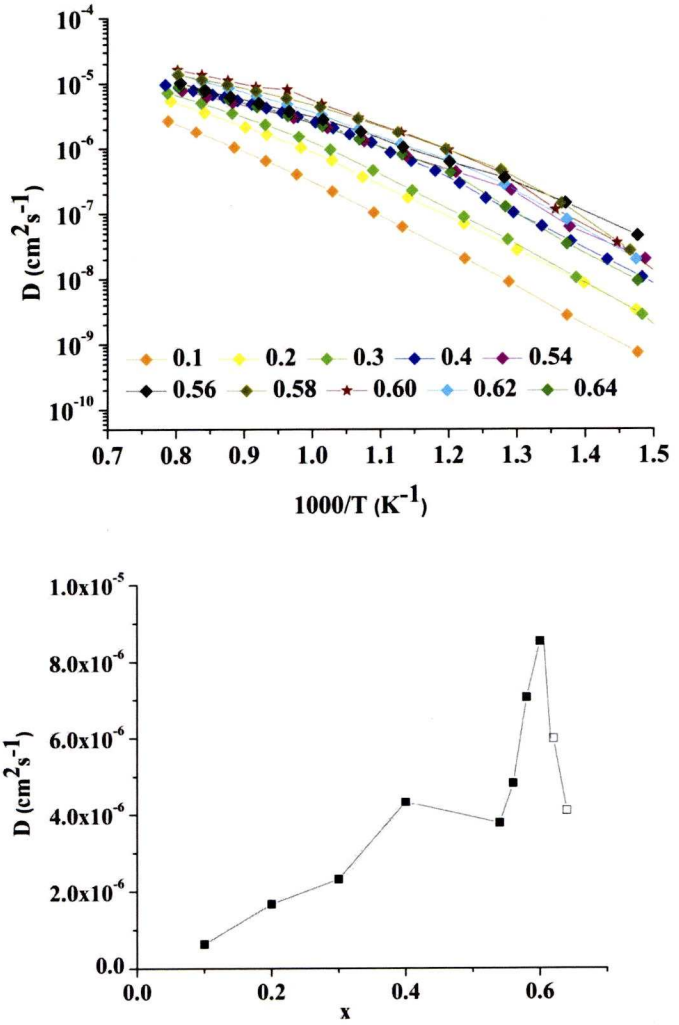

Figure 3-23 Diffusion coefficients of $La_{1+x}Sr_{1-x}Ga_3O_{7+x/2}$ (x =0-0.64) (top) and diffusion coefficient versus x at 800 °C (bottom).

3.3.4 Stability in differing atmospheres.

To investigate the stability of the higher melilites in varying atmospheres samples were annealed in 1%CO_2 in Ar (gas also used for pO_2 measurement) 5%H_2 in N_2 and O_2. One concern was that the material may be less stable in CO_2 as compounds such as SrO show a tendency to pick up CO_2, despite the post pO_2 measurement not showing any decomposition a quenched sample was annealed at 600°C in 1%CO_2 for 72 hours. Post annealing the XRD measurement shows no evidence of decomposition.

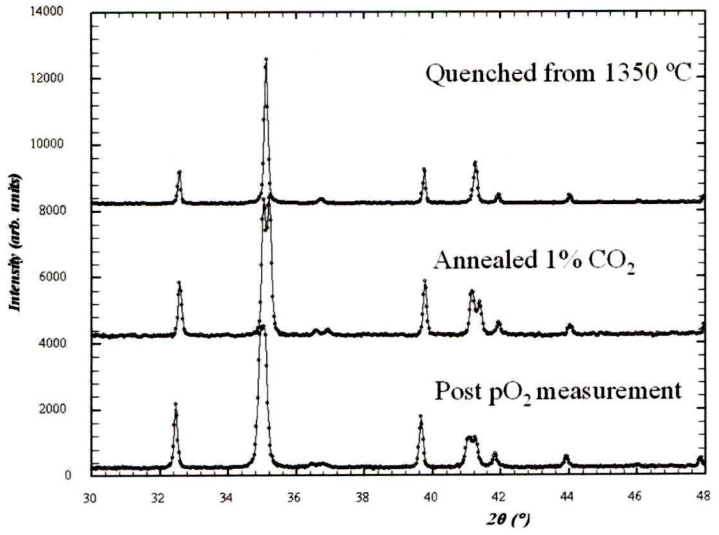

Figure 3-24 $La_{1.64}Sr_{0.36}Ga_3O_{7.32}$ Quenched sample before annealing and after annealing in 1% CO_2 for 72 hours at 600 °C. Also shown is the XRD pattern of the pO_2 sample (Figure 3-17) post measurement. As the annealed and post-measurement samples have been heated above 400 °C the tetragonal quenched phase has partially converted back to the orthorhombic phase.

Previously x = 0.54 has been shown to begin to decompose in a 5%H_2 mixture at 800 °C although the kinetics are very slow[8]. For x = 0.64 at 800 °C in 5%H_2 the kinetics of decomposition appear to be much quicker (partial decomposition being observed after 12 hours vs 100 hours) . Annealing at 700 °C in 5%H_2 for 12 hour fails produce the perovskite impurity seen as a result of the higher temperature annealing.

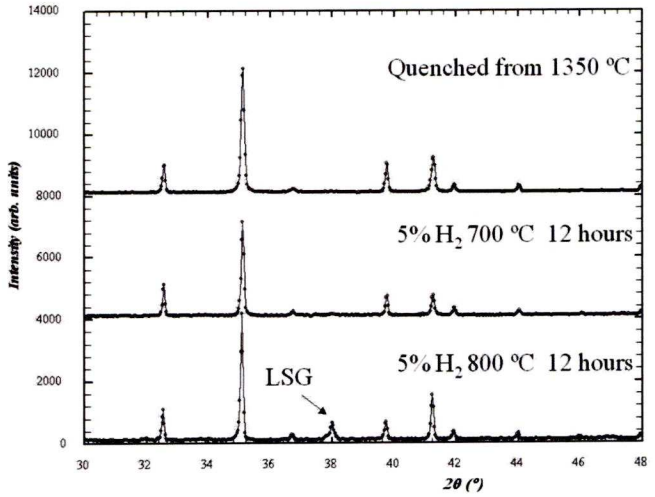

Figure 3-25 $La_{1.64}Sr_{0.36}Ga_3O_{7.32}$ Quenched sample before annealing and after annealing in 5%H_2 in N_2 for 12 hours at 700 °C and 800 °C

Annealing in O_2 and N_2 was also carried out showing that the stability of the melilite in N_2 is unchanged while melilite is slightly less stable in a pure O_2 atmosphere when compared to air.

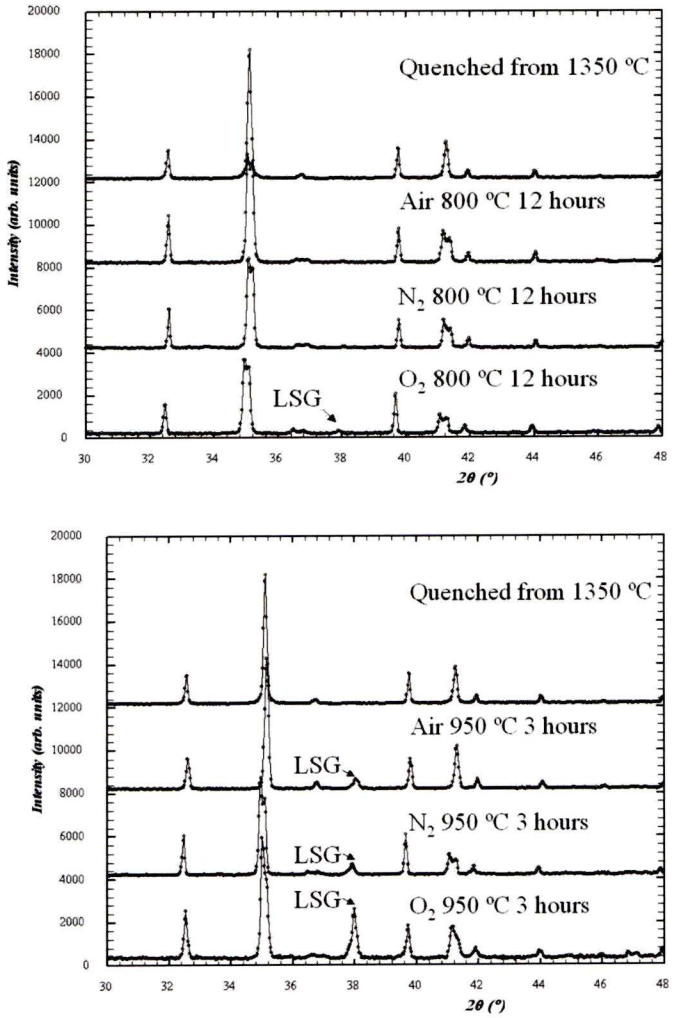

Figure 3-26 $La_{1.64}Sr_{0.36}Ga_3O_{7.32}$ Quenched sample before annealing and after annealing in air, N_2 and O_2 for 12 hours at 800 °C (top) and after annealing in air, N_2 and O_2 for 3 hours at 950 °C (bottom).

3.3.5 Comparison with other Melilite systems

The lanthanum gallate melilites can accommodate both Ca and Ba in place of Sr, the structure of $La_{1.64}Ca_{0.36}Ga_3O_{7.32}$ [2] having been studied in detail. In this section the synthesis of the Ba and Ca melilites is compared to the synthesis procedure for the Sr melilites. The effect that the differing alkaline earths have on the conductivity of the melilite is also considered.

3.3.5.1 Synthesis and characterization

The synthesis of $La_{1+x}Ca_{1-x}Ga_3O_{7+0.5x}$ and $La_{1+x}Ba_{1-x}Ga_3O_{7+0.5x}$ follows the same procedure as the $La_{1+x}Sr_{1-x}Ga_3O_{7+0.5x}$ materials. Ceramic synthesis with slight excess Ga_2O_3 affords the $La_{1+x}Ca_{1-x}Ga_3O_{7+0.5x}$ ($x \leq 0.64$) and $La_{1+x}Ba_{1-x}Ga_3O_{7+0.5x}$ ($x \leq 0.35$). The amounts of excess Ga used for Ca and Ba melilites was the same as the amounts used for the Sr equivalents namely 1.7% excess Ga was required by to form $x \geq 0.58$, 2% excess Ga for $x = 0.6$ and $x = 0.62$, and 2.3% excess Ga for $x = 0.64$. All compositions were initially fired as powders at 1200 °C then pressed into pellets and fired at 1400 °C ($x = 0$-0.54) or 1350 °C ($x = 0.56$-0.64)

When the Sr in the system $La_{1+x}Sr_{1-x}Ga_3O_{7+0.5x}$ is substituted for Ca or Ba the solid solution limit remains the same for Ca ($x = 0.64$) but drops to $x = 0.35$ for Ba. Ba retains the tetragonal structure over the entire solid solution range ($x = 0$-0.35) but both Ca and Sr show a reduction in symmetry at higher values of x (> 0.5 for Ca and > 0.6 for Sr).

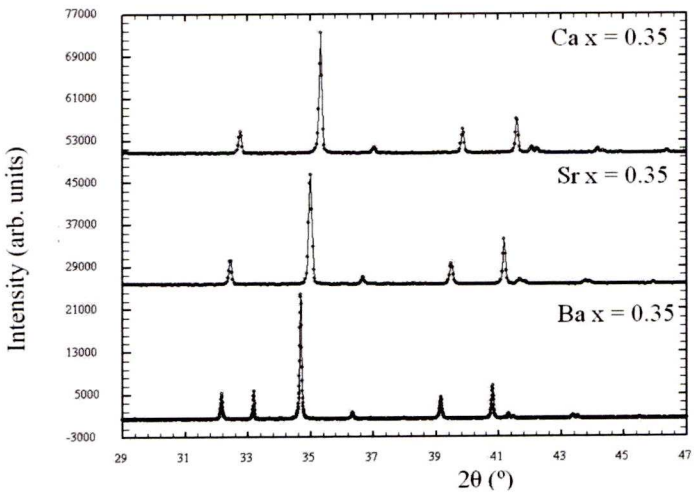

Figure 3-27 XRD patterns of the as synthesized $La_{1+x}M_{1-x}Ga_3O_{7+x/2}$ M= Ca, Sr, Ba and x=0.35. All samples show single-phase tetragonal structure.

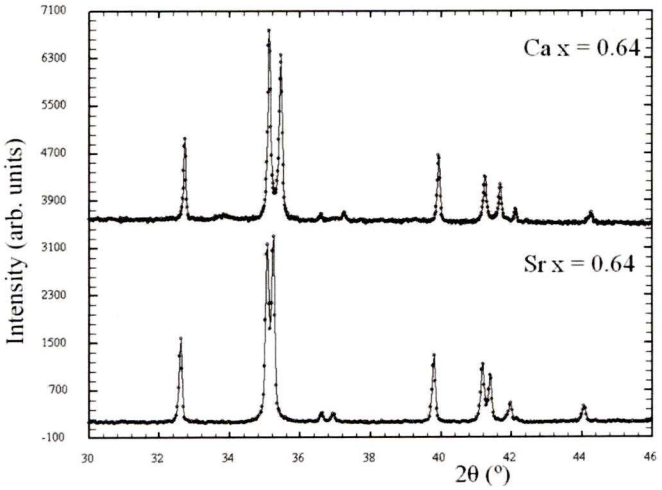

Figure 3-28 XRD patterns of the $La_{1+x}M_{1-x}Ga_3O_{7+x/2}$ M= Ca, Sr, and x=0.64. Both samples show splitting of main peak as symmetry is now pseudo-orthorhombic.

Comparing the conductivity at the solid solution limits (x = 0.35 for Ba and x = 0.64 for Sr and Ca) gives the results shown in Figure 3-29. A clear feature of this figure is the crossover of the conductivities of Ca and Sr x = 0.64 at 550-600 °C. At high temperatures the Ca material has the higher conductivity while the Sr material having the greater conductivity at lower temperatures. All three samples show a change in conductivity behavior at approximately 600 °C consistent with the T to O phase transition for Sr at 565 °C (Figure 3-6) caused by the interstitial ordering. As the change is more pronounced in the Ca the ordering of the interstitials has a stronger effect on the conductivity indicating that the ordering interaction is stronger for Ca materials.

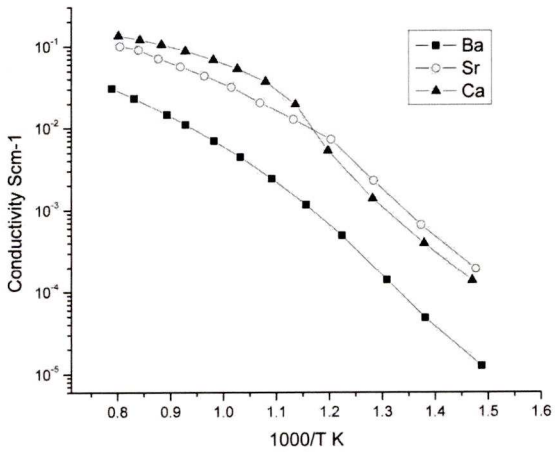

Figure 3-29 Conductivity data for the solid solution limits (x=0.64 for Ca and Sr, 0.35 for Ba).

If the activation energies are calculated the difference between the high temperature (> 600° C) and low temperature (< 600° C) is clear (Table-1).

Table-1 Activation energies $La_{1+x}M_{1-x}Ga_3O_{7+0.5x}$ in the two different temperature regimes.

M	X	E_a >600 °C (eV)	E_a < 600 °C (eV)
Ca	0.64	0.45(2)	0.95(1)
Sr	0.64	0.57(2)	1.2(1)
Ba	0.35	0.76(2)	0.97(1)

Despite Ba x = 0.35 remaining tetragonal throughout the temperature range studied the ordering of the interstitials still causes a reduction in conductivity and a change in activation energy. Such behavior is also observed for Sr x = 0.54 (Figure 3-15) which also remains tetragonal throughout the conductivity measurement. In $La_{1.64}Ca_{0.36}Ga_3O_{7.32}$ the pentagonal rings of the melilite structure have been shown to distort to accommodate the interstitial [1, 2]. By putting an interstitial oxide ion into one channel not only that channel but also the neighboring channels distort even if they are empty. If these distortions are taken into account with the interstitial

ordering the most distorted neighboring channel to a filled channel with an interstitial not shared with other filled channels. Preventing the most distorted channel being shared is therefore key in the ordering of the interstitials in the melilite structure.

3.4 Conclusion

The solid solution range in $La_{1+x}Sr_{1-x}Ga_3O_{7+0.5x}$ has been shown to extend to $x = 0.64$, comparable to the $La_{1+x}Ca_{1-x}Ga_3O_{7+0.5x}$ system. The high interstitial oxide content drives a structural phase transition at $x > 0.6$ from a high temperature tetragonal phase to a low temperature pseudo-orthorhombic phase (<565 °C) which strongly reduces the ionic conductivity, consistent with the transition being produced by static structural order of the interstitial charge carriers. The highest conductivities at any temperature are found in materials where the tetragonal structure is stable and interstitial ordering does not occur, because of the strong influence of short-range ordering associated with the T/O phase transition at temperatures above the transition, and the associated effect on the temperature and dopant density dependence of the conductivity.

The pure ionic conductivity is desirable for SOFC applications as is the conductivity that is comparable to LSGM (Figure 3-13).

3.5 References

[1] C. I. Thomas, X. Kuang, Z. Deng, H. Niu, J. B. Claridge, M. J. Rosseinsky, *Chemistry of Materials* **2010**, *22*, 2510

[2] M.-R. Li, X. Kuang, S. Y. Chong, Z. Xu, C. I. Thomas, H. Niu, J. B. Claridge, M. J. Rosseinsky, *Angew Chem Int Ed Engl* **2010**, *49*, 2362.

[3] K. Q. Huang, R. S. Tichy, J. B. Goodenough, *Journal of the American Ceramic Society* **1998**, *81*, 2565.

[4] A. A. Kaminskii, L. Bohaty, P. Becker, J. Liebertz, P. Held, H. J. Eichler, H. Rhee, J. Hanuza, *Laser Physics Letters* **2008**, *5*, 845.

[5] M. Rozumek, P. Majewski, L. Sauter, F. Aldinger, *Journal of the American Ceramic Society* **2004**, *87*, 662.

[6] M. Rozumek, P. Majewski, H. Schluckwerder, F. Aldinger, K. Kunstler, G. Tomandl, *Journal of the American Ceramic Society* **2004**, *87*, 1795.

[7] E. S. Raj, S. J. Skinner, J. A. Kilner, *Solid State Ionics* **2005**, *176*, 1097.

[8] X. Kuang, M. A. Green, H. Niu, P. Zajdel, C. Dickinson, J. B. Claridge, L. Jantsky, M. J. Rosseinsky, *Nature Materials* **2008**, *7*, 498.

[9] S. Nakayama, T. Kageyama, H. Aono, Y. Sadaoka, *Journal of Materials Chemistry* **1995**, *5*, 1801.

[10] E. Kendrick, M. S. Islam, P. R. Slater, *Journal of Materials Chemistry* **2007**, *17*, 3104.

[11] F. Goutenoire, O. Isnard, R. Retoux, P. Lacorre, *Chemistry of Materials* **2000**, *12*, 2575.

[12] P. Lacorre, F. Goutenoire, O. Bohnke, R. Retoux, Y. Laligant, *Nature* **2000**, *404*, 856.

[13] I. R. Evans, J. A. K. Howard, J. S. O. Evans, *Chemistry of Materials* **2005**, *17*, 4074.

[14] L. Wang, *http://www.dssc.ece.cmu.edu/news/seminars/lunch05/headsmedia/042605.pdf* **2005**, 1, 6.

[15] R. Aleksiyko, M. Berkowski, J. Fink-Finowicki, P. Byszewski, R. Diduszko, E. Kowalska, International Conference on Solid State Crystals 2000: Growth, Characterization, and Applications of Single Crystals **2001**, 4412, 50.

[16] J. Ahman, G. Svensson, J. Albertsson, Acta Crystallographica Section C-Crystal Structure Communications **1996**, 52, 1336.

[17] H. Yoshioka, *Chemistry Letters* **2004**, *33*, 392.

[18] L. Leon-Reina, E. R. Losilla, M. Martinez-Lara, M. C. Martin-Sedeno, S. Bruque, P. Nunez, D. V. Sheptyakov, M. A. G. Aranda, *Chemistry of Materials* **2005**, *17*, 596.

[19] J. B. Goodenough, Annual Review of Materials Research **2003**, 33, 91.

[20] T. S. Zhang, J. Ma, H. Cheng, S. H. Chan, *Materials Research Bulletin* **2006**, *41*, 563.

[21] B. C. H. Steele, *Solid State Ionics* **2000**, *129*, 95.

[22] S. Li, F. Schonberger, P. Slater, *Chemical Communications* **2003**, 2694.

[23] F. Schonberger, E. Kendrick, M. S. Islam, P. R. Slater, *Solid State Ionics* **2005**, *176*, 2951.

[24] K. H. Lee, J. H. Kim, H. L. Kim, S. Kim, H. L. Lee, *Japanese Journal of Applied Physics* **2005**, *44*, 254.

[25] F. Giannici, D. Messana, A. Longo, L. Sciortino, A. Martorana, *Journal of Physics: Conference Series* **2009**, *190*, 012077.

[26] T. Ishihara, J. A. Kilner, M. Honda, Y. Takita, *Journal of the American Chemical Society* **1997**, *119*, 2747.

[27] D. K. Hohnke, Journal of Physics and Chemistry of Solids **1980**, 41, 777.

[28] M. D. Hurley, D. K. Hohnke, *Journal of Physics and Chemistry of Solids* **1980**, *41*, 1349.

[29] H. Yamamura, H. Nishino, K. Kakinuma, K. Nomura, *Solid State Ionics* **2003**, *158*, 359.

Chapter 4 : Pyrochlores and fluorites for use as solid oxide fuel cell anodes

4.1 Introduction

Pyrochlores and fluorites are some of the most common materials used in solid oxide fuel cells with the fluorites yttria-stabilized zirconia and gadolinium-doped ceria being used as electrolytes and a Ni/YSZ cermet being used as an anode. Despite the structural similarity, materials with pyrochlore and fluorite structure often display differing conductivity for the same composition. For example $Ln_2Ti_2O_7$ (Ln =Lu Yb Tm) [1]show a pyrochlore-fluorite transition at approximately 1700 °C which results in an increase in conductivity of 2 orders of magnitude. Fluorites however do not always have the higher conductivity. For example in $Gd_2Zr_2O_7$[2] the conductivity of 'the ordered phase (pyrochlore phase) is significantly greater than that of the disordered phase (fluorite phase)'. There are two differing explanations for this difference in conductivity between pyrochlores and fluorites depending on which structure displays the higher conductivity. If the fluorite has the higher conductivity the explanation is that the all defects in the fluorite structure are free but ordering of defects in the pyrochlore structure freezes some so reducing conductivity [3]. On the other hand if the pyrochlore has the greater conductivity then the explanation uses preferential conduction paths in pyrochlores[4] which should reduce the activation energy of oxide-ion conduction . The most energetically favorable pathway in pyrochlores is via O^{2-} ion hoping with continuous 48f ↔ 48f position jumps [19]. In the ideal fluorite structure such an energetically favorable path cannot be realized as there is significant anion disorder. When the strain energy (ΔH_σ) of the jumps was calculated [19,20] for rare earth titanates it was found that small 8 co-ordinate radii such as Lu^{3+} (97 pm) Yb^{3+} (98 pm) and Tm^{3+} (99 pm) gave the lowest strain energy.

However Wilde and Catlow[21] have suggested that cation disorder is required to allow thermally generated vacancies in the 48f sites based on static energy minimization calculations. Minervini [22] also linked this need for some cation disorder to the A and B cation size, however too great a cation disorder will drive the structure to fluorite. Fluorite ideally has total disorder and so cause the anion disorder to break the 48f ↔ 48f pathway.

In an attempt to be able to predict the structure a given $A_2B_2O_7$ would possess a literature search was conducted and the list of compounds given in the appendices compiled. Using the Shannon and Prewitt tables[5, 6] of ionic radii the 8 and 6 co ordinate ionic radii could be tabulated and the compositions plotted according to ionic radii. Figure 4-1 shows a selection of these compounds whose nominal composition is $A_2B_2O_7$ with the structures limited to pyrochlore, fluorite and zirconolite-3T. The compounds are defined as having the larger ion on the A site (y axis) while the smaller ion is on the B site (x axis). A similar treatment was reported by Vanderah[7] who notes the use of 'cation radius ratios to predict the formation of pyrochlores has been somewhat successful'. Many compositions have been reported in multiple structure types (e.g $Dy_2Hf_2O_7$) while others have been shown to transform from one structure to another under pressure (e.g $Gd_2Zr_2O_7$[8]) or with temperature (e.g $Sm_2Zr_2O_7$ at 2200 °C [9]). In general fluorites are stable in the bottom right (and at higher temperatures or higher pressures) while pyrochlores are stable in the upper left (and at lower temperatures or lower pressures).

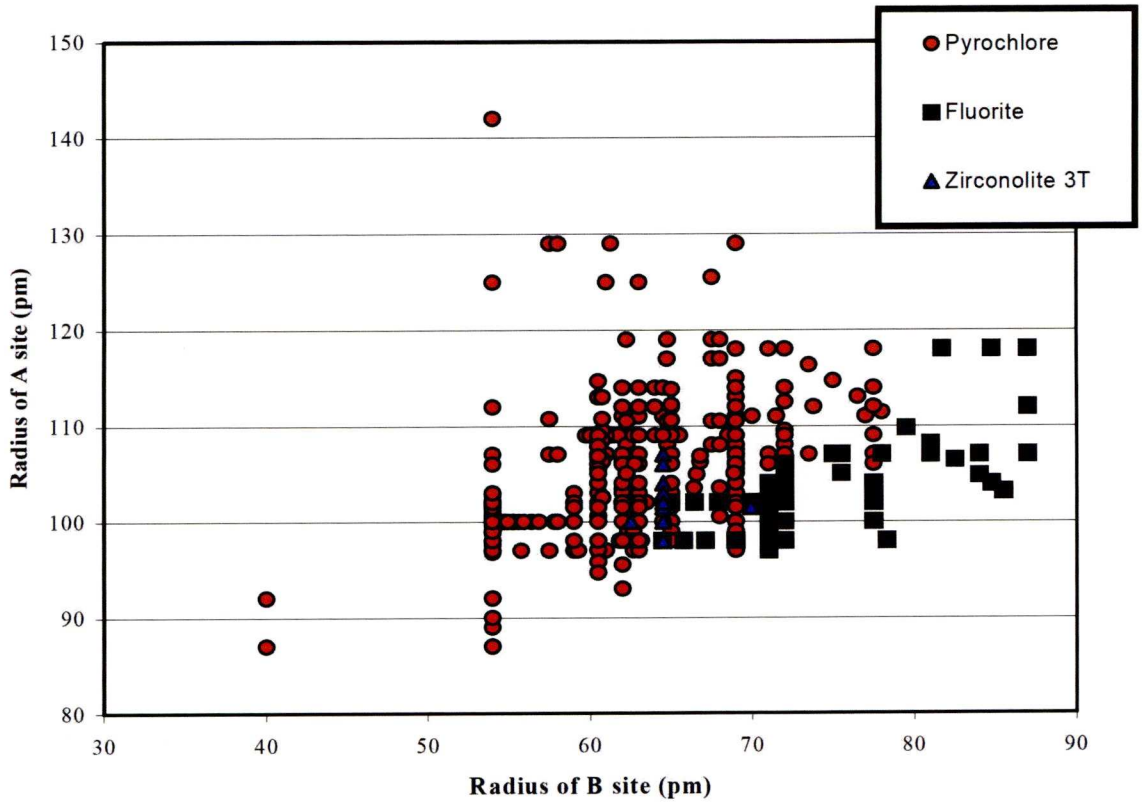

Figure 4-1 Plot of the radius of the A site versus B site in selected $A_2B_2O_7$ compositions with pyrochlore (empty diamonds) fluorite (filled black squares) and zirconolite-3T (filled grey triangles).

The work in this chapter uses this to predict structure and transitions between them and is split into three sections;

1) **Investigations into the border (4.1.1).** The border region between some pyrochlores and fluorites has been investigated as other workers have suggested that conductivity increases at the border. To test this theory solid solutions that span the border as well as lanthanide substitutions have been investigated.

2) **Incorporation of Mo^{6+} and W^{6+} into pyrochlores and fluorites (4.1.2)** A strategy to improve the total (both electronic and ionic) conductivity of pyrochlores and fluorites under reducing conditions such as those found at the anode was developed. This involved incorporating into the structure a relatively easily reducible ion. Attempts were therefore made to incorporate both Mo^{6+} and W^{6+} into pyrochlore and fluorite structures.

3) **Zirconolite-3T material (4.1.3)** During the course of investigations into the pyrochlore materials a zirconolite-3T was synthesized. The zirconolite structures have so far been overlooked for use in fuel cells. It was hoped that if a single phase material could be produced the properties could be tested for use in a fuel cell.

All the materials were synthesized with the intention of use in solid oxide fuel cells as fuel cell anodes.

4.1.1 Investigations into conductivity at the pyrochlore / fluorite border.

In a number of solid solutions a phase transition from pyrochlore to fluorite is observed as a function of composition. Yamamura[10] investigated the relationship between electrical conductivity for $Ln_2Zr_2O_7$ and $(Ln_{1-x}Ln'_x)_2Zr_2O_7$ and observed a sharp maximum at the vicinity of the phase boundary. Yamamura[3] also studied $(Y_{1-x}La_x)_2(Ce_{1-x}Zr_x)_2O_7$ but did not observe a maximum at the phase transition (x = 0.55), instead the maximum conductivity was observed at x = 0.1 which is on the border of fluorite and rare earth C. The peaks in conductivity observed in these systems at the phase transition borders may extend to other materials. By selecting pyrochlore/fluorite $A_2B_2O_7$ systems close to the border and either varying the A or B site ions or the transition from one structure to another can be studied.

Previous work in the Rosseinsky group[11] has shown $YbCaTiNbO_7$ based systems to be stable over a large range of temperatures (up to 1450 °C) and pO_2 ($1-10^{-21}$ atm). When $Yb_{0.96}Ca_{1.04}TiNbO_{6.98}$ is reduced the material is a good electronic conductor reaching 9 S/cm at 800 °C . It was however noted that the 'sluggish' redox kinetics are a barrier to practical applications. A possible solution is to replace some of the Ti^{4+} with Ce^{4+} as Ce^{4+} in CGO electrolytes has been shown to readily reduce to Ce^{3+} causing the material to become electrically conducting. This is undesirable for electrolyte applications that CGO is normally used for but is highly desirable for anodes. Also by substituting Ce for Ti in the formula$YbCaCe_{1-x}Ti_xNbO_7$ the B average radius can be tuned as the six coordinate radius of Ti^{4+} (60.5 pm) is less than Ce^{4+}(87 pm). An alternative method of changing the A:B radius ratio is to substitute the Yb for larger lanthanides giving $LnCaCeNbO_7$.

4.1.1.1 Synthesis

In the XRD patterns when the peaks are indexed using a pyrochlore cell (a ≈ 10Å) the 313 and the 115 are allowed but are forbidden in a fluorite (a ≈ 5Å). The presence of the 313 and 115 peaks present strong evidence that a pyrochlore phase has formed. Figure 4-2 shows XRD patterns for $YbCaCe_{1-x}Ti_xNbO_7$ (x = 0, 0.09, 0.19, 0.29, 0.5, 1) showing that the pyrochlore peaks appear at x = 0.29.

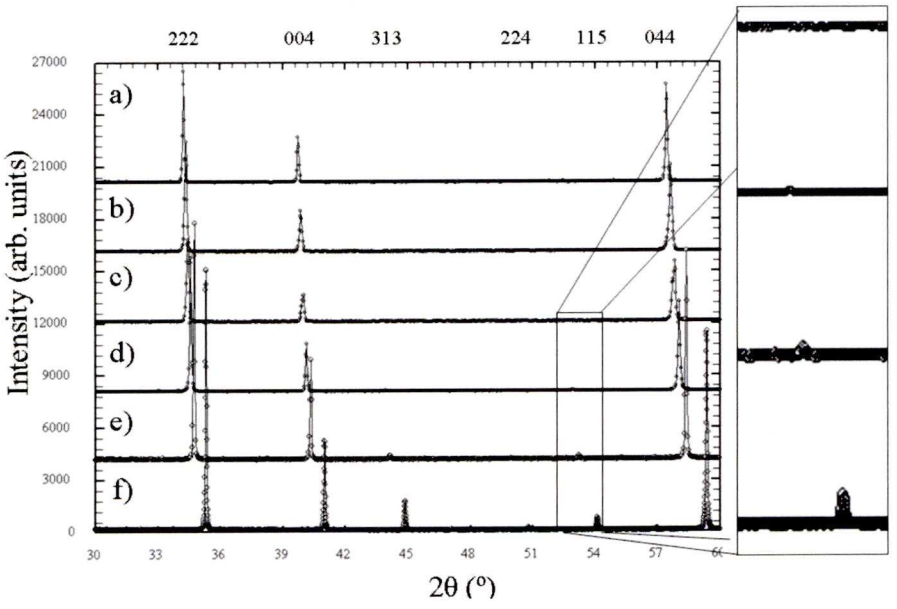

Figure 4-2 XRD patterns of $YbCaCe_{1-x}Ti_xNbO_7$ x = a) 0, b) 0.09, c) 0.19, d) 0.29, e) 0.5, f) 1
The hkl indices are for pyrochlore cell (fluorite indices half pyrochlore) with the inset showing the appearance of the 115 peak at x=0.29.

On closer inspection of the higher angle peaks splitting is observed for x = 0.09 and x = 0.19 (Figure 4-3) meaning that these phases are biphasic. This biphasic behavior in the transition across a pyrochlore/fluorite solid solution has been reported for $Nd_2(Ce_yZr_{1-y})_2O_7$ [12] where material is pyrochlore where y < 0.1, biphasic 0.1 < y < 0.5 and fluorite >0.5.

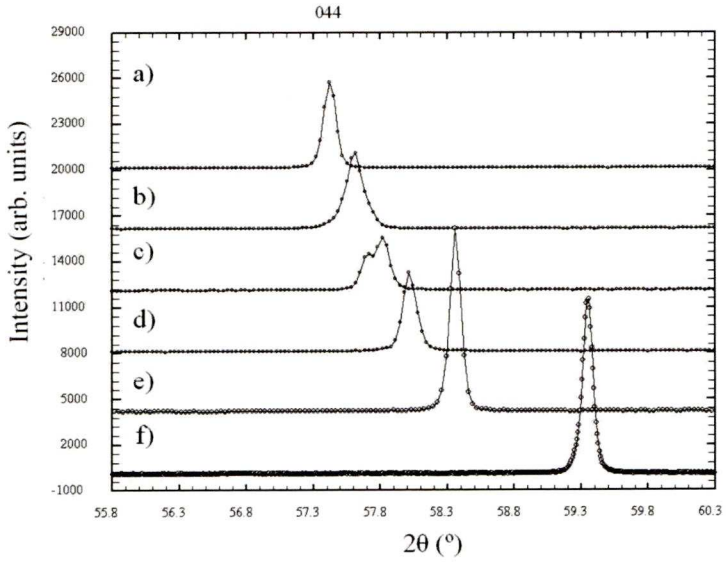

Figure 4-3 Closer inspection of the pyrochlore 044 (fluorite 022) for $YbCaCe_{1-x}Ti_xNbO_7$ x = a) 0, b) 0.09, c) 0.19, d) 0.29, e) 0.5, f) 1 showing the biphasic nature of the x=0.09 and 0.19 samples.

When synthesis of $LnCaCeNbO_7$ (Ln= Yb, Ho, Eu,) was attempted single phase fluorite were obtained for Ln = Yb-Eu (Figure 4-4).

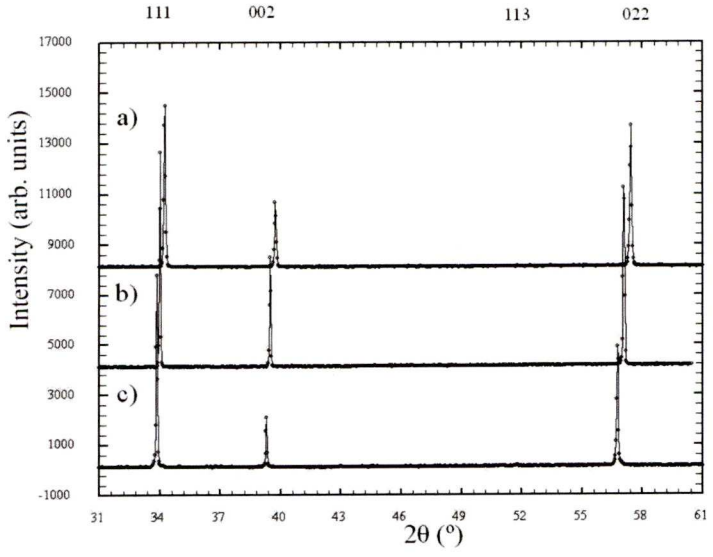

Figure 4-4 XRD of $LnCaCeNbO_7$ Ln= a) Yb, b) Ho, c) Eu with the hkl indices for a fluorite cell given .

Nd formed a mixture of phases (un reacted CeO_2 and a Nd_3NbO_7 type phase as well as a fluorite phase) even at 1700 °C (Figure 4-5).

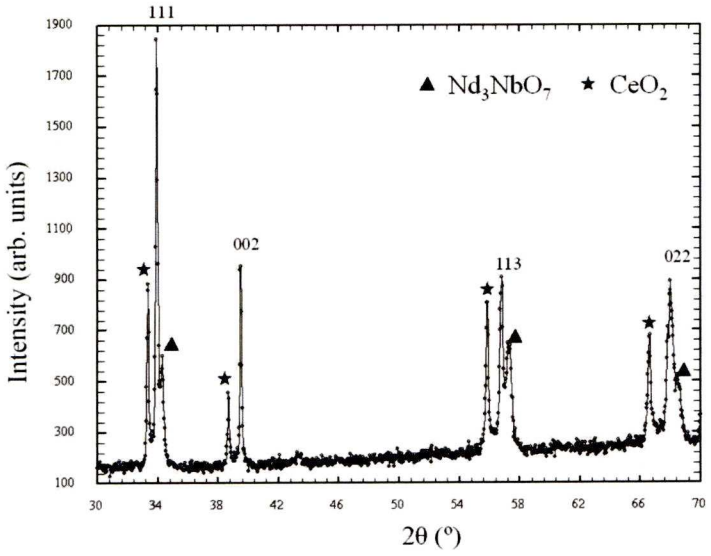

Figure 4-5 XRD of $NdCaCeNbO_7$ with the hkl indices for a fluorite cell given and peaks for CeO_2 (stars) and Nd_3NbO_7 (triangles) type phase marked.

4.1.1.2 Redox stability

Stability in reducing conditions is vital for a fuel cell anode so annealing experiments in 5% H_2 95% N_2 were conducted. The effect of the annealing could then be followed by comparing the lattice parameters from both the 'as synthesized' and the 'reduced' samples. Initially the lattice parameters were calculated from fitted peak positions obtained via the X'Pert Highscore plus software provided with the Panalytical X-Pert pro instrument. However the e.s.d's obtained were to large to confidently determine if the lattice parameters had changed or not (both values within 3 e.s.d's see Section 2.2.3.2). As a result LeBail fitting using GSAS was used to give more precision on the lattice parameter values, (5.2688(1) Å versus 5.26(2) Å for 'as synthesized' $YbCaCeNbO_7$) . The LeBail fits along with the χ^2 and wRp values are given in appendix 3.

Annealing $YbCaCeNbO_7$ at 900 °C in 5% H_2 95%N_2 produced a slight reduction of the phase indicated by a change in the lattice parameter, a= 5.2688(1) Å for as synthesized versus a= 5.2843(1) Å after annealing. Reduction in 5%H_2 95%N_2 at both 1200 °C and 1480 °C also showed a change in lattice parameter (a = 5.3146(5) Å for 1200 °C and 5.3231(2) Å for 1480 °C) but all samples showed signs of impurity. This impurity appears to be isostructural with Ca_2ErNbO_6 [13] indicating that the fluorite phase has been over reduced and has converted to a monoclinic perovskite structure. When the samples from the annealing experiments are reheated in air to the synthesis temperature of 1480 °C the original fluorite phase (a= 5.2668(6) Å for 900 °C reduction and a= 5.2688(3) Å for 1480 °C) is recovered.

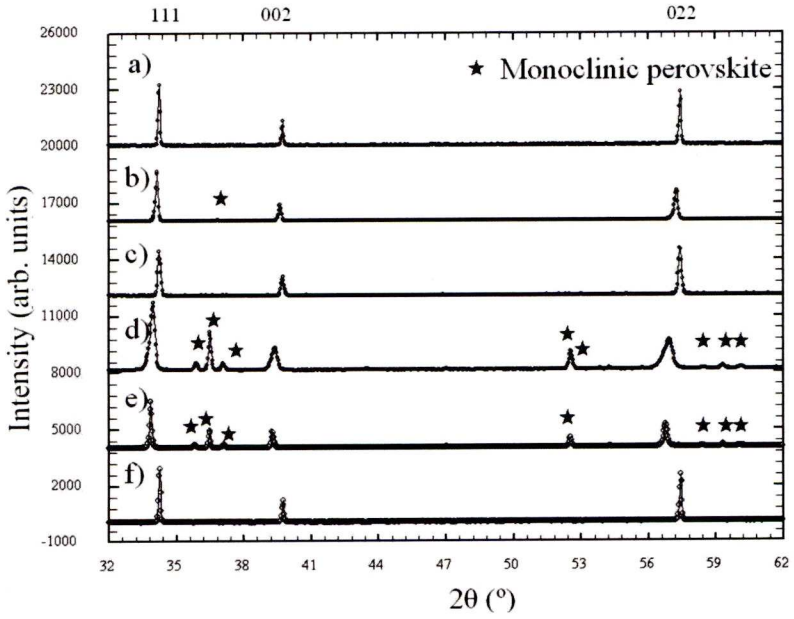

Figure 4-6 XRD $YbCaCeNbO_7$ a) Synthesized in air at 1480 °C, b) annealed in 5%H_2 at 900 °C then c) reoxidised in air at 1480 °C, d) annealed in 5%H_2 at 1200 °C e) annealed in 5%H_2 at 1480 °C then f) reoxidised in air at 1480 °C. The stars mark the peak positions of the monoclinic perovskite phase and the hkl indices are for the fluorite phase.

The TGA data in Figure 4-7 shows an initial weight loss of 0.7 %, corresponding to an oxygen loss of 0.035 per unit of $YbCaCeNbO_7$ (ideally forming only $YbCaCeNbO_{6.965}$). . Using the reduction of Ce^{4+} to Ce^{3+} this would give a average

oxidation state of +3.93 for the Ce ions which means only 7% of the Ce^{4+} ions have been reduced.

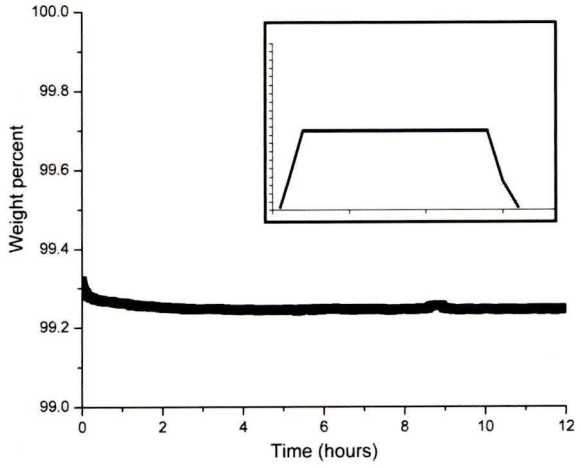

Figure 4-7 TGA of $YbCaCeNbO_7$ after initial heating to 950°C under 5% H_2 hold for 12 hours (heating profile shown in inset).

Using these results $LnCaCeNbO_7$ (Ln= Ho, Eu) were annealed in flowing 5% H_2 95% N_2 at 950 °C for 12 hours with the Ce^{4+} in the $HoCaCeNbO_7$ being reduced (determined by change in lattice parameters from a = 5.29117(7) Å to a = 5.3068(2) Å) but with monoclinic perovskite impurity. The $HoCaCeNbO_{7-x}$ sample post reduction could not then be re-oxidized by heating in air at 1480 °C like the $YbCaCeNbO_{7-x}$ case. Instead reheating $HoCaCeNbO_{7-x}$ in air at 1480 °C formed a fluorite phase with a = 5.2830(3) Å and the monoclinic perovskite remained.

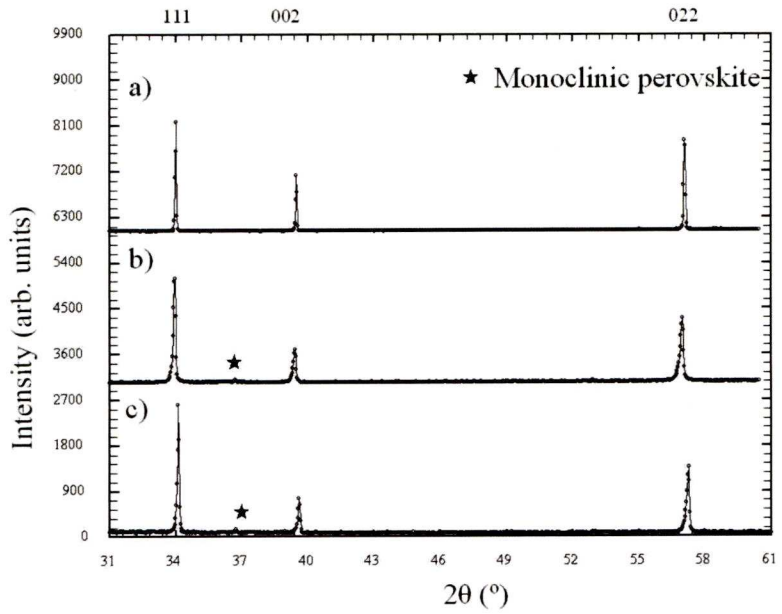

Figure 4-8 XRD of $HoCaCeNbO_7$ a) synthesized at 1480 °C b) post reduction at 950°C in 5% H_2 and c) reheated in air to 1480 °C. The hkl indices are for a fluorite cell and the monoclinic perovskite peak is marked by a star.

For the $EuCaCeNbO_7$ case the post annealing at 950 °C in 5%H_2 95%N_2 XRD (Figure 4-9) shows splitting of the peaks indicating that the material has not been fully reduced (lattice parameters go from a = 5.32277(8) Å for as synthesized to 5.3369(2) Å major phase and 5.3142(3) Å minor phase) . Annealing at 1200 °C in 5%H_2 95%N_2 resulted in the monoclinic perovskite type phase forming which upon reheating to 1580 °C in air recovers a split pattern. The lattice parameters for this process are when reduced a= 5.323(1) Å for the major phase and a = 5.34(2) Å for the minor phase which after heating in air becomes 5.31874(8) Å for the major phase and a = 5.2974(8) Å for the minor phase.

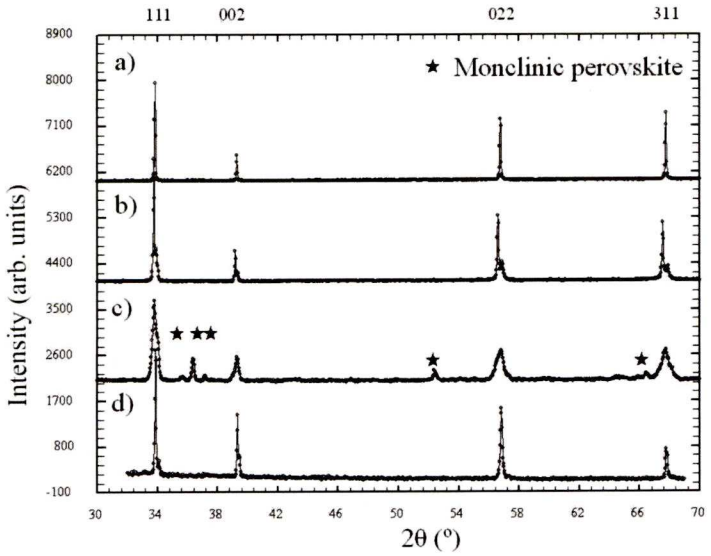

Figure 4-9 XRD of $EuCaCeNbO_7$ a) synthesized at 1600 °C b) post reduction at 950°C in 5% H_2 95% N_2 c) post reduction at 1200°C in 5% H_2 95% N_2 and d) reheated in air to 1580 °C. The hkl indices are for a fluorite cell and stars mark the monoclinic perovskite peaks.

Looking at the EDS both pre and post reduction (Figure 4-10) there is an almost total loss of Eu from the fluorite structure giving a $CaCeNbO_{5.5-\delta}$ phase at 950 °C in 5%H_2 95%N_2 . The loss could be due to gaseous Eu as elemental europium has a high vapor pressure (>100 Pa @ 950 °C) and will exist in equilibrium with the oxide (Equation 4-1). This was also observed by Haschke[18] between 1100 °C and 1450 °C who also noted that 99.1% of the theoretical weight loss was observed and Eu_3O_4 was the only solid product. In this case the $EuCaCeNbO_7$ reduction is carried out under a flowing 5%H_2 95%N_2 atmosphere which not only helps drive the equilibrium to the right be moving gaseous Eu away from the sample but also converts the Eu_3O_4 back into EuO via

$$4EuO_{(s)} \rightleftharpoons Eu_3O_{4(s)} + Eu_{(g)}$$

Equation 4-1 EuO equilibrium with Eu_3O_4 and Eu

$$Eu_3O_{4\,(s)} + H_{2(g)} \rightleftharpoons 3EuO_{(s)} + H_2O_{(g)}$$

Equation 4-2 Reduction of Eu_3O_4 in flowing 5%H_2 95%N_2

The flowing atmosphere is very important as it helps move the Eu(g) and $H_2O(g)$ along the tube away from the sample boat causing the Eu to be lost from the initial $EuCaCeNbO_7$ sample. Such equilibrium will exist for the Yb case as YbO is a known compound but the initial Yb_2O_3 is more difficult to reduce to YbO when compared to Eu_2O_3 reducing to EuO. Ho does not form HoO so no equivalent Equation 4-1 can exist for Ho and as a result metal loss is not a problem for $YbCaCeNbO_7$ and $HoCaCeNbO_7$.

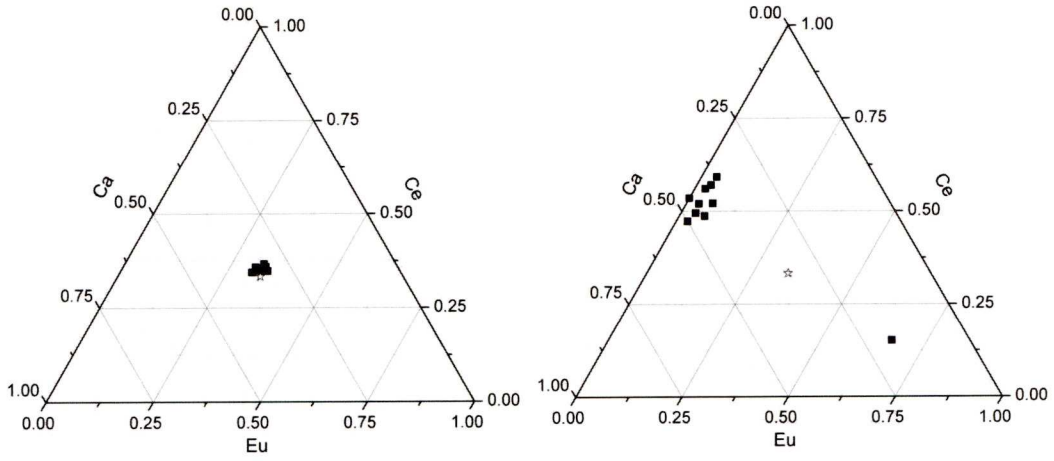

Figure 4-10 EDS of $EuCaCeNbO_7$ pre (left) and post reduction (right) at 950 °C in 5% H_2. Filled squares shown the data points while empty stars show the ideal composition, Nb has been omitted for clarity.

4.1.1.3 Conductivity measurements

The following section contains conductivity measurement on $YbCaCe_{1-x}Ti_xNbO_7$ (x = 0 – 0.5) (section 4.1.1.3.1) , $YbCaCeNbO_7$ and $HoCaCeCeNbO_7$ (section 4.1.1.3.2).

4.1.1.3.1 $YbCaCe_{1-x}Ti_xNbO_7$

Conductivity measurements across the series (Figure 4-11) were carried out in a flowing 5% H_2 95% N_2 atmosphere at 850 °C to simulate the operating conditions at the anode of a fuel cell. The results do not show a rise in conductivity at the fluorite

to pyrochlore border, instead a minimum in conductivity is observed. The pyrochlore structured materials with $x \geq 0.4$ display a higher conductivity compared to the fluorite structured materials and the pyrochlores $0.29 \leq x \leq 0.4$.

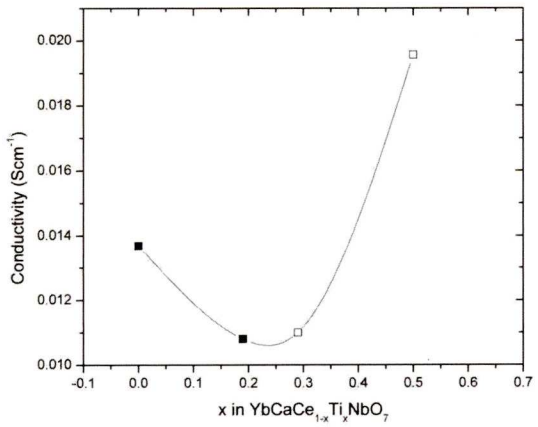

Figure 4-11 Conductivity of $YbCaCe_{1-x}Ti_xNbO_7$ (x= 0,0.19, 0.29. 0.5) with line drawn as a guide to the eye. The filled squares are for values of x where the structure is a fluorite and the empty squares where the structure is pyrochlore.

The conductivity minimum observed at the pyrochlore-fluorite border shows the explanation of conductivity in these systems is more complicated than expected. Section 4.1 described how the O2- ion hoping with continuous 48f ↔ 48f position jumps creates a preferential pathway for conduction in pyrochlores and how the cation disorder required to transform the structure to fluorite prevents this pathway. Fluorite however with its greater number of O2- vacancies should be able to compensate by increasing the number of possible paths albeit less favorable paths than 48f ↔ 48f. As the pyrochlore furthest away from the border in Figure 4-11 (x = 0.4) has a higher conductivity than the fluorite furthest away (x = 0) the pyrochlore conduction (48f ↔ 48f) dominates. This conduction path is disrupted by the increase disorder closer to the border and so conduction from this path drops faster than the multiple path mechanism can compensate. Once the border is crossed there is no 48f ↔ 48f conduction but the multiple path mechanism becomes more

favorable further away from the border as the tendency to order is weaker so conductivity rises again.

Something that complicates detailed structure analysis at the border region is that the ordering of the cation and the two oxygen positions in the pyrochlore structure can all order or disorder independently [9, 23-25]. X-ray diffraction is most sensitive to the cations as they have the greatest amount of electrons to scatter the X-rays. As the cations are the least mobile ions in the pyrochlore and fluorite structures their rearrangement is most likely the final rearrangement after the two oxygen positions. To properly investigate the degree of anion order or disorder careful neutron diffraction experiments are required to get accurate oxygen positions. The situation may be further complicated by small domains of local order in a bulk disordered structure which would benefit from detailed PDF analysis.

Conductivity verses temperature in air was measured for a sample of $YbCaTi_{0.5}Ce_{0.5}NbO_7$ giving the results in Figure 4-12.

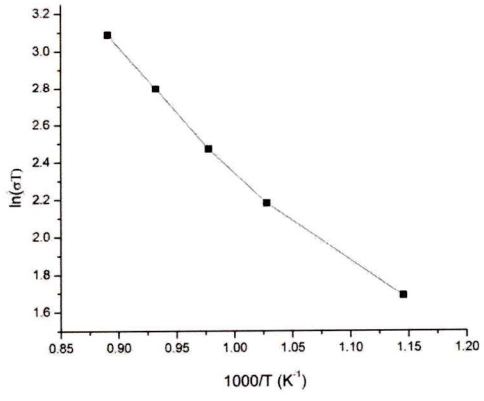

Figure 4-12 Conductivity versus temperature of $YbCaTi_{0.5}Ce_{0.5}NbO_7$

Conductivity measurements were then conducted on a sample left to dwell at 850 °C in 5% H_2 with the results shown in Figure 4-13. During the annealing the

conductivity of the sample did not change significantly indicating that the material is stable at this temperature under reducing conditions.

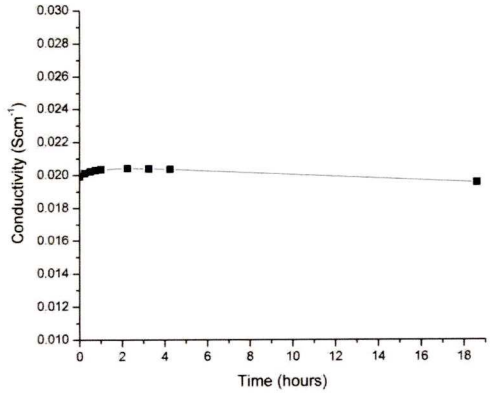

Figure 4-13 Conductivity of $YbCaTi_{0.5}Ce_{0.5}NbO_7$ in 5% H_2 95% N_2

4.1.1.3.2 Conductivity of $YbCaCeNbO_7$ and $HoCaCeCeNbO_7$

Conductivity verses temperature in air was measured for samples of $YbCaCeNbO_7$ and $HoCaCeNbO_7$ with the results shown in Figure 4-14. The data line for the Ho sample at lower temperatures is extrapolated from the data points at higher temperatures.

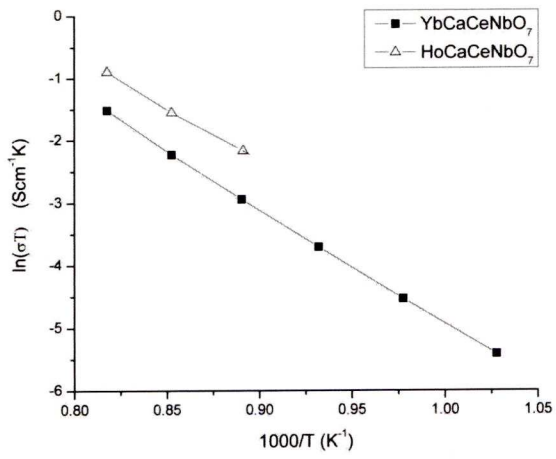

Figure 4-14 Conductivity versus temperature with $YbCaCeNbO_7$ data points marked by filled squares and $HoCaCeNbO_7$ data points being marked by empty triangles.

Conductivity measurements were then conducted on a sample left to dwell at 850 °C with the atmosphere changed from air to 5% H_2 at t = 0 with the results shown in Figure 4-15. During the first 2 hours the conductivity increases to 0.011 Scm^{-1} for $YbCaCeNbO_7$ and 0.014 Scm^{-1} for $HoCaCeNbO_7$ as the material is reduced. After 2 hours the conductivity of the sample did not change significantly indicating that the material is stable at this temperature under reducing conditions. For these materials to be useful anodes they would need to achieve conductivities of 10 Scm^{-1} under the operating conditions. Therefore both $YbCaCeNbO_7$ and $HoCaCeNbO_7$ are three orders of magnitude short of the desired performance for fuel cell anodes.

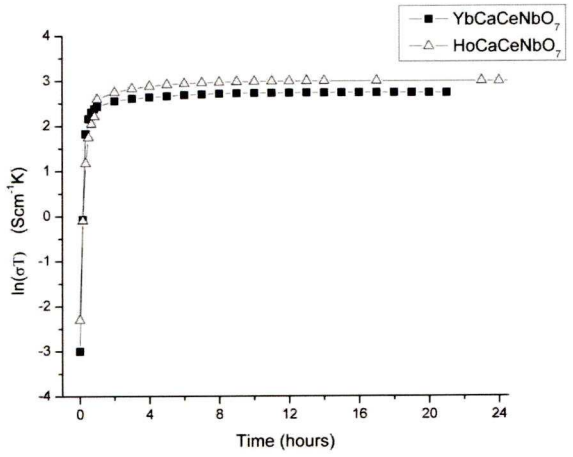

Figure 4-15 Conductivity of $YbCaCeNbO_7$ (squares) and $HoCaCeNbO_7$ (triangles) at 850°C with atmosphere changed from air to 5%H_2 at t = 0.

4.1.1.4 Summary

$YbCaCe_{1-x}Ti_xNbO_7$ for x = 0 0.29 0.5 and 1 have been successfully synthesized as single phase materials that span the fluorite pyrochlore boundary. For the compositions where x = 0.09 and 0.19 biphasic behavior was observed. Conductivity measurements across the series failed to show the expected rise in conductivity instead a conductivity minimum was observed at the fluorite pyrochlore boundary.

The series $LnCaCeNbO_7$ was investigated as changing the A site ion was seen as an alternative method of producing a series across the pyrochlore fluorite phase boundary. Synthesis of Ln = Yb, Ho and Eu fluorites proved successful but synthesis of the first predicted pyrochlore proved elusive possibly requiring a synthesis temperature greater than 1700 °C. Annealing studies in 5% H_2 show that the Ho and Yb cases are stable in reducing conditions while in the Eu case the Eu is lost from the material. Conductivity measurements were taken showing that the Ho material has a higher conductivity than the Yb but as the Nd case could not be synthesized investigation of the conductivity at the border could not be carried out. Using Figure 4-1 many other systems could be chosen to cross the pyrochlore fluorite border allowing the complex behavior of the conductivity to be better understood.

4.1.2 Investigations into Mo^{6+} and W^{6+} containing fluorites.

For anode applications a different idea was also pursued, incorporation of easily reduced ions such as Mo^{6+} and W^{6+} into pyrochlore or fluorite systems. It was hoped that the structure with its inherent vacancies would retain ionic conduction while the reduction of the Mo\W would allow for electronic conduction. The systems chosen for this investigation were $Yb_aZr_bMo_cOx$ (a + b + c = 4) and $Yb_aCe_bMo_cOx$ (a + b + c = 4) and Nd_6WO_{12}.

4.1.2.1 Synthesis

Traditional ceramic methods were used to produce $Yb_aZr_bMo_cOx$ (a + b + c = 4, $Yb_aCe_bMo_cOx$ (a + b + c = 4) and Nd_6MoO_{12} using the starting materials Yb_2O_3 MoO_3 and either CeO_2 or ZrO_2 depending on required composition or Nd_2O_3 and MoO_3.

4.1.2.2 Characterization

The characterization of the Zr and Ce material is separated into two sections with the final section on Nd_6MoO_{12}.

4.1.2.2.1 $Yb_aZr_bMo_cO_x$ (a + b + c = 4)

For $Yb_aZr_bMo_cOx$ (a + b + c = 4) the compositions were attempted.

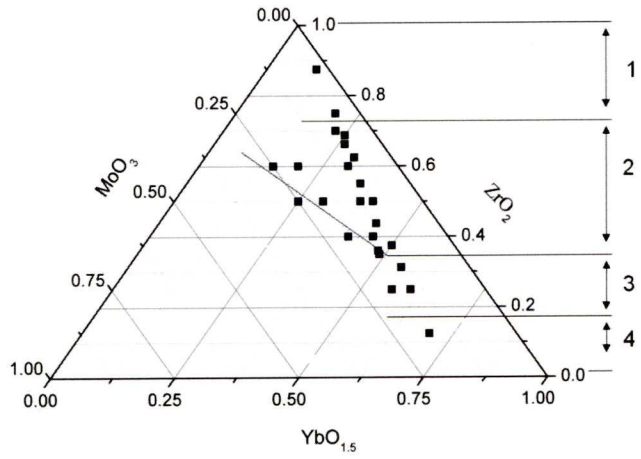

Figure 4-16 Black squares show mixed compositions in the $Yb_aZr_bMo_cOx$ (a + b + c = 4) system. The phase diagram is split into numbered regions explained in the main text.

When the composition is comparably rich in Zr (region 1) the xrd pattern shown in Figure 4-17 shows that not all of the ZrO_2 (baddeleyite phase) has reacted but a fluorite phase has formed. Region 2 xrd patterns (Figure 4-17) only show the fluorite phase with Region 3 xrd patterns (Figure 4-17) showing both a fluorite phase and a scheelite phase. Region 4 gives a complex mixture of phases including Yb_2MoO_6 and $Yb_4Zr_3O_{12}$. (Figure 4-17)

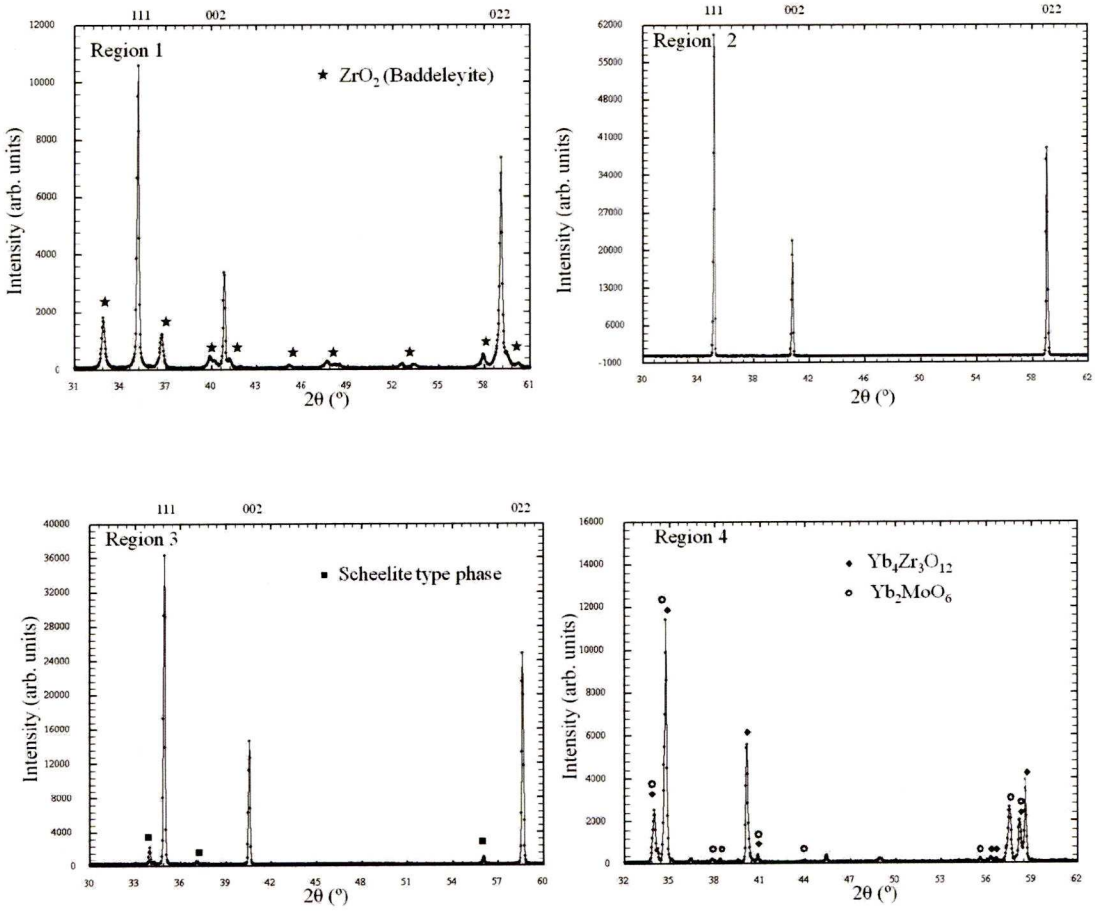

Figure 4-17 XRD of representative mixed compositions from the four regions Region 1 $Yb_{0.4}Zr_{3.5}Mo_{0.1}O_{7.9}$ fluorite phase a = 5.12(8)Å ZrO_2 marked by stars. Region 2 $Yb_{0.8}Zr_{2.4}Mo_{0.8}O_{8.4\ 9}$ fluorite phase a = 5.13(5)Å. Region 3 $Yb_{1.6}Zr_{1.6}Mo_{0.8}O_8$ fluorite phase a = 5.17(7)Å Scheelite phase marked by squares. Region 4 $Yb_{2.8}Zr_{0.5}Mo_{0.7}O_{7.3}$ with $Yb_4Zr_3O_{12}$ marked by diamonds and Yb_2MoO_6 marked by circles.

EDS of 9 different as mixed compositions from region 2 (Figure 4-18) reveals that in this single phase region the composition differs from the ratio expected from the starting materials, all compositions show a loss of molybdenum.

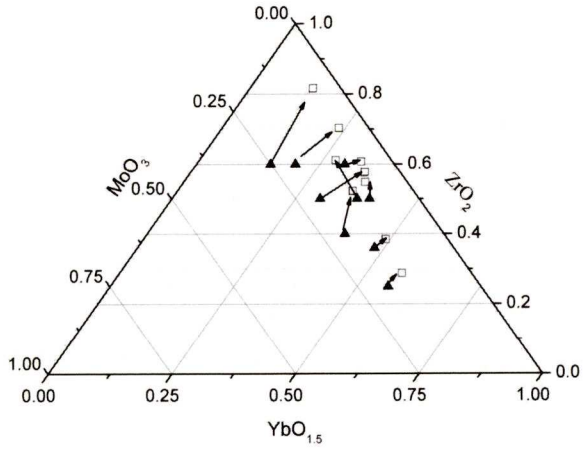

Figure 4-18 EDS of 9 compositions in region 2 with the filled triangles showing as mixed (ideal) and the empty squares experimental EDS result.

Neutron diffraction data of $Yb_{1.5}Zr_2Mo_{0.5}O_{7.75}$ shows a good agreement with the fluorite structure (Fm $\bar{3}$m)

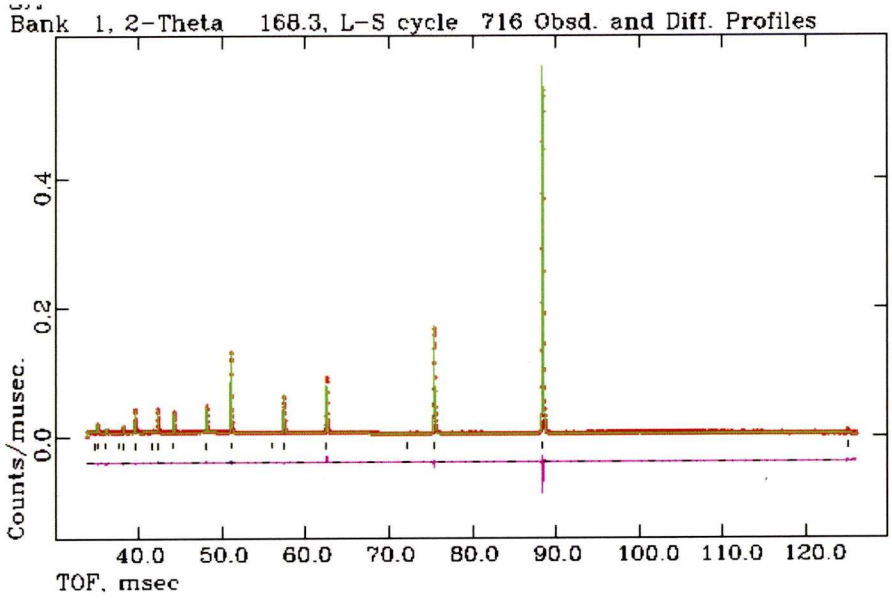

Figure 4-19 Powder neutron diffraction data of $Yb_{1.5}Zr_2Mo_{0.5}O_{7.75}$ collected at ISIS (polaris instrument) with the back scattering bank. Space group Fm $\bar{3}$m, a= 5.1769(2)Å wRp = 0.0587 χ^2 = 1.317. The red crosses are data points the green line is the fit and the purple line the difference plot with the black tick marks showing the allowed reflections.

4.1.2.2.2 $Yb_aCe_bMo_cO_x$ (a + b + c = 4)

For $Yb_aCe_bMo_cOx$ (a + b + c = 4) the compositions shown in Figure 4-20

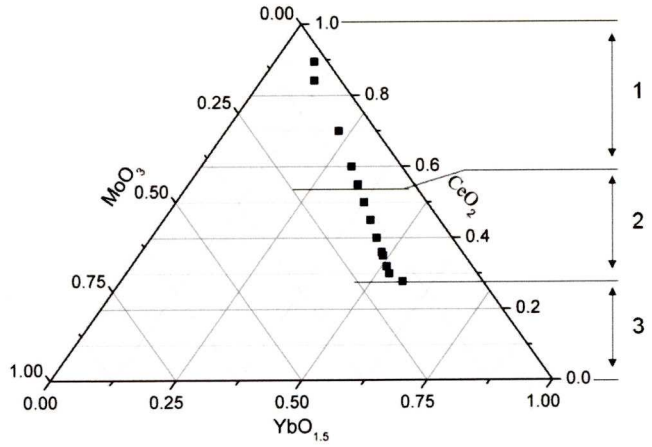

Figure 4-20 Black squares show mixed compositions in the $Yb_aCe_bMo_cOx$ (a + b + c = 4) system. The phase diagram is split into numbered regions explained in the main text.

XRD of the resulting phases reveals that the Ce based materials split into three regions with the xrds of region 1 (Figure 4-21) showing two fluorite phases while region 2 xrds (Figure 4-21) shows a single phase fluorite structure. Region 3 also gives a two phase fluorite pattern.

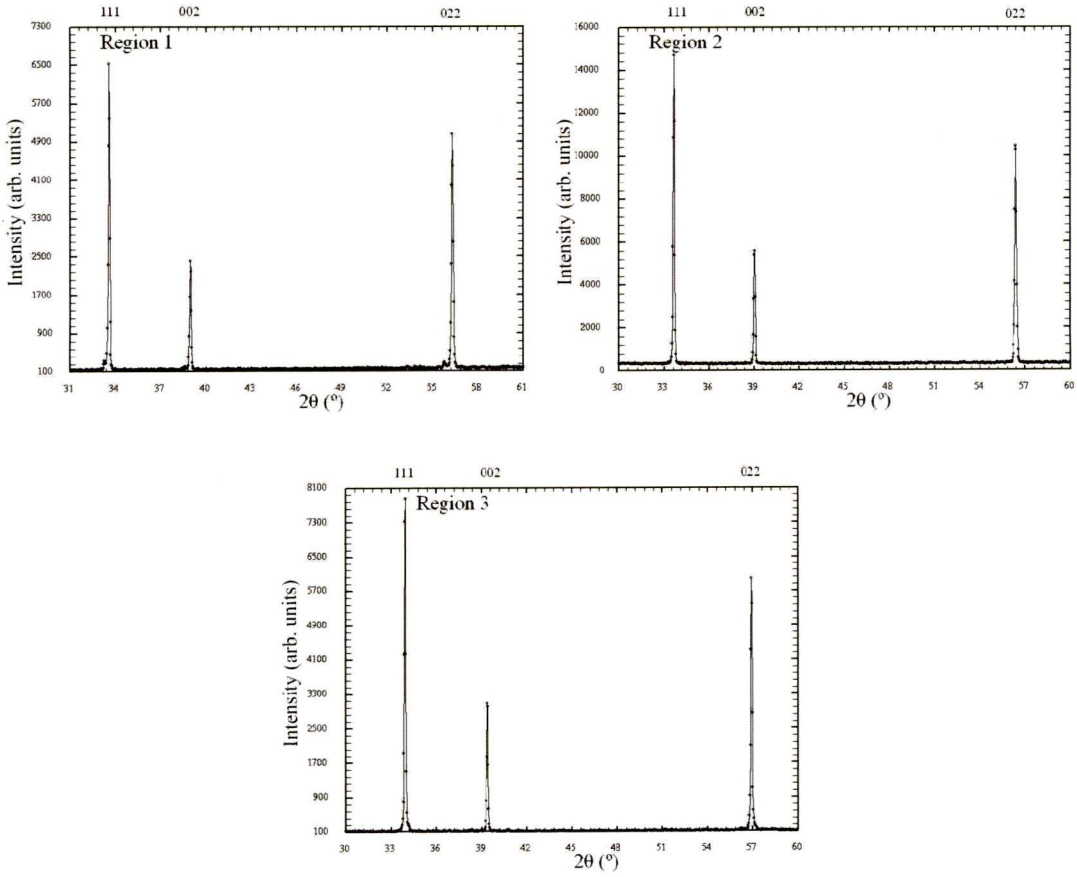

Figure 4-21 XRD of representative as mixed compositions from the three regions Region 1 $Yb_{1.2}Ce_{2.4}Mo_{0.4}O_{7.8}$ major fluorite phase a = 5.41(1) Å minor phase a = 5.36(4) Å. Region 2 $Yb_{1.5}Ce_2Mo_{0.5}O_{7.75}$ fluorite phase a = 5.30(2) Å. Region 3 $Yb_{2.1}Ce_{1.2}Mo_{0.7}O_{7.65}$ major fluorite phase a = 5.30(5) Å minor phase a = 5.27(1) Å.

EDS of 3 different compositions from region 2 (Figure 4-22) reveals that in this single phase region the composition there is a loss of Yb.

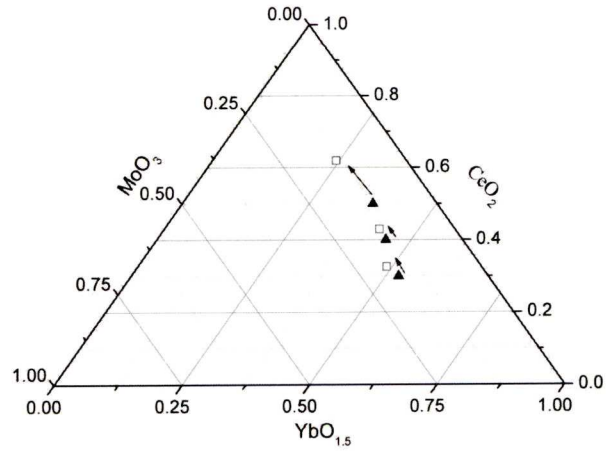

Figure 4-22 EDS of 3 compositions in region 2 with the filled triangles showing as mixed (ideal) and the empty squares experimental EDS result.

As the MoO_3 is being given off for Zr and Yb_2O_3 is being lost in Ce based systems pre-reacting the molybdenum with the Yb_2O_3 was attempted. Yb_2MoO_6 was synthesized from the oxides at 1150 °C in air for 12 hours and used as the pre-reacted Mo source. $Yb_{2.25}Ce_{1.11}Mo_{0.6}O_{7.7515}$ was chosen as the target for this reaction as previously Dr Zengqiang Deng found this single phase fluorite composition (via a combination of EDS and XRD) from an as-mixed composition of Yb_2CeMoO_8. The resulting XRD pattern is given in Figure 4-23. Until 1400 °C there remains evidence of un-reacted starting oxides and Yb_2MoO_6, at 1400 °C the single phase fluorite is observed. Weight loss during this reaction was also observed (Table 4-1 and Figure 4-24) with the sample being fired at 1100 °C then 1150 °C (12 hours each firing) before being split. One half of the split sample was fired at 1200 °C while the other was fired at 1400 °C.

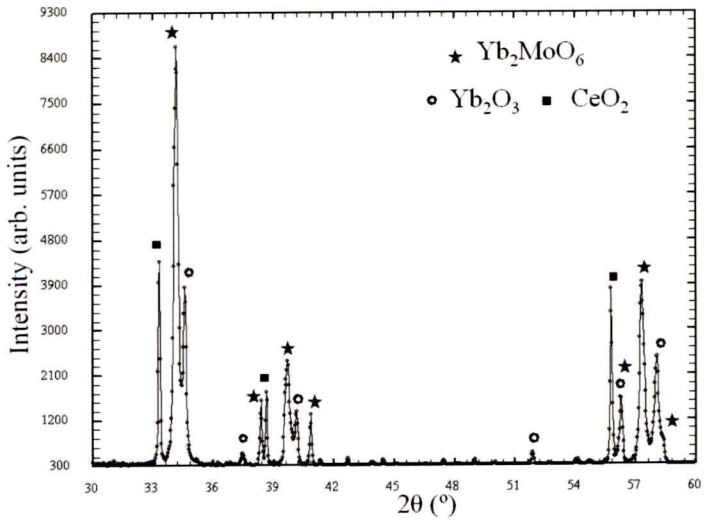

Figure 4-23 XRD using Yb_2MoO_6 as Mo source with Yb_2Mo_6 marked by stars, Yb_2O_3 by circles and CeO_2 by squares.

Table 4-1 Weight loss in $Yb_{2.25}Ce_{1.11}Mo_{0.64}O_{7.515}$ through the firing regime described in main text. In the as-mixed powder 8.5% of the initial weight is Mo.

Firing Temperature	**1100 °C**	**1150 °C**	**1200 °C**	**1400 °C**
Weight before	1.9250 g	1.8914 g	0.2797 g	1.5173 g
Weight after	1.9217 g	1.8841 g	0.2689 g	1.4723 g
Weight loss	0.0033 g	0.0073 g	0.0108 g	0.0450 g
% weight loss	0.1714 %	0.3860 %	3.8613 %	2.9658 %

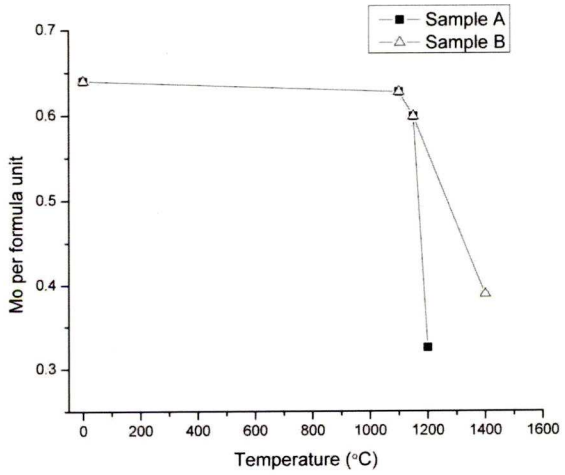

Figure 4-24 Plot of Mo loss for the as mixed composition Temperature = 0 is taken as the as mixed composition

Neutron data for $Yb_{2.25}Ce_{1.11}Mo_{0.64}O_{7.517}$ was collected at (Figure 4-25) showing the fluorite structure with lattice parameter a = 5.3045(3) Å.

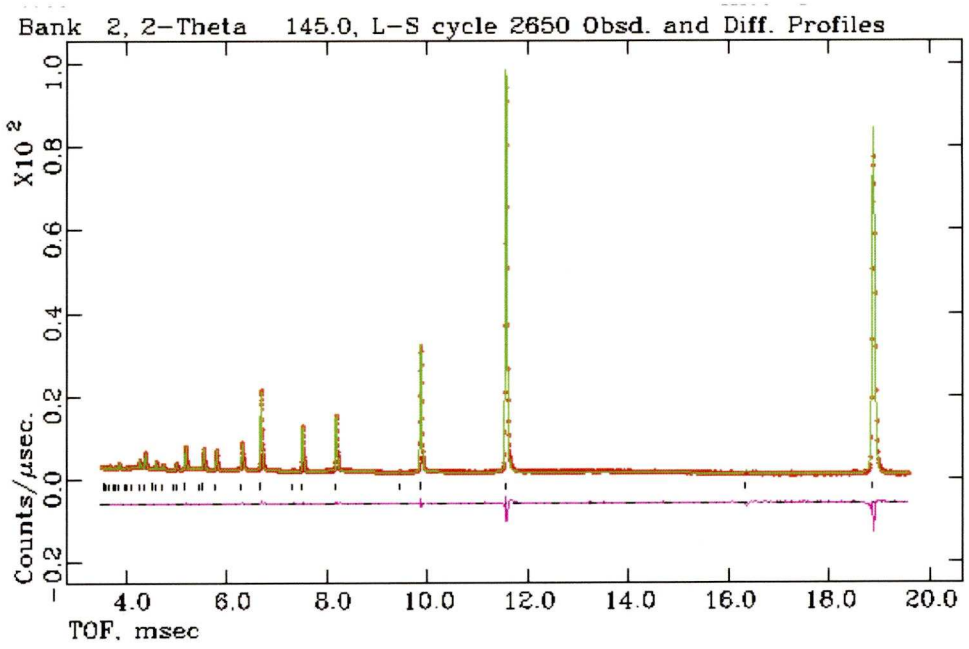

Figure 4-25 Powder neutron diffraction data of $Yb_{2.25}Ce1.11_2Mo_{0.6}O_{7.515}$ collected at ISIS Polaris station with the back scattering bank shown. Space group Fm $\bar{3}$m, a= 5.3045(3)Å wRp = 0.0165 χ^2 = 2.58. The red crosses are data points the green line is the fit and the purple line the difference plot with the black tick marks showing the allowed reflections.

Raman data for $Yb_{1.5}Ce_{0.5}Mo_{0.5}O_{7.75}$ was collected by Dr Jared Smit with the results given in Figure 4-26

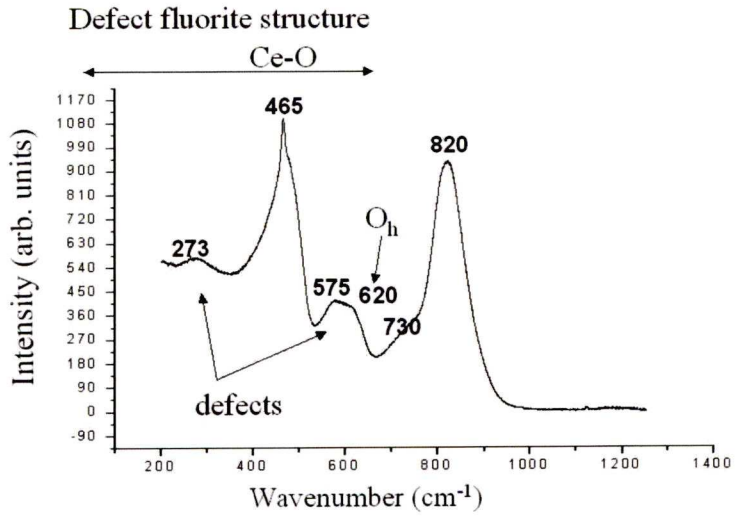

Figure 4-26 Raman data for $Yb_{1.5}Ce_{0.5}Mo_{0.5}O_{7.75}$

The assignment of the Raman stretches was made with reference to Mandal[14] . In pure CeO_2 the 465 cm^{-1} is seen and assigned to the Ce-O vibrational unit in eightfold coordination so in $Yb_{1.5}Ce_{0.5}Mo_{0.5}O_{7.75}$ the 465 cm^{-1} band is likely to be Ce-O. Mandal reports that doping into ceria usually results in three defect weak bands at approximately 260 cm^{-1}, 540 cm^{-1} and 600 cm^{-1}. In $Yb_{1.5}Ce_{0.5}Mo_{0.5}O_{7.75}$ these defect weak bands are seen at 273 cm^{-1}, 575 cm^{-1} and 620 cm^{-1} . The two stretches at higher wavenumbers (730 cm^{-1} and 820 cm^{-1}) correspond to bond lengths of 1.84 Å and 1.78 Å and are most likely Mo-O.

To ensure the Mo in the structure is in the 6+ state a XANES experiment on the Mo edge was carried out at station 9.3 at the SRS . $Yb_{1.5}Ce_{0.5}Mo_{0.5}O_{7.75}$ was compared to Mo foil, $Ce_2(MoO_4)_3$, $(NH_4)_6Mo_7O_{25}$ and $SrMoO_4$ with the $SrMoO_4$ compound proving to be the most suitable match. $SrMoO_4$ is a scheelite type compound where Mo^{6+} is in tetrahedral coordination and Sr^{2+} is in an eight fold bisdisphenoid. Further evidence for tetrahedral Mo^{6+} was sought in the EXAFS region with the aid of Dr Ian Harvey. Figure 4-27 shows the fitting from the EXAFS

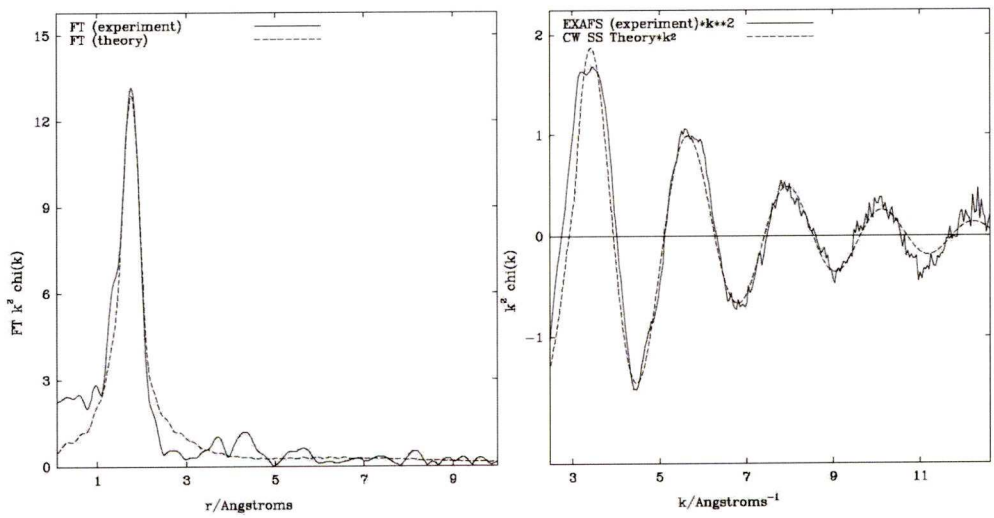

Figure 4-27 Fitting of the EXAFS parameters solid line experimental dotted theory. Fourier Transform (left) weighted data (right).

The result of the fitting gives the Mo-O bond length as 1.812 Å but the coordination can be seen by plotting coordination number (N1) versus the Debye-Waller factor (A1) in an energy contour plot (shown in Figure 4-28) .The bond length from EXAFS corresponds well to that found by Raman (1.81 Å is the average of 1.84 Å and 1.78 Å).

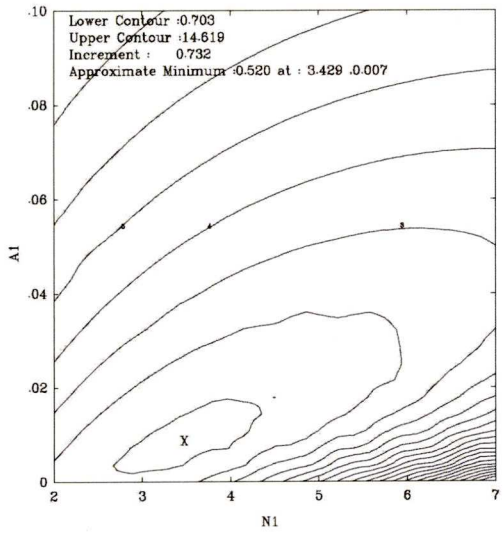

Figure 4-28 Contour plot from EXAFS data where x marks the spot where the energy is lowest.

4.1.2.2.3 Nd_6MoO_{12}

Another Mo containing fluorite type derivative that was reported by Czesklebra-Kerner is Nd_6MoO_{12}[15] . Nd_6MoO_{12} has the same rhombohedrally distorted fluorite structure as La_6MoO_{12} Pr_6MoO_{12} and Y_6UO_{12}.

The synthesis procedure for Nd_6MoO_{12} was 48h at 1000 °C then 48h at 1200 °C then repeated firings at 1200 °C. The XRD pattern (Figure 4-29) shows the presence of unreacted Nd_2O_3 but no evidence of MoO_3 as at the synthesis temperature the MoO_3 is volatile.

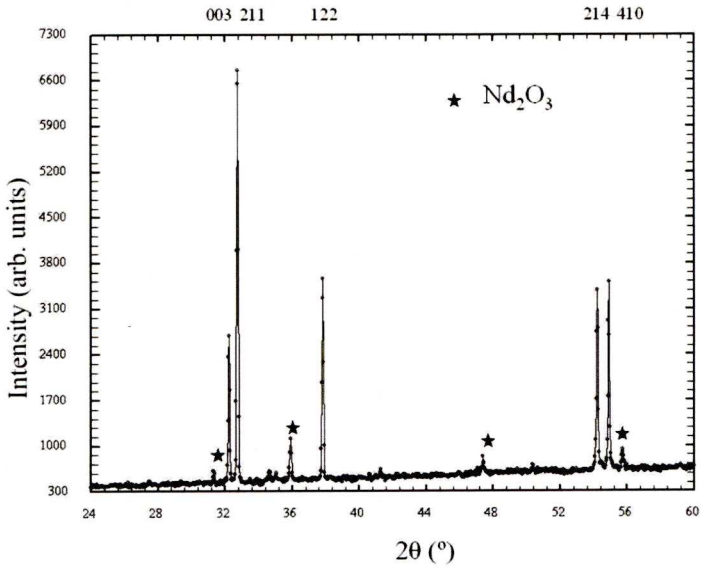

Figure 4-29 XRD of Nd_6MoO_{12} with unreacted Nd_2O_3 shown by stars. The hkl indices are for the Nd_6MoO_{12} phase.

Conductivity measurements were carried out on the system(Figure 4-30). As the conductivity only reaches 5 x 10^{-3} Scm^{-1} at 950 °C, work on the system was discontinued.

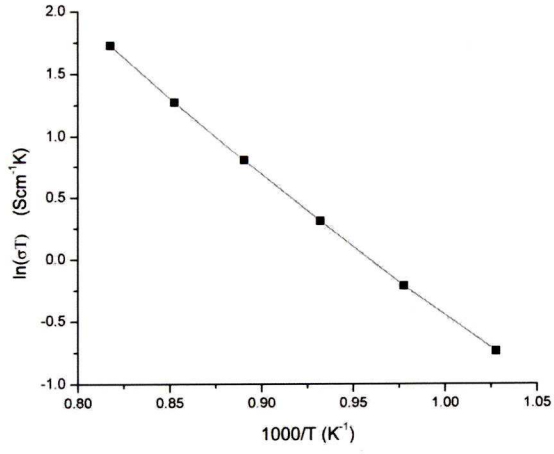

Figure 4-30 Conductivity versus temperature data for Nd_6MoO_{12} in air.

4.1.2.2.4 Investigation into $Ln_2W_{0.6}Ce_{1.4}O_7$: a material on the pyrochlore fluorite border with W^{6+}.

As the size of the A site cation increases while the size of the B site cation remains constant (78.3 pm), the structure is expected to change from fluorite to pyrochlore when A site reaches approximately 110 pm (Figure 4-1). The first lanthanide with an eight coordinate ionic radius greater than 110 pm is neodymium with an ionic radius of 112 pm.

The XRD of the Nd sample shows no evidence of pyrochlore Figure 4-31. As the lanthanide size increases the temperature at which a single phase fluorite increases from 1400 °C for Yb (98 pm) to 1500 °C for Ho(102 pm) 1550 °C for Eu(107 pm) and 1600 °C for Nd (112 pm).

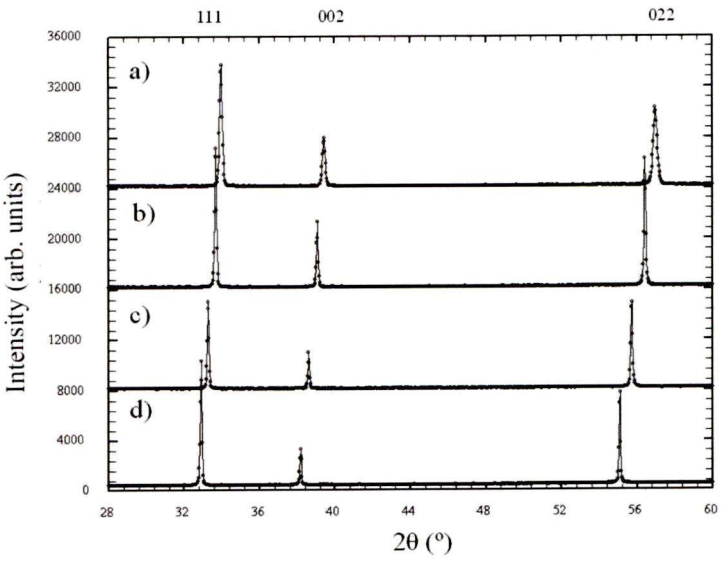

Figure 4-31 XRD $Ln_2W_{0.6}Ce_{1.4}O_7$ a) Ln =Yb synthesized in air at 1400 °C a = 5.30(3) Å , b) Ln =Ho synthesized in air at 1500 °C a = 5.34(7) Å c) Ln =Eu synthesized in air at 1550 °C a = 5.41(1) Å d) Ln = Nd synthesized in air at 1600 °C a = 5.47(1) Å. Indices are for fluorite cell.

La with an eight coordinate ionic radius of 118 pm is predicted to be a pyrochlore with a lattice parameter of 11.03 Å however when fired at 1400 °C and 1650 °C a $La_{1.75}WO_{5.625}$ impurity is formed along with a fluorite a = 5.53(1) Å (Figure 4-32).

As the synthesis trend is higher synthesis temperature for larger lanthanides it may be possible to synthesise single phase $La_2W_{0.6}Ce_{1.4}O_7$ at temperatures > 1650 °C.

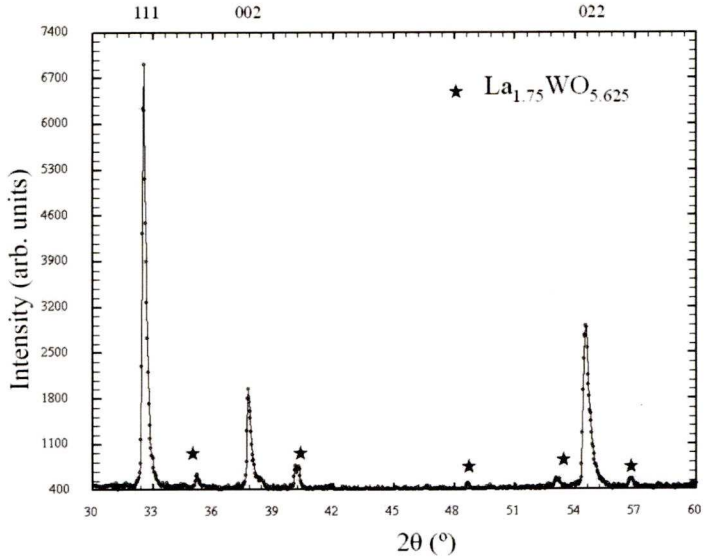

Figure 4-32 XRD of $La_2W_{0.6}Ce_{1.4}O_7$ with stars marking $La_{1.75}WO_{5.625}$ and indices shown for a fluorite phase a = 5.53(1) Å

4.1.2.3 Summary of investigations into Mo^{6+} and W^{6+} containing fluorites

Incorporation of readily reducible ions such as Mo and W has been attempted with single phase fluorites being synthesized with general formulas $Yb_aZr_bMo_cO_x$ and $Yb_aCe_bMo_cO_x$ with a + b + c = 4. In both systems control of the stoichiometry of the phase synthesised has proved to be complex. For these materials to be properly investigated for fuel cells this stoichiometry problem must be overcome. Methods such as large excesses of Mo and sealed tubes may prove successful but such methods are of limited use for producing the bulk quantities used in commercial fuel cells.

Synthesis of the rhombohedraly distorted fluorite Nd_6MoO_{12} was completed albeit with a Nd_2O_3 impurity and the conductivity tested. Nd_6MoO_{12} shows a conductivity of 5 x 10^{-3} Scm^{-1} at 950 °C .

$Ln_2W_{0.6}Ce_{1.4}O_7$ fluorite materials with Ln = Yb, Ho, Eu, Nd have successfully been prepared despite the predicted transition to pyrochlore for Ln = Nd. Attempts at producing the La equivalent proved unsuccessful possibly requiring a synthesis temperature greater than 1700 °C.

4.1.3 Zirconolite-3T investigations arising from co-doping studies.

Introducing Mo^{6+} into pyrochlore is problematic due to its high charge instead Mo Mo^{4+} pyrochlores such as in $Re_2Mo_2O_7$ and Re_2MoTiO_7 are found. Compounds such as $Sm_{2-x}Sr_xMo_2O_7$ however show that higher valent Mo in pyrochlores is possible. In 2008 Deng[11] succeeded in introducing Mo^{6+} into a pyrochlore along with Mg giving $(Yb_{1.9}Ca_{0.1})(Ti(Mo_{0.5}Mg_{0.5}))O_{6.95}$. The Mo/Mg combination was 'found to promote the desired redox activity in the pyrochlore structure' when compared to $Yb_{0.96}Ca_{1.04}TiNbO_{6.98}$.

Introducing W^{6+} with Mg^{2+} was tried for $Yb_2Ti(W_{0.5}Mg_{0.5})O_7$ which was expected to be a pyrochlore/fluorite however the resulting XRD pattern showed the material had also formed the zirconolite-3T structure. Attempts at synthesising the zirconolite-3T phase in a phase pure sample were carried out with the results described in this section.

4.1.3.1 Synthesis

Traditional ceramic synthesis was tried at 1480 °C using Yb_2O_3 TiO_2 WO_3 and MgO The resultant material showed both a pyrochlore phase and a zirconolite-3T phase with the zirconolite-3T phase dominating. A quenching experiment from 1480 °C was attempted as one or other of the phases may only have formed on cooling however the experiment produced a mixed phase. Further experiments at 1600 °C and 1650 °C also failed to produce a single phase material.

4.1.3.2 Characterization

XRD diffraction patterns of $Yb_2Ti(Mg_{0.5}W_{0.5})O_7$ clearly show the 222 reflection of the pyrochlore phase appearing at 35.66° 2θ between the 202 and 006 peaks of the zirconolite-3T phase. Le Bail refinement (Figure 4-33) gives the lattice parameters of the zirconolite-3T phase as a = 7.2715(2) Å and c = 17.0941(4) Å space group $P3_12_1$. Theses values compare to the known zirconolite-3T phase $Er_2Mn_{2/3}Re_{4/3}O_7$ [16] where a= 7.3174(6) Å c= 17.365(1) Å space group $P3_12_1$. While the Le Bail refinement gives the lattice parameters of the pyrochlore phase as 10.1203(7) Å which compare to 10.0905(1) Å for $Yb_2Ti_2O_7$.[17]

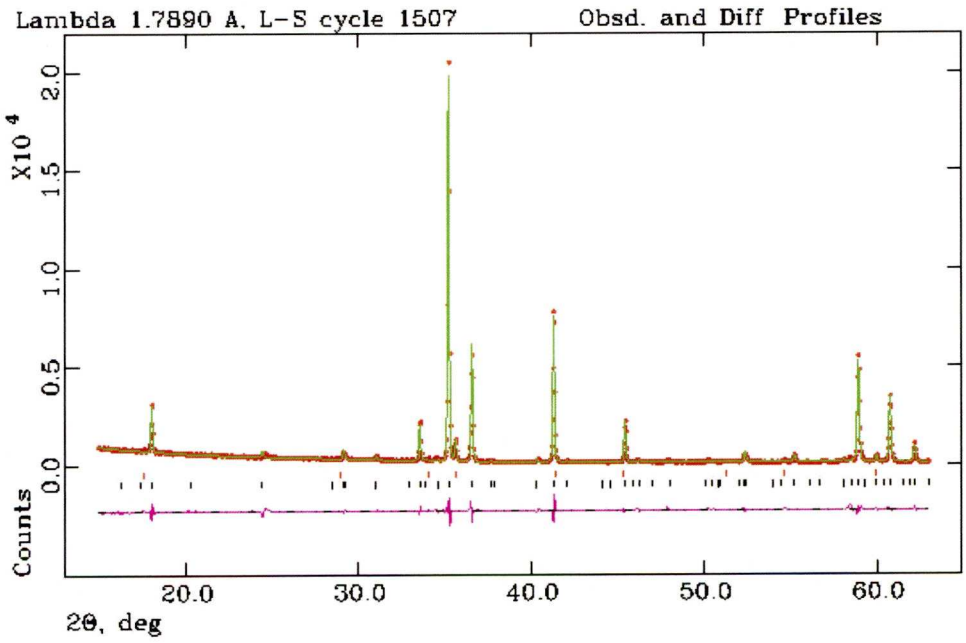

Figure 4-33 LeBail Refinement of $Yb_2Ti(Mg_{0.5}W_{0.5})O_7$ χ^2 =4.521 wRp = 0.0986 Lower black tick marks zirconolite-3T space group $P3_12_1$ upper red tick marks pyrochlore phase Fd $\bar{3}$m. The red crosses are data points the green line is the fit and the purple line the difference plot.

EDS (Figure 4-34) shows the crystallites clustered around the ideal point, the points have all been normalized to one Ti per formula unit so Ti is omitted from the diagram. The EDS shows that if there is a compositional difference between the pyrochlore and zirconolite-3T it is very subtle.

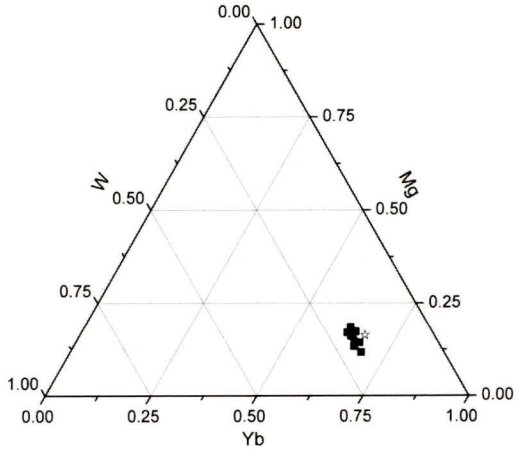

Figure 4-34 EDS of $Yb_2Ti(Mg_{0.5}W_{0.5})O_7$ Filled squares shown the data points while empty stars show the ideal composition

4.1.3.3 Summary of co-doping studies

Simultaneous doping of W and Mg into the pyrochlore structure was investigated in the compound $Yb_2Ti(Mg_{0.5}W_{0.5})O_7$. XRD showed the resulting material to contain a pyrochlore phase and a zirconolite-3T phase of similar composition. The close structural relationship between pyrochlore and zirconolite-3T complicates attempts to produce single-phase zirconolite-3T. Varying the synthesis temperature and cooling rate failed to produce phase pure samples. Zirconolites provide an interesting and relatively unexplored area for fuel cell materials having been studied predominantly for nuclear waste storage.

4.2 Conclusion to work on pyrochlores and fluorites.

Throughout this chapter a number of pyrochlores and fluorites have been investigated as potential materials for fuel cells with a focus on use as anodes. Two main strategies have been pursued. The first strategy involved looking at the phase transition between pyrochlore and fluorite as compositions in this region have previously been reported as having highest conductivities. $LnCaCeNbO_7$ where Ln = Yb , Ho and Eu were studied in reducing conditions. $YbCaCeNbO_7$ could be reduced and reoxidised although there is a monoclinic perovskite phase that is present in the reduced samples. For $HoCaCeNbO_7$ reduction at 950 °C was possible but again the monoclinic perovskite forms but unlike the $YbCaCeNbO_7$ case did not reoxidise to the fluorite phase. $EuCaCeNbO_7$ behaved differently to the other two materials, namely the reducing conditions caused the Eu to be lost from the fluorite. The system $YbCaCe_{1-x}Ti_xNbO_7$ was also investigated under reducing conditions. The conductivity of all these materials was found to be significantly less than the 10 Scm^{-1} required for use in fuel cell anodes.

The second strategy involved trying to incorporate readily reducible ions such as W^{6+} and Mo^{6+} into pyrochlore and fluorites.

Unfortunately the conductivity at the border between pyrochlore and fluorite materials tested failed to show the reported increase, instead a slight decrease was observed.

Incorporation of W^{6+} and Mo^{6+} proved successful however control over the resulting stochiometry of $Yb_a(Ce/Zr)_bMo_cO_7$ (a + b + c = 4) phases proved challenging.

A co doping strategy was also attempted in $Yb_2Ti(Mg_{0.5}W_{0.5})O_7$ where a zirconolite-3T phase was observed along with a pyrochlore phase of similar composition.

4.3 References

[1] A. V. Shlyakhtina, L. G. Shcherbakova, A. V. Knotko, A. V. Steblevskii, *Journal of Solid State Electrochemistry* **2004**, *8*, 661.

[2] S. M. Haile, S. Meilicke, *Materials Research Soicety Symposium Proceedings* **1996**, *398 (Thermodynamics and Kinetics of Phase Transformations)*, 599.

[3] H. Yamamura, H. Nishino, K. Kakinuma, K. Nomura, *Solid State Ionics* **2007**, *178*, 233.

[4] H. Nishino, H. Yamamura, T. Arai, K. Kakinuma, K. Nomura, *Journal of the Ceramic Society of Japan* **2004**, *112*, 541.

[5] R. D. Shannon, C. T. Prewitt, *Acta Crystallographica B* **1969**, *25*, 925.

[6] R. D. Shannon, C. T. Prewitt, *Acta Crystallographica B* **1970**, *26*, 1046

[7] T. A. Vanderah, I. Levin, M. W. Lufaso, *European journal of Inorganic Chemistry* **2005**, 2895.

[8] F. X. Zhang, J. Lian, U. Becker, R. C. Ewing, J. Hu, S. K. Saxena, *Physical Review B* **2007**, *76*, 214104.

[9] B. J. Wuensch, K. W. Eberman, C. Heremans, E. M. Ku, P. Onnerud, E. M. E. Yeo, S. M. Haile, J. K. Stalick, J. D. Jorgensen, *Solid State Ionics* **2000**, *129*, 111.

[10] H. Yamamura, H. Nishino, K. Kakinuma, K. Nomura, *Solid State Ionics* **2003**, *158*, 359

[11] Z. Q. Deng, H. J. Niu, X. J. Kuang, M. Allix, J. B. Claridge, M. J. Rosseinsky, *Chemistry of Materials* **2008**, *20*, 6911.

[12] J. D. Faktor, J. A. Kilner, B. C. H. Steele, *Studies in Inorganic Chemistry* **1983**, *3(Solid State Chem)*, 207.

[13] V. K. Trunov, L. I. Konstantinova, Y. A. Velikodnyi, A. A. Evdokimov, A. M. Frolov, *Zhurnal Neorganicheskoi Khimii* **1981**, *26*, 3241

[14] B. P. Mandal, V. Grover, M. Roy, A. K. Tyagi, *Journal of the American Ceramic Society* **2007**, *90*, 2961.

[15] H. Czeskleba-Kerner, B. Cros, G. Tourne, *Journal of Solid State Chemistry* **1981**, *37*, 294

[16] G. V. Bazuev, T. I. Chupakhina, *Inorganic Materials* **2008**, *45*, 409.

[17] A. Shlyakhtina, A. Sokolov, V. Ul'yanov, V. Trunov, M. Boguslavskiĭ, A. Levchenko, L. Shcherbakova, *Crystallography Reports* **2009**, *54*, 25.

[18] J. M. Haschke, H. A. Eick, , *The Journal of Physical Chemistry* **1969**, *73*, 374.

[19] M. P. van Dijk, K. J. de Vries, A. J. Burggraaf, Solid State Ionics **1983** 9/10 913

[20] R. M. Dell, A. Hooper *Solid Electrolytes* **1978** 291

[21] P. J. Wilde, C. R. A. Catlow, *Solid State Ionics* **1998** 112 173

[22] L. Minervini, R. W. Grimes, K. E. Sickafus, *Journal of the American Ceramic Society* **2000** 83 1873

[23] S. M. Haile, B. J. Wuensch, E. Prince, *Material Research Society Symposium Proceedings* **1990** 166 81

[24] C. Heremans, B. J. Wuensch, J. K. Stalick, E. Prince, *Material Research Society Symposium Proceedings* **1993** 293 349

[25] C. Heremans, B. J. Wuensch, J. K. Stalick, E. Prince, *Journal of Solid State Chemistry* **1995** 117 108

Chapter 5 : Other materials synthesised for use in solid oxide fuel cells

5.1 Introduction

Other structures apart from pyrochlores and fluorites have been studied as candidates for use in solid oxide fuel cells often these are perovskite based, two other structure types are investigated in this chapter.

The chapter is split into two sections, one for each of the structures and are arranged as follows:

i. **Sr_2CeO_4 (Section 5.2).** The aim of this section was to introduce oxygen vacancies in the Sr_2PbO_4 structured Sr_2CeO_4 compound to induce a proton conduction. $SrCeO_3$ has already been shown to be a proton conductor when heated in a humid atmosphere with the mechanism thought to rely on Ce^{4+} being reduced to Ce^{3+} causing oxygen vacancies to charge compensate.

ii. **RP2 (Section 5.3)** The aim of this section was to use RP2 phases as mixed electronic and ionic conductors for use as fuel cell electrodes. Manganese-based RP2 phases have been studied more for their magnetic behaviour such as magnetoresistance than for fuel cells.

Both these structure types show promise as fuel cell materials and demonstrate the importance of investigating structures apart from those commonly used.

5.2 Sr_2CeO_4

As described in the introduction solid oxide fuel cells can use H^+ rather than O^{2-} as the charge carriers across the electrolyte. Some of the more promising materials for this application are Y doped $MCeO_3$ M=Sr, Ba. Ranløv[2] notes that oxygen vacancies are responsible for the transport processes in cerates.

Sr_2CeO_4 was first reported in 1966 [3] and again in 1998 by Danielson[1] as having the Sr_2PbO_4 structure. Recently the materials has received a great deal of attention due to its luminescence properties[4] with maxima at 310 nm and 485 nm, and a lifetime of 51 μs. However as the structure contains chains of edge shared octahedra (described in the introduction) each octahedron has two isolated oxygens. If the oxygens that are not involved in the edge sharing could be removed this would create oxygen vacancies and possibly allow for ionic conduction down the chain. To get the desired vacancies, substitution of the Ce^{4+} ion with Y^{3+} or Yb^{3+} ($Sr_2Ce_{1-x}M_xO_{4-x/2}$) was tried as these ions are approximately the same size as Ce^{4+} 90 and 86.8 pm (Y , Yb) vs 87 pm (Ce).

5.2.1 Synthesis and Characterisation

Traditional ceramic methods were used with $SrCO_3$ and CeO_2 as initial oxide materials with Y_2O_3 or Yb_2O_3 as required. The successful firing procedure for Sr_2CeO_4 used was the same as that used by Danielson,[1] essentially heat at 1000°C until no more perovskite impurity is observed. A control of Sr_2CeO_4 was run alongside the Y and Yb x = 0.3 doped cases and required 168 hours (with regrinding and repeletisation after 48 and 96 hours) to generate a single phase sample (Figure 5-1). Following the reaction by

XRD shows the amount of $SrCeO_3$ perovskite being reduced in the parent compound but the impurity remaining constant in the Y and Yb doped cases.

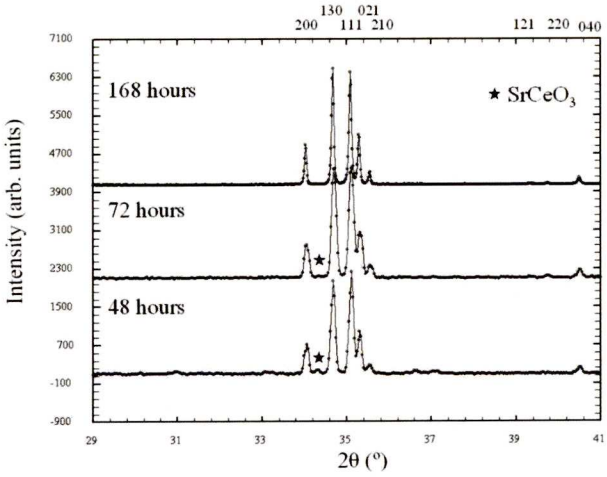

Figure 5-1 XRD showing the phase evolution of the pure Ce case after firing at 1000 °C for 48, 72 and 168 hours with the hkl indices marking the main Sr_2CeO_4 phase and the star showing the 112 peak of the $SrCeO_3$ type phase.

The refinement of Sr_2CeO_4 (Figure 5-2) gives the lattice parameters in Table 5-1

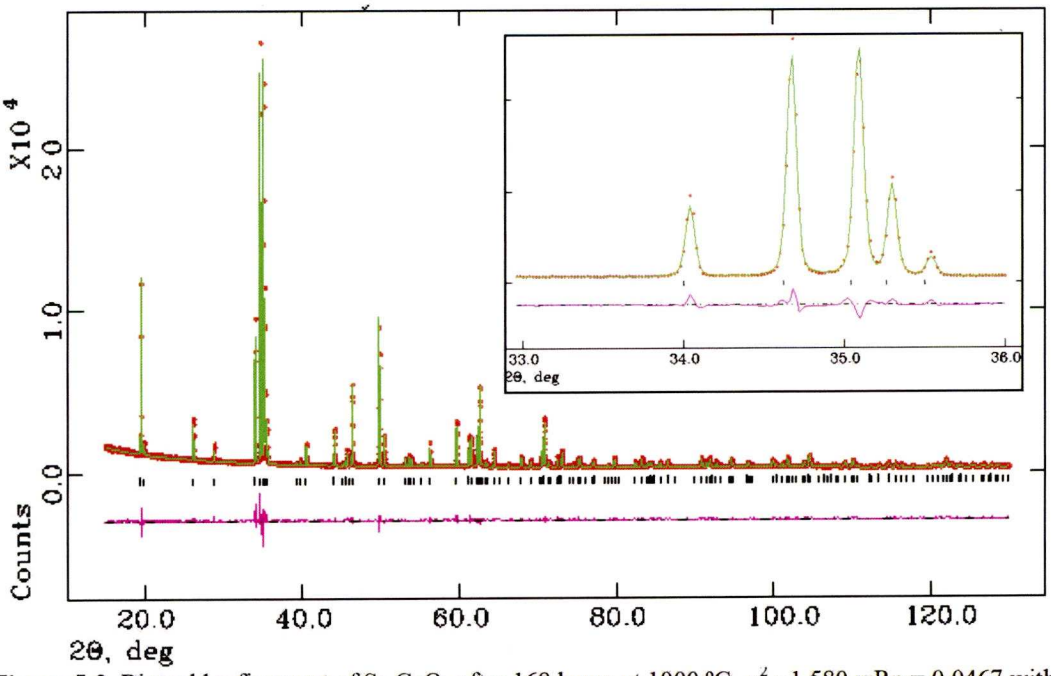

Figure 5-2 Rietveld refinement of Sr_2CeO_4 after 168 hours at 1000 °C. χ^2 =1.580 wRp = 0.0467 with tick marks indicating allowed reflections. The inset shows 2Θ 33-36 which shows no evidence of the $SrCeO_3$ phase with 112 expected to be at 34.3°. The red crosses are data points the green line is the fit and the purple line the difference plot with the black tick marks showing the allowed reflections.

Table 5-1 Lattice parameters of Sr_2CeO_4

Sr_2CeO_4	a	b	c
Data	6.1193(7)	10.3500 (14)	3.5972(4)
Danielson[1]	6.11897(9)	10.3495(2)	3.5970(1)

It did not prove possible to purify the Y and Yb cases this way as the initial $SrCeO_3$ type impurity gives way to an SrY_2O_4 or $SrYb_2O_4$ type impurity on repeated firings (Figure 5-3).

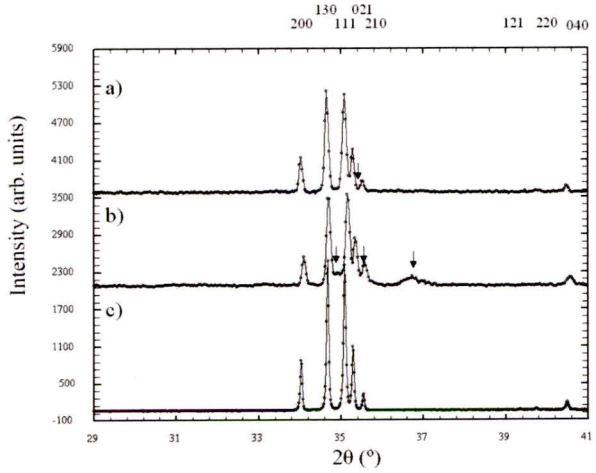

Figure 5-3 XRD of a) $Sr_2Ce_{0.7}Y_{0.3}O_{3.85}$ b) $Sr_2Ce_{0.7}Y_{0.3}O_{3.85}$ c) Sr_2CeO_4 all after 168 hours at 1000 °C. Indices are for the main Sr_2CeO_4 type phase with the arrows showing the remaining SrY_2O_4 type impurity.

EDS measurement of $Sr_2Ce_{0.7}Y_{0.3}O_{3.85}$ also shows the material to be mixed phase shown in Figure 5-4 by the crystallites being spread over a wide area.

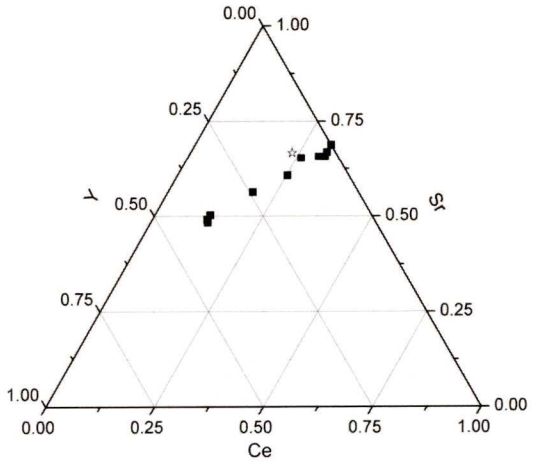

Figure 5-4 EDS of 10 crystallites of $Sr_2Ce_{0.7}Y_{0.3}O_4$ with the black squares giving data points and empty star giving ideal composition.

Cocco[3] in his study stated Sr_2CeO_4 is stable between 1430 °C and 1100 °C. Above 1430 °C Sr_2CeO_3 and SrO are formed (although Sr_2CeO_3 is not reported elsewhere in the CAS) and below 1100 °C $SrCeO_3$ and other impurities form. Using this information quenching from high temperatures, both 1200 °C and 1400 °C was attempted to no avail (Figure 5-5).

As water can often be used as a mineralising agent, ball milling with firing in wet O_2 atmosphere was attempted, again to no avail (Figure 5-5). It appears that the trivalent ions of Y and Yb stabilise the $Sr(Y/Yb)_2O_4$ type impurity preventing further reaction to form the desired Sr_2PbO_4 phase. The wet O_2 atmosphere was generated by passing the O_2 gas through a water bubbler before the gas stream entered the tube furnace.

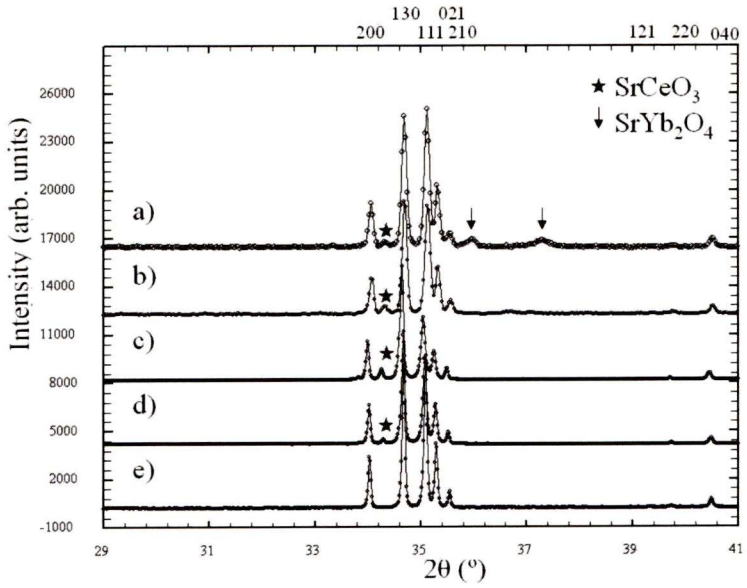

Figure 5-5 Selected XRD patterns of other attempted methods a) $Sr_2Ce_{0.9}Yb_{0.1}O_{3.9}$ ball milled in ethanol fired at 1000 °C for 72 hours. b) $Sr_2Ce_{0.9}Yb_{0.1}O_{3.9}$ ball milled in ethanol fired at 1000 °C in humidified O_2 for 24 hours. c) Sr_2CeO_4 quenched from 1200 °C after 48h d) Sr_2CeO_4 quenched from 1400 °C after 48h e) Sr_2CeO_4 all after 168 hours at 1000 °C. Indices are for the main Sr_2CeO_4 type phase with the arrows showing the remaining SrY_2O_4 type impurity and stars showing $SrCeO_3$ type impurity.

In 2008 Gerlach[5] reported synthesizing Y_2O_3-doped Sr_2CeO_4 as an intermediate for Y_2O_3-doped CeO_2 (the Sr being removed by acid washing). Gerlach states that the XRD patterns show no major diffraction peaks due to impurities and that there is a slight shift in peak positions.

5.2.2 Summary

Unfortunately attempts at introducing vacancies into Sr_2CeO_4 by doping Y^{3+} or Yb^{3+} for Ce^{4+} proved unsuccessful, instead producing a combination of Sr_2CeO_4, Ln-doped $SrCeO_3$ and Ce-doped $SrLn_2O_4$ where Ln = Y or Yb. A possible future direction is to use hydrothermal methods such as those used by Wu[6] to produce Sr_2SnO_4 via a $Sr_2Sn(OH)_8$ intermediate. However hydrothermal methods do not produce dense phases, which would make measurement difficult even if the material could be synthesised.

5.3 Ruddlesden Popper n = 2 phases

As the RP2 phases with the general formula Sr_3M_2O7 are able to incorporate many different metals such as Ti[7], Co[8], Fe[9], Mn[9] there is a possibility of mixed conduction. This is aided by the fact that many of the RP2 phases are non-stoichiometric due to mixed 3+/4+ valence on the M site studied in detail by Mitchell for the Mn case[10]. The introduction of the mixed valence allows for some oxygen vacancies to form and raising the possibility of oxide ion conduction due to vacancy hoping. As fixed valent ions such as Al^{3+} and Ga^{3+} can also be introduced[11, 12] there is a possibility of fixing the amount of oxygen ion vacancies and allowing high ionic conduction while still allowing electronic conduction . Such properties would make the RP2 materials useful as electrodes for solid oxide fuel cells.

5.3.1 Synthesis and characterisation

The starting oxides and carbonate for traditional ceramic methods used were $SrCO_3$ MnO_2 and depending on the dopant Al_2O_3 Ga_2O_3 Cr_2O_3, Mn_2O_3 , MgO CuO or ZnO. Synthesis temperatures varied depending on the material ranging from 1200 °C to 1650 °C described in the relevant section.

5.3.1.1 $Sr_3Mn_2O_7$

Starting with the parent material $Sr_3Mn_2O_7$ firing at 1650 °C for 12 hours resulted in RP1 as well as the desired RP2 phase. Mitchell[10] used a quenching method (dropping into liquid nitrogen from 1650 °C) to get pure $Sr_3Mn_2O_7$. When quenching experiments were carried out (Figure 5-7) the amount of RP2 relative to RP1 increases as evidenced by the appearance of RP2 002 at 10 ° 2θ and the intensity of RP2 0010 versus RP1 114.

Quenching was done with an Al block as quenching in liquid N_2 forms a gaseous N_2 barrier between pellet and liquid resulting in a poor thermal contact and slower rate of cooling. The lack of pure RP2 phase is most likely due to the temperature not being high enough to drive the equilibrium between RP1 and RP2 over to the RP2 side.

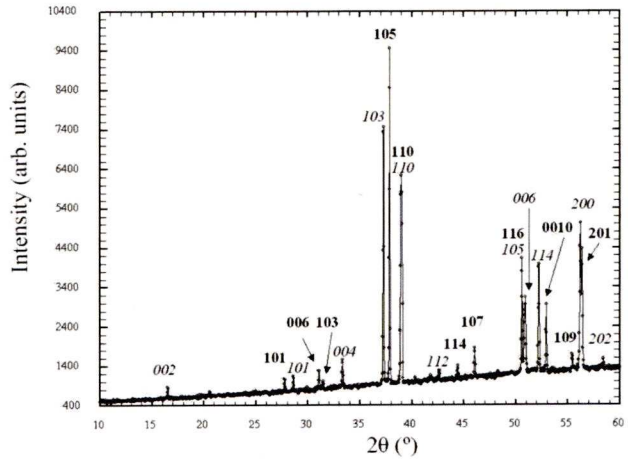

Figure 5-6 XRD of $Sr_3Mn_2O_7$ fired at 1650 °C for 12 hours with the bold indices marking RP2 phase and italic indices marking RP1phase.

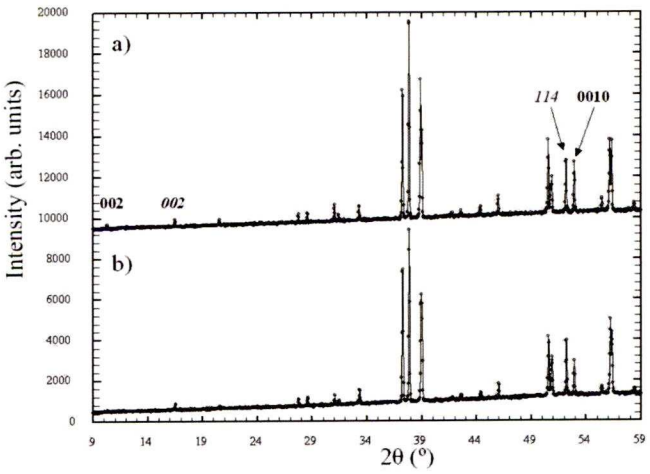

Figure 5-7 XRD of $Sr_3Mn_2O_7$ fired at 1650 °C for 12 hours and then a) quenched and b) furnace cooled with the bold indices marking RP2 phase and italic indices marking RP1phase (full index Figure 5-6).

Annealing in O_2 was tried and resulted in $Sr_7Mn_4O_{15}$ and $Sr_4Mn_3O_{10}$ forming.

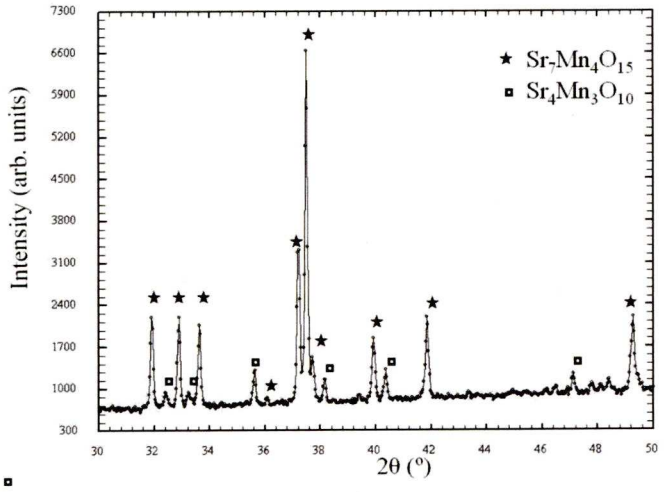

Figure 5-8 XRD of $Sr_3Mn_2O_7$ fired at 1650 °C for 12 hours and then annealed in flowing O_2 at 1250 °C for 48 hours. Stars show peaks due to $Sr_7Mn_4O_{15}$ and squares show peaks due to $Sr_4Mn_3O_{10}$. No peaks due to RP1 or RP2 were observed.

As differing starting materials may have an influence on the phases formed, Mn_2O_3 was tried as a starting material. The results of this experiment did not differ from the MnO_2 experiments. Previous work by Gillie[13] reports that using Mn_2O_3 and firing at 1350 °C in a N_2 atmosphere produces an oxygen non-stoichiometric phase written as $Sr_3Mn_2O_{6+\delta}$. The value of δ could be tuned depending on calcination history in N_2 (δ =0.3-0.15), H_2/N_2 mixtures at low temperatures (590 °C) (δ =0-0.15) or at 400 °C in O_2 (δ =0.3-1). Synthesis of $Sr_3Mn_2O_{6+\delta}$ was attempted using a firing regime of 1350 °C in flowing N_2 for 48h followed by regrinding and firing at 1350 °C in flowing N_2 for a further 24h with the results shown in Figure 5-9.

The problems associated with this type of synthesis are repeated firings in differing atmospheres (N_2 and O_2) making this synthetic procedure only suitable for small scale laboratory use.

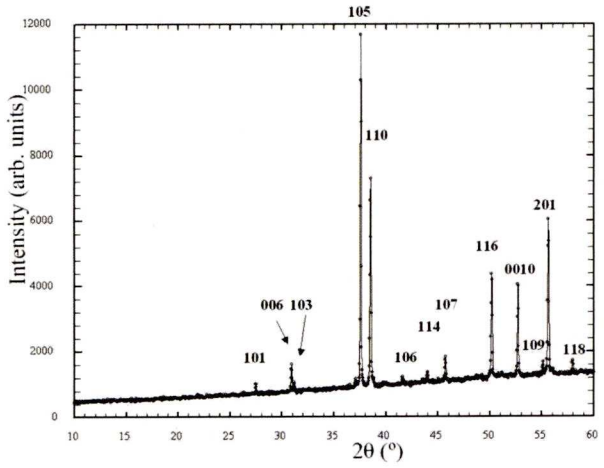

Figure 5-9 XRD of $Sr_3Mn_2O_{6+\delta}$ post 72 hours at 1350 °C in flowing N_2. The peaks are indexed using the $Sr_3Mn_2O_7$ cell i.e. $\delta = 1$.

Explanation of the behaviour of $Sr_3Mn_2O_7$ is aided by comparison to the phase formation behaviour of $LaSr_2Mn_2O_7$ reported by Yankin[14]. In the report the oxides first form RP1 (Sr_2MnO_4) and perovskite ($LaMnO_3$) that the go on to react together to form the RP2 ($LaSr_2Mn_2O_7$). This RP2 phase ($LaSr_2Mn_2O_7$) is reported to decompose on reduction in temperature and reduction in oxygen pressure back to the RP1 and perovskite.

Grundy[15] studied the thermodynamics of the Sr-Mn-O system and found that $Sr_3Mn_2O_7$ was only stable between 1600 °C and 1741 °C.

5.3.1.2 $Sr_3Mn_{2-x}M_xO_{7-x/2}$ (M= Al, Cr, Ga,)

Introduction of 3+ ions apart from Mn was hoped to reduce the temperature required for RP2 phase formation and help stabilise the RP2 phase once it had formed. The firing regime that was tried was 1200 °C 48h then 1400 °C for 48h, at 1400 °C, M = Ga melts while M = Cr also shows partial melting .

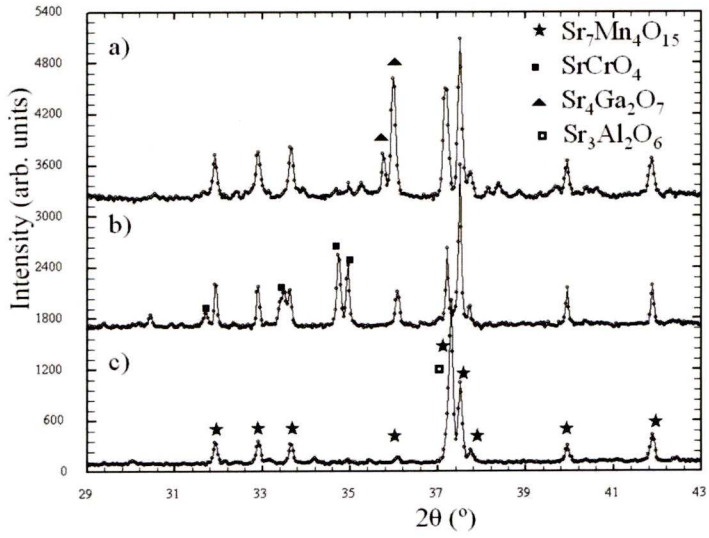

Figure 5-10 XRD of $Sr_3MnMO_{6.5}$ (M= a) Ga b) Cr c) Al) post firing for 48 hours at 1200 °C . Stars show $Sr_7Mn_4O_{15}$, filled squares $SrCrO_4$ triangles $Sr_4Ga_2O_7$ empty squares $Sr_3Al_2O_6$. All samples show peaks for $Sr_7Mn_4O_{15}$ but for clarity they are only marked for the M = Al case.

The Al doped sample appeared to have the smallest amount of impurities so a lower value of x (0.1) was fired at 1650 °C resulting in the same phase mixture being present albeit with differing ratios.

$Sr_7Mn_4O_{15}$ is observed as an impurity in all cases. $Sr_7Mn_4O_{15}$ has pairs of face sharing octahedra[16] leading to Feltz[17] describing the structure as a double octahedra version of the K_2NiF_4 structure.. Grundy[15] also noted the presence of $Sr_7Mn_4O_{15}$ in the pure Sr-Mn-O system giving its stability range as < 1550 °C after which it decomposes into RP1 and perovskite.

5.3.1.3 $Sr_3Mn_{2-x}M_xO_{7-x}$ (M= Mg and Zn)

Attempts at introducing 2+ ions were made as the lower valence would mean more vacancies per quantity of dopant when compared to 3+ ions. Firing regimes of 1300 ºC and 1400 ºC for 48 hours were tried

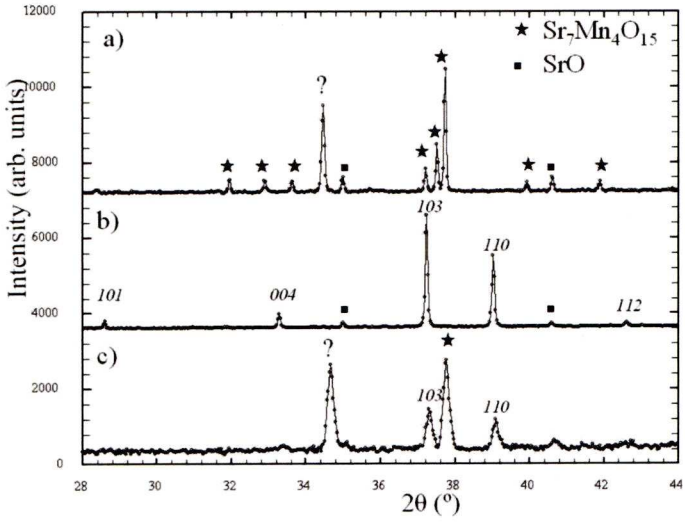

Figure 5-11 XRD of $Sr_3Mn_{1.5}M_{0.5}O_{6.5}$ (M= a)+b) Zn c) Mg) post firing for 48 hours at a) 1300 ˚C b) and c) 1400 ˚C . Stars show $Sr_7Mn_4O_{15}$, filled squares SrO indices for Sr_2MnO_4 RP1 phase, ? gives possible $Sr_4Mn_2MO_9$ phase.

Doping of the 2+ ions (Zn, Mg) differs from the 3+ cases (Al, Cr, Ga) ,as for 2+ ions, unreacted SrO remains visible in the powder XRD measurement. A possible explanation for this is that the 3+ ions react in a similar way to the parent Mn ions but the conditions where the RP2 is stable are either inaccessible or require quenching. For the 2+ case the 2+ ions appear not to react.

5.3.2 Summary of RP2 attempts

$Sr_3Mn_2O_7$-based RP2 materials require quenching to reduce the RP1 phase content but quenching is not a viable synthesis method for fuel cell materials. The compositions and conditions studied did not produce a single phase RP2 material. However if a suitable dopant could be found that lowered the synthesis temperature and removed the requirement for quenching RP2 phases could prove useful materials for fuel cell testing.

5.4 Conclusion

Both Sr_2CeO_4 and $Sr_3Mn_2O_7$ based materials have been investigated for use in solid oxide fuel cells, Sr_2CeO_4 as an electrolyte and $Sr_3Mn_2O_7$ as electrodes. For the Sr_2CeO_4 case it proved unsuccessful to introduce the vacancies by introducing Y^{3+} or Yb^{3+}, required for ionic conduction. $Sr_3Mn_2O_7$ based materials either required synthesis methods (such as quenching) unsuitable for fuel cells or competing phases were present. Investigations into other structures for use in fuel cells will continue but as the YSZ and CGO fluorite based systems become commercial the performance of the new materials needs to be a considerable improvement to break through.

5.5 References

[1] E. Danielson, M. Devenney, D. M. Giaquinta, H. Golden. J, R. C. Haushalter, E. W. McFarland, D. M. Poojary, C. M. Reaves, W. H. Weinberg, X. D. Wu, *Journal of Molecular Structure* **1998**, *470*, 229

[2] J. Ranlov, B. Lebech, K. Nielsen, *Journal of Materials Chemistry* **1995**, *5*, 743.

[3] A. Cocco, *Universita degli Studi di Trieste, Istituto di Chimica Applicata, [Pubblicazioni]* **1966**, 22, 15.

[4] S. Chen, X. Chen, Z. Yu, J. Hong, Z. Xue, X. You, *Solid StateCommunications* **2004**, *130*, 281 285.

[5] R. G. Gerlach, S. S. Bhella, V. Thangadurai, *Inorganic Chemistry* **2009**, - *48*. 257

[6] M. Wu, X. Li, G. Shen, J. Li, R. Xu, D. M. Proserpio ,*Journal of Solid State Chemistry* , 2000, 151, 56.

[7] S. N. Ruddlesden, P. Popper, *Acta Crystallographica* **1957**, *11*, 54

[8] X. L. Wang, H. Sakurai, E. Takayama-Muromachi, *Journal of Applied Physics* **2005**, *97*, 10M519

[9] N. Mizutani, A. Kitazawa, N. Ohkuma, M. Kato, *Kogyo Kagaki Zasshi* **1970**, *73*, 1097.

[10] J. F. Mitchell, J. E. Millburn, M. Medarde, D. N. Argyriou, J. D. Jorgensen, *Journal of Applied Physics* **1999**, *85*, 4352.

[11] C. Navas, H. L. Tuller, H.-C. Zur Loye, *Journal of the European Ceramic Society* **1999**, *19*, 737

[12] C. Navas, H.-C. zur Loye, *Solid State Ionics* **1997**, *93*, 171.

[13] L. J. Gillie, A. J. Wright, J. Hadermann, G. Van Tendeloo, C. Greaves, *Journal of Solid State Chemistry* **2003**, *175*, 188

[14] A. M. Yankin, O. M. Fedorova, I. A. Zvereva, T. S. G., V. F. Balakirev, *Glass Physics and Chemistry* **2006**, *32*, 574

[15] A. N. Grundy, B. Hallstedt, L. J. Gauckler, *Journal of Phase Equilibria and Diffusion* **2004**, *25*, 311

[16] J. F. Vente, J. R. Plaisier, D. J. W. Ijdo, K. V. Kamenev, *Materials Research Bulletin* **2000**, *35*, 2437

[17] A. Feltz, R. Kriegel, W. Polzl, *Journal of Materials Science Letters* **1999**, *18*, 1693

Chapter 6 : Materials synthesized under high pressure

6.1 Introduction

This chapter reports the synthesis and characterization of materials that have been synthesized using high pressure methods. This chapter is divided into three main subsections as follows:

i. **$Na(BiLa)MgWO_6$ (Section 6.2)**. Woodward synthesized $NaLaMgWO_6$ and showed it to be one of the few examples of an A and B site ordered double perovskite. By using high pressure methods it has been possible to produce and characterize the Bi-containing compound $NaBiMgWO_6$.

ii. **$Sc(MnNi)O_3$ (Section 6.3)**. Singh predicted multiferroic properties in MnNi perovskites with small A site ions. High pressure methods, instead of producing a 1:1 Mn:Ni, produced a 2/3 : 1/3 phase which has been studied here.

iii. **$Bi(FeCr)O_3$ (Section 6.4)**. Baettig and Spaldin predicted a new multiferroic with the composition Bi_2FeCrO_6 [1, 2] which was then synthesized as a thin film[3] . By using high pressure methods it has been possible to produce and characterize bulk Bi_2FeCrO_6 however the predicted ordering is absent . There is also a conference abstract reporting Bi_2FeCrO_6[4] with a different structure however the authors have so far not published the details.

The results of the investigation into the Bi_2FeCrO_6 material were published in early 2007.[5]

6.2 $NaLa_{1-x}Bi_xMgWO_6$

In 2006 Knapp & Woodward published a study on A and B-site-ordered double perovskites[6]. Of the compounds studied, $NaLaMgWO_6$ (which had previously been investigated by Arillo [7] and Sekiya [8]) showed total order over both sites. As bismuth and lanthanum are approximately the same size (118 vs 111 pm for VIII coordinate) and have the same charge (+3) a solid solution of $NaLa_{1-x}Bi_xMgWO_6$ was attempted. The motivation for attempting to incorporate Bi was to generate a ferroelectric moment by utilizing the Bi lone pair. Initially synthesis of the x = 1 end member was attempted at ambient pressure to no avail, instead producing Na_2WO_4 and unreacted MgO and Bi_2O_3 and so the high pressure press was used.

6.2.1 Synthesis

Ambient pressure synthesis using traditional ceramic methods was attempted using Na_2CO_3 MgO, Bi_2O_3 WO_3 and La_2O_3 as starting materials. For high pressure synthesis instead of using Na_2CO_3 Na_2WO_4 was used as both a source of Na and W (extra W being provided by WO_3 to achieve the correct stoichiometry). This was necessary as the Na_2CO_3 used for the ambient pressure synthesis decomposes giving Na_2O solid and CO_2 gas, which isn't a problem in the furnace as it vents to the atmosphere. In the high-pressure press however the CO_2 gas can become trapped, building pressure until it releases suddenly in a blow out which can cause damage to the WC cubes. Excess Na and Mg (10%) was used for both types of synthesis as Woodward notes that an excess of these elements is required to form the x = 0 phase.

6.2.2 Characterization

6.2.2.1 Structure

Figure 6-1 shows the structure of the phase that results from the refinement in Figure 6-2.

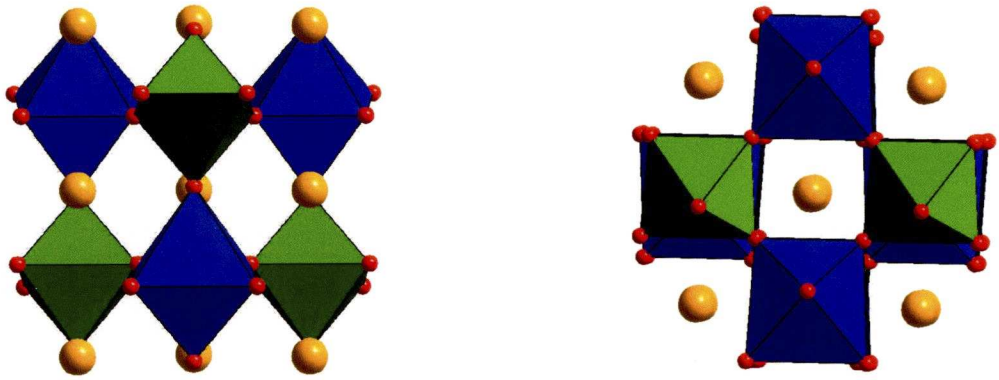

Figure 6-1 The structure of (NaBi)$MgWO_6$ showing the two types of B site (Mg blue W green octahedra)). Orange spheres give A site positions with random Na/Bi. The small red spheres show the oxygen positions. On the left is the view is down the [100], on the right the view is along [001].

The result was a single phase double perovskite however the A site order is lost as can be seen from the refinement in Figure 6-2 as the 001 peak that would be at 13 degrees two theta if A site order was present is absent.

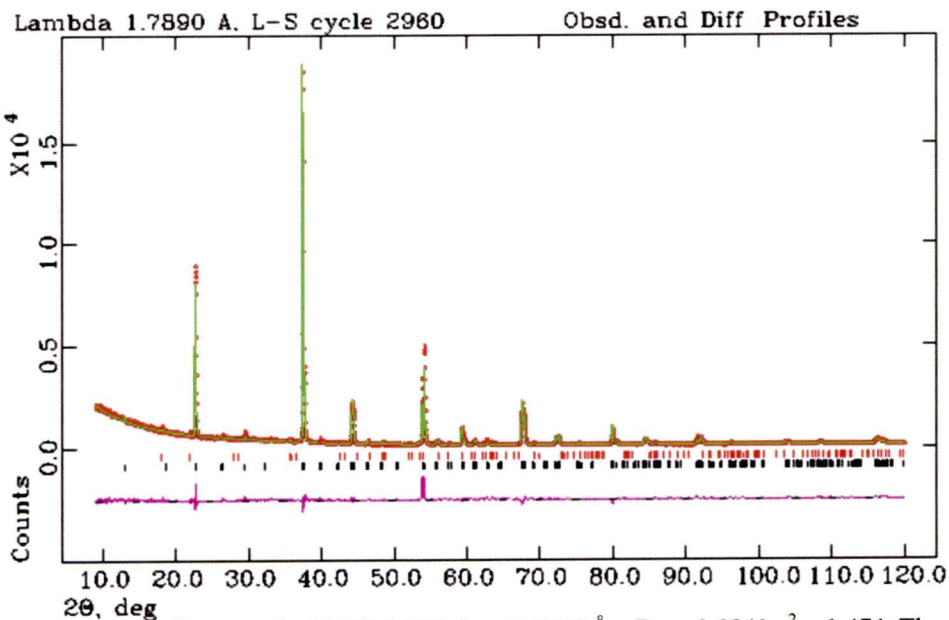

Figure 6-2 XRD refinement for $NaBiMgWO_6$ $\lambda = 1.78901$Å wRp = 0.0841 $\chi^2 = 1.474$. The red crosses are data points the green line is the fit and the purple line the difference plot lower black tick marks are $NaBiMgWO_6$, upper red tick marks give the 0.0015% of $MgWO_4$

Table 6-1 Lattice parameters for $NaBiMgWO_6$ at room temperature

Parameter	XRD	Parameter	XRD
a	5.5418(4) Å	α	90°
b	5.5704(4) Å	β	89.92(1)°
c	7.9023(6) Å	γ	90°

Table 6-2 Crystallographic data of $NaBiMgWO_6$ at room temperature

Atom	Wyckoff position	Oxidation	x	y	z	U_{iso} ($Å^2$)	Occupancy
Na1	2e	+1	0.2563(11)	0.25	0.0012(10)	0.2028(16)	0.52(2)
Bi1	2e	+3	0.2563(11)	0.25	0.0012(10)	0.2028(16)	0.48(2)
Na2	2e	+1	0.2479(7)	0.25	0.4960(5)	0.0859(8)	0.48(2)
Bi2	2e	+3	0.2479(7)	0.25	0.4960(5)	0.0859(8)	0.52(2)
Mg1	2e	+2	0.7628(1)	0.25	0.2326(1)	0.0473(12)	0.94(2)
W1	2e	+6	0.7628(1)	0.25	0.2326(1)	0.0473(12)	0.06(2)
Mg2	2e	+2	0.7500(4)	0.25	0.7512(2)	0.0584(5)	0.06(2)
W2	2e	+6	0.7500(4)	0.25	0.7512(2)	0.0584(5)	0.94(2)
O1	4f	-2	0.5020(1)	0.4780(1)	0.7080(1)	0.063(4)	1
O2	4f	-2	0.0470(1)	0.0080(1)	0.2240(1)	0.071(4)	1
O3	2e	-2	0.8067(1)	0.25	0.5171	0.088(6)	1
O4	2e	-2	0.8160(1)	0.25	0.9890(1)	0.059(4)	1

The refinement was carried out in the space group $P2_1/m$ as used by Arillo[7] for $NaLaMgWO_6$ which allows two A sites and two B sites. Other compounds that adopt the $P2_1/m$ double perovskite structure are $MLaMgTeO_6$ (M = Na, K)[9] and $NaLaMWO_6$ (M= Ni, Co)[10]. Refinement of the data also provided proof of the lack of A site order but retention of B site order and as can be seen from Figure 6-2. The fit between the model and the data is reasonable. When both sites were allowed to

refine freely the result was 51:48 split for the A sites while a 98:2 split is observed on the B sites consistent with the description of full B site order and full A site disorder.

Woodward refined $NaLaMgWO_6$ in the space group $C2/m$[6] rather than the $P2_1/m$ used by Arillo [7]. This space group assignment was made on the basis of improving the fit of the pseudo-cubic 440 and 225 peaks. Figure 6-3 shows the fit of these peaks with both the $P2_1/m$ and the C2/m space group. Neither space group fits the peaks of interest at 80° 2θ well but the other peaks such as the collection of peaks at 72° 2θ are fitted slightly better in $P2_1/m$. This is borne out by the statistics as C2/m has wRp = 0.0928 $\chi^2 = 3.073$ versus $P2_1/m$ with wRp = 0.0851 $\chi^2 = 2.586$

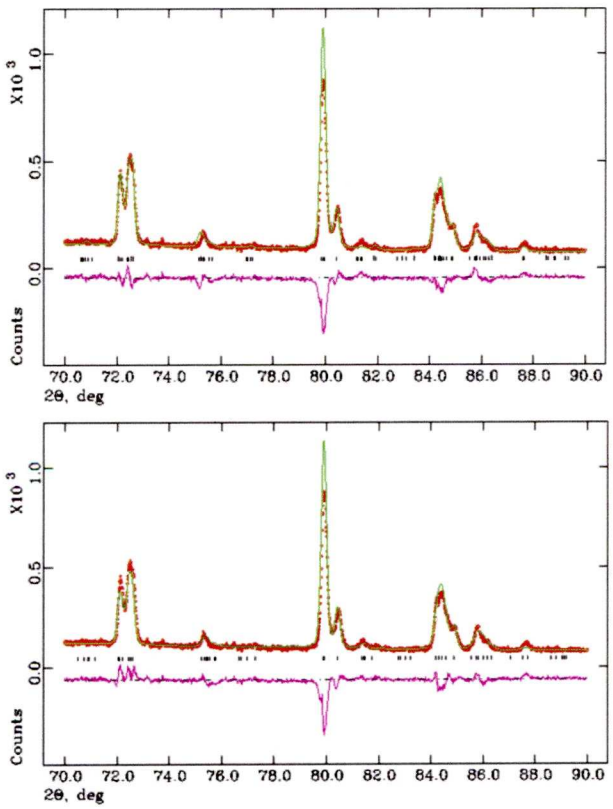

Figure 6-3 Fits of the poorly fitted pseudocubic 440 and 225 in $P2_1/m$ (top) and C2/m bottom) space group. The red crosses are data points the green lines are the fits and the purple lines are the difference plots and the black tick marks are the allowed reflections.

Later detailed HRTEM by Woodward showed the $NaLaMgWO_6$ compound exhibits octahedral tilt twinning and compositional modulation[11-13] causing the material to

appear striped ($12a_p$ periodicity) in the HRTEM. Compositional modulation was also observed for $KLaMnWO_6$ [13] however the modulation observed is of a chessboard type. No evidence for striping was seen for $NaBiMgWO_6$.

6.2.2.2 Thermal stability

To test the thermal stability of $NaBiMgWO_6$ in ambient pressure (as many compounds produced under high pressure are only metastable at ambient pressure) a sample was sent to the SRS station 9.1 λ = 0.802541 Å for variable temperature work.

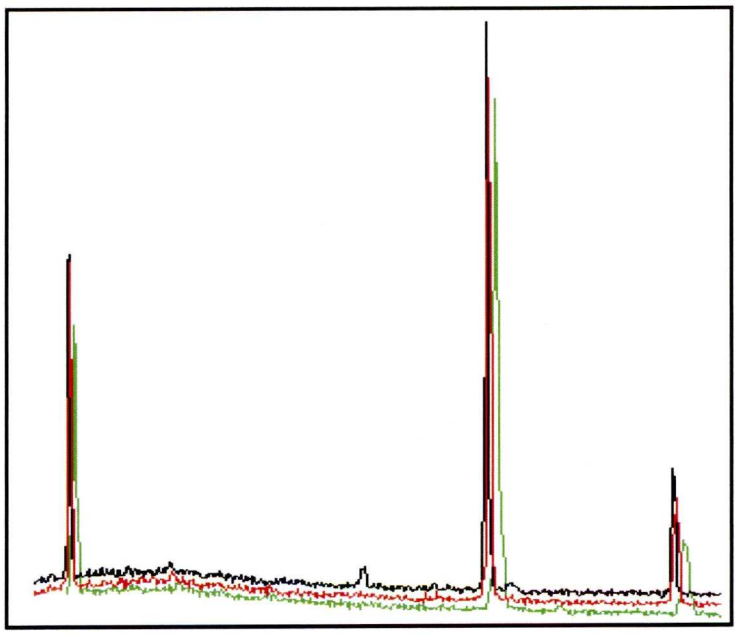

Figure 6-4 Green RT Red 500 °C Black 600 °C

Peaks shown in Figure 6-4 are, 111 112/020 and 121 and for comparison with the refinement the SRS data correspond to a two theta range of 22 - 46° on the PANalytical machine on which the refinement data was collected. The figure clearly shows that the structure starts to decompose between 500 – 600 °C as there is the appearance of new peaks that correspond to bismuth oxide, bismuth oxide was also seen as a decomposition product in Bi_2FeCrO_6 (see Figure 6-31).

6.2.2.3 Dielectric measurements

Dielectric measurements were carried out below 400 °C to ensure the data is from the $NaBiMgWO_6$ phase not a mixture of the decomposition products.

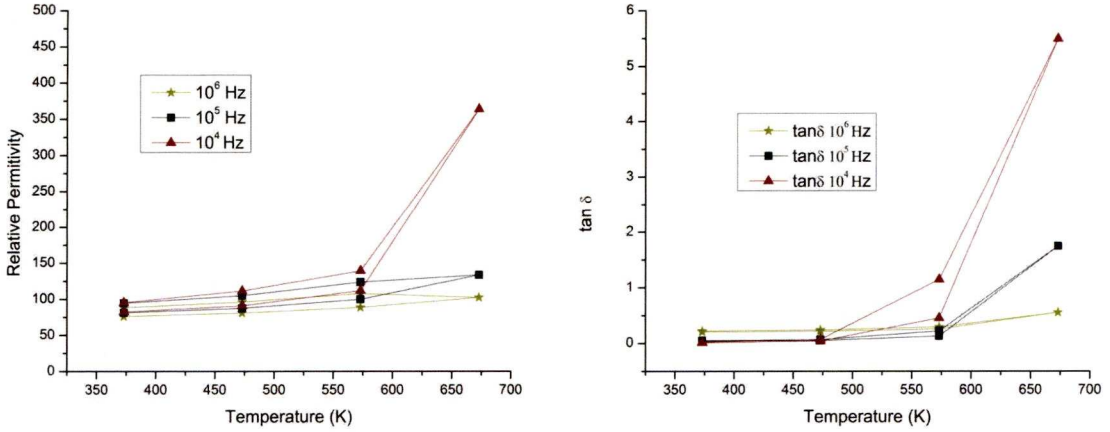

Figure 6-5 Relative permittivity data (left) and tan δ data (right) for $NaBiMgWO_6$

Dielectric measurements were taken using silver paste electrodes on a pellet of $NaLaMgWO_6$. The plateau at approximately 100 between 373 K and 573 K corresponds to a plateau in tan δ (0.23 at 10^6 Hz and 0.04 for 10^3 and 10^4 Hz) over the same temperature range. At 673 K the tan δ rises and so does the relative permittivity indicating that the sample has become too conducting to measure. There also appears to be small frequency dependence with higher frequencies having lower relative permittivity values.

6.2.2.4 Solid solution $NaLa_{1-x}Bi_xMgWO_6$

Attempts have also been made to synthesize two of the intervening compounds of the expected solid solution $NaLa_{1-x}Bi_xMgWO_6$ namely x = 0.25 x = 0.75. Both of these were attempted at high pressure although x = 0.25 was also attempted at ambient using the same conditions that were used for the x = 0 case. However the results for all the samples seem to be a non-homogeneous mixture of perovskites and doped Bi_2O_3 and Bi_2WO_6 among other phases, seen in the XRD (Figure 6-6) as broad ill-defined peaks (indicating a mixture of similar phases) and extra peaks (indicating separate structure) respectively. The 001 peak at 13° 2θ is present for the ambient synthesis x = 0.25 although as the XRD pattern is inhomogeneous it is likely that this is due to the formation of the parent phase $NaLaMgWO_6$. The same composition under high pressure synthesis also shows an inhomogeneous XRD pattern but now the 001 is gone showing that the ordering in $NaLaMgWO_6$ is very sensitive to composition.

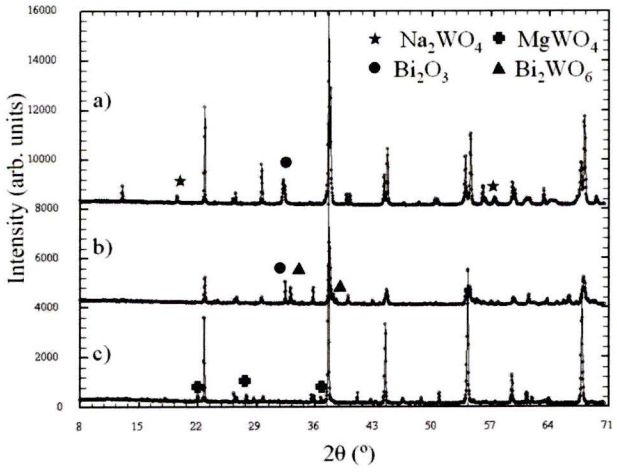

Figure 6-6 XRD patterns of $NaLa_{1-x}Bi_xMgWO_6$ a) x=0.25 at synthesized at ambient pressure b) x=0.25 synthesized at high pressure c) x = 0.75 synthesized at high pressure. All three samples are impure with the major non perovskite impurities indicated.

EDS analysis confirms the presence of mixed phases including some phases containing mostly bismuth with small amount of the other elements.

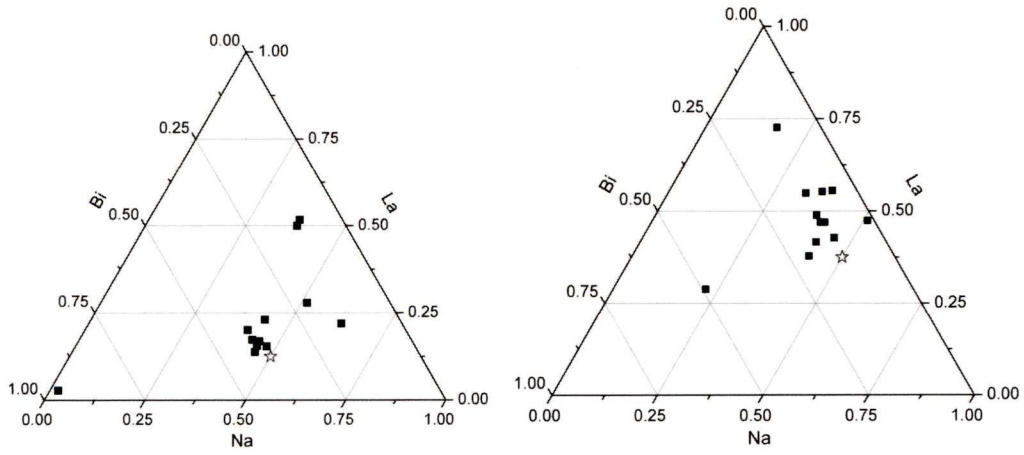

Figure 6-7 EDS of 12 crystallites of $NaLa_{1-x}Bi_xMgWO_6$ x = 0.75 (left) and x = 0.25 (right), stars show positions of the ideal composition.

The fact that a solid solution does not appear to form is quite interesting as usually in the perovskite structure the size and charge of the ions are the most important factors to consider and as already mentioned bismuth and lanthanum are approximately the same size and are both 3+. One thing the bismuth has that lanthanum does not is an active lone pair. It is this lone pair that makes bismuth so useful in ferroelectrics as the lone pair causes a displacement from the ideal in the structures resulting in an electric moment (see Seshadri[14]). It seems that the Na(LaBi)MgWO6 structure is unable to accommodate a LaBi mixture, this is despite the fact that the structure can accommodate the single elements in $NaLaMgWO_6$ and $NaBiMgWO_6$.

6.2.2.5 Solid solutions of LaNa LaK and LaLi

Bian investigated $La_{(2-x)/3}Na_x(Mg_{0.5}W_{0.5})O_3$ [15] and observed an orthorhombic phase for $0 \leq x < 0.3$ and the monoclinic phase between $0.3 \leq x \leq 0.5$. Arillo also looked at varying the Na:La ratio using $Na_{1-3x}La_{1+x}$ $(MgW)O_6$ (x=0, 0.11 and 0.22)[7]. Arillo also replaced the Na with K ($K_{1-3x}La_{1+x}$ $(MgW)O_6$)but the layered A site remained intact for x = 0 (i.e. $KLaMgWO_6$), when x is increased the excess La enters the K layers along with vacancies causing disorder. In $La_{(2-x)/3}Li_x(Mg_{0.5}W_{0.5})O_3$ Katsumata[16] found the Mg and W remain ordered on the B sites. On the two A sites the Li ions only occupy one of the possible sites, this site is only partially occupied by the Li and La ions, while the other A site is almost fully occupied by La ions. These investigations show that the A site of MgW double perovskites is able to accommodate more than just the NaLa pair. Change of the +1 ion away from Na is possible but the +3 ion appears to be more problematic unless in the case of Bi when all the La is replaced and material synthesized under high pressure.

6.2.2.6 Substitution of Mg^{2+} for Co^{2+} or Ni^{2+}

As attempts at substitution on the A site proved unsuccessful, substitution on the B site was attempted. Previously both $NaLaCoWO_6$ and $NaLaNiWO_6$ had been synthesised at ambient pressure by Arillo[10]. Co^{2+} and Ni^{2+} have six coordinate ionic radii of 74.5 pm and 69 pm respectively which compares to Mg^{2+} with an ionic radii of 72 pm. Synthesis of $NaBiCoWO_6$ and $NaBiNiWO_6$ was therefore attempted with XRD showing CoO or NiO respectively and Bi_2O_3 as well as the perovskite $P2_1/m$ phase.

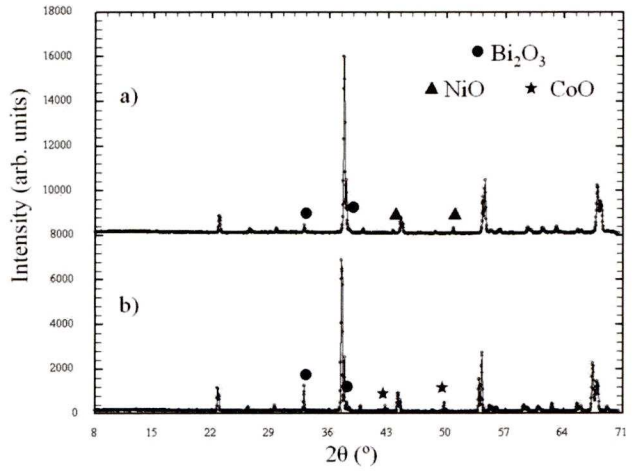

Figure 6-8 XRD of a) $NaBiNiWO_6$ and b) $NaBiCoWO_6$ with Bi_2O_3 and NiO/CoO impurities marked.

6.2.2.7 $NaBiMgMoO_6$

As replacing the 2+ B site ion proved unsuccessful, substitution of the W^{6+} for Mo^{6+} was attempted. Mo^{6+} and W^{6+} have comparable six coordinate ionic radii (59 pm versus 60 pm) and identical charges, so would be expected to form similar compounds. High pressure synthesis of $NaBiMgMoO_6$ was therefore attempted, resulting in Bi_2MoO_6 and $Bi_2Mo_3O_{12}$ as well as a perovskite phase.

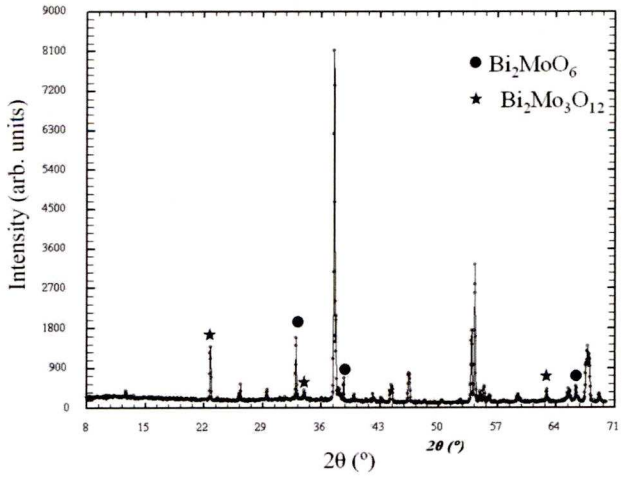

Figure 6-9 XRD of $NaBiMgMoO_6$ with peaks from Bi_2MoO_6 and $Bi_2Mo_3O_{12}$ marked.

6.2.3 Summary of $NaBiMgWO_6$ based work

Synthesis of a new A-site and B-site-ordered double perovskite with the formula $NaBiMgWO_6$ was attempted using high pressure methods. The resulting phase showed B-site order but not the expected A-site order as $NaBiMgWO_6$ was expected to be isostructural with $NaLaMgWO_6$. Other MgW double perovskites such as $NaLiMgWO_6$ [17] and $NaLnMgWO_6$ (Ln = Ce-Ho)[18, 19] show A-site and B-site order making the $NaBiMgWO_6$ material unusual. Although $NaLaMgWO_6$ can be synthesized, attempts at making a complete solid solution between $NaBiMgWO_6$ and $NaLaMgWO_6$ were unsuccessful. Further investigation into why $NaLaMgWO_6$ orders but $NaBiMgWO_6$ could be carried out using PDF methods to investigate the differences in the local structure of the La and Bi. However as the high pressure synthesis method affords so little sample multiple $NaBiMgWO_6$ samples would have to be added together.

6.3 Scandium manganese nickel based perovskites

Recently Singh[20] proposed a mechanism for obtaining polar behaviour in ferromagnetic Ni-Mn double perovskites such as $(La,Lu)_2MnNiO_6$. The proposed mechanism relies on the B site ions being fully ordered in a rock salt fashion, and to produce the polarization the A site ions must be displaced off their ideal sites in the perovskite structure without disrupting the B site ions. The role of the Lu^{3+} in Singh's study is to induce displacement due to its relatively small size compared to other lanthanides that form Ln_2MnNiO_6. In a similar study Kumar[21] predicts multiferroic behaviour in Y_2NiMnO_6 with Y^{3+} being used as the small A site ion that drives the polarization producing distortion. Sc^{3+} is smaller than both Lu^{3+} and Y^{3+} (0.87Å vs 0.98 Å, 1.019 Å respectively for VIII coordinate ionic radius Shannon[22]) so may induce a greater distortion. Parise [23] also noted that across the series $MCrO_3$

(M = La-Lu, In, Sc) that the smaller the M ion the greater the tilting of the octahedra reaching a maximum at In. The lower value of octahedral tilting for Sc was reasoned as Sc having a greater displacement from the centre of the A site cavity.

Few A site scandium perovskites are known with the two most common examples, $ScAlO_3$[26] and $ScCrO_3$[23] both requiring high pressure synthesis. Attempts by several groups to synthesize perovskite $ScMnO_3$ at high pressure have so far proved unsuccessful instead producing hexagonal $ScMnO_3$. [24] Our initial target composition was Sc_2MnNiO_6 as it was hoped that the Sc^{3+} would provide the distortion for ferroelectric properties while the Mn^{4+} and Ni^{2+} would provide the ferromagnetism.

6.3.1 Synthesis

Initial attempts at synthesizing Sc_2MnNiO_6 were carried out using traditional ceramic techniques at ambient pressure. However the results were hexagonal $ScMnO_3$, $NiMn_2O_4$ and unreacted oxides. High pressure methods were then employed using the equipment detailed in Chapter 2. Stoichiometric amounts of Sc_2O_3 (Alfa Aesar, 99.998%), MnO_2 (Sigma-Aldrich, 99.99%), NiO (Alfa Aesar, 99.998%), were ground together and reacted at a pressure of 6-7 GPa with a temperature of 1200°C for 30 minutes, then quenched to room temperature by turning the furnace power off. The pressure was then gradually released before the material could be extracted and analysed.

The composition of the materials obtained from the high pressure press as determined by EDS, for the initial Sc_2MnNiO_6 target the crystallites clustered into two groups. One of these groups has the Mn:Ni elemental ratio of 2/3:1/3 with the other group with less crystallites observed has the inverse ratio (Figure 6-10). It is

useful to note that $BiMn_{2/3}Ni_{1/3}O_3$ can be prepared at ambient pressure while Bi_2NiMnO_6 , $BiNiO_3$ and $BiMnO_3$ all require high pressure methods indicating that $Mn_{2/3}Ni_{1/3}$ helps to stabilize the distorted perovskite structure.

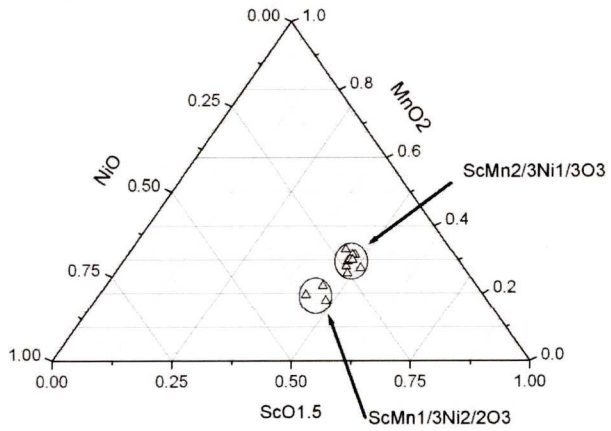

Figure 6-10 Shows the EDS for 10 crystallites for the nominal composition Sc_2MnNiO_6 (left) . The crystallites form two groups indicated on the figure.

Both groups of crystallites appeared to be slightly scandium deficient with an Sc:(Mn/Ni) ratio of 0.88:1 leading to the ratio Sc:Mn:Ni of 0.88:0.66:0.33. Using this ratio the composition would be $Sc_{0.88}Mn_{0.66}Ni_{0.33}O_{3-\delta}$ i.e. there would be A site vacancies, so if the metals are renormalized to 2 the target composition becomes $Sc_{0.94}Mn_{0.71}Ni_{0.35}O_3$. To make this composition ABX_3 0.06 of manganese will have to be present on the A site otherwise the A site will be deficient while the B site in excess. Manganese is known to be present on the A site of the high pressure perovskites $MnMO_3$ where M = Ge[51], Sn[52], Si[53], Ti[54] or V[55]. Belik also states that Mn is present on the A site in the B site ordered $(In_{1-y}Mn_y)MnO_3$ [56]. The EDS average composition for the second target composition gives $Sc_{0.94}Mn_{0.68}Ni_{0.36}O_{3-d}$ which compares to the $Sc_{0.94}Mn_{0.71}Ni_{0.35}O_3$ ideal. (**Figure 6-11**) .

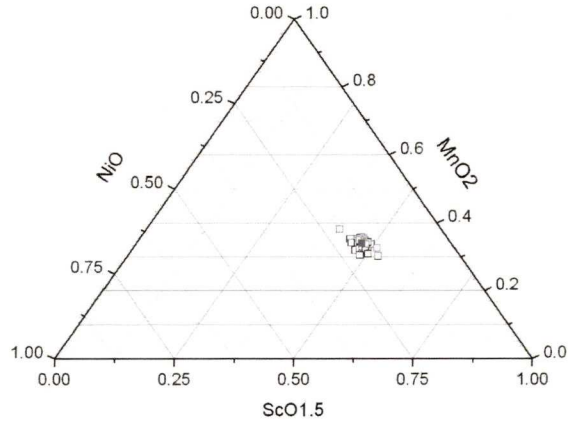

Figure 6-11 EDS for 30 crystallites of $(Sc_{0.94}Mn_{0.06})Mn_{0.65}Ni_{0.35}O_3$. Filled light grey square shows ideal point for $(Sc_{0.94}Mn_{0.06})Mn_{0.65}Ni_{0.35}O_3$ while dark grey square shows average value $(Sc_{0.94}Mn_{0.68}Ni_{0.36}O_3)$ for the 30 crystallites.

6.3.2 Characterization

6.3.2.1 Structure

(Figure 6-12) shows the structure of the phase that is the result of the refinements in Figure 6-14 .

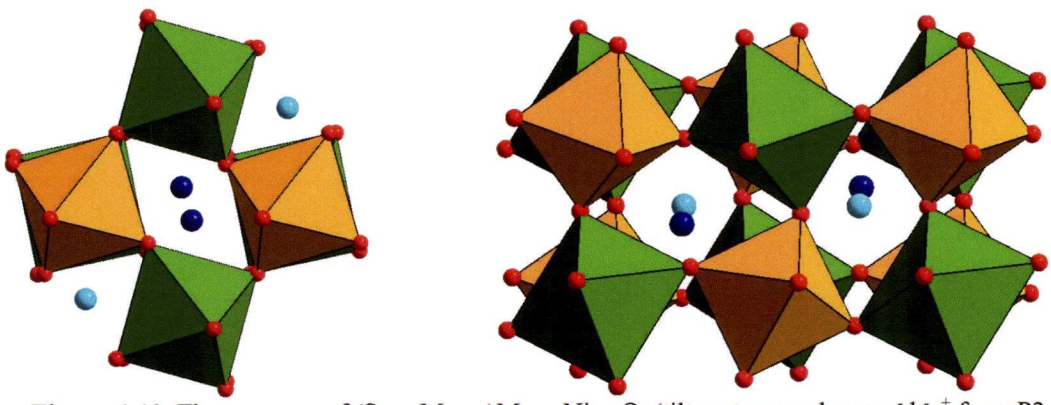

Figure 6-12 The structure of $(Sc_{0.94}Mn_{0.06})Mn_{0.65}Ni_{0.35}O_3$ (tilt system as shown $a^-b^-c^+$ from $P2_1/n$ from $P2_1/c$ tilt system $\mathbf{a^+ b^- c^-}$) showing the two types of A site (cyan spheres are pure Sc sites while dark blue spheres are Sc with Mn sites). Orange octahedra show pure Mn sites while green octahedra show mixed Mn/Ni sites. The small red spheres show the oxygen positions. On the left is the view is down the [001], on the right the view is along [110].

The initial refinement was carried out using structural parameters from $LuNiO_3$[25] in $P2_1/n$ however an improved fit was obtained when $P\bar{1}$ was used (Figure 6-13). This can most clearly be seen by comparing the $P2_1/n$ fit and the $P\bar{1}$ in Figure 6-13

particularly the –110 and the 021 & 200 peaks at 14.9 ° and 21.7 – 21.9 ° 2θ respectively which are much better fitted in the $P\bar{1}$ case.

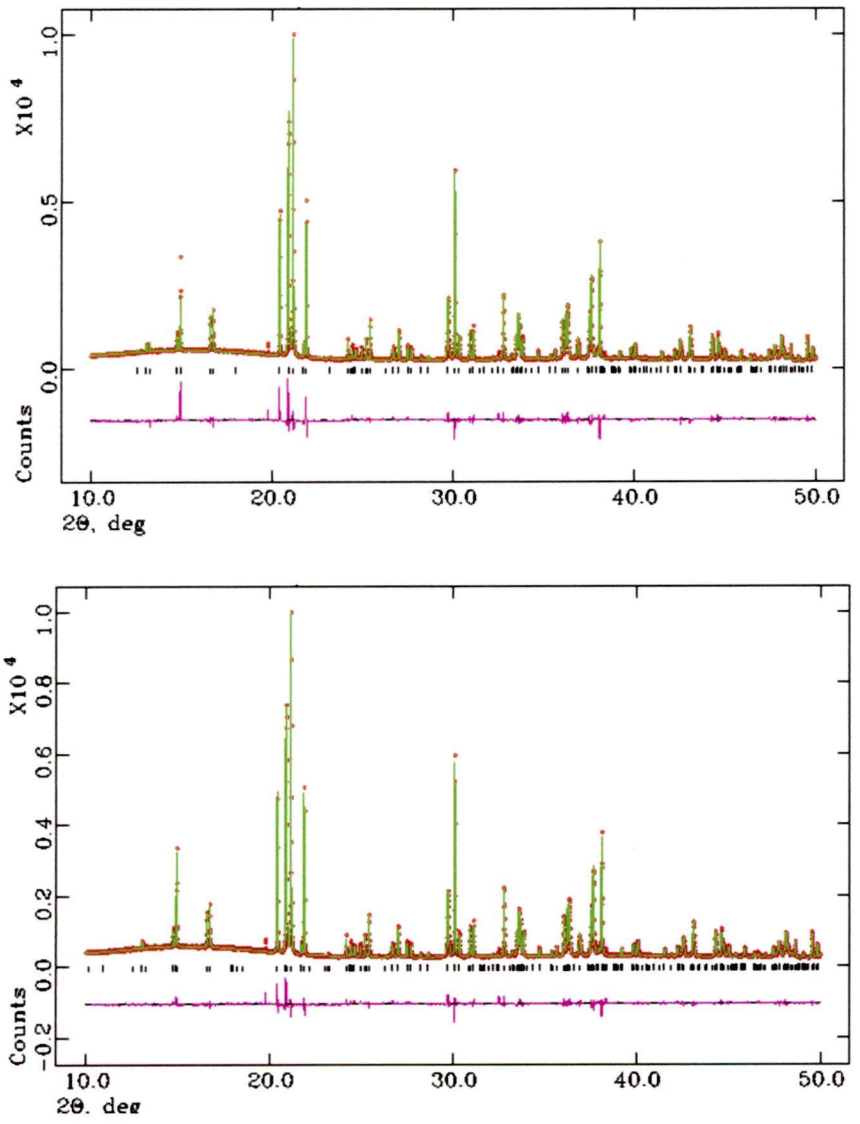

Figure 6-13 Rietveld refinement of $P2_1/n$ (top) Rwp = 0.0629 and **$P\bar{1}$** (bottom) Rwp = 0.0517 . In both cases λ = 0.949831Å. The red crosses are data points the green lines are the fits and the purple lines are the difference plots, the tick marks are given for allowed reflections.

On moving from $P2_1/n$ to $P\bar{1}$ the A site splits in two while both B sites also split giving a total of two A sites and four B sites in $P\bar{1}$. (Table 6-4) shows how the A site manganese is only found on one of the two possible A sites and that the nickel is present on only two of the possible four B sites.

To refine the site occupancies a combined XRD and PND refinement was carried out where lattice parameters were free to refine independently. The occupancies and fractional coordinates for the XRD and PND were refined together meaning values for these parameters were the same for both refinements.

When the B site ions are free to refine without constraints on overall composition or site occupancy the Mn occupancies on 1f and 1c refine to greater than 1 while the Ni occupancies on the same site remain close to 0. On the 1g and 1d site the Ni:Mn ratio refines to 70:30 and 66:26 (with vacancies) respectively with the A sites refining all Mn on one A site. As a result the Mn occupancies on the 1f and 1c were fixed at 1, the Mn and Ni occupancies on 1g and 1d were constrained so that both sites had an occupancy of 1 and overall Mn to Ni ratio of 2:1. The A sites were constrained to have an overall composition of $Sc_{0.94}Mn_{0.06}$.

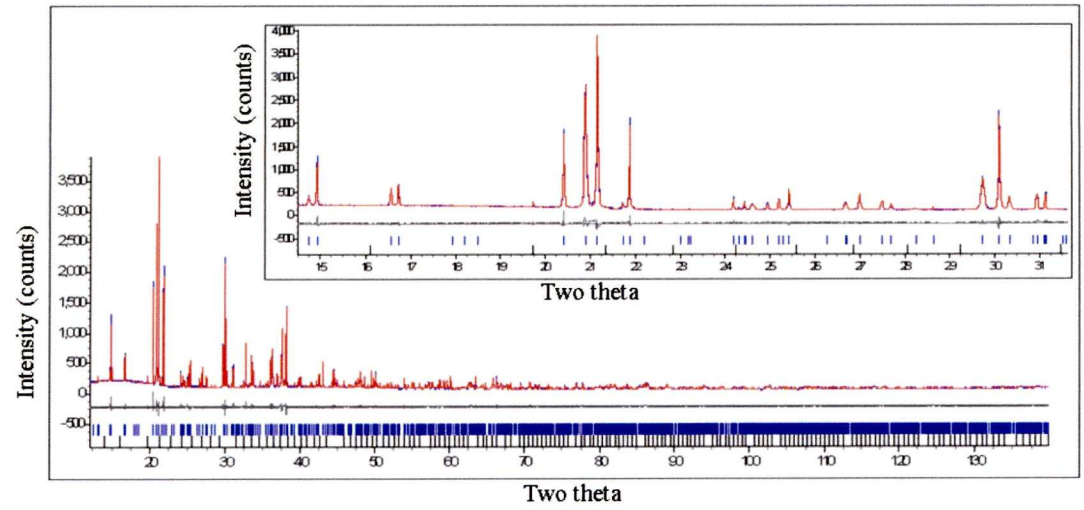

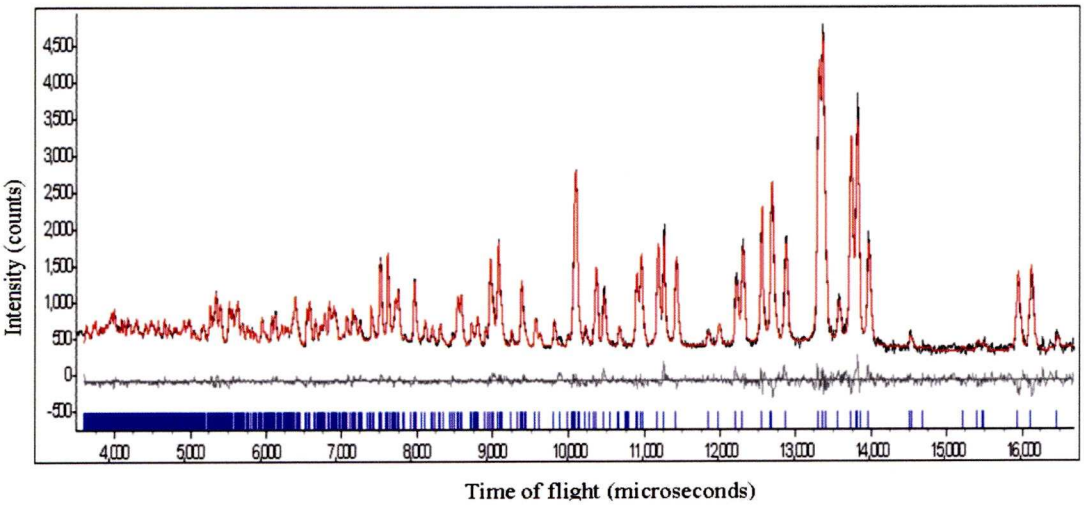

Figure 6-14 Combined refinement of XRD (upper) λ = 0.949831Å and neutron data(lower) (back scattering bank Polaris) Rwp = 0.05249. Blue tick marks are given for allowed reflections, in the XRD pattern the lower black tick marks refer to 0.01% of a Mn doped Sc_2O_3 impurity phase. Black dots are the data, red lines are the fits and the grey line is the difference plot.

Table 6-3 Lattice parameters for $(Sc_{0.94}Mn_{0.06})Mn_{0.65}Ni_{0.35}O_3$ at room temperature

Parameter	XRD	PND
a	5.0043(2) Å	5.0074(4) Å
b	5.3582(3) Å	5.3455(5) Å
c	7.4042(6) Å	7.4146(6) Å
α	90.00(15)°	90.01(4)°
β	89.02(4)°	89.13(1)°
γ	90.01(10)°	90.00(4)°

Table 6-4 Crystallographic data of $(Sc_{0.94}Mn_{0.06})Mn_{0.65}Ni_{0.35}O_3$ at room temperature.

Atom	Wyckoff position	Oxidation	x	y	z	B_{iso} (Å^2)	Occupancy
Sc1	2i	+3	0.9734(5)	0.9230(6)	0.7473(4)	0.35(4)	1.00(8)
Sc2	2i	+3	0.5230(5)	0.4263(6)	0.7582(4)	0.91(5)	0.88(8)
Mn6	2i	+2	0.5231(5)	0.4264(6)	0.7582(4)	0.91(5)	0.12(8)
Mn1	1f	+4	0.5	0	0.5	0.49(6)	1
Mn2	1c	+4	0	0.5	0	0.22(6)	1
Mn3	1g	+3	0	0.5	0.5	0.27(6)	0.307(10)
Mn4	1d	+3	0.5	0	0	0.27(6)	0.293(10)
Ni1	1g	+2	0	0.5	0.5	0.27(6)	0.693(10)
Ni2	1d	+2	0.5	0	0	0.27(6)	0.707(10)
O1	2i	-2	0.6832(9)	0.6740(9)	0.9462(6)	0.35(4)	1
O2	2i	-2	0.7990(9)	0.1886(10)	0.5715(6)	0.01(1)	1
O3	2i	-2	0.3739(10)	0.0550(1)	0.7386(7)	0.05(5)	1
O4	2i	-2	0.1454(10)	0.5657(1)	0.7560(7)	0.03(3)	1
O5	2i	-2	0.8325(9)	0.1906(10)	0.9337(6)	1.39(28)	1
O6	2i	-2	0.6888(10)	0.7085(10)	0.5830(6)	0.42(17)	1

The $P\bar{1}$ space group is described as $a^+ b^- c^-$ ($a^- b^- c^+$ when derived from $P2_1/c$) , where the rotations around the x, *y* and *z* axes have differing magnitude with x

rotations being in phase and y and z rotations being anti-phase. This relates to the monoclinic $P2_1/c$ tilting system $a^+ b^- b^-$ ($b^- b^- c^+$ non standard setting $P2_1/n$) The tilting angle of the octahedra can be defined as $\varphi = (180 - \Phi)/2$, where Φ is the Ni/Mn-O-Mn bond angle $\Phi = 180°$ for a cubic perovskite making $\varphi = 0$). From (Table 6-5), average tilt angles of 20.5(2)° down 1–10, 20.9(2)° down 110 and 22.1(2)° down 001 at RT are calculated, in good agreement with the expected $a^+ b^- c^-$ Glazer tilt system.

Table 6-5 bond lengths (Å), selected angles (°) and bond valence sums (BVS) of $(Sc_{0.94}Mn_{0.06})Mn_{0.65}Ni_{0.35}O_3$ at room temperature

Bond (X-O)	Lengths (Å)	BVS	Ideal BVS	Bond (B1-O-B2)	Angle (°)
Sc1/ - O	2.44(9)	Sc1 2.83	+3		
	2.22(1)				
	3.08(2)				
	2.67(5)				
	2.12(6)				
	3.55(4)				
	3.54(1)				
	2.13(4)				
	2.10(5)				
	3.59(0)				
	2.64(9)				
	2.10(1)				
Sc2/Mn6 - O	2.02(5)	Sc2 2.90	+3		
	2.84(1)	Mn 2.4	+2		
	3.59(6)				
	3.44(6)				
	2.14(4)				

	2.31(9) 3.20(6) 2.08(9) 2.39(0) 3.52(9) 2.46(8) 2.12(4)				
Mn1- O	1.88(9) 1.88(9) 1.88(9) 1.88(9) 1.92(6) 1.92(6)	Mn1 4.02	+4	Mn1-O3-Ni2/Mn4 Mn1-O2-Ni1/Mn3 Mn1-O6-Ni1/Mn3 Mn1-O3-Ni2/Mn4 Mn1-O2-Ni1/Mn3 Mn1-O6-Ni1/Mn3	139.2(3) 139.8(3) 137.2(3) 139.2(3) 139.8(3) 137.2(3)
Mn2 - O	1.92(5) 1.92(5) 1.88(5) 1.88(5) 1.97(2) 1.97(2)	Mn2 3.76	+4	Mn2-O1-Ni2/Mn4 Mn2-O4-Ni1/Mn3 Mn2-O5-Ni2/Mn4 Mn2-O1-Ni2/Mn4 Mn2-O4-Ni1/Mn3 Mn2-O5-Ni2/Mn4	140.3(3) 132.4(2) 137.5(3)
Ni1/Mn3 - O	2.00(6) 2.00(6) 2.07(5) 2.07(5) 2.01(2) 2.01(2)	Ni1 2.17 Mn3 2.89	+2 +3	Ni1/Mn3-O2-Mn1 Ni1/Mn3-O4-Mn2 Ni1/Mn3-O6-Mn1 Ni1/Mn3-O2-Mn1 Ni1/Mn3-O4-Mn2 Ni1/Mn3-O6-Mn1	139.8(3) 132.4(2) 137.2(3) 139.8(3) 132.4(2) 137.2(3)
Ni2/Mn4 - O	2.00(8) 2.06(9) 2.00(4) 2.00(8) 2.06(9) 2.00(4)	Ni2 2.20 Mn4 2.93	+2 +4	Ni2/Mn4-O1-Mn2 Ni2/Mn4-O3-Mn1 Ni2/mn4-O5-Mn2 Ni2/Mn4-O1-Mn2 Ni2/Mn4-O3-Mn1 Ni2/mn4-O5-Mn2	140.3(3) 139.2(3) 137.5(3) 140.3(3) 139.2(3) 137.5(3)

The Glazer tilt angles signal a strong deviation from the cubic perovskite structure that is confirmed by four Sc – O bonds for each site being longer than 3 Å. Figure 6-15 shows the Sc coordination environments of both Sc1 and Sc2 with the dark gray spheres showing the calculated centre of the oxygen polyhedron. The Sc1 site is displaced by 0.540(2) Å along the vectors ± $\begin{pmatrix} 3 \\ 10 \\ 0 \end{pmatrix}$ and the Sc2Mn6 site is displaced by 0.515(6) along the vectors ± $\begin{pmatrix} -2 \\ 9 \\ -1 \end{pmatrix}$.

This compares to $ScCrO_3$[23] where the displacement is 0.503(1) Å along the vectors ± $\begin{pmatrix} -2 \\ 9 \\ 0 \end{pmatrix}$ and $ScAlO_3$ investigated by Ross[26] where the displacement is 0.452(1) Å along the vectors ± $\begin{pmatrix} -2 \\ 8 \\ 0 \end{pmatrix}$.

These displacements show that the displacement of both the Sc1 and Sc2 sites is predominantly along the b axis but that the Sc2 also has opposing displacements in a and c where Sc1 only has an a displacement in same direction as b. The magnitude of the displacements show Sc2Mn6 is displaced by 0.025 Å less than the Sc1 site. Although the difference is relatively small (5% of the total displacement) the lower displacement from ideal of the Sc2 site means it is the Sc2 site that has the Mn rather than the more displaced Sc1 site.

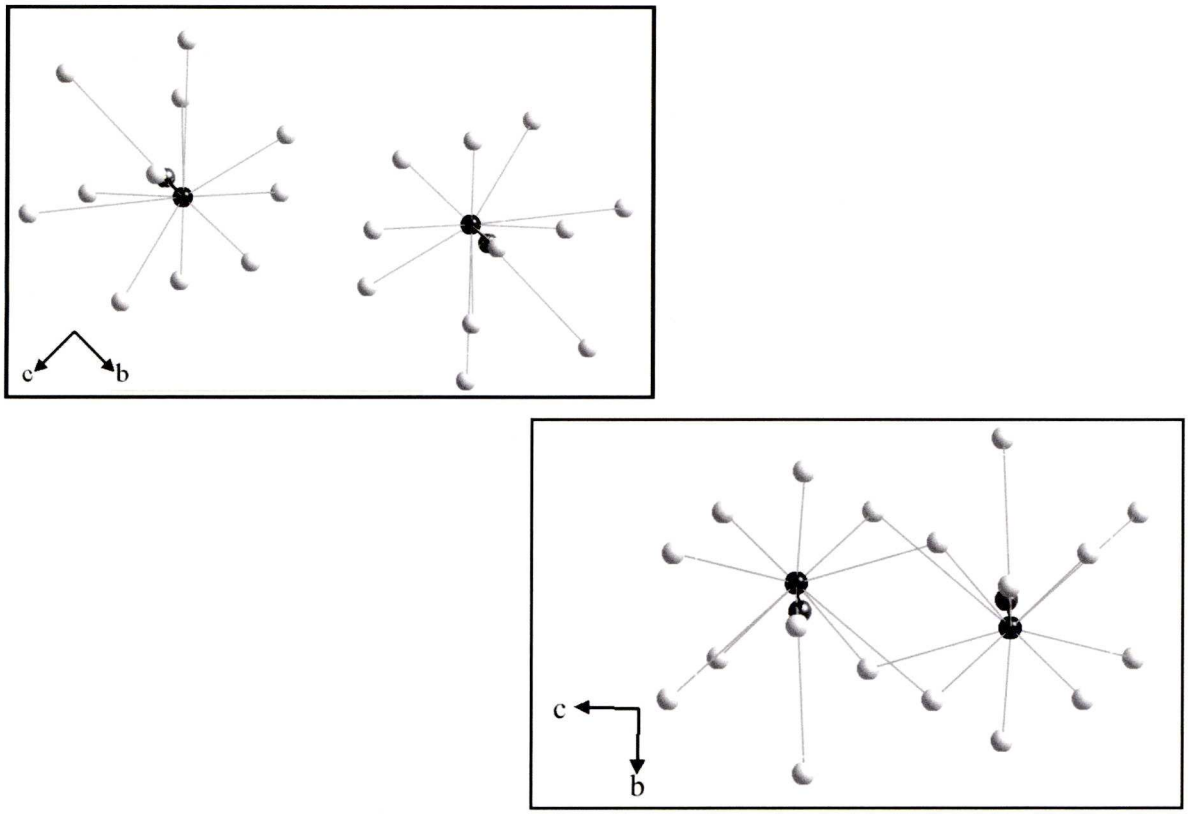

Figure 6-15 A site environments for the Sc ions in the unit cell, Sc1 top left and Sc2 (note Mn6 also on site) bottom right. Light grey spheres are oxygen, black spheres are Sc, dark grey spheres are the calculated centres of the oxygen coordination sphere, black arrows are the displacement vectors.

Another method of investigating the distortion away from ideal is to use the Goldschmidt tolerance factor described in chapter 1. For $(Sc_{0.94}Mn_{0.06})Mn_{0.65}Ni_{0.35}O_3$ a tolerance factor of 0.81 is calculated which is below the suggested stability limit for perovskites of $t \approx 0.85$ [27]. Having such a low tolerance factor supports the observation that $(Sc_{0.94}Mn_{0.06})Mn_{0.65}Ni_{0.35}O_3$ requires high pressures to form [28].

Other perovskites that have been reported with the tilt scheme $a^+ b^- c^-$ Ca_2LaRuO_6 [29] and Sr_2YTaO_6 [30, 31] although both these compounds have also been described as $P2_1/n$ tilt scheme $b^- b^- c^+$ [32-34]. The tolerance factors for these two compounds are 0.85 and 0.91 respectively.

The relatively small difference between the tilts of 1-10 and 110 (0.44°) indicate that deviation from the monoclinic structure where the tilts would be equal is minor. The driving force behind this deviation appears to be the preferential ordering of the manganese on one of the A sites in the $P\bar{1}$ structure, something that is not possible in the $P2_1/n$ structure as there is only one A site. When the 0.06 of Mn is free to refine the coordinates relative to the Sc on that A site are shown in Table 6-6

Table 6-6 Comparison of mixed A site coordinates when Mn is free to refine unconstrained to Sc.

Sc			**Mn**		
	Value	**error**		**Value**	**error**
x	0.52381	0.00065	**x**	0.52242	0.00163
y	0.42603	0.00070	**y**	0.42654	0.00146
z	0.75865	0.00041	**z**	0.75319	0.00154

As the B sites also split from 2 to 4 if the B site environment was the driving force behind lowering the symmetry the four B sites should alter substantially from the original 2. However (Table 6-4) shows 2 sites remain fully occupied with Mn^{4+} while 2 sites show Mn^{3+}/Ni^{2+} in an equal ratio demonstrating that the ordering on the B sites is the same as that for $P2_1/n$.

6.3.2.2 Electron diffraction

Dr Zhongling Xu carried out electron diffraction with an example of the results shown in Figure 6-16.

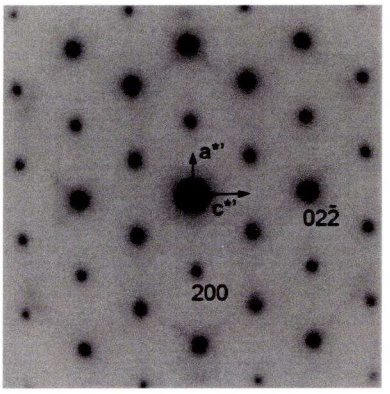

Figure 6-16 Electron diffraction for $Sc_{0.94}Mn_{0.71}Ni_{0.35}O_3$ using $P2_1/n$ setting

Analysis of the electron diffraction gives possible space groups of $P2_1/c$ ($P2_1/n$) P2/c (P2/n) or Pc (Pn). It appears that as the deviation from monoclinic to triclinic is so small the electron diffraction is unable to resolve it giving the higher symmetry $P2_1/n$ solution. Twinning is also likely to be problematic which may cause higher symmetry to be seen by electron diffraction.

6.3.2.3 Variable Temperature XRD experiments

Highly distorted perovskite phases often exhibit higher symmetry at elevated temperatures and occasionally these higher symmetry phases can be trapped. High pressure perovskite phases however have an added complication as many are metastable so decompose on heating. A preliminary set of variable temperature experiments were carried out in the laboratory with the results appearing to show the material as stable to 800 °C. At 1100 °C the material irreversibly decomposes into NiO Sc_2O_3 and hexagonal $ScMnO_3$ but measurements at intermediate temperatures showed no evidence of higher symmetry.

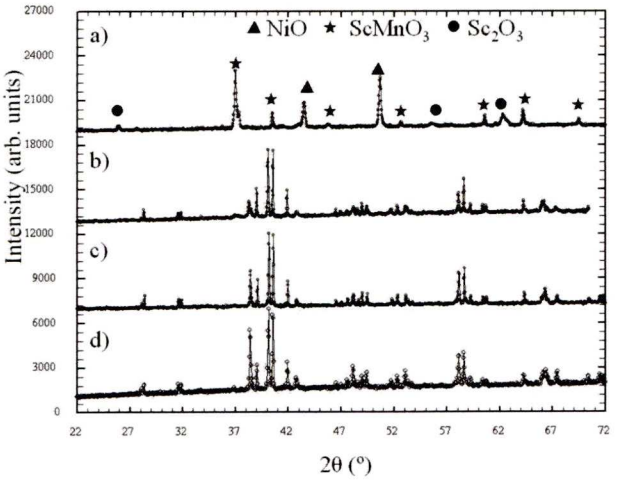

Figure 6-17 Lab variable temperature for $Sc_{0.94}Mn_{0.71}Ni_{0.35}O_3$ at RT (d) and post annealing at 400 °C (c) 800 °C (b) 1100 °C (a). The peaks from the various decomposition products are marked for the post 1100 °C XRD.

A variable temperature in-situ experiment was carried out at station I11 at the Diamond light source to test for higher symmetry phases at elevated temperatures. At elevated temperatures peaks broadened and show splitting raising the possibility that other, possibly higher symmetry, phases are forming when the material is heated. However attempts at fitting higher symmetry phases to the data have so far proved unsuccessful.

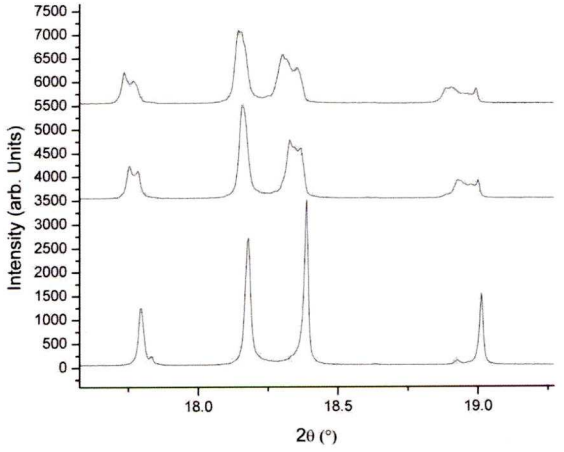

Figure 6-18 Diamond Ill in situ XRD λ = 0.826394 Å at 600 °C(top) 400 °C (middle) RT (bottom).

6.3.2.4 Single crystal diffraction measurements

As the material for a standard run forms as small black shiny crystals an attempt was made at growing a single crystal. The standard ambient pressure method involves melting the constituent oxides and cooling very slowly typically 0.1° per minute. To replicate this in the press the premix was heated up to 1500 °C held, for 30 mins and cooled at 0.01 % power per second (the slowest possible for the press). The resulting material had formed irregular columns of crystals reminiscent of the basalt columns of Giant's causeway. One of these columns was broken off and cut into a smaller piece for a single crystal experiment at station I19 at the Diamond light source.

Single crystal studies are complicated by the low symmetry and the small degree of splitting and also the tendency for perovskites to twin and undergo phase transitions. Analysis by Dr John Basca appears to show 3 obvious twin domains (possibly 4) with many of the spots being very close together. As a result single crystal information is of limited use. To ensure the material was the same structure as the bulk the columns were ground and a powder XRD was taken. Figure 6-19 shows that the single crystal source material while having a greater amount of impurities has the overwhelming majority triclinic perovskite structure of the bulk.

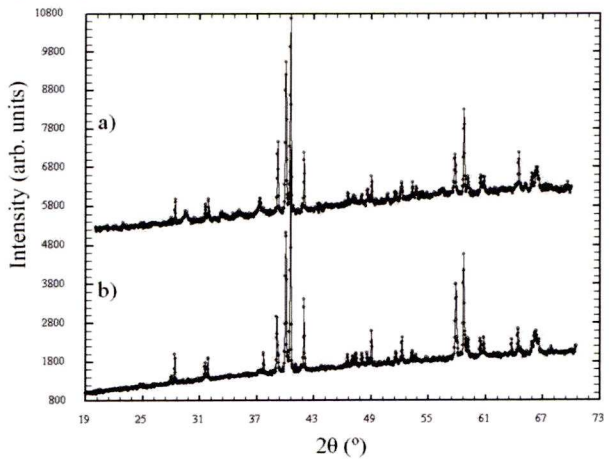

Figure 6-19 XRD of the ground columns used for single crystal experiment (a) compared to standard bulk material (b). Comparison of the XRD patterns shows that the columns were $Sc_{0.94}Mn_{0.71}Ni_{0.35}O_3$.

6.3.2.5 Magnetic properties

When the inverse susceptibility (Figure 6-20) is fitted between 170 and 280 K the values for the Curie Weiss law are C = 2.11(6)emuK/mole (μeff = 4.11 μB/f.u.) and θ = -95(4) K these compare to the calculated values for C of;

- 2.07 emuK/mole (μ_{eff} = 4.07 μ_B/f.u.) for all nickel being +2 and the manganese being half in the +3 oxidation state and half in the +4 oxidation state.
- 2.77 emuK/mole (μ_{eff}= 4.71 μ_B/f.u.) for all nickel and manganese being +3
- 2.09 emuK/mole (μ_{eff} = 4.09 μ_B/f.u.) for the formula $(Sc^{3+}_{0.94}Mn^{2+}_{0.06})(Mn^{4+}_{0.41}\ Mn^{3+}_{0.09})\ (Mn^{3+}_{0.15}Ni^{2+}_{0.35})O_3$.

The magnetism is therefore consistent with the distribution of oxidation states obtained via bond valence sums (i.e. $(Sc^{3+}_{0.94}Mn^{2+}_{0.06})(Mn^{4+}_{0.41}\ Mn^{3+}_{0.09})\ (Mn^{3+}_{0.15}Ni^{2+}_{0.35})O_3$). The negative Weiss temperature indicates the presence of dominant antiferromagnetic interactions with the ZFC/FC giving a Neel temperature of 15 K. However the FC and ZFC diverge below 15 K normally associated with weak ferromagnetism or spin glass behaviour.

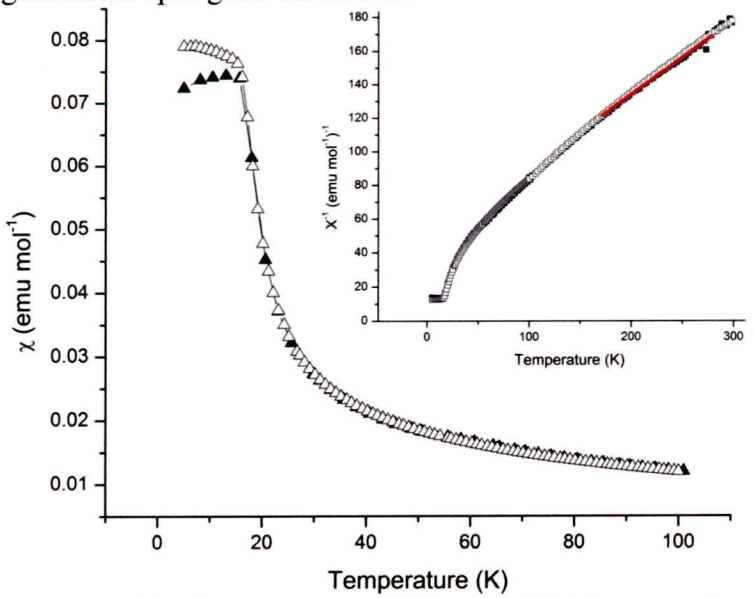

Figure 6-20 zero field cooled (ZFC empty squares) field cooled (FC filled squares) measurement with 100 Oe measuring field. Inset shows inverse susceptibility with Curie Weiss behaviour above 50 K . Fit in red between 170 and 280 K with R^2 = 0.995 C=2.11(6) emuK/mole θ = -95(4)K.

The hysteresis at 5 K (Figure 6-21) shows a small coercive field but the loop does not saturate.

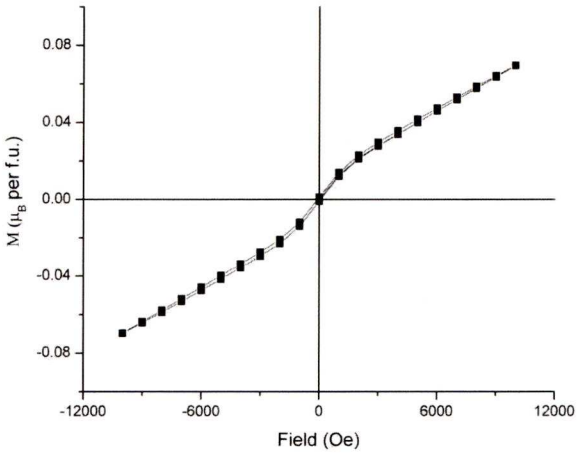

Figure 6-21 Hystersis loop at 5 K for $Sc_{0.94}Mn_{0.71}Ni_{0.35}O_3$ with coercive field of 72Oe and remnant magnetisation of 0.001 μ_B per formula unit.

6.3.3 $ScLnMnNiO_6$ Ln= Lu, Ho

In Singh's study the compound under investigation $(LaLu)MnNiO_6$ had two different elements on the A site aiding the ferroelectric distortion. To gradually increase the size difference between the two A site ions one Sc^{3+} was replaced by Lu^{3+} and then by Ho^{3+}.

$ScLuMnNiO_6$ was synthesized 1300 °C at 6 GPa. The EDS shows that the material has formed a 1:1 Sc:Lu perovskite with a B site ratio 1:0.8 Mn:Ni. The deficiency in the Ni may be due to either a true deficiency in Ni or a fitting problem as the Ni K (7.48 keV) and the Lu L (7.64 keV) peaks overlap. This causes more of a problem for the Ni fitting as the Ni K is the only major peak used while the Lu has the Lu M

(1.59 keV) peak also fitting. As no Ni rich impurities were found and the XRD shows clean $P2_1/n$ the fitting issue seems most probable.

To further expand the size mismatch on the A site $ScHoMnNiO_6$ was synthesized again using high pressure (6 GPa 1300 °C) and again a single phase double perovskite was formed.

Magnetic measurements were made on both $ScLuMnNiO_6$ and $ScHoMnNiO_6$ with the results given in Figure 6-22, Figure 6-23, Figure 6-24 and Figure 6 25

6.3.3.1 $ScLuMnNiO_6$

When the inverse susceptibility (Figure 6-22) is fitted between 170 and 280 K the values for the Curie Weiss law are C = 3.565(6) emuK/mole (μ_{eff} = 5.34 μ_B/f.u.) and θ = 0.06 (40) K these compare to the calculated values for C of;

- 2.87 emuK/mole (μ_{eff} = 4.79 μ_B/f.u.) for all nickel being +2 and the manganese being in the +4 oxidation state.

- 4.85 emuK/mole (μ_{eff} = 6.22 μ_B/f.u.) for all nickel and manganese being +3

- 3.86 emuK/mole (μ_{eff} = 5.56 μ_B/f.u.) for half nickel 2+ half nickel 3+ and half manganese being 4+ and half 3+

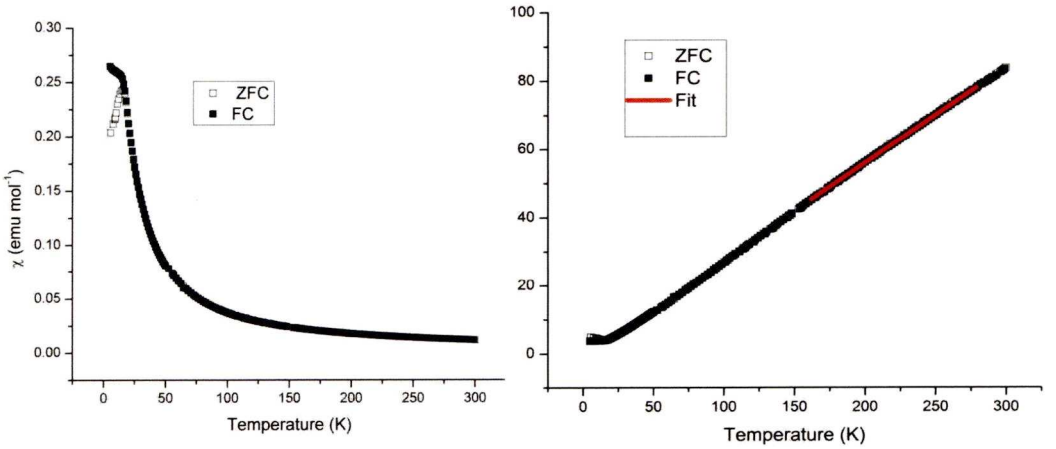

Figure 6-22 Magnetic measurements of $ScLuMnNiO_6$ χ versus T (left) and inverse χ versus T (right) with ZFC shown by empty squares and FC by filled squares and fit shown by red line ($R^2 = 0.9998$ C = 3.565(6) emuK/mole (μ_{eff} = 5.34 μ_B/f.u.) and θ = 0.06 (40) K). Measuring field 100 Oe.

The hysteresis at 5 K Figure 6-23 shows a small coercive field but the loop does not saturate.

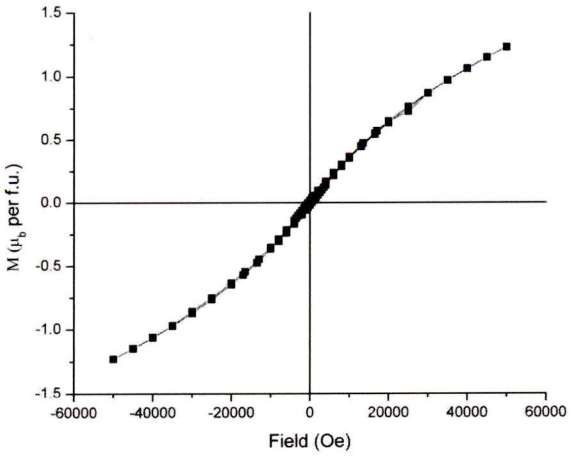

Figure 6-23 Hystersis loop for $ScLuMnNiO_6$ with coercive field of 460 Oe and remnant magnetisation of 0.02 μ_B per formula unit.

6.3.3.2 $ScHoMnNiO_6$

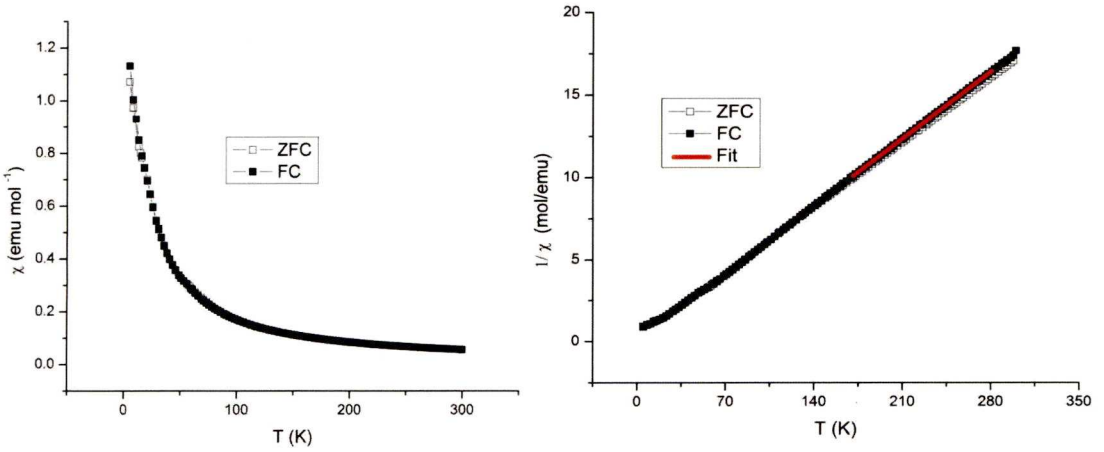

Figure 6-24 Magnetic measurements of $ScHoMnNiO_6$ χ versus T (left) and inverse χ versus T (right) with ZFC shown by empty squares and FC by filled squares fit shown by red line ($R^2 = 0.9999$ C = 17.31(2) emuK/mole (μ_{eff} = 11.77 μ_B/f.u.) and θ = -3.5(3) K). Measuring field 100 Oe.

When the inverse susceptibility is fitted between 170 and 280 K the values for the Curie Weiss law are C = 17.31(2) emuK/mole (μ_{eff} = 11.77 μ_B/f.u.) and θ = -3.5(3) K these compare to the calculated values for C of;

- 16.92 emuK/mole (μ_{eff} = 11.62 μ_B/f.u.) for all nickel being +2 and the manganese being in the +4 oxidation state.

- 18.91 emuK/mole (μ_{eff} = 12.30 μ_B/f.u.) for all nickel and manganese being +3

- 17.92 emuK/mole (μ_{eff} = 11.97 μ_B/f.u.) for half nickel 2+ half nickel 3+ and half manganese being 4+ and half 3+

The experimentally observed value for C = 17.31 emuK/mole (μ_{eff} = 11.77 μ_B/f.u.) which is between the all Mn 4+ all Ni 2+ and the half Mn 4+ half 3+ half Ni 2+ half Ni 3+ case. A fourth case is then 80% Mn 4+ and Ni 2+ , 20% Mn 3+ and Ni 3+

which would give a values of C = 17.31 emuK/mole (μ_{eff} = 11.77 μ_B/f.u.) showing that the 80:20 Mn4+:Mn3+ is the closest to the experimentally observed.

The large increase in the magnetic moment compare to the ScLu A site case is due to the presence of the highly magnetic Ho^{3+} ion in the formula that if in an isolated complex would have a moment of 10.6 μ_B.

The hysteresis at 5 K shows a small coercive field with the loop tending towards a saturation of 6 μ_B above 5T (Figure 6-25).

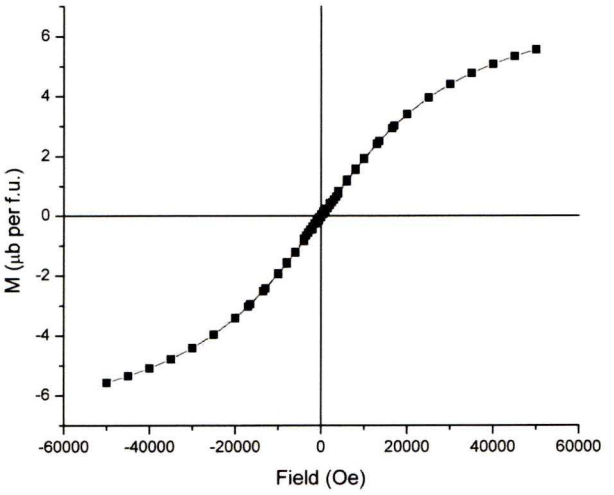

Figure 6-25 Magnetic Hysteresis loop coercive field 220 Oe remnant magnetization 0.04 μ_B per fu

6.3.4 Summary of Scandium manganese nickel based perovskites

$(Sc_{0.94}Mn_{0.06})Mn_{0.65}Ni_{0.35}O_3$ can be prepared using a high pressure high temperature route. The material crystallizes in $P\bar{1}$ with Glazer tilting $a^+ b^- c^-$. Susceptibility measurements show $(Sc_{0.94}Mn_{0.06})Mn_{0.65}Ni_{0.35}O_3$ to be an antiferromagnet with a Neel temperature of 15 K however the ZFC/FC divergence indicates the true story is more complex.. The fitted paramagnetic moment (μ_{eff} = 4.11 μ_B/f.u.) closely corresponds to the spin-only value (μ_{eff} = 4.09 μ_B/f.u.) for $(Sc^{3+}_{0.94}Mn^{2+}_{0.06})(Mn^{4+}_{0.41}Mn^{3+}_{0.09})(Mn^{3+}_{0.15}Ni^{2+}_{0.35})O_3$.

$ScLuMnNiO_6$ and $ScHoMnNiO_6$ can also be prepared using a high pressure high temperature route. Both theses structures appear to be in the more common $P2_1/n$ space group. Magnetic measurements on these materials show similar ZFC/FC diverange as the $(Sc_{0.94}Mn_{0.06})Mn_{0.65}Ni_{0.35}O_3$ with good fits to Curie Weiss at higher temperatures. The hysterysis loop for $ScHoMnNiO_6$ also appears to be saturating at 6T while both $ScLuMnNiO_6$ and $(Sc_{0.94}Mn_{0.06})Mn_{0.65}Ni_{0.35}O_3$ do not saturate at all. As $ScHoMnNiO_6$ can be synthesised attempts with larger lanthanides such as Eu, Nd and possibly even La attempted to see how great a size mismatch on the a site can be tolerated.

6.4 Bi_2FeCrO_6

Theorectical work by Spaldin papers[1, 2] on the compound $Bi_2FeCr_2O_6$ predicted $Bi_2FeCr_2O_6$ would crystallize in the space group R3. The predicted R3 structure is similar to the observed R3c structure of $BiFeO_3$[35] except that every other Fe^{3+} along the [111] direction is replaced with Cr^{3+}. In the paper this alternation of Fe^{3+} and Cr^{3+} ions gives rise to ferrimagnetic order while the displacement of the Bi^{3+} generates a ferroelectric moment allowing the theoretical compound to be a multiferroic. Ordering is described by the Setter Cross rules [36] but Fe and Cr will only show a weak tendency to order as they are of the same charge and are similar in size. High pressure has previously been shown to aid ordering in perovskite materials such as $CaFeTi_2O_6$, $CaFe_3Ti_4O_{12}$ and $Tl_2Ba_2CuO_{6+d}$[28, 37]. Hazen[28, 37] notes it appears that pressure induces both cation and anion ordering in the perovskite structure.

6.4.1 Synthesis

Stoichiometric amounts of Bi_2O_3, Fe_2O_3 and Cr_2O_3 were ground together before loading into the octahedra assembly for the high pressure experiment. Many different cooling regimes were tried in a failed attempt to induce the Fe^{3+} and Cr^{3+} ions to order.

Table 6-7 Summary of firing regimes at 6 GPa in an attempt to induce B site ordering in Bi_2FeCrO_6.

TARGET TEMPERATURE (°C)	DWELL TIME (HOURS)	COOLING RATE
1100	0.5	Not set
1100	0.5	5% per 30 mins
1100	0.75	QUENCH
1100 then....	0.5	Cool to 700 °C not set
.....700	12	Cool to 25 °C not set
.....700	3	0.01 power% per second
.....700	0.75	QUENCH
.....700	3	0.01 power% per second

6.4.2 Characterisation

6.4.2.1 Structure

The diffraction patterns for the samples produced showed that the compound crystallizes in the R3c space group indicating the Fe^{3+} and Cr^{3+} are randomly distributed with respect to one another. High quality powder X-ray diffraction (XRD) data were collected on station 9.1 of the Synchrotron Radiation Source (SRS) using $\lambda = 0.9587$ Å (Figure 6-27); neutron powder diffraction (PND) were collected on the GEM station diffractometer at ISIS (Figure 6-28). Both data sets could be refined in the R3c space group with the XRD lattice parameters given in Table 6-8 . These lattice parameters were then used in the neutron refinement as neutron diffraction is more sensitive to oxygen positions and possible B site order. If it were present B site order would be clearly seen in neutron diffraction as the scattering

lengths of Fe^{3+} and Cr^{3+} differ significantly (9.45 fm vs 3.64 fm). It is interesting to note that some of the samples displayed small structural peaks when measured immediately after extraction from the press, which disappeared after annealing at 200 °C for 1 hour. It is thought that these peaks were due to residual strain in the sample as a consequence of the high pressure method used. Residual strain has been observed in $FeSiO_3$ (allowing the C2/c phase to be observed at ambient pressure) and for Sr_2CuO_{3+d}[38] and La_2CuO_4[39] [40](where strain is released by annealing at low temperatures).

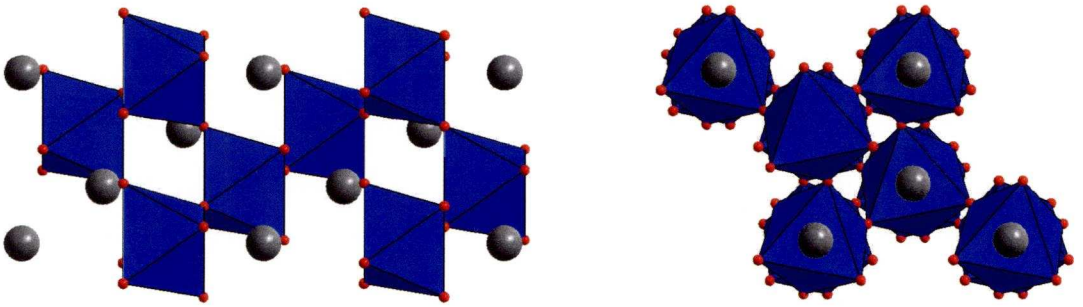

Figure 6-26 Structure of $Bi(Fe_{1/2}Cr_{1/2})O_3$ down the hexagonal a axis (left) and c axis (right). light grey spheres Bi red spheres O and blue octahedra showing lack of B site order.

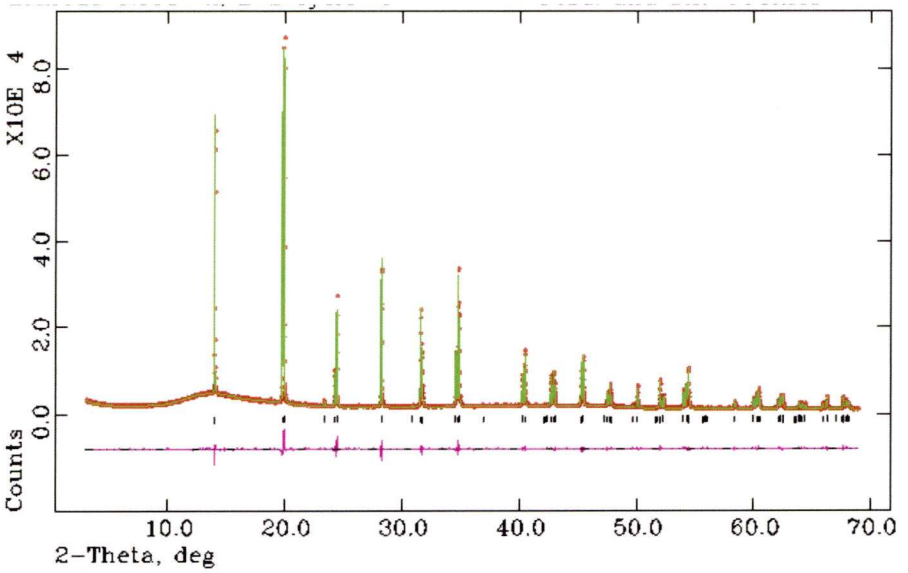

Figure 6-27 Refinement of $Bi(Fe_{1/2}Cr_{1/2})O_3$ at room temperature from XRD SRS 9.1 λ=0.958685 χ^2 = 2.546 R_{wp} = 0.0447. The red crosses are data points the green line is the fit and the purple line the difference plot with the black tick marks showing the allowed reflections.

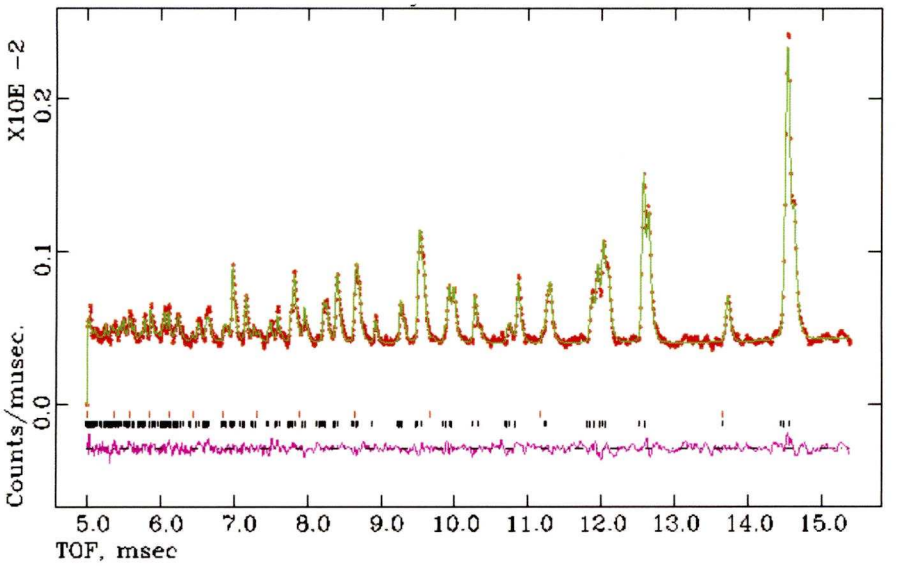

Figure 6-28 Refinement of $Bi(Fe_{1/2}Cr_{1/2})O_3$ at room temperature from PND GEM backscattered back $\chi^2 = 2.031$ $R_{wp} = 0.0429$. The red crosses are data points the green line is the fit and the purple line the difference plot with the black tick marks showing the allowed reflections, the upper red tick marks indicate the positions of peaks due to the vanadium can.

Table 6-8 Lattice parameters for $Bi(Fe_{1/2}Cr_{1/2})O_3$ at room temperature from XRD refinement

Parameter	Hex	Rho
a	5.5437(1) Å	5.5760(1) Å
b	5.5437(1) Å	5.5760(1) Å
c	13.6980(4) Å	5.5760(1) Å
α	90 °	59.6(2) °
β	90 °	59.6(2) °
γ	120 °	59.6(2) °

Table 6-9 Crystallographic data of $Bi(Fe_{1/2}Cr_{1/2}O_3$ in the hexagonal setting at room temperature

Atom	Wyckoff position	Oxidation	x	y	z	U_{iso} (Å^2)	Occupancy
Bi1	6a	+3	0	0	0	0.0195(1)	1
Fe1	6a	+3	0	0	0.2222(10)	0.0030(4)	1
Cr1	6a	+3	0	0	0.2222(10)	0.0030(4)	1
O	18b	-2	0.4450(10)	0.0148(11)	0.9572(3)	0.0088(14)	1

Table 6-10 Bond lengths (Å), selected angles (°) and bond valence sums (BVS) of $Bi(Fe_{1/2}Cr_{1/2}O_3$ at room temperature

Bond (X-O)	Length (Å)	BVS	Ideal BVS	Bond (B1-O-B2)	Angle (°)
Bi - O	3x 2.504(5)	Bi 2.709	+3	N/a	N/a
Bi - O	3x 2.300(5)	Bi 2.709	+3	N/a	N/a
Bi - O	3x 3.167(5)	Bi 2.709	+3	N/a	N/a
Bi -O	3x 3.345(5)	Bi 2.709	+3	N/a	N/a
Fe- O	3x 2.067(5)	Fe 3.09	+3	Fe1-O4-Fe1 Fe1-O4-Cr1	156.77(23) 156.77(23)
Fe - O	3x 1.951(5)	Fe 3.09	+3	Fe1-O4-Fe1 Fe1-O4-Cr1	156.77(23) 156.77(23)
Cr - O	3x 2.067(5)	Cr 2.811	+3	Cr1-O4-Cr1 Cr1-O4-Fe1	156.77(23) 156.77(23)
Cr - O	3x 1.951(5)	Cr 2.811	+3	Cr1-O4-Cr1 Cr1-O4-Fe1	156.77(23) 156.77(23)

Bond valence sums (Table 6-10) show a slight over bonding of Fe^{3+} and a slight under-bonding of Cr^{3+} is consistent with the difference in ionic radi (Fe^{3+} 64.5 pm Cr^{3+} 61.5 pm) and a disordered site. The Bi is displaced by 0.56 Å along the hexagonal c axis compared to the ideal position of the perovskite structure. The displaced Bi causes a displacement of the Fe and Cr ions (0.22 Å) again along the hexagonal c axis compared to the ideal position at the centre of the octahedra. These displacements lead to a static polarization of 63 $\mu C/cm^2$ calculated using the ionic charge model with the direction of the polarisation being along the hexagonal 001.

Electron diffraction was carried out by Dr Mathieu Allix and supports the structural model used for the XRD and PND.

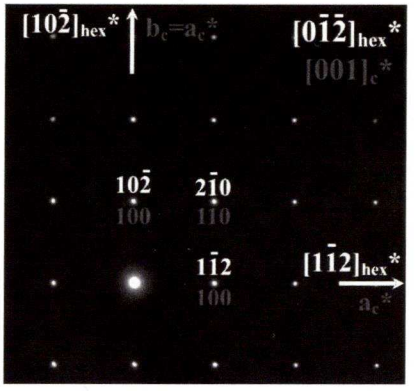

Figure 6-29 TEM of Bi_2FeCrO_6 indexing of both the hexagonal setting and the pseudocubic.

Elemental analysis was carried out using energy dispersive spectroscopy (EDS). The results of the EDS showed that the ratio of the metal ions was 1:0.5:0.5 (Bi:Fe:Cr) indicating that the target composition had been made.

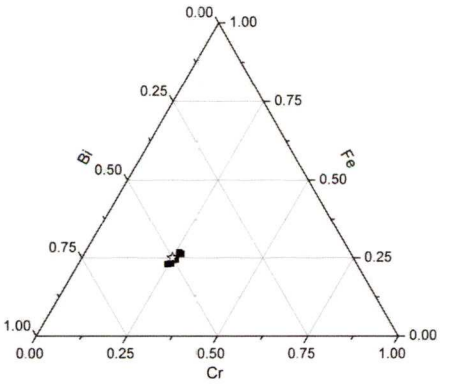

Figure 6-30 EDS of Bi_2FeCrO_6 star shows ideal composition.

6.4.2.2 Variable temperature

Variable temperature experiments show that $Bi_2FeCr_2O_6$ is stable in air up to 400 °C with no structural change. Above 400 °C the sample begins to decompose with a

γ Bi_2O_3 phase being present (Figure 6-31). There is no evidence of a phase transition in the main perovskite phase up to 500 °C.

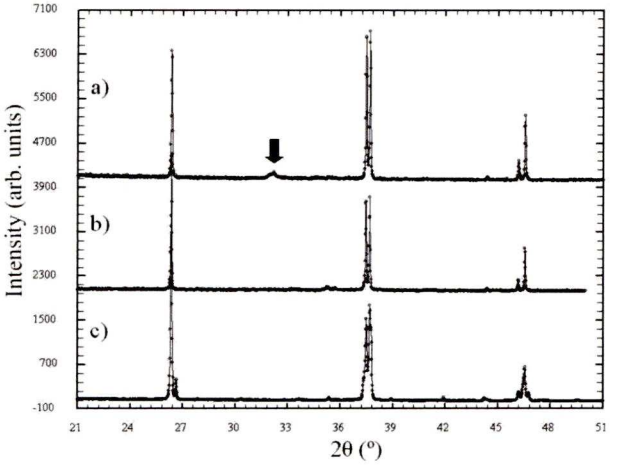

Figure 6-31 XRD of Bi_2FeCrO_6 at RT c) and after annealing at 400 °C b) and 500 °C d) . The arrow shows the emergence of γ Bi_2O_3 signalling the onset of decomposition above 400 °C

Kamba[41] was able to measure Bi_2FeCrO_6 films up to 900 K without observing any decomposition. The source of this stability in the film form is the strain induced by the mismatch of the substrate. Such strain acts on the material in a similar way to pressure making the thin film at 900 K equivalent to the bulk ceramic in the press. Note the synthesis temperature at 6 GPa is above the decomposition point at atmospheric pressure so in situ experiments would be possible at elevated temperatures. Kamba did however observe phonon anomalies near 600 K and postulated that these anomalies were responsible for the decomposition above 400 °C in bulk Bi_2FeCrO_6. Thermogravimetric data (Figure 6-32) were collected in air between 60 °C and 400 °C and showed no evidence for phase transitions or oxygen loss in this temperature range.

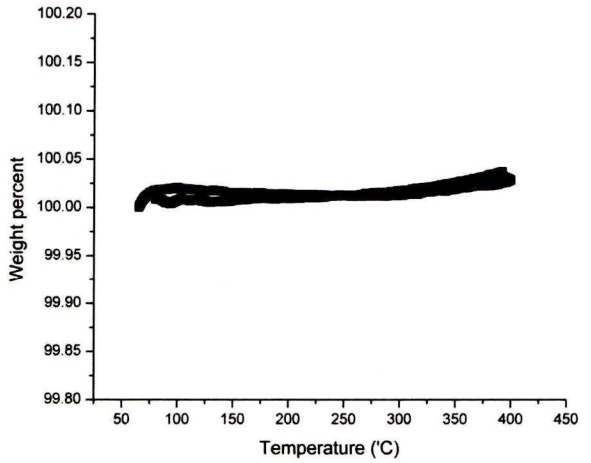

Figure 6-32 TGA of Bi_2FeCrO_6 showing no weight loss to 400 °C

6.4.2.3 Conductivity data

Conductivity data reveals Bi_2FeCrO_6 is a semiconductor with a conductivity of ~ $1x10^{-5}$ Ω-cm^{-1} at 25 °C decreasing to ~$5x10^{-2}$ Ω-cm^{-1} at 400 °C.

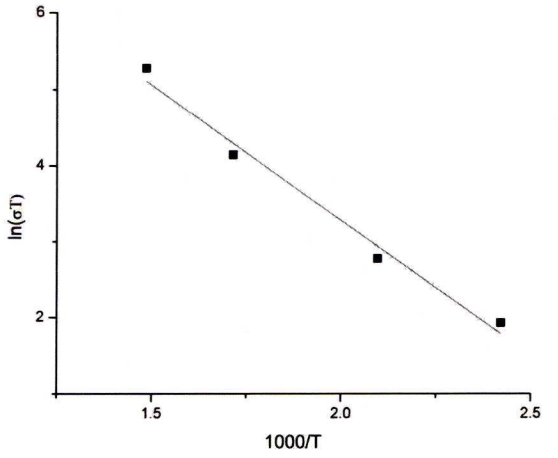

Figure 6-33 Conductivity data of Bi_2FeCrO_6

6.4.3 Magnetic properties

6.4.3.1 SQUID

Magnetic characterization was complicated by the presence of very small amounts of ferromagnetic impurities. These impurities dominate at 100 Oe so differential high field measurements were carried to gain a clearer picture using fields of 50 kOe and 30 kOe. The differential plot (Figure 6-34) reveals an antiferromagnetic transition (T_N) at ~ 130 K. Data above T_N can be fitted quite well to paramagnetic Curie-Weiss behaviour, with a Weiss temperature (θ) of -425(4) K and a Curie constant (C) of 2.66(3) emu K/mole. This value is similar to the value (3.13 emu K/mole) theoretically predicated for an equimolar *B'* mixture of high-spin d^5 Fe^{3+} and d^3 Cr^{3+} cations. The slight difference between the experimental value and the theoretical value may be explained by slight magnetic frustration above T_N or simply by the fact that more data over a greater range of temperature is required for an accurate fit. A large negative θ suggests strong antiferromagnetic coupling but a low T_N suggests the presence of competing interactions. However as the Weiss temperature is of the same magnitude as the temperature range studied (425 versus 400) this may be indicative of more complex higher temperature behaviour. If the region 200 – 400 K is actually a very slight curving region rather than a linear region then the true Curie paramagnetic region could be at a much higher temperature. Unfortunately the SQUID setup used in this thesis for magnetic measurements has a maximum temperature of 400 K so the desired high temperature (> 400 K) measurements would need to be performed elsewhere.

M vs H plots at both 10 K and 300 K show no saturation or significant hysteresis (Figure 6-35), the small hysteresis observed being attributed to the ferromagnetic impurities.

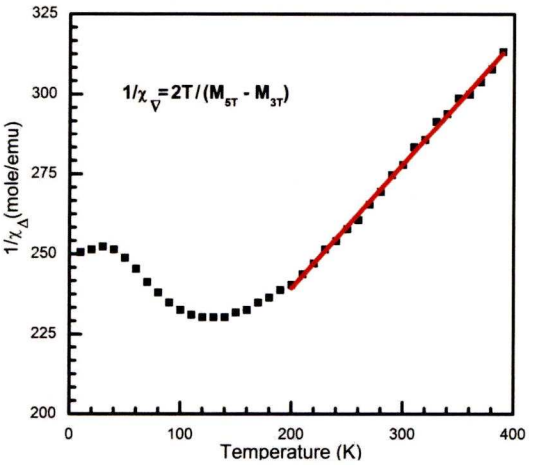

Figure 6-34 Inverse χ plot of Bi_2FeCrO_6 where data values collected at 3T were subtracted from those collected at 5T line guide to linear part of plot above 200 K. The fit is shown by the red line R^2= 0.998 θ= -425 (4) K and C = 2.66 (3) emu K/mole.

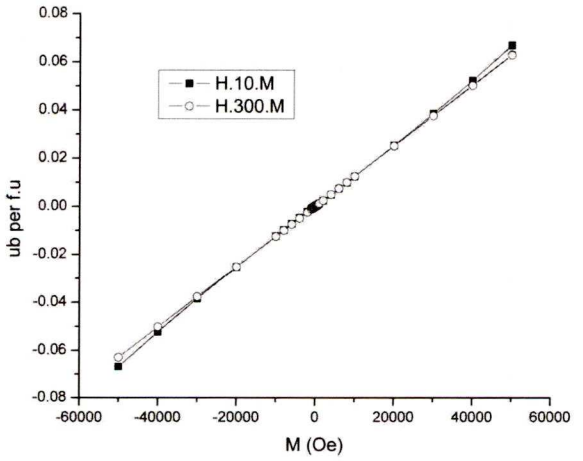

Figure 6-35 M versus H at 10K (filled) and 300 K (open) for Bi_2FeCrO_6

An example of how the magnetic impurities complicate the interpretation of the magnetic properties is given in Figure 6-36. This demonstrates the differing behaviours of two different samples below 2T (where the ferromagnetic impurities appear to saturate) and so the necessity for the differential treatment (Figure 6-34).

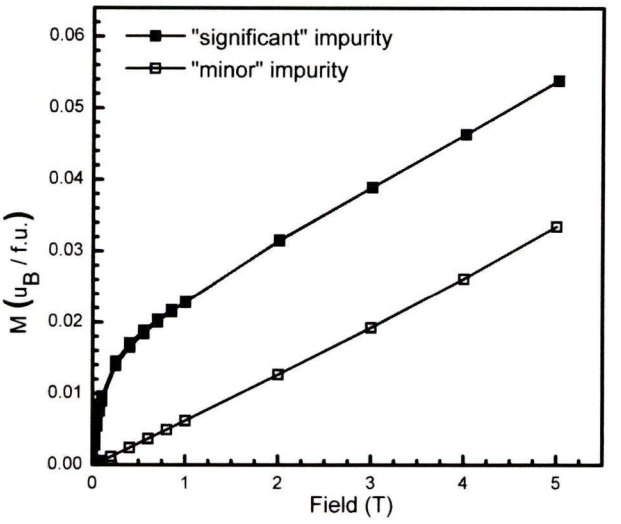

Figure 6-36 M versus H for two samples of Bi_2FeCrO_6 with differing amounts of impurity the filled squares having the greater amount.

6.4.3.2 Mössbauer spectroscopy

Mössbauer data collection and analysis (Figure 6-37) was carried out by Dr Michael Thomas using a conventional constant acceleration Mössbauer spectrometer incorporating a ~25mCi source of Co^{57} in a Rh matrix. Analysis of the data for Bi_2FeCrO_3 at 300 K shows no sign of magnetic ordering. Conversely at 80 K magnetic ordering is observed. The doublet seen at 300 K in Figure 6-37 can be fitted using the isomer shift (δ) of 0.39(1) mm/s (with respect to bcc Fe) and quadrupole splitting (Δ) of 0.48(1) mm/s. The value of δ is characteristic of a Fe^{3+} ion with Δ being consistent with a distorted octahedral environment. At 80 K (Figure 6-37) the six line pattern can be fitted using a δ of 0.43(3) (again characteristic of Fe^{3+}) and a Δ of 0.45(5). The similarity in the values for the quadrupole splitting at both 300 K and 80 K suggest that the orientation of the magnetic moments is parallel to the direction of highest symmetry. In the R3c structure this is along the 3-fold c axis of the hexagonal setting which is also the direction of the calculated polarization.

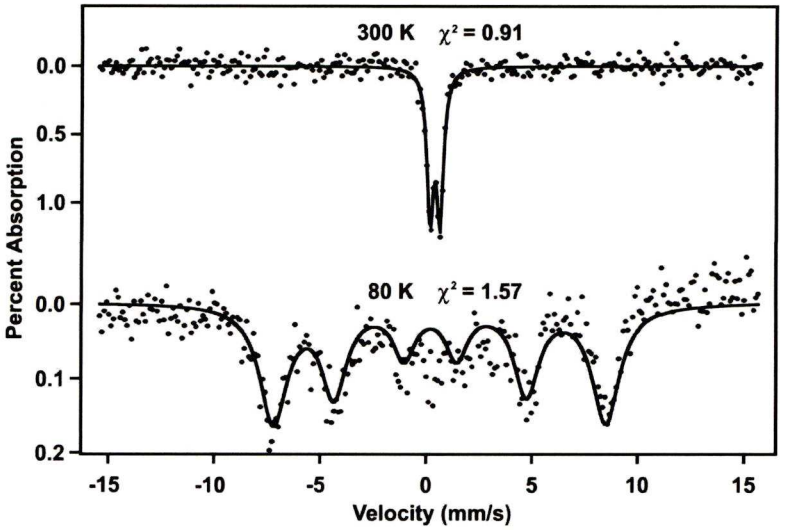

Figure 6-37 Mössbauer data of Bi_2FeCrO_6 at 300 K and 80 K

6.4.3.3 Relationship to structure

The magnetic properties relate to the structure as the lack of B site order prevents the spontaneous magnetic moment from forming. Instead the interactions that dominate are the antiferromagnetic Cr^{3+} - Cr^{3+} and Fe^{3+} – Fe^{3+} interactions which are frustrated by the ferromagnetic Fe^{3+} - Cr^{3+} . For the bulk material to realise the predicted magnetization a technique must be found that imposes order on the Fe^{3+} and Cr^{3+}.

6.4.4 Continued work on Bi_2FeCrO_6 thin films by other groups

Since the publication of this work in 2007 investigations by other groups into the thin film form of the material have continued. Both Nechache et al [3, 42-46] and Kim et al [47] have used pulsed Laser Deposition (PLD) with dense ceramic targets to produce their thin film samples. The targets used either contained a mixture of phases but retained the overall stoichiometry Bi_2FeCrO_6[3, 42, 43], or two separate alternating targets with nominal compositions of $BiFeO_3$ and $BiCrO_3$[47] were used. Nechache

has also used a different technique called dual cross PLD[48] where two targets and two beams are used with alternating pulses.

Initially Nechache[3] reported a dielectric polarisation of 2.8 μC /cm^2 however by optimising the growth conditions [42] a remnant polarisation of 55-60 μC /cm^2 is observed. Kim et al have also investigated Bi_2FeCrO_6 films finding a polarisation of 60 μC /cm^2 which is close to the calculated value of 63 μC/cm^2 that was found in the bulk form (section 6.4.2.1). Kim et al use a random distribution of Fe and Cr on the B site which they argue is consistent with the linear response of magnetization with field showing dominant antiferromagnetic order. Nechache however argues the magnetic properties of their films indicate that the Fe/Cr ordering has been achieved giving rise to ferrimagnetism ($\approx 2\mu_B$ per f.u.)[42] with bond angle distortion causes lower magnetisation than predicted. A neutron diffraction experiment would be able to show the presence of ordering or not but such experiments on films are more complex than similar experiments in the bulk.

In bulk form Li[49]synthesized $Bi(Fe_{1-x}Cr_x)O_3$ (x = 0, 0.1 and 0.2) via a nitrate combustion method and found samples showed a small hysteresis with saturation moments of 0.1, 0.13 and 0.17 μ_B per f.u. respectively.

6.4.5 Summary of Bi_2FeCrO_6 work

In conclusion, high pressure solid-state synthesis methods have been used successfully to prepare bulk Bi_2FeCrO_6 although no B site ordering is observed. As a result the compound could be described as $Bi(Fe_{1/2}Cr_{1/2})O_3$ as this representation indicates that Fe and Cr share occupancy of a crystallographic site and are not ordered. The compound is found to crystallize in the R3c space group with a structure similar to $BiFeO_3$ rather that C2 similar to $BiCrO_3$[50]. The compound is

polar but has no cation order or room temperature magnetic order, however low temperature antiferromagnetic order is observed. There is a possibility that the B site ordering just doesn't happen at the pressures achievable in our apparatus and other techniques such as diamond anvil cells may prove more successful. In situ high pressure studies such as those available at ISIS may also be useful to determine what if any pressure can induce B site order.

6.5 Conclusion to high pressure materials

In this chapter materials have been synthesised at high pressure that could not be formed at ambient pressure such as $NaBiMgWO_6$ and Bi_2FeCrO_6. Despite the use of high pressure a solid solution between $NaBiMgWO_6$ and the ambient phase $NaLaMgWO_6$ proved unsuccessful. Bi_2FeCrO_6 was predicted to be a multiferroic but due to lack of B site order the bulk phase fails to live up to this promise although other workers appear to be having success in thin films. Also presented was the unusual $(Sc_{0.94}Mn_{0.06})Mn_{0.65}Ni_{0.35}O_3$ with a triclinic structure, three Mn oxidation states on three sites one of which is the A site of the perovskite.

High-pressure methods have proved a valuable tool in the search for multiferroics especially as many high-pressure phases are being synthesised as thin films as well.

6.6 References

[1] P. Baettig, C. Ederer, N. A. Spaldin, *Phys. Rev. B* **2005**, *72*, 214105.

[2] P. Baettig, N. A. Spaldin, *Applied Physics Letters* **2005**, *86*, 012505.

[3] R. Nechache, C. Harnagea, A. Pignolet, F. Normandin, T. Veres, L.-P. Carignan, D. Menard, *Applied Physics Letters* **2006**, *89*, 102902.

[4] J. Yu, M. Itoh, *MRS fall meeting 2005* **2005**, U6.6.

[5] M. R. Suchomel, C. I. Thomas, M. Allix, M. J. Rosseinsky, A. M. Fogg, M. F. Thomas, *Applied Physics Letters* **2007**, *90*.

[6] P. M. Woodward, M. C. Knapp, *Journal of Solid State Chemistry* **2006**, *179*, 1076.

[7] M. A. Arillo, J. Gomez, M. L. Lopez, C. Pico, M. L. Veiga, *Solid State Ionics* **1997**, *95*, 241.

[8] T. Sekiya, T. Yamamoto, Y. Torii, *Bulletin of the chemical society of Japan* **1984**, *57*, 1859

[9] M. L. Lopez, M. L. Veiga, C. Pico, *Journal of Materials Chemistry* **1994**, *4*, 547.

[10] M. A. Arillo, J. Gomez, M. L. Lopez, C. Pico, M. L. Veiga, *Journal of Materials Chemistry* **1997**, *7*, 801.

[11] G. King, S. Garcia-Martin, P. M. Woodward, *Acta Crystallographica Section B-Structural Science* **2009**, *65*, 676.

[12] S. Garcia-Martin, E. Urones-Garrote, M. C. Knapp, G. King, P. M. Woodward, *Journal of the American Chemical Society* **2008**, *130*, 15028.

[13] S. Garcia-Martin, E. Urones-Garrote, M. C. Knapp, G. King, P. M. Woodward, *Materials Research Soicety Symposium Proceadings* **2009**, *1148*, PP15.

[14] R. Seshadri, N. A. Hill, *Chemistry of Materials* **2001**, *13*, 2892.

[15] J. J. Bian, K. Yan, J. Ji, *Journal of the European Ceramic Society* **2006**, *26*, 1957.

[16] T. Katsumata, M. Takahata, N. Mochizuki, Y. Inaguma, *Solid State Ionics* **2004**, *171*, 191.

[17] G. King, P. M. Woodward, *Journal of Materials Chemistry* **2010**, *20*, 5785.

[18] G. King, S. Thimmaiah, A. Dwivedi, P. M. Woodward, *Chemistry of Materials* **2007**, *19*, 6451.

[19] G. King, L. M. Wayman, P. M. Woodward, *Journal of Solid State Chemistry* **2009**, *182*, 1319.

[20] D. J. Singh, C. H. Park, *Physical Review Letters* **2008**, *87*, 601.

[21] S. Kumar, G. Giovannetti, J. van den brink, S. Picozzi, *Condensed Mater Preprints* **2009**, *arXiv*, 0909.1439v1.

[22] R. D. Shannon, C. T. Prewitt, *Acta Crystallographica B* **1969**, *25*, 925.

[23] J. H. Park, J. B. Parise, *Materials Research Bulletin* **1997**, *32*, 1617.

[24] K. Uusi-Esko, J. Malm, N. Imamura, H. Yamauchi, M. Karppinen, *Materials Chemistry and Physics* **2008**, *112*, 1029.

[25] J. A. Alonso, M. J. Martinez-Lope, M. T. Casais, J. L. Garcia-Munoz, M. T. Fernandez-Diaz, *Physical Review B* **2000**, *61*, 1756.

[26] N. L. Ross, *Physics and Chemistry of Minerals* **1998**, *25*, 597.

[27] J.-W. G. Bos, J. P. Attfield, *Zeitschrift fuer Anorganische und Allgemeine Chemie* **2004**, *630*, 2248.

[28] A. Navrotsky, *Chemistry of Materials* **1998**, *10*, 2787.

[29] P. D. Battle, *Materials Research Bulletin* **1981**, *16*, 397.

[30] P. M. Woodward, *PhD Thesis Oregon State University* **1997**.

[31] R. H. Mitchell, *Perovskires modern and ancient*, Almaz, Thunder Bay **2002**.

[32] P. D. Battle, J. B. Goodenough, R. Price, *Journal of Solid State Chemistry* **1983**, *46*, 234.

[33] C. Sakai, Y. Doi, Y. Hinatsu, *Journal of Alloys and Compounds* **2006**, *408*, 608.

[34] C. J. Howard, P. W. Barnes, B. J. Kennedy, P. M. Woodward, *Acta Crystallographica Section B-Structural Science* **2005**, *61*, 258.

[35] C. Michael, J.-M. Moreau, G. D. Achenbach, R. Gerson, W. J. James, , *Solid State Communications* **1969**, *7*, 701

[36] N. Setter, L. E. Cross, *Journal of Materials Science* **1980**, *15*, 2478.

[37] R. M. Hazen, A. Navrotsky, *American Mineralogist* **1996**, *81*, 1021.

[38] Q. Q. Liu, H. Yang, X. M. Qin, Y. Yu, L. X. Yang, F. Y. Li, R. C. Yu, C. Q. Jin, S. Uchida, *Physical Review B* **2006**, *74*.

[39] J. P. Attfield, A. L. Kharlanov, J. A. McAllister, *Nature* **1998**, *394*, 157.

[40] D. HughJones, T. Sharp, R. Angel, A. Woodland, *European Journal of Mineralogy* **1996**, *8*, 1337.

[41] S. Kamba, D. Nuzhnyy, R. Nechache, K. Zaveta, D. Niznansky, E. Santava, C. Harnagea, A. Pignolet, *Physical Review B* **2008**, *77*.

[42] R. Nechache, C. Harnagea, L. P. Carignan, O. Gautreau, L. Pintilie, M. P. Singh, D. Menard, P. Fournier, M. Alexe, A. Pignolet, *Journal of Applied Physics* **2009**, *105*.

[43] R. Nechache, C. Harnagea, L. P. Carignan, D. Menard, A. Pignolet, *Integrated Ferroelectrics* **2008**, *101*, 152.

[44] R. Nechache, C. Harnagea, L. P. Carignan, D. Menard, A. Pignolet, *Philosophical Magazine Letters* **2007**, *87*, 231.

[45] R. Nechache, L. P. Carignan, L. Gunawan, C. Harnagea, G. A. Botton, D. Menard, A. Pignolet, *Journal of Materials Research* **2007**, *22*, 2102.

[46] R. Nechache, P. Gupta, C. Harnagea, A. Pignolet, *Applied Physics Letters* **2007**, *91*.

[47] D. H. Kim, H. N. Lee, M. D. Biegalski, H. M. Christen, *Applied Physics Letters* **2007**, *91*.

[48] R. Nechache, C. Harnagea, L. Gunawan, L. P. Carignan, C. Maunders, D. Menard, G. A. Botton, A. Pignolet, *Ieee Transactions on Ultrasonics Ferroelectrics and Frequency Control* **2007**, *54*, 2645.

[49] J.-B. Li, G. H. Rao, J. K. Liang, Y. H. Liu, J. Luo, J. R. Chen, *Applied Physics Letters* **2007**, *90*, 162513.

[50] S. Niitaka, M. Azuma, M. Takano, E. Nishibori, M. Takata, M. Sakata, *Solid State Ionics* **2004**, *172*, 557.

[51] E. Ito, Y. Matsui, *Physics and Chemistry of Minerals* **1979**, *4*, 265.

[52] K. Leinenweber, W. Utsumi, Y. Tsuchida, T. Yagi, K. Kurita, *Physics and Chemistry of Minerals* **1991**, *18*, 244.

[53] K. Fujino, K. Suzuki, D. Hamane, Y. Seto, T. Nagai, N. Sata, *American Mineralogist* **2008**, *93*, 653.

[54] N. L. Ross, J. Ko, C. T. Prewitt, *Physics and Chemistry of Minerals* **1989**, *16*, 621.

[55] Y. Syono, S.-I. Akimoto, Y. Endoh, *Journal of Physics and Chemistry of Solids* **1971**, *32*, 243.

[56] A. A. Belik, Y. Matsushita, M. Tanaka, E. Takayama-Muromachi, *Angewandte Chemie International Edition* **2010**, *asap 6/09/10*, n/a.

Chapter 7 : Conclusions and future directions

Throughout this thesis new functional ceramics with a focus on fuel cell materials and multiferroic materials have been synthesised and their properties investigated.

Chapter 1 explained the background to both fuel cells and multiferroics which will be important technologies in the future. The structures of the materials investigated in the thesis were also introduced.

Chapter 2 discussed the synthesis methods used and the methods of characterizing the resultant products. Of particular importance to the thesis (especially chapter 6) the multianvil equipment is introduced allowing synthesis to take place at high pressures as well as high temperatures.

Chapter 3 focused on development of a possible solid oxide fuel cell electrolyte with melilite structure. Melilite was previously found to be an interstitial oxide conductor and within this thesis the amount of interstitials in the structure was increased. It was hoped that the more interstitials that were incorporated the greater the ionic conductivity would be. However as the amount of interstitials increased there was a structural transition probably caused by long-range order of the interstitials, which decreased the conductivity of the highest doped samples. It was shown that at higher temperatures all melilites tested have the tetragonal structure with the pseudo-orthorhombic phase of the higher doped samples only appearing on cooling. Quenching provided a method of trapping the structure in the high temperature form allowing the conductivity of the two structures to be directly compared. The quenched tetragonal phase was found to have a significantly higher conductivity than

the pseudo orthorhombic but converts to the pseudo-orthorhombic structure on heating before reconverting to tetragonal at higher temperatures.

Investigations into the conductivity of the Ca and Ba Melilite are ongoing in Liverpool with the aim of producing a full study on the structure and conductivity of the $La_{1+x}M_{1-x}Ga_3O_{7+x/2}$ (M = Ca, Sr, Ba) systems. To try and understand further the effect of local structure, PDF measurements have been conducted and are beginning to be analysed.

Chapter 4 focused on using pyrochlores and fluorites as potential fuel cell anodes with particular attention to the border region and Mo doping. The first strategy used was to investigate the border region between pyrochlore-structured materials and fluorite-structured materials. Previous reports had suggested that this region would provide maximum conductivity however experimental results on the materials synthesised in this thesis actually showed a minimum at the border. Also some intermediate compositions of $YbCaCe_{1-x}Ti_xNbO_7$ (x = 0.09 and 0.19) were biphasic, meaning a solid solution could not be completed.

An alternative strategy to improve the performance of the pyrochlores and fluorites performance involved trying to incorporate readily reducible ions such as W^{6+} and Mo^{6+} into the structures. Both W and Mo could be incorporated into the structures but control over the resulting stoichiometry proved elusive.

Synthesis of a rhombohedrally-distorted fluorite (Nd_6MoO_{12}) was also attempted but a single-phase sample was not produced.

Finally co-doping of W^{6+} with Mg^{2+} was attempted with an unexpected result, as well as the expected pyrochlore, a material with the zirconolite-3T structure was also present in sample. Attempts were made to produce samples of one phase or another but these proved unsuccessful. Slightly altering the composition may cause one structure to be favoured over the other and so single phase materials might be obtained. Although quenching experiments were tried, if there is a single non-quenchable phase at high temperatures an in situ experiment might be the only way to observe the phase transformations.

Pyrochlores and fluorites have been and will continue to be extensively investigated for fuel cells but in this thesis a zirconolite-3T and a rhombohedrally-distorted fluorite phase have been investigated. Both structures could be further investigated along with new border spanning pyrochlore / fluorite systems to try and better understand the conductivity of the $A_2B_2X_7$ type phases shown on Figure 4.1.

Other structures apart from pyrochlore / fluorites and melilites were investigated in Chapter 5. The structures investigated for fuel cell materials were new RP2 materials as potential anodes and doped Sr_2PbO_4-structured materials as potential proton conducting electrolytes. Unfortunately the RP2 structures were always present with RP1 structures in the samples despite varied synthesis techniques including quenching and varying the atmosphere.

Doping Y^{3+} and Yb^{3+} Sr_2CeO_4 also proved elusive with Y or Yb impurities always being present. In both cases alternative synthesis methods may result in single phase materials (quenching or hydrothermal) but production of large amounts of dense ceramic will be challenging.

Investigations into solid oxide fuel cell materials will continue as commercial units start to be installed outside of testing laboratories. YSZ, CGO and LSGM are just some of the materials that are being used in these first commercial units. Melilites have been shown to have conductivities comparable to LSGM raising its potential use in real devices if, when incorporated into a real fuel cell, properties such as corrosion, durability etc are also comparable.

Chapter 6 departed from the fuel cell theme instead focusing on the use of high pressure synthesis with the aim of producing new multiferroics for novel memory applications. The chapter was split into three sections with each section describing a group of linked materials.

$NaBiMgWO_6$ was successfully synthesised using high pressure methods and compared to the known ambient pressure phase $NaLaMgWO_6$. Synthesis of the solid solution between the two was also attempted but proved unsuccessful despite the use of high-pressure synthesis. It remains intriguing that $NaLaMgWO_6$ and $NaBiMgWO_6$ show such a difference. $NaLaMgWO_6$, synthesised at ambient pressure shows NaLa order while $NaBiMgWO_6$ requires high pressure synthesis and shows no NaBi order despite the fact that both La and Bi are 3+ and have comparable sizes. Bi^{3+} does however have a lone pair and this may be the reason for the observed difference. It may be possible for PDF to investigate the local structure of the Na and La/Bi to see if that provides the cause of the differences.

Attempts at synthesis of Sc_2MnNiO_6 resulted in separation into two phases with B site compositions $Mn_{4/3}Ni_{2/3}$ and $Mn_{2/3}Ni_{4/3}$. The $Mn_{4/3}Ni_{2/3}$ case was chosen for

further investigation as this phase appeared to be more crystalline based on TEM. Investigations of the structure actually showed that the composition is Sc deficient and some Mn is found on the A site of the perovskite cell giving $(Sc_{0.94}Mn_{0.06})Mn_{0.5}(Mn_{0.15}Ni_{0.35})O_{3+\delta}$. Bond valance calculations give the Mn existing in three separate oxidation states, Mn^{2+} on the A site, Mn^{4+} on the two Mn only B sites and Mn^{3+} on the two Mn/Ni mixed sites. Overall $Sc_{0.94}Mn_{0.06})Mn_{0.5}(Mn_{0.15}Ni_{0.35})O_{3+\delta}$ crystallises in a triclinic structure with tilt angles of 20.5(2)° down 1–10, 20.9(2)° down 110 and 22.1(2)° down 001.

$ScLuMnNiO_6$ and $ScHoMnNiO_6$ have been synthesised and found to adopt the $P2_1/n$ structure. Magnetic measurements show similar behaviour to $(Sc_{0.94}Mn_{0.06})Mn_{0.65}Ni_{0.35}O_3$ although the hysteresis loop for $ScHoMnNiO_6$ saturates at 6T while $ScLuMnNiO_6$ and $(Sc_{0.94}Mn_{0.06})Mn_{0.65}Ni_{0.35}O_3$ do not.

The series might be extendable to $ScEuMnNiO_6$, $ScNdMnNiO_6$ and possibly $ScLaMnNiO_6$.

The double perovskite Bi_2FeCrO_6 had been predicted to be a multiferroic with the magnetism being reliant on the B site ordering. When synthesis of this was attempted in bulk form, the B site order proved unobtainable and so the magnetic properties failed to reach those predicted. However the single perovskite that was synthesised $Bi(Fe_{0.5}Cr_{0.5})O_3$ is polar with a polarisation of 63 $\mu C/cm^2$. Since the work was published B site order was achieved using thin film techniques using substrate phase mismatch as a source of pressure. In situ high-pressure neutron diffraction (such as available on PEARL at ISIS) could be used to determine the pressure required for the Fe and Cr ions to order.

Synthesis of room temperature multiferroic materials where there is strong coupling between ferro-magnetic ordering and ferroelectric ordering remains a great challenge in solid state science.

Investigation of functional ceramic materials is set to continue, as major materials challenges are still to be met both in the field of energy (fuel cells) and in electronics (multiferroics). In this thesis many new materials have been synthesised and characterised and future work on these some of these types of materials may lead to real world devices.

Appendix 1: Compounds used in Figure 4.1

The compounds listed here are the ones used in Figure 4.1 in Chapter 4 . Compounds are written in $A_2B_2X_7$ format where if there is more than one atom type on a site an average radius is taken. The larger ion is always taken as residing on the A site. Some compounds are reported as multiple structures due to differing synthesis procedures, in such cases all structures were used as co-ordinates for Figure 4.1.

Pyrochlores

Pyrochlores	A (pm)	B (pm)
(MgLa)(MgTa)O6	103.5	68
(MgNd)(MgTa)O6	100.5	68
(Na1/3Ce2/3)2Ti2O7	114.6667	60.5
Ba2V2O7	142	54
BaSmHfNbO7	125.5	67.5
Bi0.1Tl1.9Mn2O7	100.55	54
Bi0.2Tl1.8Mn2O7	101.1	54
Bi0.3Tl1.7Mn2O7	101.65	54
Bi0.4Tl1.6Mn2O7	102.2	54
Bi0.4Y1.6Ru2O7	103.4	62
Bi0.5Tl1.5Mn2O7	102.75	54
Bi1.55Zn0.42 (Zn0.49Nb1.51)O7	104.925	66.5725
Bi1.5Zn0.45 (Zn0.46Nb1.54)O7	103.5	66.415
Bi1.63Zn0.35 (Zn0.53Nb1.47)O7	106.215	66.7825
Bi1.6Y0.4Ru2O7	109.1	62
Bi1.6Zn0.40 (Zn0.53Nb1.47)O7	106.8	66.7825
Bi2FeSbO7	111	62.75
Bi2GaTaO7	111	63
Bi2InTaO7	111	71.5
Bi2Ru2O6.9	111	62
Bi2SbInO7	111	70
Bi2Sn2O7	111	69
Bi2Tc2O7	111	64.5
Bi2YTaO7	111	77
BiYRu2O7	106.25	62
Ca0.0072Gd1.9928Sn2O7	106.0216	69
Ca0.0114Gd1.9886Sn2O7	106.0342	69
Ca0.06Gd1.94Sn2O7	106.18	69
Ca0.93CeTi2.035O7	100.58	60.5
Ca1.5Cd0.5Os2O7	110.75	57.5
Ca2Nb2O7	112	64

Ca2Ru2O7	112	62
Ca2Ta2O7	112	64
Ca2V2O7	112	54
CaCeNb2O7	113	69
CaCeTi2O7	113	60.5
CaDyNb2O7	107.5	69
CaErNb2O7	106	69
CaGdNb2O7	109	69
CaHoNb2O7	107	69
CaLaNb2O7	115	69
CaNdNb2O7	112	69
CaPrNb2O7	113	69
CaPuTi2O7	104	60.5
CaSmHfNbO7	110.5	67.5
CaSmNb2O7	110.5	69
CaSmNbSnO7	110.5	64.75
CaSmNbTiO7	110.5	62.25
CaSmNbZrO7	110.5	68
CaTbNb2O7	108	69
CaTmNb2O7	105.5	69
CaUTi2O7	106	60.5
CaYbNb2O7	105	69
CaYNb2O7	106.75	69
Cd0.1Tl1.9Mn2O7	100.35	54
Cd0.2Tl1.8Mn2O7	100.7	54
Cd2Nb2O7	107	69
Cd2Os2O7	107	57.5
Cd2Re2O7	107	58
Cd2Sb2O7	107	61
Cd2V2O7	107	62
Cd2V2O7	107	54
CdBiCr0.5Sb1.5O7	109	61.125
CdBiCrWO7	109	59.75
CdBiFe0.5Sb1.5O7	109	61.875
CdBiFeWO7	109	61.25
CdBiGa0.5Sb1.5O7	109	61.25
CdBiGaWO7	109	60
CdBiIn0.5Sb1.5O7	109	65.5
CdBiInWO7	109	68.5
CdBiMnWO7	109	61.5
CdBiRh0.5Sb1.5O7	109	62.375
CdBiRhWO7	109	62.25
CdBiSc0.5Sb1.5O7	109	64
CdBiScWO7	109	65.5
CdBiV0.5Sb1.5O7	109	61.75
CdBiVWO7	109	61
CdGdTiSbO7	106.5	60.75
CdNdTiSbO7	109.5	60.75

CdSmHfNbO7	108	67.5
CdSmNbSnO7	108	64.75
CdSmNbTiO7	108	62.25
CdSmNbZrO7	108	68
CdYbTiSbO7	102.5	60.75
Ce2Zr2O7	114	72
Dy0.2Lu1.8Mn2O7	97.6	54
Dy0.6Lu1.4Mn2O7	98.8	54
Dy1.6Lu0.4Mn2O7	101.8	54
Dy1Lu1Mn2O7	100	54
Dy2Fe1.333W0.66O7	103	62.33333
Dy2Hf2O7	103	71
Dy2Mn1.33W0.66O7	103	62.6666
Dy2Mn2O7	103	54
Dy2Mo2O7	103	65
Dy2Pt2O7	103	63
Dy2Ru2O7	103	62
Dy2Sn2O7	103	69
Dy2Ti2O7	103	60.5
Dy2V2O7	103	59
Er2Fe1.333W0.66O7	100	62.33333
Er2Mn1.33W0.66O7	100	62.6666
Er2Mn2O7	100	54
Er2Mo2O7	100	65
Er2Pt2O7	100	63
Er2Sn2O7	100	69
Er2Ti2O7	100	60.5
Er2V2O7	100	59
Eu2Hf2O7	107	71
Eu2Ir2O9	107	63
Eu2Mn1.33W0.66O7	107	62.6666
Eu2Mo2O7	107	65
Eu2Pb2O7	107	77.5
Eu2Pt2O7	107	63
Eu2Ru2O7	107	62
Eu2Sn2O7	107	69
Eu2Ti2O7	107	60.5
Eu2Zr1.8Ce0.2O7	107	73.5
Eu2Zr2O7	107	72
Eu2Zr2O7	107	72
EuGdZr2O7	106.5	72
EuNdZr2O7	109.5	72
EuSmZr2O7	108	72
Gd1.2Nd0.8Ti2O7	108.4	60.5
Gd1.4Nd0.4Ti2O7	107.8	60.5
Gd1.8Nd0.2Ti2O7	106.6	60.5
Gd1.90Sr0.05Ce0.05Zr2O7	106.25	72
Gd1.925Sr0.0375Ce0.0375Zr2O7	106.1875	72

Gd1.95Sr0.025Ce0.025Zr2O7	106.125	72
Gd2Fe1.333W0.66O7	106	62.33333
Gd2Hf2O7	106	71
Gd2Mn1.33W0.66O7	106	62.6666
Gd2Mo2O7	106	65
Gd2Pb2O7	106	77.5
Gd2Pt2O7	106	63
Gd2Ru2O7	106	62
Gd2Sn2O7	106	69
Gd2Ti2O7	106	60.5
Gd2TiMoO7	106	62.75
Gd2Zr2O7	106	72
Hg2Nb2O7	114	64
Hg2Ru2O7	114	62
Ho2(Ti1.8Ho0.2)O6.9	102	63.46
Ho2(Ti1.9Ho0.1)O6.95	102	61.98
Ho2Fe1.333W0.66O7	102	62.33333
Ho2Mn1.33W0.66O7	102	62.6666
Ho2Mn2O7	102	54
Ho2Mo2O7	102	65
Ho2Pt2O7	102	63
Ho2Ru2O7	102	62
Ho2Sn2O7	102	69
Ho2Ti2O7	102	60.5
Ho2V2O7	102	59
In0.1Tl1.9Mn2O7	99.6	54
In0.25Tl1.75Mn2O7	99	54
In0.5Tl1.5Mn2O7	98	54
In0.8Tl1.2mn2O7	96.8	54
In2Mn2O7	92	54
In2Si2O7	92	40
La1.2Y0.8Ce0.8Zr1.2O7	111.4	78
La1.4Y0.6Ce0.6Zr1.4O7	113.05	76.5
La1.6Y0.4Ce0.4Zr1.6O7	114.7	75
La1.8Y0.2Ce0.2Zr1.8O7	116.35	73.5
La2Hf2O7	118	71
La2Pb2O7	118	77.5
La2Sn2O7	118	69
La2Zr2O7	118	72
LaEuZr2O7	112.5	72
Lu2Ge2O7	97	54
Lu2Mn1.33W0.66O7	97	62.6666
Lu2Mn2O7	97	54
Lu2Pt2O7	97	63
Lu2Sn2O7	97	69
Lu2Ti2O7	97	60.5
Lu2V2O7	97	59
Mg2V2O7	89	54

Mn2Sb0.5V1.5O7	97	55.75
Mn2Sb1.5V0.5O7	97	59.25
Mn2Sb2O7	97	61
Mn2SbVO7	97	57.5
Mn2V2O7	97	54
Mn2V2O7	93	62
MnCdV2O7	102	54
Na0.5Dy1.5TiSbO7	106.25	60.75
Na0.5Gd1.5TiSbO7	108.5	60.75
Na0.5Nd1.5TiSbO7	113	60.75
Na0.5Sm1.5TiSbO7	110.75	60.75
Na0.5Yb1.5TiSbO7	102.5	60.75
Nd2Ce0.24Zr1.76O7	112	73.8
Nd2Mo2O7	112	65
Nd2Pb2O7	112	77.5
Nd2Pt2O7	112	63
Nd2Ru2O7	112	62
Nd2Sn2O7	112	69
Pb2Nb2O7	129	69
Pb2Os2O7	129	57.5
Pb2Re2O7	129	58
PbSmHfNbO7	119	67.5
PbSmNbSnO7	119	64.75
PbSmNbTiO7	119	62.25
PbSmNbZrO7	119	68
Pr2Pb2O7	114	77.5
Pr2Pt2O7	114	63
Pr2Ru2O7	114	62
Pr2Sn2O7	114	69
Pr2Te2O7	114	64.5
Pu2Zr2O7	107	72
Sc0.18Yb1.82ti2O7	97.01	60.5
Sc0.4Yb1.6Ti2O7	95.8	60.5
Sc0.6Yb1.4Ti2O7	94.7	60.5
Sc2Mn2O7	87	54
Sc2Si2O7	87	40
Sm1.4Sr0.6 Mo2O7	113.8	65
Sm1.6Sr0.4Mo2O7	112.2	65
Sm1.8Sr0.2Mo2O7	110.6	65
Sm2Mn1.33W0.66O7	109	62.6666
Sm2Mo2O7	109	65
Sm2Pb2O7	109	77.5
Sm2Pt2O7	109	63
Sm2Sn2O7	109	69
Sm2Ti2O7	109	60.5
Sm2Zr2O7	109	72
Sr2Os2O6	125	63
Sr2Sb2O7	125	61

Sr2V2O7	125	54
SrSmHfNbO7	117	67.5
SrSmNbSnO7	117	64.74
SrSmNbZrO7	117	68
Tb2Mn1.33W0.66O7	104	62.6666
Tb2Mo2O7	104	65
Tb2Pt2O7	104	63
Tb2Ru2O7	104	62
Tb2Sn2O7	104	69
Tb2Yi2O7	104	60.5
Tl2Mn1.4Ru0.6O7	100	56.4
Tl2Mn1.6Ru0.4O7	100	55.6
Tl2Mn1.6Sc0.4O7	100	57.8
Tl2Mn1.6Ti0.4O7	100	55.3
Tl2Mn1.7Ru0.3O7	100	55.2
Tl2Mn1.7Sc0.3O7	100	56.85
Tl2Mn1.8Ru0.2O7	100	54.8
Tl2Mn1.8Sc0.2O7	100	55.9
Tl2Mn1.8Ti0.2O7	100	54.65
Tl2Mn1.95Ru0.05O7	100	54.2
Tl2Mn1.95Sc0.05O7	100	54.475
Tl2Mn1.9Ru0.1O7	100	54.4
Tl2Mn1.9Sc0.1O7	100	54.95
Tl2Mn2O7	100	54
Tl2MnRuO7	100	58
Tl2Os2O7	100	63
Tl2Pt2O7	100	63
Tl2Ru2O6.7	100	62
Tm2Fe1.333W0.66O7	99	62.33333
Tm2Mn1.33W0.66O7	99	62.6666
Tm2Mn2O7	99	54
Tm2Mo2O7	99	65
Tm2Sn2O7	99	69
Y2Ir2O7	101.5	63
Y2Mn1.33W0.66O7	101.5	62.6666
Y2Mn2O7	101.5	54
Y2Mo2O7	101.5	65
Y2Pt2O7	101.5	63
Y2Ru2O7	101.5	62
Y2Sn2O7	101.5	69
Y2Ti2O7	101.5	60.5
Y2V2O7	101.5	59
Yb2(Ti1.8Yb0.2)O6.9	98	63.13
Yb2(Ti1.9Yb0.1)O6.95	98	61.815
Yb2Fe1.333W0.66O7	98	62.33333
Yb2Mn1.33W0.66O7	98	62.6666
Yb2Mn2O7	98	54
Yb2Mo2O7	98	65

Yb2Pt2O7	98	63
Yb2Ru2O7	98	62
Yb2Sn2O7	98	69
Yb2Ti2O7	98	60.5
Yb2V2O7	98	59
YbCaNbTiO7	105	62.25
YbCaTi0.5Ce0.5NbO7	105	68.875
YbMn(Mn0.5Sb1.5)O7	95.5	62
Zn2V2O7	90	54
Sm1.89Mg0.11Ti2O7	107.9	60.5
Sm1.78Mg0.22Ti2O7	106.8	60.5
Sm1.65Mg0.35Ti2O7	105.5	60.5
Sm1.6Mg0.4Ti2O7	105	60.5
Sc2Ge2O7	87	54
In2Ge2O7	92	54
Yb2Ge2O7	98	54
Tm2Ge2O7	99	54
Er2Ge2O7	100	54
Tl2Ge2O7	100	54
Y2Ge2O7	101.5	54
Ho2Ge2O7	102	54
Dy2Ge2O7	103	54
Gd2Ge2O7	106	54
Er2Tc2O7	100	64.5
Ho2Tc2O7	102	64.5
Sm2Tc2O7	109	64.5
Pb2ReFeO6	129	61.25

Fluorites

Fluorites	A (pm)	B (pm)
Dy2Hf2O7	103	71
Dy2Pb2O7	103	77.5
DyEuZr2O7	105	72
Er2Hf2O7	100	71
Er2Pb2O7	100	77.5
Er2Zr2O7	100	72
ErEuZr2O7	103.5	72
Eu2Ce0.4Zr1.6O7	107	75
Eu2Ce0.8Zr1.2O7	107	78
Eu2Ce1.2Zr0.8O7	107	81
Eu2Ce1.6Zr0.4O7	107	84
Eu2Ce2O7	107	87
EuHoZr2O7	104.5	72
EuTmZrO7	103	72
EuYZr2O7	104.25	72
Gd2Zr2O7	106	72

Ho2Hf2O7	102	71
Ho2Pb2O7	102	77.5
HoCaCeNbO7	107	75.5
La2(ce0.8Ti0.2)2O7	118	81.7
La2Ce1.7Zr0.3O7	118	84.75
La2Ce2O7	118	87
Lu2Hf2O7	97	71
Nd2Ce2O7	112	87
Tb2Hf2O7	104	71
Tb2Pb2O7	104	77.5
Tm2Hf2O7	99	71
Y2Hf2O7	101.5	71
Y2Pb2O7	102	77.5
Y2Zr2O7	102	72
Yb2Hf2O7	98	71
Yb2Zr2O7	98	72
YbCaCeNbO7	105	75.5
La0.2Y1.8Ce1.8Zr0.21O7	103.15	85.5
La0.3Y1.7Ce1.7Zr0.3O7	103.975	84.75
La0.4Y1.6Ce1.6Zr0.4O7	104.8	84
La0.6Y1.4Ce1.4Zr0.6O7	106.45	82.5
La0.8Y1.2Ce1.8Zr0.2O7	108.1	81
La1Y1Ce1Zr1O7	109.75	79.5
Ho2(Ti1.7Ho0.3)O6.85	102	64.94
Ho2(Ti1.6Ho0.4)O6.8	102	66.42
Ho2(Ti1.5Ho0.5)O6.75	102	67.9
Ho2(Ti1.33Ho0.66)O6.656	102	69.9655
Yb2(Ti1.7Yb0.3)O6.85	98	64.445
Yb2(Ti1.6Yb0.4)O6.8	98	65.76
Yb2(Ti1.5Yb0.5)O6.75	98	67.075
Yb2(Ti1.33Yb0.66)O6.656	98	68.976
Y2(Zr1.9Mn0.1)O7	102	71.1
Yb2(Ce1.4W0.6)O7	98	78.3

Zirconolite 3T

Zirconolite 3T	A (pm)	B (pm)
Y2MnTaO7	101.5	64.5
Eu2MnTaO7	107	64.5
Gd2MnTaO7	106	64.5
Tb2MnTaO7	104	64.5
Dy2MnTaO7	103	64.5
Ho2MnTaO7	102	64.5
Er2MnTaO7	100	64.5
Yb2MnTaO7	98	64.5
Y2Cd0.66Re1.33O7	101.5	69.92
Er2MnWO7	100	62.5

Appendix 2: Melilite Refinement

Using the tetragonal melilite model used by Kuang (*Nature Materials* **2008**, *7*, 498) example refinements for $La_{1+x}Sr_{1-x}Ga_3O_{7+x/2}$ (x = 0 and x=0.54) melilites are given here. Also given in this section is further data from the refinement of $La_{1.54}Sr_{0.46}Ga_3O_{7.27}$ annealed at 950 °C for 24 hours.

A2.1 $LaSrGa_3O_7$

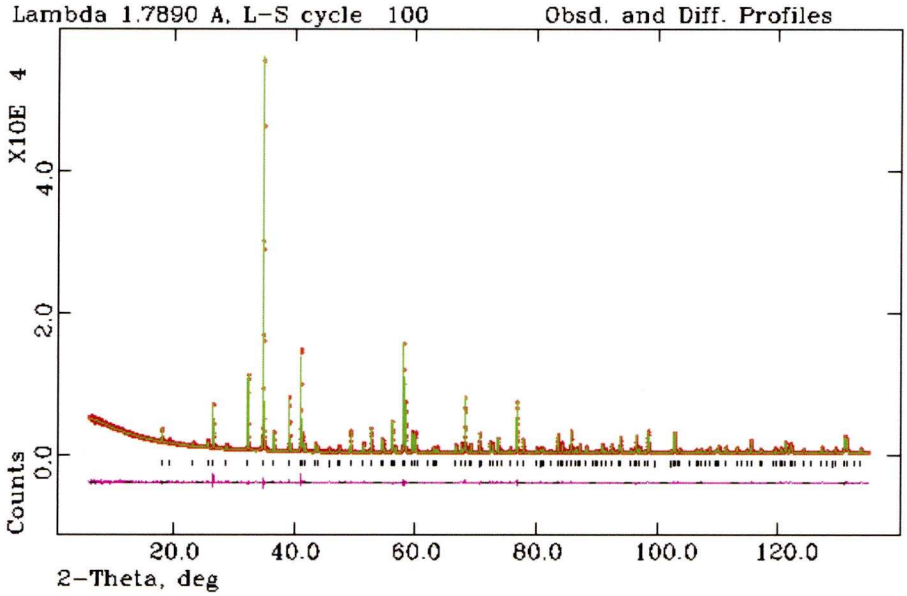

Figure A 2.1.1 Rietveld refinement of $LaSrGa_3O_7$ with the tick marks showing allowed reflections for the tetragonal melilite phase ($\mathbf{P\bar{4}2_1m}$). (λ = 1.7890 Å Rwp = 3.88% χ^2 = 1.553).

Table A2.1.1 Lattice parameters for $LaSrGa_3O_7$ at room temperature

Parameter	XRD	Parameter	XRD
a	8.05336(2) Å	α	90°
b	8.05336(2) Å	β	90°
c	5.33293(2) Å	γ	90°

Table A2.1.2 Crystallographic data of $LaSrGa_3O_7$ at room temperature.

Atom	Wyckoff position	Oxidation	x	y	z	U_{iso} ($Å^2$)	Occupancy
Sr1	4e	+2	0.66264(5)	0.83735(5)	0.4917(2)	0.0162(4)	0.5
La1	4e	+3	0.66264(5)	0.83735(5)	0.4917(2)	0.0162(4)	0.5
Ga1	2a	+3	0	0	0	0.0112(5)	1
Ga2	4e	+3	0.85705(8)	0.64294(8)	0.0342(2)	0.0113(5)	1
O1	2c	-2	0.5	0	0.8195(9)	0.018(3)	1
O2	4e	-2	0.8601(5)	0.6398(5)	0.6941(9)	0.022(3)	1
O3	8f	-2	0.9116(4)	0.8389(6)	0.2001(8)	0.018(1)	1

A2.2 $La_{1.54}Sr_{0.46}Ga_3O_{7.27}$

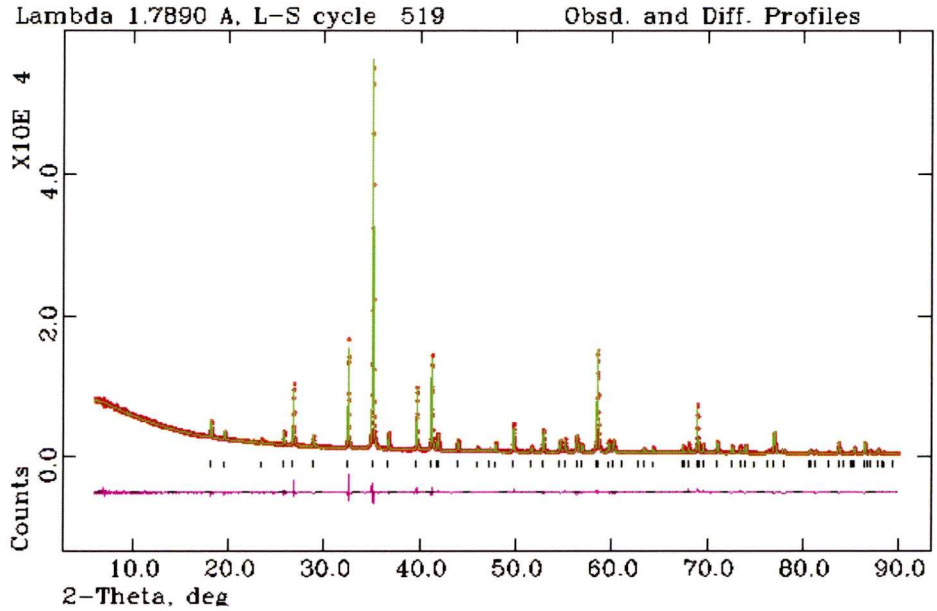

Figure A 2.2.1 Rietveld refinement of $La_{1.54}Sr_{0.46}Ga_3O_{7.27}$ with the tick marks showing allowed reflections for the tetragonal melilite phase ($\mathbf{P\bar{4}2_1m}$). (λ = 1.7890 Å Rwp = 3.71% χ^2 = 2.2601).

Table A2.2.1 Lattice parameters for $La_{1.54}Sr_{0.46}Ga_3O_{7.27}$ at room temperature

Parameter	XRD	Parameter	XRD
a	8.04332(5) Å	α	90°
b	8.04332(5) Å	β	90°
c	5.27799(4) Å	γ	90°

Table A2.2.1 Crystallographic data of $La_{1.54}Sr_{0.46}Ga_3O_{7.27}$ at room temperature

Atom	Wyckoff position	Oxidation	x	y	z	U_{iso} ($Å^2$)	Occupancy
Sr1	4e	+2	0.6637(1)	0.8362(1)	0.4921(4)	0.0411(5)	0.23
La1	4e	+3	0.6637(1)	0.8362(1)	0.4921(4)	0.0411(5)	0.77
Ga1	2a	+3	0	0	0	0.019(1)	1
Ga2	4e	+3	0.8573(2)	0.6426(2)	0.0355(6)	0.0288(7)	1
O1	2c	-2	0.5	0	0.824(3)	0.051(6)	1
O2	4e	-2	0.8629(7)	0.6370(7)	0.674(1)	0.0 (3)	1
O3	8f	-2	0.9188(8)	0.8429(7)	0.210(1)	0.036(3)	1
O4	4e	-2	0.330(6)	0.169(6)	0.02(2)	0.07(2)	0.136

A2.3 $La_{1.54}Sr_{0.46}Ga_3O_{7.27}$ Post 5%H_2 annealing

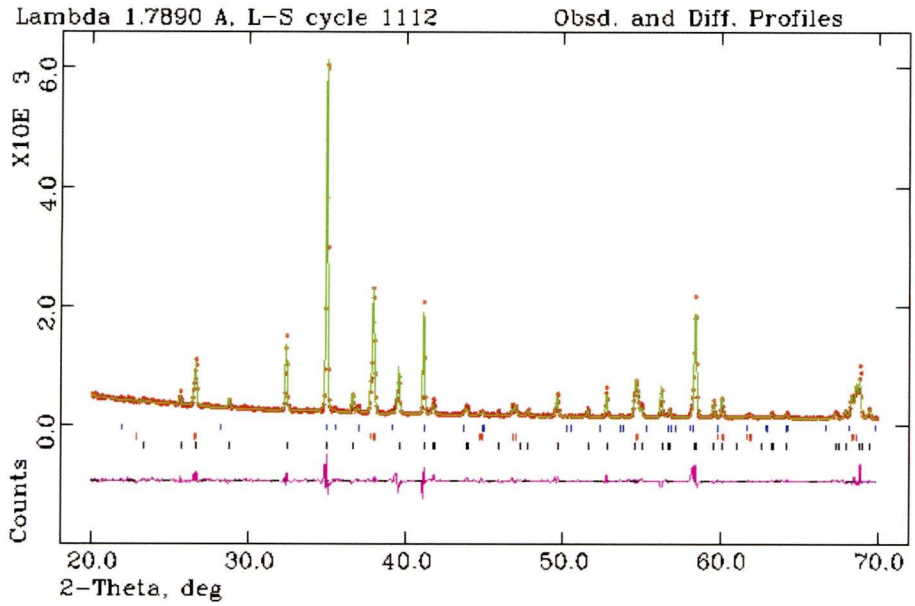

Figure A 2.3.1 Rietveld refinement of $La_{1.54}Sr_{0.46}Ga_3O_{7.27}$ (bottom black tick marks) annealed at 950 °C for 24 hours (λ = 1.7890 Å Rwp = 8.95%). The other phases in the refinement are $La_{0.77}Sr_{0.23}GaO_{2.885}$ (middle red tick marks) and β -Ga_2O_3 (upper blue tick marks).

Below are the refined lattice parameters for all three phases and the crystallographic data of the annealed melilite phase ($P\bar{4}2_1m$). The crystallographic data for the $La_{0.77}Sr_{0.23}GaO_{2.885}$ (Ibmm) and β -Ga_2O_3 (C12/M1) was not refined instead taken directly from the cif files (see section 3.3.1 for references).

Table A2.3.1 Lattice parameters for melilite phase post annealing at 950 °C for 24 hours

Parameter	XRD	Parameter	XRD
a	8.04323(30) Å	α	90°
b	8.04323(30) Å	β	90°
c	5.28230(24) Å	γ	90°

Table A2.3.2 Lattice parameters for the $La_{0.77}Sr_{0.23}Ga_3O_{2.885}$ phase post annealing at 950 °C for 24 hours

Parameter	XRD	Parameter	XRD
a	5.5219(4) Å	α	90°
b	5.4897(4) Å	β	90°
c	7.7692(5) Å	γ	90°

Table A2.3.3 Lattice parameters for the β-Ga_2O_3 phase post annealing at 950 °C for 24 hours

Parameter	XRD	Parameter	XRD
a	12.241(6) Å	α	90°
b	3.0261(15) Å	β	103.82(5)°
c	5.8013(21) Å	γ	90°

Table A2.3.4 Crystallographic data of the melilite phase post annealing at 950 °C for 24 hours

Atom	Wyckoff position	Oxidation	x	y	z	U_{iso} ($Å^2$)	Occupancy
Sr1	4e	+2	0.6626(5)	0.8373(5)	0.494(2)	0.011(4)	0.23
La1	4e	+3	0.6626(5)	0.8373(5)	0.494(2)	0.011(4)	0.77
Ga1	2a	+3	0	0	0	0.01 (8)	1
Ga2	4e	+3	0.8596(9)	0.6403(9)	0.037(3)	0.00 (5)	1
O1	2c	-2	0.5	0	0.77(2)	0.00(3)	1
O2	4e	-2	0.868(4)	0.631 (4)	0.669(8)	0.00 (2)	1
O3	8f	-2	0.908(3)	0.833(4)	0.222(9)	0.00(1)	1
O4	4e	-2	0.336(6)	0.164(2)	0.04(9)	0.00(2)	0.136

Appendix 3: LeBail Refinements for Section 4.1.1.2.

In this section of the appendices the fits for the LeBail refinements used in section 4.1.1.2 to provide the lattice parameters. All the data was collected on the Panalytical instrument using a short Phase ID scan (10-70° 2θ over 30 minutes).

A3.1 $YbCaCeNbO_7$

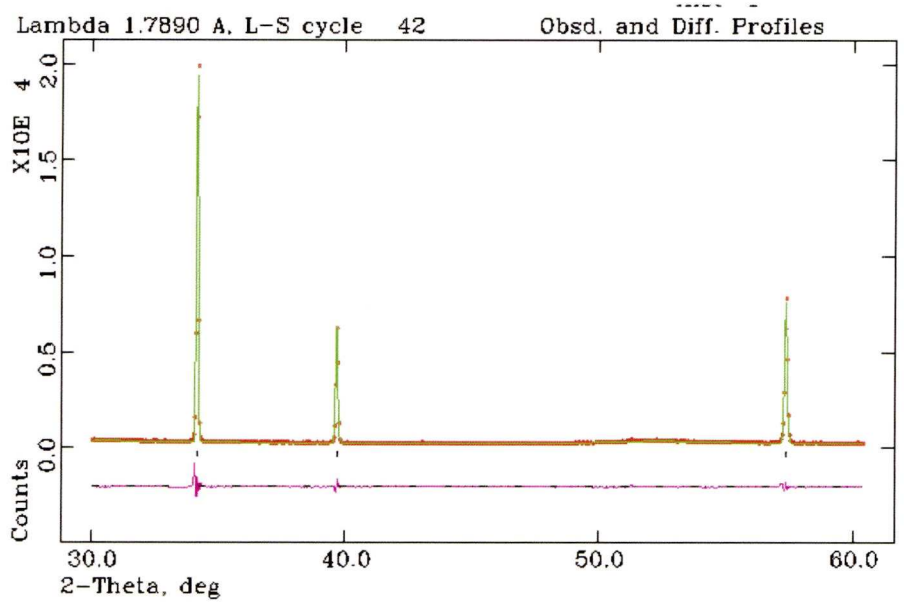

Figure A3.1. 1 LeBail refinement of 'as synthesized' $YbCaCeNbO_7$ (1480 °C in air) with the tick marks showing allowed reflections for the fluorite phase. The red crosses are data points the green line is the fit and the purple line the difference plot. (λ = 1.7890 Å Rwp = 6.3% χ^2 = 1.428).

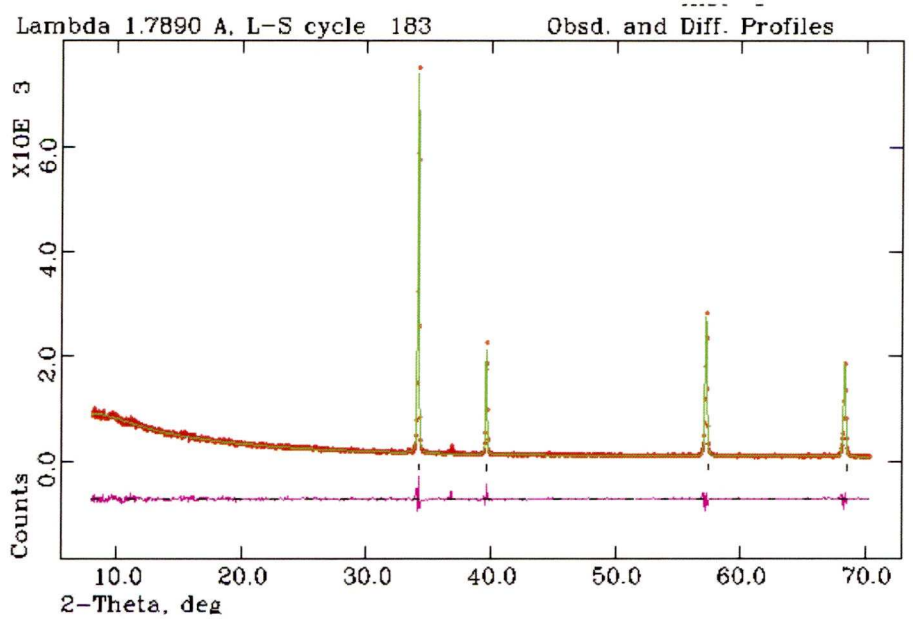

Figure A3.1. 2 LeBail refinement of 'reduced' $YbCaCeNbO_7$ (900 °C in 5%H_2 95%N_2) with the tick marks showing allowed reflections for the fluorite phase. The red crosses are data points the green line is the fit and the purple line the difference plot. (λ = 1.7890 Å Rwp = 7.14% χ^2 = 1.432).

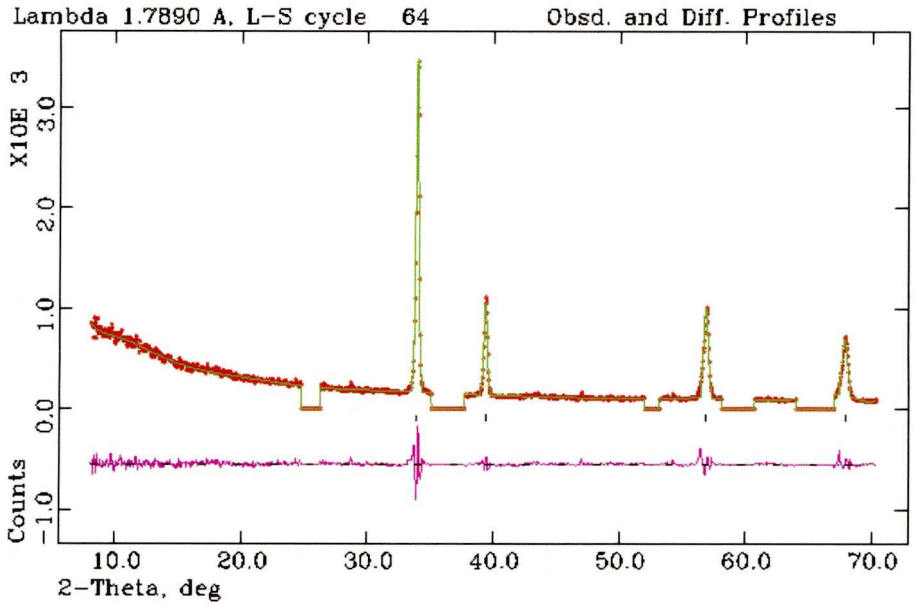

Figure A3.1. 3 LeBail refinement of 'reduced' $YbCaCeNbO_7$ (1200 °C in $5\%H_2$ $95\%N_2$) with the tick marks showing allowed reflections for the fluorite phase. The red crosses are data points the green line is the fit and the purple line the difference plot the excluded regions are to exclude peaks due to monoclinic perovskite. (λ = 1.7890 Å Rwp = 8.65% $\chi 2$ = 2.069).

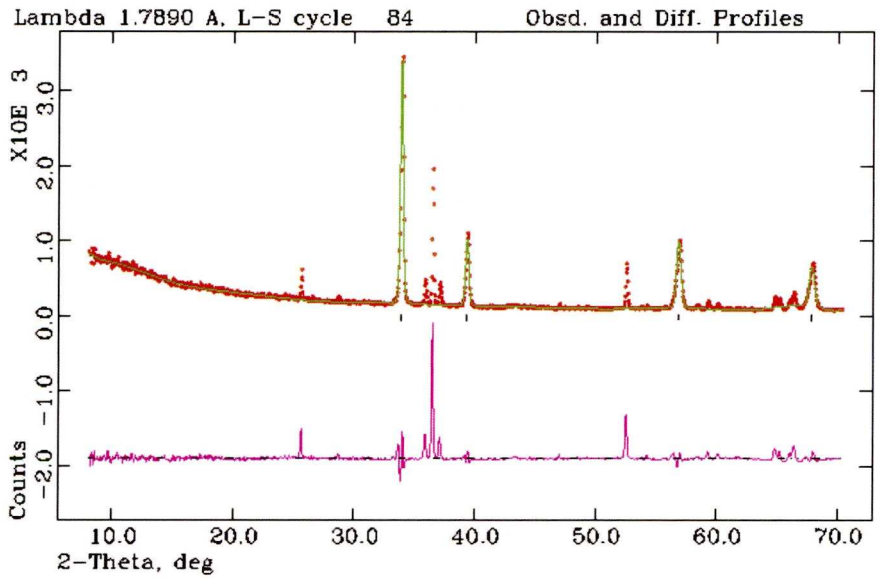

Figure A3.1. 4 LeBail refinement of the same data as A3.1.3 but without the excluded regions (λ = 1.7890 Å Rwp = 19.05% $\chi 2$ = 9.580).

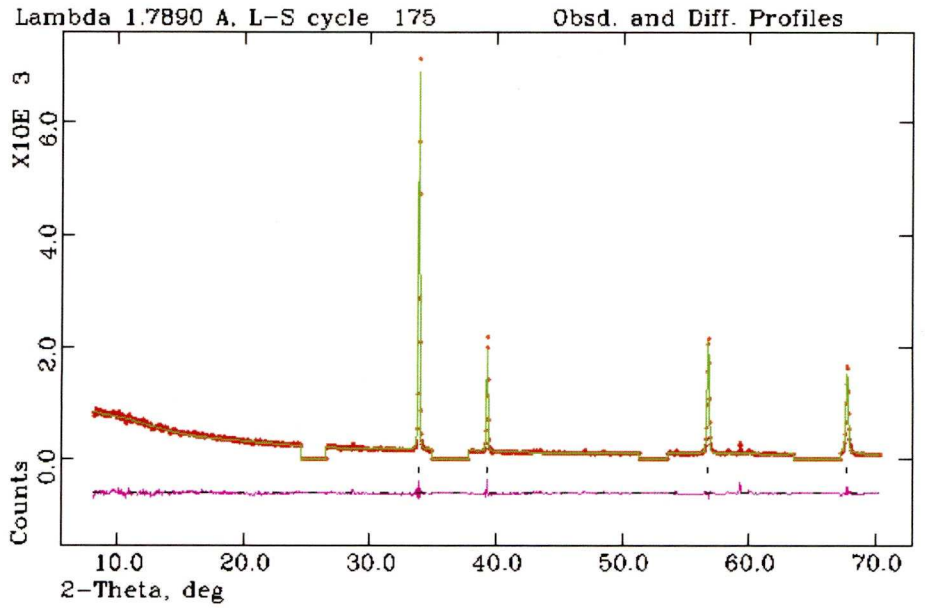

Figure A3.1. 5 LeBail refinement of 'reduced' $YbCaCeNbO_7$ (1480 °C in $5\%H_2$ $95\%N_2$) with the tick marks showing allowed reflections for the fluorite phase. The red crosses are data points the green line is the fit and the purple line the difference plot the excluded regions are to exclude peaks due to monoclinic perovskite. (λ = 1.7890 Å Rwp = 8.28% $\chi 2$ = 1.936).

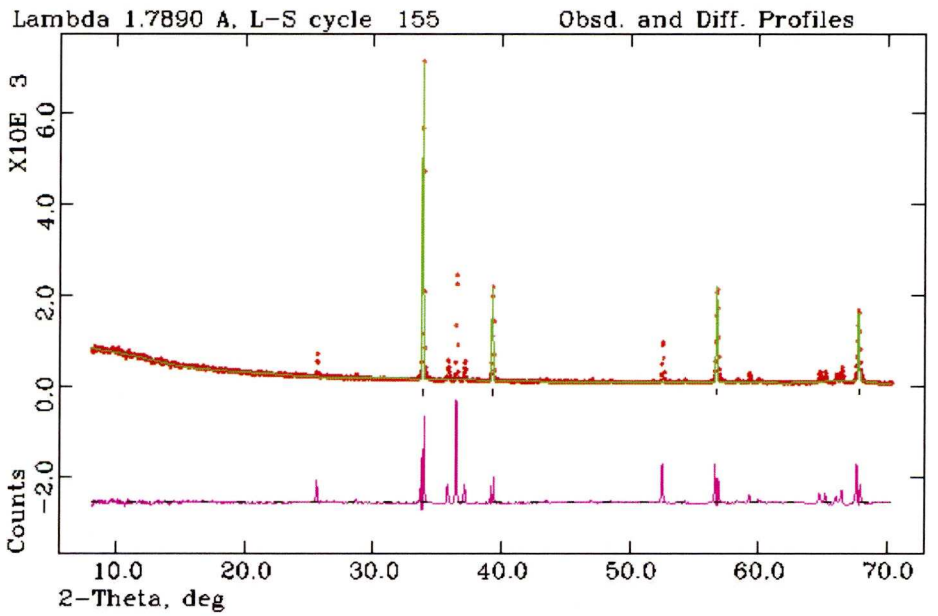

Figure A3.1. 6 LeBail refinement of the same data as A3.1.5 but without the excluded regions (λ = 1.7890 Å Rwp = 2.19% $\chi 2$ = 15. 80).

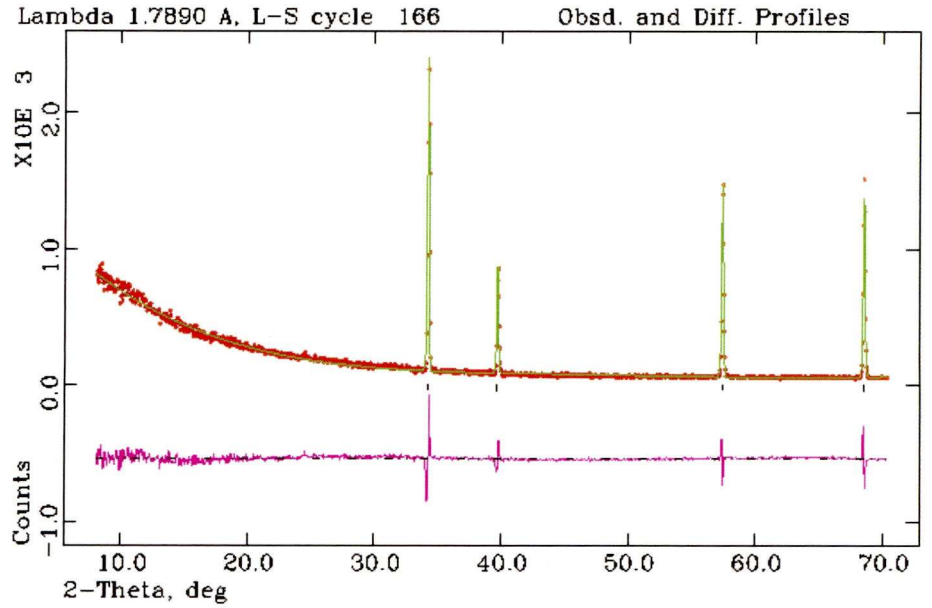

Figure A3.1. 7 LeBail refinement of 'reduced' $YbCaCeNbO_7$ (900 °C in $5\%H_2$ $95\%N_2$) that has been 're-oxidised' (1480 °C in air) with the tick marks showing allowed reflections for the fluorite phase. The red crosses are data points the green line is the fit and the purple line the difference plot. (λ = 1.7890 Å Rwp = 10.34% $\chi 2 = 2.094$).

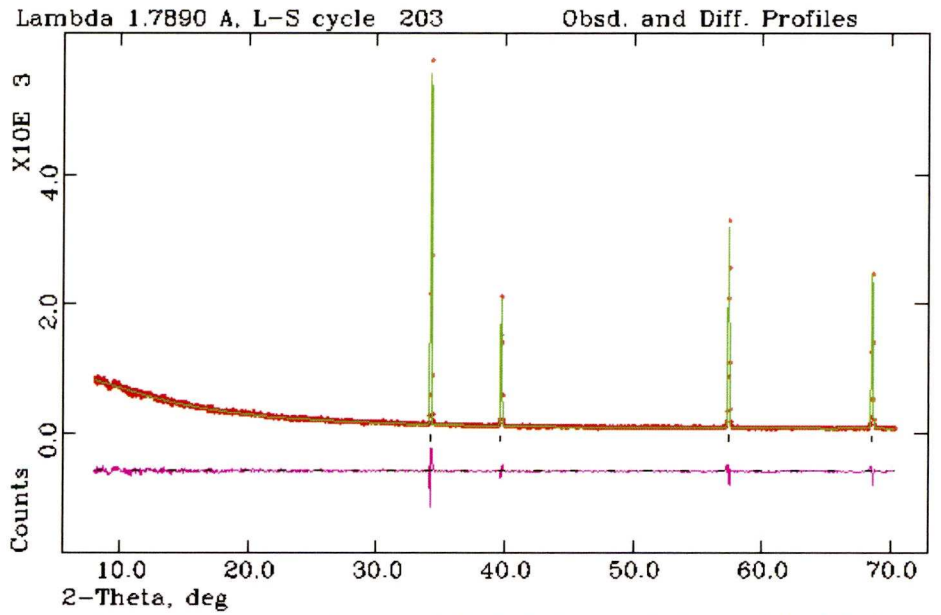

Figure A3.1. 8 LeBail refinement of 'reduced' $YbCaCeNbO_7$ (1480 °C in $5\%H_2$ $95\%N_2$) that has been 're-oxidised' (1480 °C in air) with the tick marks showing allowed reflections for the fluorite phase. The red crosses are data points the green line is the fit and the purple line the difference plot. (λ = 1.7890 Å Rwp = 7.54% $\chi 2 = 1.254$).

A3.2 $HoCaCeNbO_7$

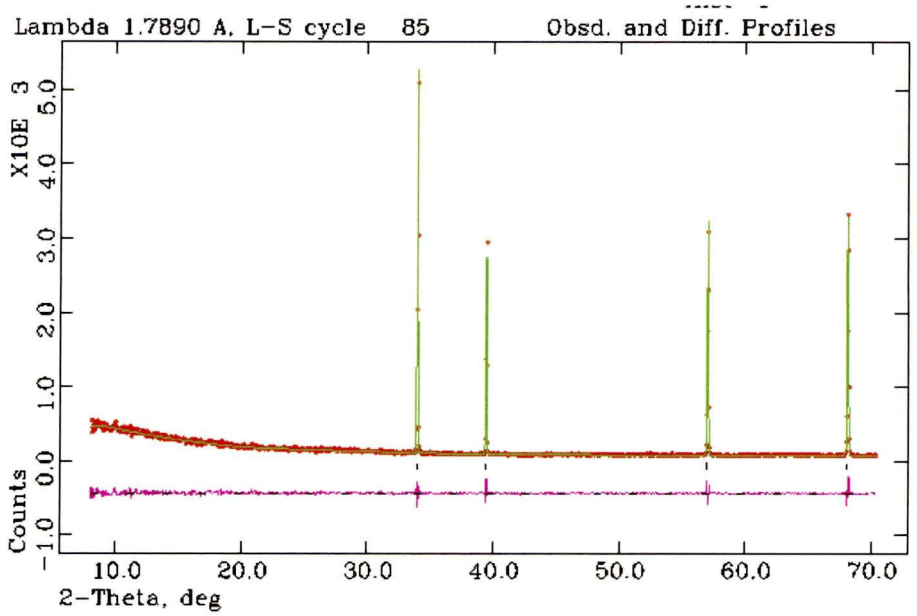

Figure A3.2. 2 LeBail refinement of 'as synthesized' $HoCaCeNbO_7$ (1480 °C in air) with the tick marks showing allowed reflections for the fluorite phase. The red crosses are data points the green line is the fit and the purple line the difference plot. (λ = 1.7890 Å Rwp = 8.6% χ^2 = 1.256).

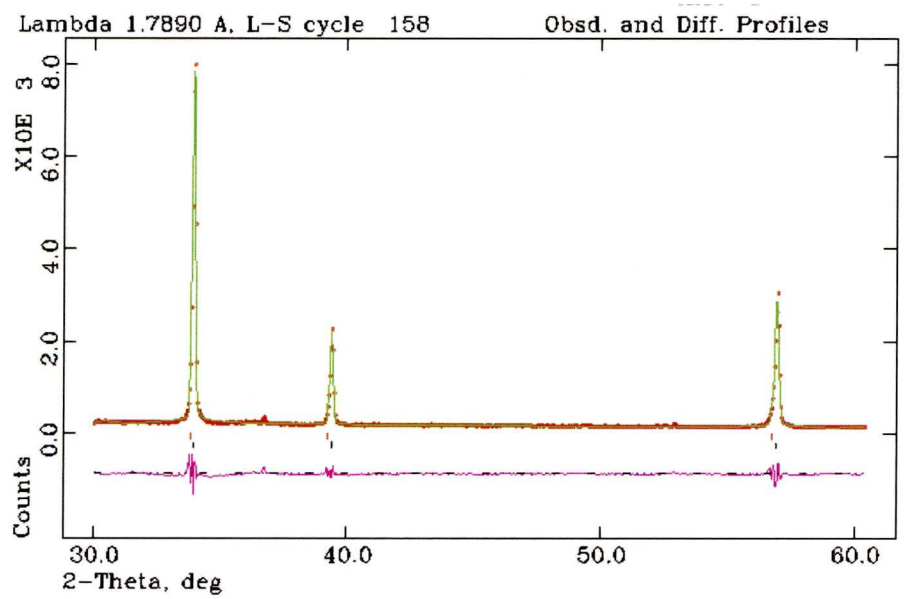

Figure A3.2. 2 LeBail refinement of 'reduced' $HoCaCeNbO_7$ (950 °C in 5%H_2 95%N_2) with the lower tick marks showing allowed reflections for the fluorite phase. The upper tick marks are take account of a shoulder on main peak which may be a second fluorite phase but only this shoulder is seen. The red crosses are data points the green line is the fit and the purple line the difference plot. (λ = 1.7890 Å Rwp = 10.37% χ^2 = 2.742).

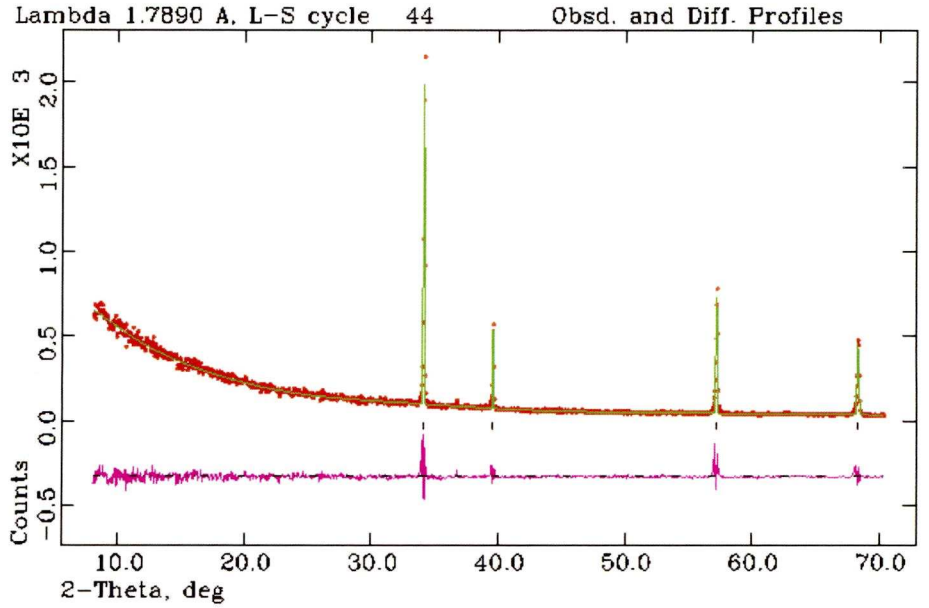

Figure A3.2. 3 LeBail refinement of 'reduced' $HoCaCeNbO_7$ (950 °C in 5%H_2 95%N_2) that has been 're-oxidised' (1480 °C in air) with the tick marks showing allowed reflections for the fluorite phase. The red crosses are data points the green line is the fit and the purple line the difference plot. (λ = 1.7890 Å Rwp = 9.96% χ^2 = 1.496).

A3.3 $EuCaCeNbO_7$

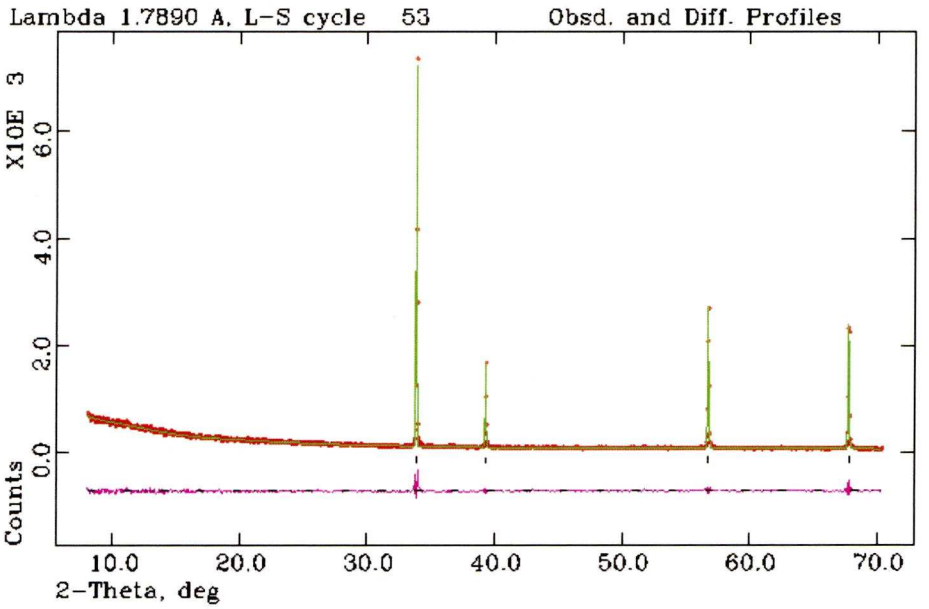

Figure A3.3. 3 LeBail refinement of 'as synthesized' $EuCaCeNbO_7$ (1600 °C in air) with the tick marks showing allowed reflections for the fluorite phase. The red crosses are data points the green line is the fit and the purple line the difference plot. (λ = 1.7890 Å Rwp = 8.41% χ^2 = 1.368).

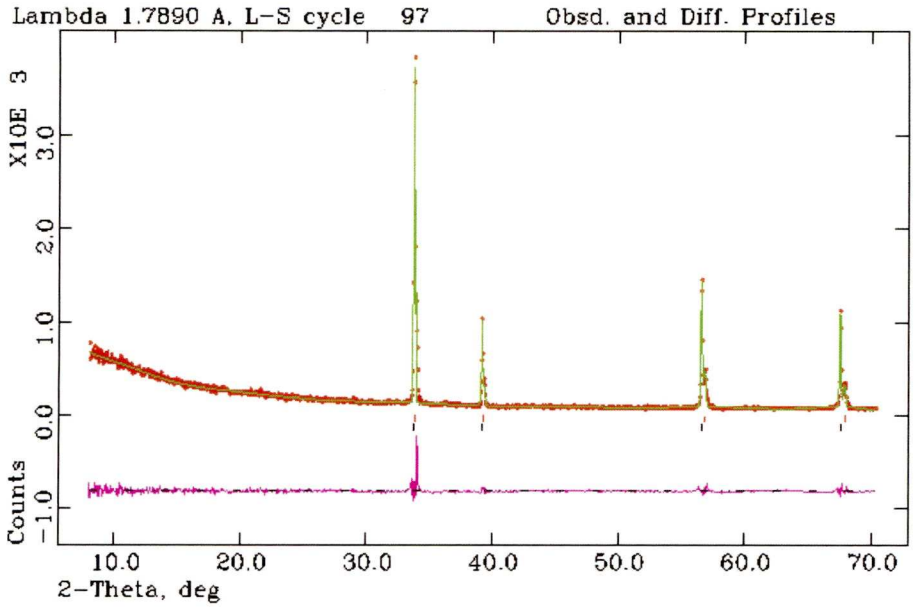

Figure A3.3. 2 LeBail refinement of 'reduced' $EuCaCeNbO_7$ (950 °C in $5\%H_2$ $95\%N_2$) with the lower tick marks showing allowed reflections for the main fluorite phase and the upper tick marks the minor fluorite phase. The red crosses are data points the green line is the fit and the purple line the difference plot. (λ = 1.7890 Å Rwp = 9.57% χ^2 = 1.710).

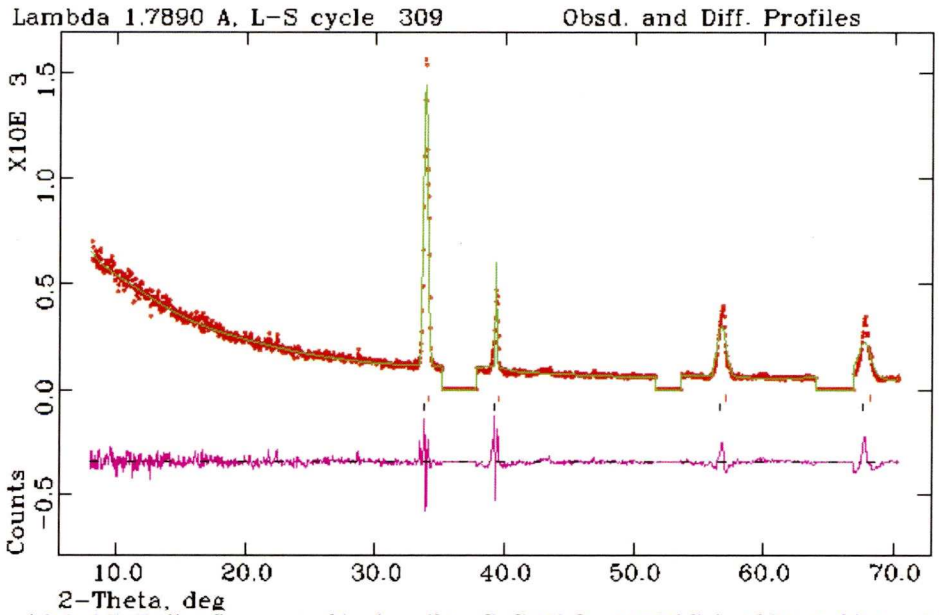

Figure A3.3. 3 LeBail refinement of 'reduced' $EuCaCeNbO_7$ (1200 °C in $5\%H_2$ $95\%N_2$) with the upper tick marks showing allowed reflections for the major fluorite phase and the lower tick marks the minor phase. The red crosses are data points the green line is the fit and the purple line the difference plot the excluded regions are to exclude peaks due to monoclinic perovskite. (λ = 1.7890 Å Rwp = 11.26% $\chi 2$ = 2.501).

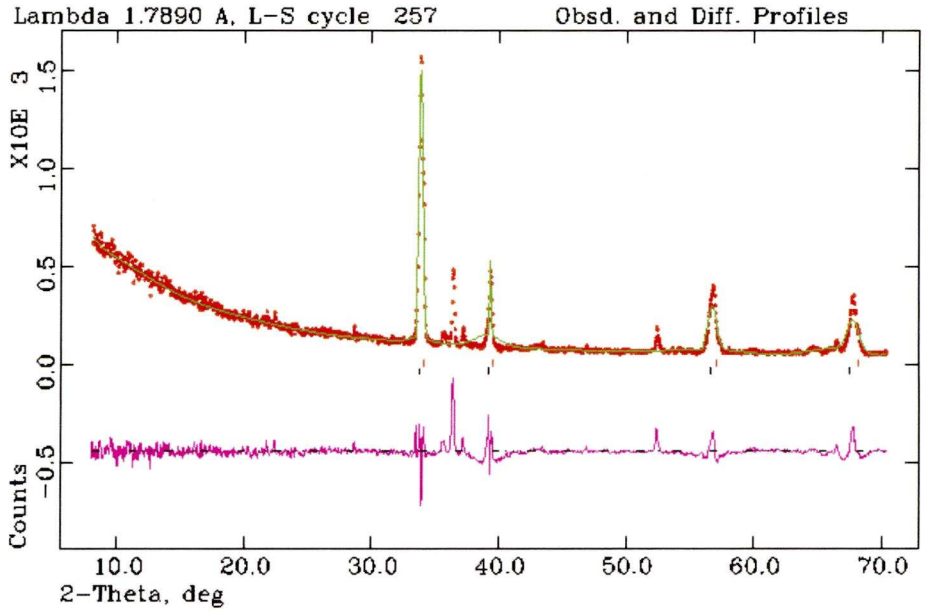

Figure A3.3. 4 LeBail refinement of the same data as A3.3.3 but without the excluded regions (λ = 1.7890 Å Rwp = 15.18% $\chi 2 = 4.041$).

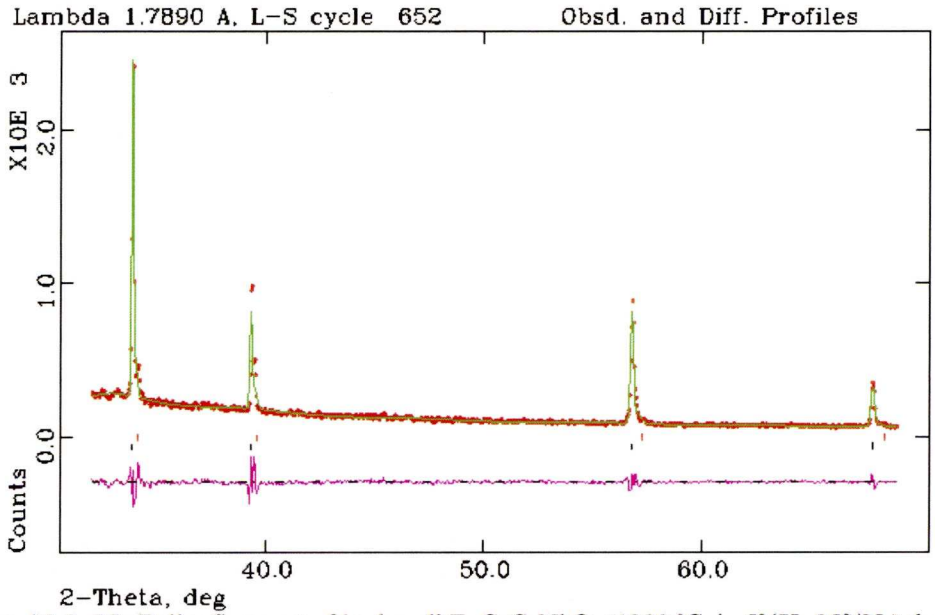

Figure A3.3. 5 LeBail refinement of 'reduced' $EuCaCeNbO_7$ (1200 °C in $5\%H_2$ $95\%N_2$) that has been 're-oxidised' (1580 °C in air) with the lower tick marks showing allowed reflections for the major fluorite phase and the lower tick marks the minor fluorite phase. The red crosses are data points the green line is the fit and the purple line the difference plot. Note due to lack of sample this refinement was carried out between 35-70° 2θ over 2 hours. (λ = 1.7890 Å Rwp = 8.72% $\chi^2 = 1.131$).